UNIVERSITY OF CALIFORNIA SAN DIEGO

Precision glycocalyx engineering strategies to modulate interactions at the cell surface

A dissertation submitted in partial satisfaction of the
requirements for the degree Doctor of Philosophy

in

Chemistry

by

Sean Cameron Purcell

Committee in charge:

Professor Kamil Godula, Chair
Professor Michael Burkart
Professor Karen Christman
Professor Neal Devaraj
Professor Jerry Yang

2022

The Dissertation of Sean Cameron Purcell is approved, and it is acceptable in quality and form for publication on microfilm and electronically.

University of California San Diego

2022

DEDICATION

To my family unit.

EPIGRAPH

In the midst of chaos, there is also opportunity.

Sun Tzu, *The Art of War*

TABLE OF CONTENTS

LIST OF FIGURES

LIST OF SCHEMA

ACKNOWLEDGEMENTS

I am grateful for the support of all of those who have helped me achieve this longstanding goal and educational milestone.

I am grateful to have had a dedicated and supportive research mentor in Dr. Kamil Godula. Thank you for your mentorship throughout my graduate career. You encouraged me to ask difficult scientific questions and allowed me the creative freedom to explore and grow independently while guiding my efforts. You challenged me to pursue elegant solutions and develop chemical tools with the potential to transform current practices. Thank you for supporting my goals and for the many lessons on science and leadership. I am proud of the work we have accomplished together over the past six years and am excited to see the lab's continued successes.

I am also grateful for the support of members of the Godula research group, past and present, who shared their expertise and enthusiasm for all things chemical glycobiology with me. I've had the great privilege of working closely with and learning from so many of you on various projects which collectively expand our understanding of the biological roles of glycocalyx and their underlying mechanisms, and my graduate experience has been all the richer for it. Special thanks are owed to Nate Marroquin and Hans Ng, talented and hardworking undergraduate scientists who tirelessly supported our projects and are now pursuing their own graduate educations. I would also like to specifically thank Dr. Yinan Wang and Dr. Mia Huang for exceptional training and guidance early in my research, which helped to set the trajectory for my projects.

Teaching has been an important part of my graduate career, and I am thankful for the mentors who helped me to grow as a leader and educator. Working with the lab development team led by Dr. Michelle Douskey at UC Berkeley and on the NSF-EAGER project led by Dr. Stacey Brydges at UC San Diego helped foster my passion for making chemistry accessible and showed me the great impact that can be realized when work extends into the broader community. Special thanks are also due to Dr. Joachim Latzer for giving me the opportunity to put my training to practice at Southwestern College. And to Dr. Brian Leigh, thank you for sharing your passion for teaching and ethics with me - I enjoyed working on AIR cases together and looked forward to the ensuing discussions.

To my early scientific mentors: Dr. David Spiciarich, Dr. Julea Vlassakis, Dr. Carolyn Bertozzi, and Dr. Amy Herr — thank you for sharing your time and knowledge with me. I could not be in this position without your guidance and mentorship. I'd also like to thank the collaborators I've had the privilege of working alongside, who've helped to shape the way I approach scientific problems and become friends. Working with Esko and Gordts lab members was particularly fulfilling and expanded my understanding of glycobiology profoundly.

Finally, I wish to thank my family for their unwavering support and encouragement throughout, and long before I began, my studies at UC San Diego. It's been an eventful six years and I am so glad it was spent together in San Diego.

Chapter one, in full, is a reprint of the material as it appears: Purcell S.C., Godula, K. Synthetic glycoscapes: addressing the structural and functional complexity of the glycocalyx. Interface Focus, 2019, 9: 20180080. The dissertation author is the primary co-author of this work.

Chapter two, in full, is a reprint of the material as it appears: Huang, M.; Purcell, S.; Verespy, S.; Wang, Y.; Godula K. Glycocalyx Scaffolding with Synthetic Nanoscale Glycomaterials. *Biomater. Sci.* 2017, 5, 1537-1540. The dissertation author is a co-author of this work.

Chapter three, in full, is a reprint of the material as it appears in a manuscript submitted for publication: Purcell, S.; Zhang, M.Z.; Honigfort, D.J.; Ng, H.J.C.; Michalak, A.L.; Godula, K. Glycocalyx photoengineering enables modeling of cell-surface mucin shedding dynamics. The dissertation author is a primary co-author of this work.

Chapter four, in full, is work in preparation for publication: Purcell, S.; Naticchia, M.R.; Marroquin, N.; Ng, H.J.C.; Godula, K. Proteoglycan chimeras selectively potentiate neural differentiation in embryonic cells. The dissertation author is the primary co-author of this work.

Chapter five, in part, contains unpublished work which was co-authored: Purcell, S.; Porell, R.; Follmar, J.; Godula, K. Chapter 5.3, Covalent heparin conjugates for glycocalyx engineering. The dissertation author is the primary co-author of this work.

VITA

2016 Bachelor of Science, Chemical Biology, UC Berkeley

2016 – 2021 Teaching Assistant, UC San Diego

2016 – 2022 Graduate Researcher, Godula Laboratory, UC San Diego

2018 Master of Science, Chemistry & Biochemistry, UC San Diego

2018 Adjunct Instructor, Physical Sciences, Southwestern College

2022 Doctor of Philosophy, Chemistry, UC San Diego

Publications

Michalak, A.; **Purcell, S.**; Marotz, L.; Zengler, K.; Godula, K. Soluble DNA-encoded mucin mimetic microarrays enable profiling of glycan interactions in live cell populations. (*In preparation, 2022*)

Purcell, S.; Naticchia, M.R.; Marroquin, N.; Ng, H.J.C.; Godula, K. Proteoglycan chimeras selectively potentiate neural differentiation in embryonic cells. *(In preparation, 2022)*

Porell R.; Follmar J.; **Purcell, S.**; Timm B.; Laubach, L.; Kozirovskiy, D.; Thacker, B.; Glass, C.; Gordts, P.L.S.M.; Godula, K. Development of biologically derived neoproteoglycans for protein binding and functional bioassays. (*In preparation, 2022)*

Purcell, S.; Zhang, M.Z.; Ng, H.J.C.; Michalak, A.L.; Godula, K. Glycocalyx photoengineering enables modeling of cell-surface mucin shedding dynamics. (*submitted*, *2022*)

Trieger, G.W.; Pessentheiner, A.R.; **Purcell, S.**; Green, C.R.; Deforest, N.; Willert, K.; Majithia, A.; Metallo, C.M.; Godula, K.; Gordts, P.L.S.M. Glycocalyx engineering with heparan sulfate mimetics attenuates Wnt activity during adipogenesis to promote glucose uptake and metabolism. *(submitted, accessible on BioRxiv 2021)*

Naticchia, M.R.; Laubach, L.K.; Honigfort, D.J.; **Purcell, S.**; Godula, K. Spatially controlled glycocalyx engineering for growth factor patterning in embryoid bodies. *Biomater. Sci.* 2021, 9, 1652-1659.

Purcell, S.; Godula, K. Synthetic Glycoscapes: addressing the structural and functional complexity of the glycocalyx. *J. R. Soc. Interface Focus.* 2019, 9: 20180080.

Huang, M.; **Purcell, S.**; Verespy, S.; Wang, Y.; Godula K. Glycocalyx Scaffolding with Synthetic Nanoscale Glycomaterials. *Biomater. Sci.* 2017, 5, 1537-1540.

Spiciarich, D.; Nolley, R.; Maund, S.; **Purcell, S.**; Herschel, J.; Iavarone, A.; Peehl, D.; Bertozzi, C. Bioorthogonal labeling of human prostate cancer tissue slice cultures for glycoproteomics. *Angew. Chem. Int. Ed.* 2017, 56, 8992-8997.

Purcell, S.; Pande, P.; Lin, Y.; Rivera, E.; PawU, L.; Smallwood, L.; Kerstiens, G.; Armstrong, L.; Robak, M.; Baranger, A.; Douskey, M. Extraction and Antibacterial Properties of Thyme Leaf Extracts: Authentic Practice *of* Green Chemistry. *J. Chem. Educ.* 2016, 93(8), 1422-1427.

Fellowships and Awards

2012 UC Berkeley Regents' and Chancellor's Scholar

2016 Teaching Assistant Excellence Award, Dept. of Chemistry, UC San Diego

2017 Honorable Mention, National Science Foundation Graduate Research Fellowship Program

2018 US Dept. of Education Graduate Assistance in Areas of National Need (GAANN) Research Fellowship, Dept. of Chemistry, UC San Diego

2019 Teaching Assistant Excellence Award, Dept. of Chemistry, UC San Diego

Fields of Study

Major fields: Chemistry and Chemical Glycobiology

Studies in Glycan Engineering, Bioconjugation, and Synthetic Nanomaterials

Professor Kamil Godula

ABSTRACT OF THE DISSERTATION

Precision glycocalyx engineering strategies to modulate interactions at the cell surface

by

Sean Cameron Purcell

Doctor of Philosophy in Chemistry

University of California San Diego, 2022

Professor Kamil Godula, Chair

The ability to systematically manipulate the glycocalyx, composed of the collection of glycoconjugates extending from the cell surface, is paramount to understanding structure-function relationships in glycan-mediated biological processes including cell signaling, development, and pathogenesis. Diverse approaches for glycan engineering have emerged, drawing upon chemical, chemoenzymatic, and genetic techniques to augment, edit, or remove cell surface glycoconjugates. Among these strategies, methods to build complexity at the cellular boundary *de novo* have been particularly effective in revealing the complex relationships between glycan organization within the glycocalyx and the exchange of information between a cell and its environment. While major strides have been made in glycocalyx engineering through the combination of genetic knockouts

paired with synthetic glycomaterials that can be inserted into the glycocalyx, these methods generally lack specificity and dynamic control, limiting their biological applications. In this work, several cell surface engineering strategies are reported which collectively address these challenges. First, the ability to spatially program glycan binding activity at the cell surface by scaffolding an artificial glycocalyx comprising both distally presented glycopolymers and surface-proximal glycolipids is presented. Next, utilizing materials bearing photolabile membrane anchors, the ability to spatiotemporally pattern glycocalyx interactions is demonstrated in the context of the mucosal barrier. This glycocalyx photoengineering technique enabled study of the effects of lectin crosslinking on mucin shedding, a key process in pathogenesis. Next, glycomaterials composed of a targeting aptamer unit and bioactive glycodomain were used to program activity in a cell and developmental-stage specific manner in the context of stem cell differentiation, where enhanced differentiation outcomes were observed. Together, these precision glycocalyx engineering strategies enable selective activation or deactivation of glycan dependent interactions and may shed light on the roles of the glycocalyx in therapeutically relevant biological processes.

1 Synthetic Glycoscapes

1.1 Addressing the structural and functional complexity of the glycocalyx

The glycocalyx is an information-dense network of biomacromolecules extensively modified through glycosylation populating the cellular boundary. The glycocalyx regulates biological events ranging from cellular protection and adhesion to signaling and differentiation. Due to the characteristically weak interactions between individual glycans and their protein binding partners, multivalency of glycan presentation is required for the high-avidity interactions needed to trigger cellular responses. As such, biological recognition at the glycocalyx interface is determined by both the structure of glycans that are present as well as their spatial distribution. While genetic and biochemical approaches have proven powerful in controlling glycan composition, modulating the three-dimensional complexity of the cell surface “glycoscape” at the sub-micrometer scale remains a considerable challenge in the field. This focused review highlights recent advances in glycocalyx engineering using synthetic nanoscale glycomaterials, which allows for controlled *de novo* assembly of complexity with precision not accessible with traditional molecular biology tools. We discuss several exciting new studies in the field that demonstrate the power of precision glycocalyx editing in living cells in revealing and controlling the complex mechanisms by which the glycocalyx regulates biological processes.

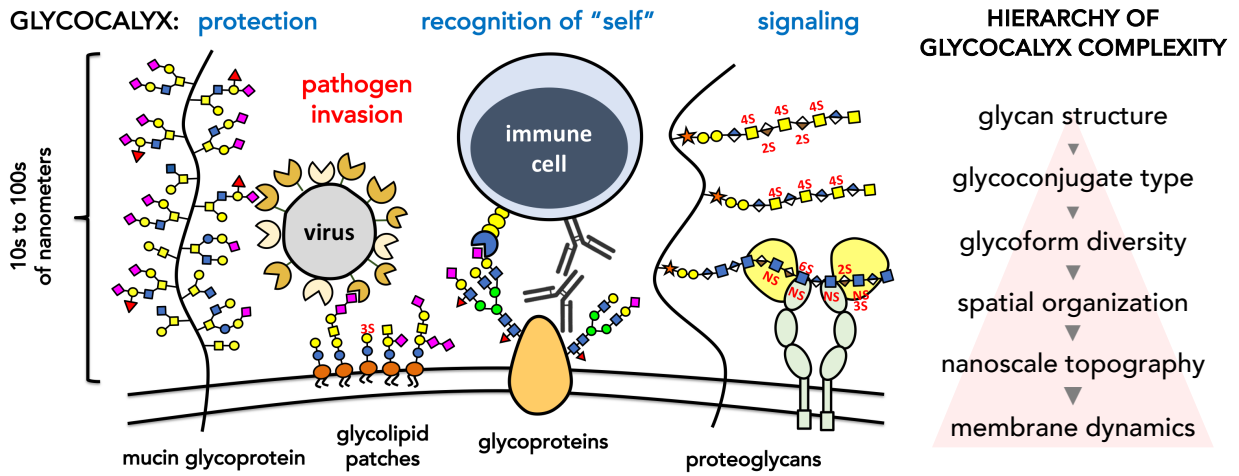

Figure 1.1 Glycocalyx complexity. The cellular glycocalyx is a biological interface mediating the exchange of information between cells and their surroundings. Composed of glycolipids and glycoproteins bearing a large diversity of glycan structures, the glycocalyx is a complex and dynamic macromolecular network, which harbors both signatures of "self" as well as molecular targets for opportunistic pathogens.

1.2 Introduction

The cellular glycocalyx,[1] a biological interface composed of membrane-bound glycolipids and glycoproteins, controls major biological events including protection from pathogens, regulation of immune responses, and mediation of cellular communication, among others.[2] The complexity of the glycocalyx, which is the product of the combined chemical diversity of its glycan structures and their lipid and protein carriers, can be advantageous from a biological standpoint but complicates its study and manipulation (Figure 1.1). While individual glycans provide structural basis for affinity and selectivity in protein recognition, their nanoscale organization within glycoconjugates and across the glycocalyx dictate the localization and extent of their activity.[1] As such, the "glycoscape" at the cell surface needs to be considered in its entirety to fully understand the biological processes occurring at the cell surface.

One important outcome of evolution is the selection of glycans to serve as chemical determinants of "self" at the surfaces of cells,[3] while providing a barrier against pathogenic invasion (Figure 1). The non-templated biosynthesis of glycoconjugates offers a means to rapidly generate unique molecular signatures to limit the adhesion of pathogens, which constantly adapt to exploit cell surface glycans to enter the cell.[4] Interestingly, as the glycoscape continuously changes to minimize pathogenic threats, it must maintain its unique "self" signature to avoid triggering an immune response. The centrality of glycans in these two concurrent but divergent functions raises the intriguing question of what molecular patterns define "self" at the cell surface.

The mammalian glycome is constructed from a relatively small pool of building blocks (~ 10 monosaccharides).[5] While still affording a vast structural space of possible linear and branched glycans, only a small fraction of this space is actually occupied based on the availability and specificity of glycosyltransferase enzymes that catalyze the formation of glycosidic bonds.[5] To overcome the limitations on the diversity of biosynthetically accessible glycan structures, additional complexity can be derived from glycan presentation in glycoconjugates and the distribution of the glycoconjugates throughout the glycocalyx. The individual glycan structures can be organized within the glycocalyx to present unique molecular patterns, which are recognized by the various components of the innate and adaptive immune systems (Figure 1).[6,7] Since the most accessible terminal glycan modifications (e.g., sialic acids) are often the target of protein receptors, it is conceivable that the molecular patterns that define "self" may be assembled from diverse set of glycans, as long as the terminal modifications are attached

through an appropriate glycosidic linkage needed for recognition and are optimally distributed within the glycocalyx.[7]

Understanding the ways in which cells utilize glycan presentation to maintain a specific “signal” within the “noise” of the evolving glycocalyx will be critical to fully account for the various biological functions of glycans. Defining how spatial organization of glycans determines biological responses should be of great interest to the biomedical community for its potential value in the development of therapeutics that discriminate between host cells and pathogens or that harness the protective functions of the immune response for therapeutic gain.[8,9]

Answering these questions will necessitate systematic cataloging of the composition and spatial organization of the glycocalyx and correlating this information with its biological functions. Current techniques to control the composition of the glycocalyx[10, 11] rely primarily on genetic[12] approaches that target the expression of specific glycan biosynthesis enzymes to influence glycan assembly, chemoenzymatic methods[13] for editing of existing cell-surface glycan structures, and metabolic strategies[14] for the introduction of non-natural monosaccharide modifications across the glycome. While powerful, these techniques result in the addition or subtraction of a specific glycan feature across entire classes of glycoconjugates and, thus, induce a global perturbation in the glycocalyx without control over cell surface presentation and nanoscale organization.

More recently, efforts to recapitulate the structural and organizational complexity of the glycocalyx have borrowed from synthetic biology; chemical tools have enabled the synthesis of nanoscale glycomaterials that mimic the various components of the

glycocalyx and can be used to edit or even build synthetic glycoscapes on the surface of living cells (Figure 1.2). Our aim is to highlight some recent advances in the field of synthetic glycobiology that enable the creation of *de novo* display of glycans, glycoconjugates, and mimetics in analytical platforms and on surfaces of living cells with enhanced spatial and temporal control over glycan structure and organization. Sometimes referred to as “precision glycocalyx editing”, this approach is becoming increasingly integrated with more traditional methods aiming to answer fundamental questions in glycobiology.

In principle, the bottom-up nature of precision glycocalyx editing allows for the assembly of cellular glycoscapes composed of virtually unlimited combinations of glycan structures and macromolecular scaffolds. However, the power of this approach will ultimately lie in the ability to reliably recapitulate biologically relevant architectures found within the native glycocalyx. The glycocalyx has so far resisted detailed characterization of its composition and organization at the molecular level. However, advances in MS-based glycoproteomics, super resolution optical imaging and cryoelectron microscopy, and chemical approaches to capture and spatially correlate interactions within the glycocalyx provide hope for a more clear view of the cellular glycocalyx and its biological functions in the near future.

Nanoscale mimetics of macromolecular constituents of the glycocalyx

Synthetic glycomaterials have long provided a vital tool for analyzing glycan protein interactions.[15] Used extensively as soluble ligands with controlled multivalent glycan presentation, they have helped reveal the mechanisms that allow glycan binding proteins

to recognize and engage glycan displays on glycoproteins to transfer biological information.[16,17,18] Modern macromolecular synthesis methods and protein- and nucleic acid-templated[19] material assembly strategies provide access to chemically defined 1D linear glycopolymers,[20] 3D glycodendrimers,[21] and even extended 2D glycoarrays[22] where individual glycans can be presented with exquisite control over glycan valency and spatial organization at the nanometer scale (Figure 1.2).

Among the many contributions to the field over the last three decades,[23] some studies stand out as particularly powerful examples of the utility of synthetic glycomaterials in revealing the mechanisms that underpin the biological recognition of glycans. In a series of early reports, the groups of Bovin, Whitesides and Kiessling employed linear glycopolymers to investigate the effects of glycan valency and spacing on avidity of viral hemagglutinin[24,25] and lectin[26,27] binding. Notably, the Kiessling group later developed a set of simple high-throughput assays that allowed them to delineate the relationships between nanoscale architecture of macromolecular glycoconjugates (i.e., compact globular vs. extended linear structures) and their ability to promote distinct binding events such as lectin inhibition or receptor clustering.[16] Since these pioneering studies, a wide range of glycoconjugate mimetic scaffold architectures have been proposed and investigated as inhibitors or modulators of glycan-binding receptor activities with an eye toward biomedical applications.[28,29] More recently, the predictability and programmability of nucleic acid assembly into nanoscale materials has enabled the generation of glycomaterials with sub-nanometer precision in glycan presentation. These advanced materials have provided further insights into glycan interactions in a biological context,[30,31] allowing for controlled assembly of glycan microheterogeneity[32] and the

selection of optimal glycoconjugate-receptor pairs using dynamic assembly[19] and directed evolution[33,34] of glycoconjugates.

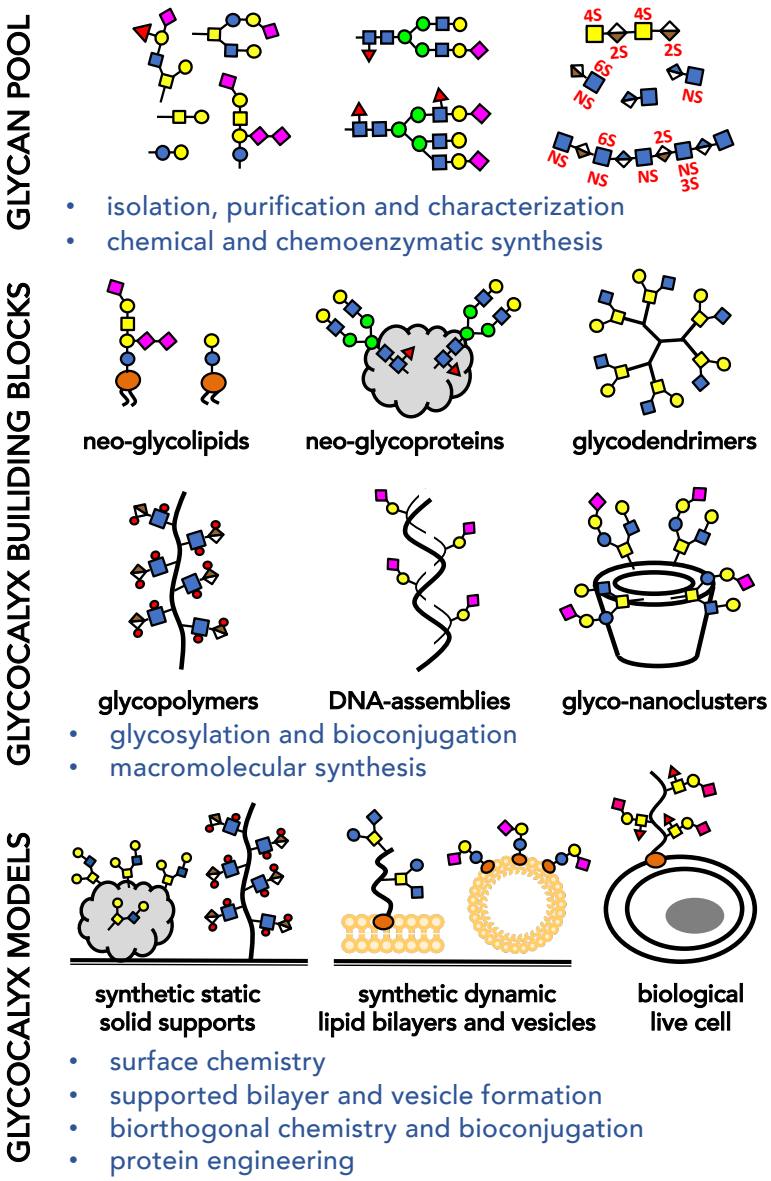

Figure 1.2 Synthetic glycobiology toolkit for addressing glycocalyx complexity. An increasingly large pool of glycan structures is becoming available due to advancements in glycan isolation and purification and in chemical and chemoenzymatic methods for their synthesis. Individual glycans can be assembled into synthetic and semi-synthetic glycoconjugates, which mimic the architecture of natural glycolipids and glycoproteins. Structurally well-defined glycomimetics serve as building blocks for the *de novo* construction of glycocalyx models by immobilization on solid supports or by anchoring in lipid bilayers, lipid vesicles, or directly in the plasma membranes of living cells.

1.3 Static surface supported glycocalyx models

As nanoscale glycomaterials became indispensable tools for probing the molecular interactions of glycoconjugates with glycan binding proteins, it became evident that the properties of glycoconjugates in solution could not fully recapitulate their ensemble behavior at surfaces. For instance, glycans functionalized with alkanethiolates forming self-assembled monolayers (SAM) on gold surfaces revealed that the modulation of surface glycan density can result in a switch in lectin binding specificity and may act as an “on-off” switch for downstream biological processes.[35] Similarly, variations in macromolecular glycoconjugate and polysaccharide architecture and surface grafting density introduces additional considerations for evaluating their recognition by glycan-binding proteins (Figure 1.2). The immobilization of macromolecular glycoconjugates on surfaces can enhance multivalency and avidity of glycan displays[36] but also alter their molecular conformation and dynamics (e.g., mushroom to brush polymer transitions) affecting protein diffusion. [37,38] A close proximity of glycoconjugates on surfaces can also promote higher-order binding interactions, such as crosslinking of neighboring glycoconjugates by multimeric lectins (Figure 1.3).[39]

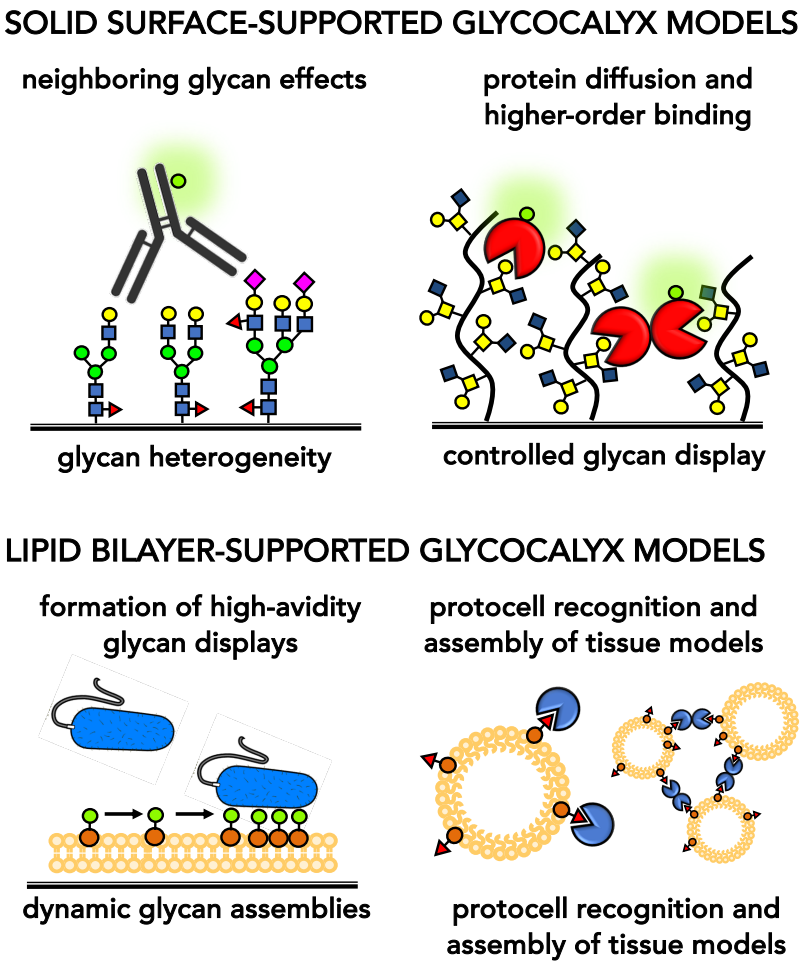

Figure 1.3 Synthetic glycoscapes. Static glycocalyx models immobilized on solid supports offer control over glycan composition and presentation and facile integration with common analytical platforms. Glycocalyx structures anchored in model membranes can dynamically reorganize to provide optimal presentations for high-avidity binding. Lipid vesicle carriers allow for investigation of the relationships between membrane curvature and glycocalyx organization and to model glycan-mediated assembly of multicellular systems.

An intriguing property of surface glycoconjugate displays is the possibility to generate glycocalyx models with spatially addressable structural complexity. It is increasingly recognized that changes in the microheterogeneity of glycan environments within the cellular glycocalyx can have profound influence on cellular functions.[40] The glycan microarray provides a powerful platform for rapid profiling of protein interactions with surface-immobilized glycans.[41] Established initially as a way to present individual glycans,[42] the array concept was later expanded to include well defined synthetic

glycoconjugates, such as neo-glycoproteins,[43,44] glycodendrimers[45] or glycopolymers,[39,46,47] allowing for presentation of glycans in a number of modes with control over scaffold geometry, glycan valency and spacing, and surface density of glycoconjugates. Most recently, glycan arrays prepared by immobilization of glycan mixtures within individual spots revealed that the presence of neighboring glycans may result in higher avidity antibody binding to target epitope and that both density and structure of neighboring glycans can effect recognition (Figure 1.3).[48,49] These findings confirmed that glycan microheterogeneity within the cellular glycocalyx should be an important consideration in the development of therapeutics targeting glycocalyx structures on pathogens as well as human cells.

One advantage of static surface-immobilized glycan displays is the ability to utilize advances in micro- and nanofabrication technologies and high-resolution imaging techniques to create and characterize high information-content arrays. Microcontact printing of pre-functionalized glycomaterials[50] or surface-initiated *de novo* glycoconjugate synthesis using beam pen lithography[51] provide two examples illustrating the emerging opportunities for building increasingly complex models of the glycocalyx on solid supports.

1.4 Dynamic membrane-supported glycocalyx models

Despite the convenience and utility of glycoconjugate presentation on solid surfaces, these displays fail to capture the dynamic features of the native glycocalyx. There, the lateral membrane diffusion of individual glycoconjugates components is permitted and results in a highly adaptable environment in which molecular interactions occur. This property of the glycocalyx can be critical for its ability to modulate processes

such as receptor clustering, formation of the immunological synapse, or mediation of host-pathogen interactions (Figure 1.3). The supported lipid bilayer[52] serves as an excellent experimental model of the fluid plasma membrane of cells to study glycocalyx-associated phenomena.[53, 54] Supported lipid bilayer experiments have provided important insights into the effects of glycolipid density and clustering on their recognition by soluble lectins,[55] as well as by the more complex arrays of glycan-binding receptors on the surfaces of viruses[56] and bacteria.[57] The supported bilayer system can also be used to investigate the behavior of macromolecular glycoconjugates in membranes. Interferometric imaging of lipid-anchored nanoscale synthetic mimetics of mucin glycoproteins, which recapitulate the characteristic long extended architectures of mucins stemming from dense glycosylation of their core polypeptide backbones, revealed the tendency of these materials to accommodate upright orientations and project distally from the membrane surface while retaining lateral mobility in the lipid bilayer.[58] Similarly, dynamic surface presentations of hyaluronic acid and heparan sulfate glycosaminoglycan (GAG) polysaccharides in supported lipid bilayers have provided insights into biophysical behavior, mobility, and molecular recognition within sterically crowded glycocalyx environments.[38] The observed changes in GAG organization and behavior induced by protein binding and crosslinking suggest that growth factor and cytokine activity may not be limited to receptor activation but that altered glycocalyx dynamics may also contribute to signaling events.

In an effort to create increasingly realistic and complex models of the cell surface, it has become apparent that additional features of the cell surface, such as curvature and the related capacity to undergo membrane fusion and vesicle budding, need to be

considered. This is particularly relevant as the changes in glycocalyx composition and the generation of membrane curvatures and shapes are locked in an intimate reciprocal relationship.[59,60] The development of protocells with well-defined surface glycan displays offers an elegant solution to this challenge. Giant unilamellar vesicles (GUVs) serve as an artificial cell membrane upon which a synthetic glycocalyx can be constructed using cholesterol-modified glycopeptides (Figure 1.3).[61] The glycocalyx structures can be incorporated into the membrane by electroformation with lipids during GUV formation or by spiking of pre-formed vesicles. Interestingly, in phase-separated GUVs, the glycopeptides preferentially localized to the liquid-disordered domain, thus introducing a means by which to control spatial organization of glycoconjugates on the protocell surface. Systematic modification of the glycopeptide scaffold using a series of orthogonal click reactions to introduce combinations of anchors, optical probes for visualization, and glycans provided access to compositionally diverse materials for functional glycan-receptor pairing. [62] The platform proved to be an effective tool for studying the role of ABO blood group antigen on malarial rosetting, as it allowed for systematic presentation of the blood group antigen of interest on otherwise identical cells. [63] This approach led to the demonstration of receptor-specific malarial cell aggregation, or rossetting, by the *P. falciparum* parasites based on the structure of blood group antigens. Importantly, the protocell also offers an experimental system in which glycan interactions can be evaluated in the context of the assembly and organization of more complex higher order multicellular systems.[64,65] Protocell designs based on the self-assembly of glycosylated amphiphilic block copolymers and glycodendrimersomes have also recently emerged to model pathogen interactions with the glycocalyx of host cells [66] and to rapidly evaluate

the surface crosslinking and aggregation capacity of galectins in response to changes in compositional microheterogeneity of glycolipid patches,[67] respectively. Together, these studies demonstrate the power of dynamic synthetic models of the cell surface for uncovering how the spatial and organizational complexity of the cellular glycocalyx influences molecular interactions at the cellular boundary. They provide a foundation for further exploration of this intricate biological interface to ultimately identify molecular patterns that constitute the markers of “self” and “non-self” and how these signals are maintained in the rapidly evolving glycocalyx environment.

.

1.5 Precision glycocalyx editing in living cells

While synthetic models of the cellular glycocalyx have been instrumental in developing the concepts of avidity in glycan interactions and delineating the mechanisms that underlie molecular interaction of glycans at the cell surface, ultimately these findings need to be brought into the context of cellular functions. Not surprisingly, developing approaches to control glycan presentation within the glycocalyx of living cells has been an area of intense focus.[68,11] Early work focused on applying genetic,[69] enzymatic[13] and chemical[70] strategies to remove or add unique glycosylation motifs to cell surface structures. More recently, these efforts have shifted toward the development of methods for building spatially and organizationally complex glycoscapes at the cell surface with greater precision with respect to glycan organization and localization to enable the study complex biological processes, including signaling, differentiation, and tissue morphogenesis.

Among the examples illustrating the power of chemoenzymatic glycan engineering with exogenous glycosyltransferases are studies linking the regioselectivity of sialic acid

linkages to underlying glycan structures on cell surfaces to host-specificity of Influenza A viruses[71] or demonstrating that the conversion of the CD44 glycoform into an E-selectin ligand via the addition of α-1,3-linked fucose can promote mesenchymal stem cell homing into bone marrow.[72] Chemoenzymatic glycosylation alters the structure of all acceptable enzyme substrates within the glycocalyx, limiting the ability to modify specific sets of glycoconjugates. Non-covalent modification of the cellular glycocalyx through insertion of lipid-containing glycans into the plasma membrane overcomes this problem (Figure 1.4). Early studies showing that glycosphingolipids with Lewis blood group antigens isolated from plasma were taken up by the membrane of human erythrocytes[73] later led to the development of a modular platform for the synthesis of synthetic glycolipid mimetics which consists of a lipid for membrane insertion, a spacer with tunable chemical properties, and a functional end group consisting of a glycan unit. [74] The glycoconjugates were utilized to stably remodel the surface of red blood cells with analogs of blood group determinants and verified by serological analysis.[75] In a particularly compelling example of this approach, a synthetic globotriaosylceramide analogue incoported into the cell membrane inhibited infection by HIV-1 via both inhibition of viral entry and direct viral inhibition. [76]

The initial studies on membrane-supported glycocalyx models (*vide supra*), paved the way for *de novo* assembly of glycocalyx structures on the surfaces of living cells.[77] Glycopolymers or polysaccharides[78] functionalized with phospholipid or cholesterol anchors can be passively inserted into the cell membrane. The use of chemically defined glycoconjugates permits the introduction of specific glycan motifs in predefined spatial arrangement and removes the limitations of chemoenzymatic glycan engineering

imposed by the specificity of glycosyltransferase enzymes. The compositional complexity of the artificial glycocalyx that can be achieved using this method is not limited to a single glycoconjugate, as multiple glycoconjugates carrying distinct glycan structures and presentation can be introduced simultaneously at tunable ratios.[79] Thus, the composition and hierarchical organization of the cellular glycoscape can be designed and rapidly constructed to meet specific experimental needs.

The precision glycocalyx editing approach has been leveraged to elucidate and control vital cellular signaling processes. For instance, sialylated glycopolymer mimetics of mucin glycoproteins were used to recapitulate the hypersialylated glycocalyx of adenocarcinoma cells. The remodeled cells showed the ability to dampen antigen-induced natural killer (NK) cell cytotoxicity by recruiting inhibitory siglec receptors into the immunological synapse.[80] Engineering the GAG component of the cellular glycocalyx to control cellular signaling via growth factors and morphogens has also been an area of active research. Liposomes modified with chondroitin sulfate (CS) GAG polysaccharides were shown to undergo fusion with the membrane of neurons. The cell-anchored CS GAGs potentiated neurotrophin signaling and neurite outgrowth in a sulfation pattern-dependent manner.[78] HS GAG mimetic polymers with affinity for the fibroblast growth factor 2 and bone morphogenetic protein 4 have also been developed and used to edit the glycocalyx of embryonic stem cells deficient in heparan sulfate (HS) GAG biosynthesis to induce differentiation toward neural[81] and mesodermal[82] germ layer cell types. In yet another application, GAG-mimetic polymers presented at the surfaces of differentiated myotubes facilitated signaling through the motoneuron-derived protein agrin

and initiated the clustering of acetylcholine receptors, a process characteristic of the early stages of the neuromuscular synapse formation.[83]

These initial efforts to display glycans of interest with programmable hierarchal complexity at the cell surface have also identified the need for improving material specificity and imparting temporal control over their display. One challenge associated with non-covalent glycocalyx editing is the continuous cellular uptake of the glycomaterials during cell membrane turnover. Optimization of anchoring chemistry led to the discovery that the use of a cholesterylamine anchor greatly extended the cell surface residence time of the glycoconjugates via a recycling process, whereby internalized glycomaterials are shuttled back to the cell surface.[84] Similar effects can be achieved by integration of glycan motifs with cell surface proteins with extended cell-surface retention (Figure 1.4). For instance, genetic engineering of embryonic stem cells with the HaloTag protein (HTP) allowed for covalent conjugation of chloroalkane modified GAGs. This approach not only improved the surface half-life of the surface-displayed GAGs and enhanced neural differentiation of the stem cells, it also added an element of cell-specificity as only those cells stably expressing the HTP construct would undergo glycocalyx remodeling. The chemical integration of protein and glycan structures also adds another element of control to the glycocalyx editing process, where a well-defined synthetic glycoconjugate can be merged with existing receptor structures to take advantage of protein-associated biological functions. This was elegantly demonstrated by the generation of glycoprotein chimeras using an EGF receptor engineered to present an extracellular norbornene for the covalent attachment of a synthetic mucin mimetic domain.[85] In this case, the mucin mimetic was composed of a glycopolypeptide

synthesized via *N*-carboxyanhydride polymerization and terminated with a tetrazine handle to enable cell-surface cycloaddition conjugation with the pre-functionalized EGFR construct.

In constructing *de novo* glycoscapes or modulating existing glycocalyx structures on living cells, it is important to consider not only the effects on protein recognition and signaling in the new glycocalyx constructs but also their biophysical consequences. It is appreciated that bulky glycoconjugates, particularly mucins and proteoglycans, constitute a physical barrier to cells and contribute to membrane behavior.[60] The increasing thickness, density, and composition of the glycocalyx has been shown to enhance cell adhesivity and survival on soft matrices[86] and promote metastasis *in vivo.*[87] The mechanisms by which the glycocalyx facilitates integrin mediated metastasis have been shown to be largely biomechanical in nature, with bulky mucin glycoproteins funneling active integrins into clusters and applying tensile forces. Further, glycocalyx organization may force reorganization of membrane features and local curvature, as was observed in cells modified with both synthetic[59,88] and genetically encoded[89] glycoconjugates. Cells, and presumably pathogens, utilize the biophysical properties of the glycocalyx to regulate both molecular recognition events and adhesion as well as other glycan-independent signaling processes.

Undoubtedly, precision glycocalyx editing has become a powerful technique for elucidating the role of glycoconjugates at the surfaces of living cells in regulating biological outcomes. Despite the rapid progress in the field, many challenges still remain. In particular, the approaches to cell-specifically modify the glycocalyx are still limited to instances in which prior genetic manipulation of target cells is feasible. As well, the

methods with which synthetic macromolecular glycomaterials can be generated still lack sequence control, such as that provided by the cellular glycosylation machinery, although promising developments in this area are beginning to emerge.[90,91]

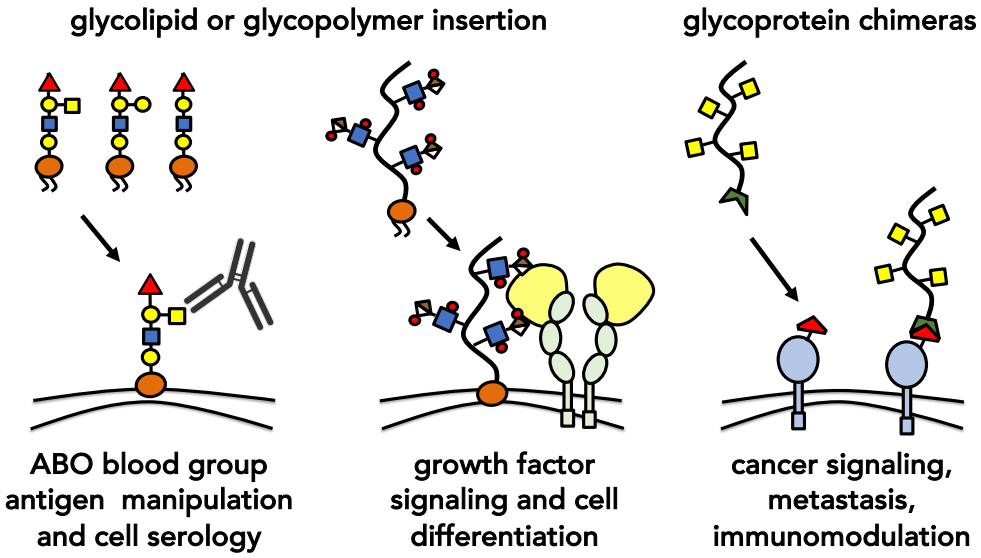

Figure 1.4 Precision glycocalyx editing. Synthetic glycocalyx building blocks can be introduced directly to the surface of living cells. Glycolipids or lipid-functionalized glycoconjugates rapidly insert into the outer leaflet of plasma membranes. Glycocalyx editing can be used to redefine blood group antigen displays on red blood cells or to promote the association of growth factors with the cell surface and activate signaling and differentiation in stem cells. Endogenous membrane proteins engineered to present chemical groups can be joined with synthetic glycoconjugates carrying functionality with complementary reactivity. The resulting glycoprotein chimeras can enhance the retention of the glycoconjugates at the cell surface and facilitate signaling.

1.6 Convergent efforts to establish the structure of the native glycocalyx

Efforts to engineer artificial glycocalyx structures have progressed parallel to work toward better understanding the organization of the native glycocalyx, which includes careful systems-level analysis, cataloging of the various glycocalyx components, and visualization of the glycocalyx and its interactions under physiological conditions. In the absence of methods for direct visualization of glycocalyx structures with molecular

resolution, mass spectrometry (MS)-based glycoproteomics technologies[7,92] have provided the main tool for the study of the composition of glycome. High-sensitivity MS techniques combined with chemical tagging and enrichment of glycoconjugates is beginning to yield information about the interactome of the glycocalyx. The use of tandem MS approaches to profile glycans after glycosidase treatment can give a more complete understanding of the composition and structure of glycans; however it is unable to capture the full repertoire of glycoproteoforms. When paired with complementary bioinformatics platforms,[93] chemical glycoproteomic approaches allow for identification of both protein identity and its glycosylation state and identification of disease-associated alterations.[94,95]

A more complete understanding of the molecular interactions and protein recognition events occurring within the compositionally heterogeneous environment of the cellular glycocalyx has been enabled by the development of shotgun glycan array techniques.[96,97] In this approach, entire collections of glycans harvested from cells are pooled, immobilized on a glass surface, and subsequently interrogated with glycan binding proteins of interest. Collections of glycans exhibiting biologically relevant activities are then analyzed by MS and can be further fractionated to determine the identity of the active glycan structures. This strategy has been utilized to identify endogenous receptors for Influenza virus A[98] and to curate glycan epitopes recognized by cancer cell-specific antibodies.[99] The development of chemical tools combining metabolic oligosaccharide engineering with proximity labeling are beginning to provide information about protein interactions within the native glycocalyx with spatial resolution. Metabolic incorporation of monosaccharides modified with diazirine photoaffinity labels into cell-surface glycoconjugates allows for photo-crosslinking of glycans directly interacting with or in

close proximity to proteins and receptors under investigation.[100] These approaches provide a steady stream of data rapidly generating a trove of knowledge about the composition of the glycocalyx and its interactions, which will guide future synthetic glycobiology efforts in their pursuit of revealing how this cellular interface regulates biological processes.

1.7 Summary and Outlook

Methods by which to systematically manipulate the glycocalyx are numerous and have been instrumental in the elucidation of many structure-function relationships in glycan-mediated biological processes. Among those, the *de novo* glycocalyx scaffolding using synthetic glycoconjugates with tunable architectures and functionality holds a prominent position as a particularly powerful tool to approximate the complexity and nanoscale organization of the native glycocalyx and to decipher how the cellular boundary regulates the exchange of information between the cell and its surroundings. The success of these strategies will ultimately rely on our ability to observe with molecular-level detail the native structures comprising the glycocalyx and define which material design parameters will be critical to building truly representative and functional glycocalyx models. Among the currently outstanding challenges is the development of strategies for targeting of synthetic glycomaterials to distinct membrane regions or to specific cells in multicellular systems and for manipulating the dynamics of glycocalyx displays with spatiotemporal control and in response to external stimuli. The field is now well-positioned to begin to turn its focus from basic biology research toward the pursuit of the glycocalyx as a target for therapeutic intervention.

1.8 Acknowledgements

Chapter one, in full, is a reprint of the material as it appears: Purcell S.C., Godula, K. Synthetic glycoscapes: addressing the structural and functional complexity of the glycocalyx. Interface Focus, 2019, 9: 20180080. The dissertation author is the primary co-author of this work.

1.9 References

1. Weinbaum S, Tarbell JM, Damiano ER. 2007 The structure and function of the endothelial glycocalyx layer. Annu. Rev. Bio. Eng. 9, 121-167, (doi:10.1146/annurev.bioeng.9.060906.1519 59).

2. Varki A, Gagneux P. 2017 Biological Functions of Glycans. In: Varki A, Cummings RD, Esko JD, et al., editors. Essentials of Glycobiology 3rd edition. Cold Spring Harbor (NY): Cold Spring Harbor Laboratory Press, 2015-2017. Chapter 7. (doi:10.1101/glycobiology.3e.007).

3. Varki A. 2008 Sialic acids in human health and disease. Trends Mol. Med. 14, 351–360, (doi: 10.1016/j.molmed.2008.06.002).

4. Springer SA, Gagneux P. 2013 Glycan Evolution in Response to Collaboration, Conflict, and Constraint, J. Biol. Chem. 288, 6904–6911, (doi: 10.1074/jbc.R112.424523).

5. Adibekian A, Stallforth P, Hecht M-L, Werz DB, Gagneux P, Seeberger PH. 2011 Comparative bioinformatics analysis of the mammalian and bacterial glycomes. Chem. Sci. 2, 337–344, (doi: 10.1039/C0SC00322K).

6. Dam TK, Brewer CF. 2009 Lectins as pattern recognition molecules: The effects of epitope density in innate immunity. Glycobiology 20, 270–279 (doi: 10.1093/glycob/cwp186).

7. Maverakis E, Kim K, Shimoda M, Gershwin ME, Patel F, Wilken R, Raychaudhuri S, Ruhaak LR, Lebrilla CB. 2015 Glycans in the immune system and The Altered Glycan Theory of Autoimmunity: A critical review, J. Autoimmun. 57, 1–13. (doi: 10.1016/j.jaut.2014.12.002).

8. Hudak JE, Bertozzi CR. 2014 Glycotherapy: New Advances Inspire a Reemergence of Glycans in Medicine. Chem. Biol. 21, 16–37, (doi: 10.1016/j.chembiol.2013.09.010).

9. Xiao H, Woods EC, Vukojicic P, Bertozzi CR. 2016 Precision glycocalyx editing as a strategy for cancer immunotherapy. Proc. Natl. Acad. Sci. U.S.A. 113, 10304–10309, (doi: 10.1073/pnas.1608069113).

10. Saxon E, Bertozzi CR. 2001 Chemical and Biological Strategies for Engineering Cell Surface Glycosylation. Annu. Rev. Cell Dev. Biol. 17, 1–23, (doi: 10.1146/annurev.cellbio.17.1.1).

11. Griffin ME, Hsieh-Wilson LC. 2016 Glycan Engineering for Cell and Developmental Biology. Cell Chem. Biol. 23, 108–121, (doi: 10.1016/j.chembiol.2015.12.007).

12. Esko JD, Stanley P. Glycosylation Mutants of Cultured Cells. In: Varki A, Cummings R, Esko J, et al., editors. Essentials of Glycobiology. 2nd edition. Cold Spring Harbor Laboratory Press; 2009. Chapter 46. Available from: https://www.ncbi.nlm.nih.gov/books/NBK1922/.

13. Lopez Aguilar A, Briard JG, Yang L, Ovryn B, Macauley MS, Wu P. 2017 Tools for Studying Glycans: Recent Advances in Chemoenzymatic Glycan Labeling. ACS Chem. Biol. 12, 611–621, (doi: 10.1021/acschembio.6b01089).

14. Dube DH, Bertozzi CR. 2003 Metabolic oligosaccharide engineering as a tool for glycobiology. Curr. Opin. Chem. Biol. 7(5), 616-625, (doi: doi.org/10.1016/j.cbpa.2003.08.006).

15. Kiessling LL, Grim JC. 2013 Glycopolymer probes of signal transduction. Chem. Soc. Rev., 42, 4476-91, (doi: 10.1039/c3cs60097a).

16. Gestwicki JE, Cairo CW, Strong LE, Oetjen KA, Kiessling LL. 2002 Influencing Receptor−Ligand Binding Mechanisms with Multivalent Ligand Architecture. J. Am. Chem. Soc. 124, 14922–14933, (doi: 10.1021/ja027184x).

17. Mammen M, Choi S-K, Whitesides GM. 1998 Polyvalent Interactions in Biological Systems: Implications for Design and Use of Multivalent Ligands and Inhibitors. Angew. Chem. Int. Ed. 37, 2754–2794, (doi: 10.1002/(SICI)1521-3773(19981102)37:20<2754::AID-ANIE2754>3.0.CO;2-3)

18. Kiessling LL, Gestwicki JE, Strong LE. 2006 Synthetic Multivalent Ligands as Probes of Signal Transduction. Angew. Chem. Int. Ed. 45, 2348–2368, (doi: 10.1002/anie.200502794).

19. Machida T, Novoa A, Gillon É, Zheng S, Claudinon J, Eierhoff T, Imberty A, Römer W, Winssinger N. 2017 Dynamic Cooperative Glycan Assembly Blocks the Binding of Bacterial Lectins to Epithelial Cells. Angew. Chem. Int. Ed. 56, 6762–6766, (doi: 10.1002/anie.201700813).

20. Miura Y, Hoshino Y, Seto H. 2015 Glycopolymer Nanobiotechnology. Chem. Rev. 116, 1673–1692, (doi: 10.1021/acs.chemrev.5b00247).

21. Turnbull WB, Stoddart JF. 2002 Design and synthesis of glycodendrimers. Rev. Mol. Biotechnol. 90, 231-255, (doi: 10.1016/S1389-0352(01)00062-9).

22. Steiner K, Hanreich A, Kainz B, Hitchen PG, Dell A, Messner P, Schäffer C. 2008 Recombinant Glycans on an S-Layer Self-Assembly Protein: A New Dimension for Nanopatterned Biomaterials. Small. 4, 1728–1740, (doi: 10.1002/smll.200701215)

23. Huang ML, Godula K. 2016 Nanoscale materials for probing the biological functions of the glycocalyx. Glycobiology. 26, 797–803, (doi:10.1093/glycob/cww022).

24. Matrosovich MN, Mochalova LV, Marinina VP, Byramova NE, Bovin NV. 1990 Synthetic polymeric sialoside inhibitors of influenza virus receptor-binding activity. FEBS Letters 272, 209–212, (doi: 10.1016/0014-5793(90)80486-3).

25. Sigal GB, Mammen M, Dahmann G, Whitesides GM. 1996 Polyacrylamides Bearing Pendant α-Sialoside Groups Strongly Inhibit Agglutination of Erythrocytes by Influenza Virus: The Strong Inhibition Reflects Enhanced Binding through Cooperative Polyvalent Interactions. J. Am. Chem. Soc. 118, 3789–3800, (doi: 10.1021/ja953729u).

26. Cairo CW, Gestwicki JE, Kanai M, Kiessling LL. 2002 Control of Multivalent Interactions by Binding Epitope Density. J. Am. Chem. Soc.124, 1615–1619, (doi: 10.1021/ja016727k).

27. Kanai M, Mortell KH, Kiessling LL. 1997 Varying the Size of Multivalent Ligands: The Dependence of Concanavalin A Binding on Neoglycopolymer Length. J. Am. Chem. Soc. 119, 9931–9932, (doi: 10.1021/ja972089n).

28. Bovin NV. 1998 Polyacrylamide-based glycoconjugates as tools in glycobiology. Glycoconj. J. 15(5), 431-446, (doi: 10.1023/A:1006963717646).

29. Restuccia A, Fettis MM, Hudalla GA. 2016 Glycomaterials for immunomodulation, immunotherapy, and infection prophylaxis. J. of Mater. Chem. B. 4, 1569–1585, (doi: 10.1039/C5TB01780G).

30. Gorska K, Huang K-T, Chaloin O, Winssinger N. 2009 DNA-Templated Homo- and Heterodimerization of Peptide Nucleic Acid Encoded Oligosaccharides that Mimick the Carbohydrate Epitope of HIV. Angew. Chem. Int. Ed. 48, 7695–7700, (doi: 10.1002/anie.200903328).

31. Novoa A, Winssinger N. 2015 DNA display of glycoconjugates to emulate oligomeric interactions of glycans. Beilstein J. of Org. Chem. 11, 707–719, (doi: 10.3762/bjoc.11.81).

32. Novoa A, Machida T, Barluenga S, Imberty A, Winssinger N. 2014 PNA-Encoded Synthesis (PES) of a 10 000-Member Hetero-Glycoconjugate Library and Microarray Analysis of Diverse Lectins. ChemBioChem 15, 2058–2065, (doi: 10.1002/cbic.201402280).

33. Matsuura K, Hibino M, Yamada Y, Kobayashi K. 2001 Construction of Glyco-Clusters by Self-Organization of Site-Specifically Glycosylated Oligonucleotides and Their Cooperative Amplification of Lectin-Recognition. J. Am. Chem. Soc. 123, 357–358, (doi: 10.1021/ja001945j).

34. Horiya S, Bailey JK, Temme JS, Guillen Schlippe YV, Krauss IJ. 2014 Directed Evolution of Multivalent Glycopeptides Tightly Recognized by HIV Antibody 2G12. J. Am. Chem. Soc. 136, 5407–5415, (doi: 10.1021/ja500678v).

35. Horan N, Yan L, Isobe H, Whitesides GM, Kahne D. 1999 Nonstatistical binding of a protein to clustered carbohydrates. Proc. Natl. Acad. Sci. U.S.A. 96, 11782–11786, (doi: 10.1073/pnas.96.21.11782).

36. Gestwicki JE , Cairo CW, Mann DA, Owen RM, Kiessling LL. 2002 Selective Immobilization of Multivalent Ligands for Surface Plasmon Resonance and Fluorescence Microscopy. Anal. Biochem. 305, 149–155, (doi: 10.1006/abio.2002.5652).

37. Meng X-L, Fang Y, Wan L-S, Huang X-J, Xu Z-K. 2012 Glycopolymer Brushes for the Affinity Adsorption of RCA120: Effects of Thickness, Grafting Density, and Epitope Density. Langmuir 28, 13616–13623, (doi: 10.1021/la302389e).

38. Migliorini E, Thakar D, Sadir R, Pleiner T, Baleux F, Lortat-Jacob H, Coche-Guerente L, Richter RP. 2014 Well-defined biomimetic surfaces to characterize glycosaminoglycan-mediated interactions on the molecular, supramolecular and cellular levels. Biomaterials 35, 8903–8915, (doi: 10.1016/j.biomaterials.2014.07.017).

39. Godula K, Bertozzi CR. 2012 Density Variant Glycan Microarray for Evaluating Cross-Linking of Mucin-like Glycoconjugates by Lectins. J. Am. Chem. Soc 134, 15732–15742, (doi: 10.1021/ja302193u).

40. Cohen M, Varki A. 2014 Modulation of glycan recognition by clustered saccharide patches. Int. Rev. Cell. Mol. Biol. Elsevier 308, 75-125, (doi: 10.1016/B978-0-12-800097-7.00003-8).

41. Oyelaran O, Gildersleeve JC. 2009 Glycan arrays: recent advances and future challenges. Curr. Opin. Chem. Biol. 13, 406–413, (doi: 10.1016/j.cbpa.2009.06.021).

42. Blixt O, Head S, Mondala T, Scanlan C, Huflejt MT, Alvarez R, Bryan MC, Fazio F, Calarese D, Stevens J, Razi N, Stevens DJ, Skehel JJ, van Die I, Burton DR, Wilson IA, Cummings RD, Bovin N, Wong C-H, Paulson JC. 2004 Printed covalent glycan array for ligand profiling of diverse glycan binding proteins. Proc. Natl. Acad. Sci. U.S.A. 101, 17033–17038, (doi: 10.1073/pnas.0407902101).

43. Zhang Y, Li Q, Rodriguez LG, Gildersleeve JC. 2010 An Array-Based Method To Identify Multivalent Inhibitors. J. Am. Chem. Soc. 132, 9653–9662, (doi: 10.1021/ja100608w)

44. Zhang Y, Campbell C, Li Q, Gildersleeve JC. 2010 Multidimensional glycan arrays for enhanced antibody profiling. Mol. BioSyst. 6, 1583, (doi: 10.1039/c002259d).

45. Parera Pera N, Branderhorst HM, Kooij R, Maierhofer C, van der Kaaden M, Liskamp RMJ, Wittmann V, Ruijtenbeek R, Pieters RJ. 2010 Rapid Screening of Lectins for Multivalency Effects with a Glycodendrimer Microarray. ChemBioChem. 11, 1896–1904, (doi: 10.1002/cbic.201000340).

46. Huang ML, Cohen M, Fisher CJ, Schooley RT, Gagneux P, Godula K. 2015 Determination of receptor specificities for whole influenza viruses using multivalent glycan arrays. Chem. Comm. 51, 5326–5329, (doi:10.1039/c4cc08613a).

47. Neumann K, Conde-González A, Owens M, Venturato A, Zhang Y, Geng J, Bradley M. 2017 An Approach to the High-Throughput Fabrication of Glycopolymer Microarrays through Thiol–Ene Chemistry. Macromol. 50, 6026–6031, (doi: 10.1021/acs.macromol.7b00952).

48. Liang C-H, Wang S-K, Lin C-W, Wang C-C, Wong C-H, Wu C-Y. 2011 Effects of Neighboring Glycans on Antibody-Carbohydrate Interaction. Angew. Chem. Int. Ed. 50, 1608–1612, (doi:10.1002/anie.201003482).

49. Shivatare VS, Shivatare SS, Lee C-CD, Liang CH, Liao K-S, Cheng Y-Y, Saidachary G, Wu C-Y, Lin N-H, Kwong PD, Burton DR, Wu C-Y, Wong C-H. 2018 Unprecedented Role of Hybrid N-Glycans as Ligands for HIV-1 Broadly Neutralizing Antibodies. J. Am. Chem. Soc. 140, 5202–5210, (doi: 10.1021/jacs.8b00896).

50. Godula K, Rabuka D, Nam KT, Bertozzi CR. 2009 Synthesis and Microcontact Printing of Dual End-Functionalized Mucin-like Glycopolymers for Microarray Applications. Angew. Chem. Int. Ed. 48, 4973–4976, (doi:10.1002/anie.200805756)

51. Bian S, Zieba SB, Morris W, Han X, Richter DC, Brown KA, Mirkin CA, Braunschweig AB. 2014 Beam pen lithography as a new tool for spatially controlled

photochemistry, and its utilization in the synthesis of multivalent glycan arrays. Chem. Sci. 5, 2023, (doi: 10.1039/C3SC53315H).

52. Sackmann E. 1996 Supported membranes: scientific and practical applications. Science 271, 43−48, (doi: 10.1126/science.271.5245.43).

53. Richter RP, Bérat R, Brisson AR. 2006 Formation of Solid-Supported Lipid Bilayers: An Integrated View. Langmuir 22, 3497–3505, (doi:10.1021/la052687c)

54. Sych T, Mély Y, Römer W. 2018 Lipid self-assembly and lectin-induced reorganization of the plasma membrane. Philos. Trans. R. Soc. Lond. B. Biol. Soc. 373(1747), (doi: 10.1098/rstb.2017.0117).

55. Mann DA, Kanai M, Maly DJ, Kiessling LL. 1998 Probing Low Affinity and Multivalent Interactions with Surface Plasmon Resonance: Ligands for Concanavalin A. J. Am. Chem. Soc.120, 10575–10582, (doi: 10.1021/ja9818506).

56. Goronzy IN, Rawle RJ, Boxer SG, Kasson PM. 2018 Cholesterol enhances influenza binding avidity by controlling nanoscale receptor clustering. Chem. Sci. 9, 2340–2347, (doi: 10.1039/C7SC03236F).

57. Zhu X-Y, Holtz B, Wang Y, Wang L-X, Orndorff PD, Guo A. 2009 Quantitative Glycomics from Fluidic Glycan Microarrays. J. Am. Chem. Soc. 131, 13646–13650, (doi: 10.1021/ja902783n)

58. Godula K, Umbel ML, Rabuka D, Botyanszki Z, Bertozzi CR, Parthasarathy R. 2009 Control of the Molecular Orientation of Membrane-Anchored Biomimetic Glycopolymers. J Am. Chem. Soc. 131, 10263–10268, (doi: 10.1021/ja903114g).

59. Aigal S, Claudinon J, Römer W. 2015 Plasma membrane reorganization: A glycolipid gateway for microbes. BBA. Mol. Cell Res. 1853, 858–871, (doi: 10.1016/j.bbamcr.2014.11.014).

60. Kuo JC-H, Gandhi JG, Zia RN, Paszek MJ. 2018 Physical biology of the cancer cell glycocalyx. Nat. Phys. 14, 658–669, (doi: 10.1038/s41567-018-0186-9).

61. Stuhr-Hansen N, Madl J, Villringer S, Aili U, Römer W, Blixt O. 2016 Synthesis of Cholesterol-Substituted Glycopeptides for Tailor-Made Glycocalyxification of Artificial Membrane Systems. ChemBioChem. 17, 1403–1406, (doi: 10.1002/cbic.201600258).

62. Stuhr-Hansen N, Vagianou C-D, Blixt O. 2017 Synthesis of BODIPY-Labeled Cholesterylated Glycopeptides by Tandem Click Chemistry for Glycocalyxification of Giant Unilamellar Vesicles (GUVs). Chem. Eur. J. 23, 9472–9476, (doi: 10.1002/chem.201702104).

63. Vagianou C-D, Stuhr-Hansen N, Moll K, Bovin N, Wahlgren M, Blixt O. 2018 ABO Blood Group Antigen Decorated Giant Unilamellar Vesicles Exhibit Distinct Interactions with Plasmodium falciparum Infected Red Blood Cells. ACS Chem. Biol. 13, 2421–2426, (doi: 10.1021/acschembio.8b00635).

64. Villringer S, Madl J, Sych T, Manner C, Imberty A, Römer W. 2018 Lectin-mediated protocell crosslinking to mimic cell-cell junctions and adhesion. Sci. Rep. 8, 1932, (doi: 10.1038/s41598-018-20230-6).

65. Ribeiro JP, Villringer S, Goyard D, Coche-Guerente L, Höferlin M, Renaudet O, Römer W, Imberty A. 2018 Tailor-made Janus lectin with dual avidity assembles glycoconjugate multilayers and crosslinks protocells. Chem. Sci. 9, 7634–7641, (doi: 10.1039/C8SC02730G).

66. Kubilis A, Abdulkarim A, Eissa AM, Cameron NR. 2016 Giant Polymersome Protocells Dock with Virus Particle Mimics via Multivalent Glycan-Lectin Interactions. Sci. Rep. 6, 32414, (doi: 10.1038/srep32414).

67. Xiao Q, Ludwig AK, Romanò C, Buzzacchera I, Sherman S-E, Vetro M, Vértesy S, Kaltner H, Reed EH, Möller M, Wilson CJ, Hammer DA, Oscarson S, Klein ML, Gabius H-J, Percec V. 2018 Exploring functional pairing between surface glycoconjugates and human galectins using programmable glycodendrimersomes. Proc. Natl. Acad. U.S.A. 115, E2509–E2518, (doi: 10.1073/pnas.1720055115).

68. Nischan N, Kohler JJ. 2016 Advances in cell surface glycoengineering reveal biological function. Glycobiology, 26, 789–796, (doi:10.1093/glycob/cww045).

69. Lowe JB, Marth JD. 2003 A Genetic Approach to Mammalian Glycan Function. Annu. Rev. Biochem. 72, 643–691, (doi:10.1146/annurev.biochem.72.121801.161809).

70. Agard NJ, Bertozzi CR. 2009 Chemical Approaches to Perturb, Profile, and Perceive Glycans. Acc. Chem. Res. 42, 788–797, (doi: 10.1021/ar800267j).

71. Rogers GN, Paulson, JC. 1983 Receptor determinants of human and animal influenza virus isolates: Differences in receptor specificity of the H3 hemagglutinin based on species of origin. Virology. 127, 361–373, (doi: 10.1016/0042-6822(83)90150-2).

72. Sackstein R, Merzaban JS, Cain DW, Dagia NM, Spencer JA, Lin CP, Wohlgemuth R. 2008 Ex vivo glycan engineering of CD44 programs human multipotent mesenchymal stromal cell trafficking to bone. Nat. Medicine, 14, 181–187, (doi: 10.1038/nm1703).

73. Marcus DM, Cass LE. 1969 Glycosphingolipids with Lewis Blood Group Activity: Uptake by Human Erythrocytes. Science. 164, 553–555, (doi: 10.1126/science.164.3879.553).

74. Korchagina E, Tuzikov A, Formanovsky A, Popova I, Henry S, Bovin N. 2012 Toward creating cell membrane 29pprox-landscapes with glycan lipid constructs. Carbohydr. Res. 356, 238–246, (doi: 10.1016/j.carres.2012.03.044).

75. Frame T, Carroll T, Korchagina E, Bovin N, Henry S. 2007 Synthetic glycolipid modification of red blood cell membranes. Transfusion. 47, 876–882, (doi: 10.1111/j.1537-2995.2007.01204.x).

76. Harrison AL, Olsson ML, Jones RB, Ramkumar S, Sakac D, Binnington B, Henry S, Lingwood CA, Branch DR. 2010 A synthetic globotriaosylceramide analogue inhibits HIV-1 infection in vitro by two mechanisms. Glycoconj. J. 27, 515–524, (doi: 10.1007/s10719-010-9297-y).

77. Rabuka D, Forstner MB, Groves JT, Bertozzi CR. 2008 Noncovalent Cell Surface Engineering: Incorporation of Bioactive Synthetic Glycopolymers into Cellular Membranes. J. Am. Chem. Soc. 130, 5947–5953, (doi: 10.1021/ja710644g).

78. Pulsipher A, Griffin ME, Stone SE, Brown JM, Hsieh-Wilson LC. 2014 Directing Neuronal Signaling through Cell-Surface Glycan Engineering. J. Am. Chem. Soc. 136, 6794–6797, (doi: 10.1021/ja5005174).

79. Huang ML, Purcell SC, Verespy S, Wang Y, Godula K. 2017 Glycocalyx scaffolding with synthetic nanoscale glycomaterials. Biomat. Sci. 5, 1537–1540, (doi: 10.1039/c7bm00289k).

80. Hudak JE, Canham SM, Bertozzi CR. 2013 Glycocalyx engineering reveals a Siglec-based mechanism for NK cell immunoevasion. Nat. Chem. Biol. 10, 69–75, (doi: 10.1038/nchembio.1388).

81. Huang ML, Smith RAA, Trieger GW, Godula K. 2014 Glycocalyx Remodeling with Proteoglycan Mimetics Promotes Neural Specification in Embryonic Stem Cells. J. Am. Chem. Soc. 136, 10565–10568, (doi: 10.1021/ja505012a).

82. Naticchia MR, Laubach LK, Tota EM, Lucas TM, Huang ML, Godula K. 2018 Embryonic Stem Cell Engineering with a Glycomimetic FGF2/BMP4 Co-Receptor Drives Mesodermal Differentiation in a Three-Dimensional Culture. ACS Chem. Biol. 13, 2880–2887, (doi: 10.1021/acschembio.8b00436)

83. Huang ML, Tota EM, Lucas TM, Godula K. 2018 Influencing Early Stages of Neuromuscular Junction Formation through Glycocalyx Engineering. ACS Chem. Neurosci. (doi: 10.1021/acschemneuro.8b00295).

84. Woods EC, Yee NA, Shen J, Bertozzi CR. 2015 Glycocalyx Engineering with a Recycling Glycopolymer that Increases Cell Survival In Vivo. Angew. Chem. Int. Ed. 54, 15782–15788, (doi: 10.1002/anie.201508783).

85. Kramer JR, Onoa B, Bustamante C, Bertozzi CR. 2015 Chemically tunable mucin chimeras assembled on living cells. Proc. Natl. Acad. U.S.A.112, 12574–12579, (doi: 10.1073/pnas.1516127112).

86. Paszek MJ, DuFort CC, Rossier O, Bainer R, Mouw JK, Godula K, Hudak JE, Lakins JN, Wijekoon AC, Cassereau L, Rubashkin MG, Magbanua MJ, Thorn KS, Davidson MW, Rugo HS, Park JW, Hammer DA, Giannone G, Bertozzi CR,

Weaver VM. 2014 The cancer glycocalyx mechanically primes integrin-mediated growth and survival. Nature 511, 319–325, (doi:10.1038/nature13535).

87. Woods EC, Kai F, Barnes JM, Pedram K, Pickup MW, Hollander MJ, Weaver VM, Bertozzi CR. 2017 A bulky glycocalyx fosters metastasis formation by promoting G1 cell cycle progression. eLife, 6, e25752, (doi: 10.7554/eLife.2575).

88. Arnaud J, Tröndle K, Claudinon J, Audfray A, Varrot A, Römer W, Imberty A. 2014 Membrane Deformation by Neolectins with Engineered Glycolipid Binding Sites. Angew. Chem. Int. Ed 53, 9267–9270, (doi: 10.1002/anie.201404568).

89. Shurer CR, Colville MJ, Gupta VK, Head SE, Kai F, Lakins JN, Paszek MJ. 2017 Genetically Encoded Toolbox for Glycocalyx Engineering: Tunable Control of Cell Adhesion, Survival, and Cancer Cell Behaviors. ACS Biomat. Sci. Eng. 4, 388–399, (doi: 10.1021/acsbiomaterials.7b00037).

90. Yilmaz G, Becer CR. 2014 Glycopolymer Code Based on Well-Defined Glycopolymers or Glyconanomaterials and Their Biomolecular Recognition. Front. Bioeng. Biotechnol. 2 (39), 1-18, (doi: 10.3389/fbioe.2014.00039).

91. Zhang Q, Collins J, Anastasaki A, Wallis R, Mitchell DA, Becer CR, Haddleton DM. 2013 Sequence-Controlled Multi-Block Glycopolymers to Inhibit DC-SIGN-gp120 Binding. Angew. Chem. Int. Ed. 52, 4435–4439, (doi: 10.1002/anie.201300068).

92. Yang Y, Franc V, Heck AJR. 2017 Glycoproteomics: A Balance between High-Throughput and In-Depth Analysis. Trends Biotechnol. 35, 598–609, (doi: 10.1016/j.tibtech.2017.04.010)

93. Palaniappan KK, Bertozzi CR. 2016 Chemical Glycoproteomics. Chem. Rev. 116, 14277–14306, (doi: 10.1021/acs.chemrev.6b00023).

94. Spiciarich DR, Nolley R, Maund SL, Purcell SC, Herschel J, Iavarone AM, Peehl DM, Bertozzi CR. 2017 Bioorthogonal Labeling of Human Prostate Cancer Tissue Slice Cultures for Glycoproteomics. Angew. Chem. Int. Ed. 56, 8992–8997, (doi:10.1002/anie.201701424).

95. Woo CM, Iavarone AT, Spiciarich DR, Palaniappan KK, Bertozzi CR. 2015 Isotope-targeted glycoproteomics (IsoTaG): a mass-independent platform for intact N- and O-glycopeptide discovery and analysis. Nat. Methods. 12, 561–567, (doi:10.1038/nmeth.3366).

96. Song X, Lasanajak Y, Xia B, Heimburg-Molinaro J, Rhea JM, Ju H, Zhao C, Molinaro RJ, Cummings RD, Smith DF. Shotgun glycomics: a microarray strategy for functional glycomics. Nat. Methods. 8, 85–90, (doi: 10.1038/nmeth.1540).

97. Smith DF, Cummings RD. 2013 Application of Microarrays for Deciphering the Structure and Function of the Human Glycome. Molec. Cell. Prot. 12, 902–912, (doi: 10.1074/mcp.R112.027110).

98. Byrd-Leotis L, Liu R, Bradley KC, Lasanajak Y, Cummings SF, Song X, Heimburg-Molinaro J, Galloway SE, Culhane MR, Smith DF, Steinhauer DA, Cummings RD. 2014 Shotgun glycomics of pig lung identifies natural endogenous receptors for influenza viruses. Proc. Natl. Acad. Sci. U.S.A. 11, E2241–E2250, (doi: 10.1073/pnas.1323162111).

99. Liau B, Tan B, Teo G, Zhang P, Choo A, Rudd PM. 2017 Shotgun Glycomics Identifies Tumor-Associated Glycan Ligands Bound by an Ovarian Carcinoma-Specific Monoclonal Antibody. Sci. Rep. 7, 14489, (doi:10.1038/s41598-017-15123-z).

100. Bond MR, Zhang H, Vu PD, Kohler JJ. 2009 Photocrosslinking of glycoconjugates using metabolically incorporated diazirine-containing sugars. Nat. Protocols 4, 1044–1063, (doi: 10.1038/nprot.2009.85).

2 Glycocalyx scaffolding with synthetic nanoscale glycomaterials

We report a method for programming complexity into the glycocalyx of live cells. Via a combination of glycomaterial synthesis and membrane remodeling, we have engineered cells to display native-like, mixed sialoglycan populations, while confining the activity of each glycan into a specific nanoscale presentation.

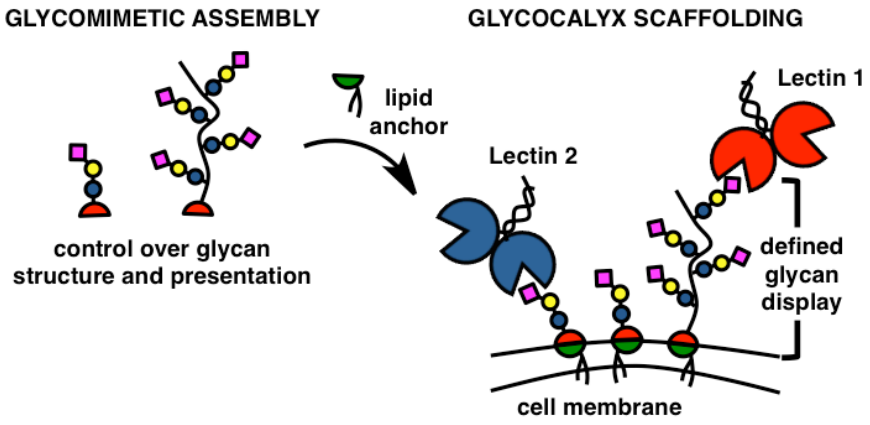

Figure 2.1 Glycocalyx scaffolding concept. Synthetic materials with controlled glycan structure and presentation are anchored to the cell membrane via a lipid moiety and can engage lectins.

2.1 Introduction

The glycocalyx is an intricate network of carbohydrate-rich biomolecules delineating the boundary between cells and the extracellular environment (Fig 2.2, left). Composed primarily of glycolipids, glycoproteins and proteoglycans, and reaching hundreds of nanometers from the cell surface, this biological interface contributes key functions to cellular and tissue physiology by providing a protective

microenvironment, mediating nutrient exchange while keeping pathogens at bay, and facilitating intercellular communication.[1]

Among the structurally diverse pool of glycans presented within the glycocalyx, sialic acids stand out as a particularly prominent class of carbohydrates (Fig 2.2). Introduced as a terminal modification on glycans during their biosynthesis, these negatively charged, nine-carbon monosaccharides are often recognized by protein receptors.[2] Over evolution, sialoglycans have acquired immunomodulatory functions and emerged as molecular markers that delineate "self" from "non-self".[3] For instance, sialic acids are prominently displayed in the glycocalyx of B lymphocytes. At concentrations close to 100 mM, as established by Paulson and co-workers,[4] they help calibrate signaling responses to antigenic challenge by masking the CD22 receptor, a sialic acid-binding negative regulator of B cell activation. Due to their high abundance on epithelial and endothelial tissues, sialic acids are also often subverted by opportunistic pathogens trying to gain entry into host cells.[5]

The sialoglycome of a cell can harbor a large degree of complexity, stemming not only from the type of sialic acid (*N*-acetylated or *N*-glycolylated) and its glycosidic linkage to underlying glycans (α2-3 or α2-6, Fig 2.3), but also from their spatial distribution within the glycocalyx (Fig 2.2).[6] Sialoglycans can be presented in the vicinity of the plasma membrane as glycolipids, or project tens to hundreds of nanometers away from the cell surface displayed on glycoprotein scaffolds. The three-dimensional organization of the glycocalyx likely contributes to its biological functions[7] and must be considered when devising methods for

engineering of the cell-matrix interface for biomedical applications. Here, we report a hierarchical *de novo* assembly of a synthetic glycocalyx with spatially targeted sialic acid activity using a combination of nanoscale glycomaterial design and non-covalent cell surface engineering (Fig 2.2, right).

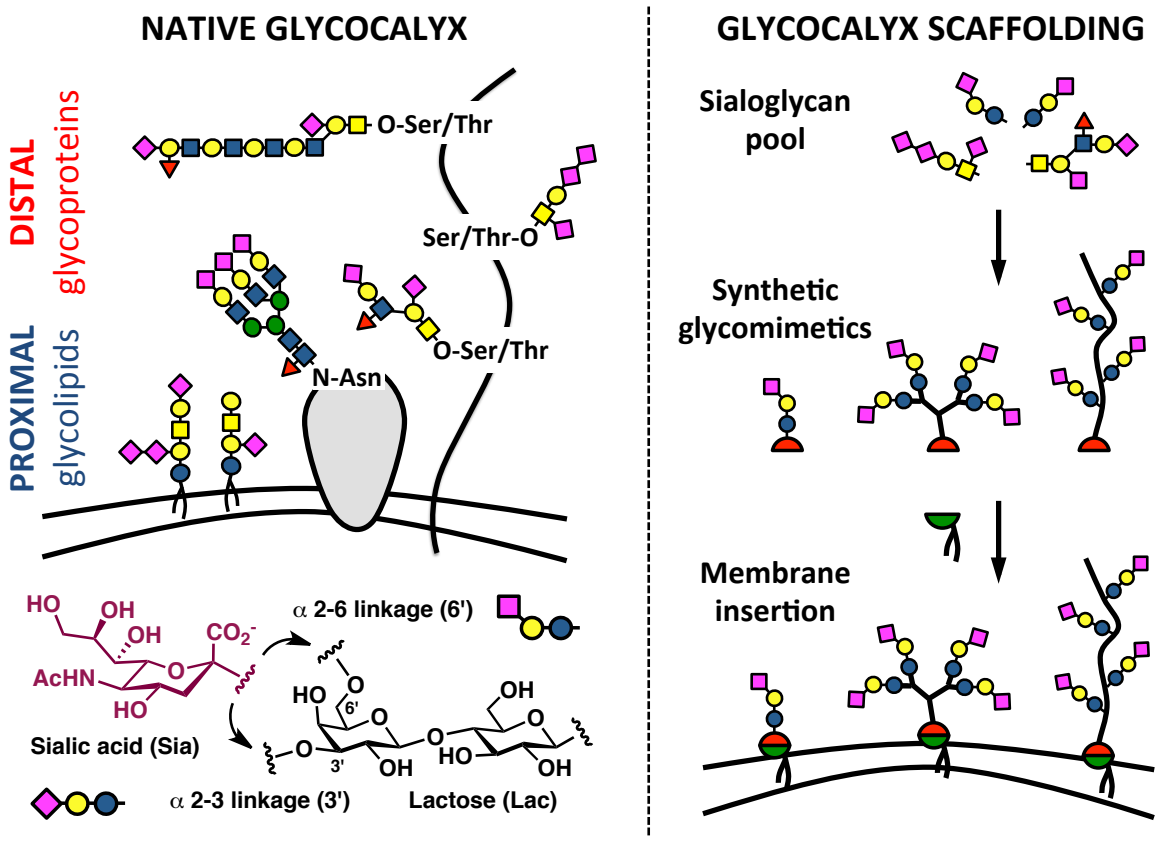

Figure 2.2 Building glycocalyx complexity. The hierarchical organization of sialoglycans in native glycocalyx (left) can be recapitulated in a controlled fashion via precision glycan engineering (right). Specific glycans are assembled into synthetic glycomimetic structures and primed with a lipid anchor for insertion into cell membranes. Delivery of unique glycans in pre-defined nanoscale arrangements to the cell surface allows for spatial organization of glycan activity in specific regions of the glycocalyx.

Synthetic glycomaterials, such as polymers or dendrimers, have long been explored as ligands for glycan-binding proteins. These materials can approximate the shape and scale of various types of glycoproteins and provide tunable

multivalent glycan presentation for high-avidity receptor binding.[8] However, the diversity of glycan structures introduced into these materials is typically limited to simple mono- and disaccharides, which is mostly due to difficulties associated with the synthesis and functionalization of more complex carbohydrates.[8] We have recently reported a general method for directly introducing reducing glycans, including an array of increasingly complex sialoglycans, into polymeric scaffolds armed with *N*-methylaminooxy side chains.[9,10] When furnished with hydrophobic phospholipid anchors, such materials can be targeted to the plasma membranes of live cells to incorporate new glycan structures into their glycocalyx.[11,12,13]

2.2 Results and Discussion

To test whether this approach can be used to systematically build glycan complexity at the cell surface, we set to install both α2-3 and α2-6 linked sialoglycans simultaneously, while maintaining control over their presentation within the glycocalyx. Whereas the latter would be introduced as a monovalent 6'-sialyllactose glycolipid and form the underbrush of the glycocalyx, the former would be presented as 3'-sialyllactose glycopolymer with predefined nanoscale glycan organization (Fig 2.2).

We synthesized the glycocalyx building block precursors, 6'-sialyllactoside (**1**) and a 3'-sialyllactose glycopolymer (**2**), as azide-conjugates for the attachment of dibenzocyclooctyne-phospholipids via the strain promoted azide-alkyne cycloaddition (SPAAC) reaction (Fig 2.3).[14] We chose, the post-synthetic introduction of lipid anchors for its increased generality, because it obviates the need for the *de novo* synthesis of individual lipid conjugates, and for the improved

solution properties and long-term stability of the azide precursors. Whereas the monovalent β-azido glycoside **1** was prepared in a single step from 6'-sialyllactose,[15,16] (Fig. 2.S1-2.S3) polymer **2** was assembled by ligation of 3'-sialyllactose to a RAFT-derived polyacrylamide precursor (DP = 22, M_n = 6,800, Đ = 1.13) with pendant *N*-methylaminooxy groups and end-labelled with AlexaFluor 488 for visualization.[9] (Fig. 2.S1-2.S8) The efficiency of the glycan ligation step, as determined by ^{1}H NMR spectroscopy, was 45%, giving glycopolymer **2** with a sialoglycan valency of ~ 10. (Fig. 2.S9) The resulting glycoconjugates **1** and **2** were then primed for membrane insertion via an overnight reaction with the dibenzocyclooctyne-functionalized PEG-lipid conjugate, DBCO-PEG2000-DSPE (**3**, 1.1 equiv). (Fig. 2.S10-2.S11)

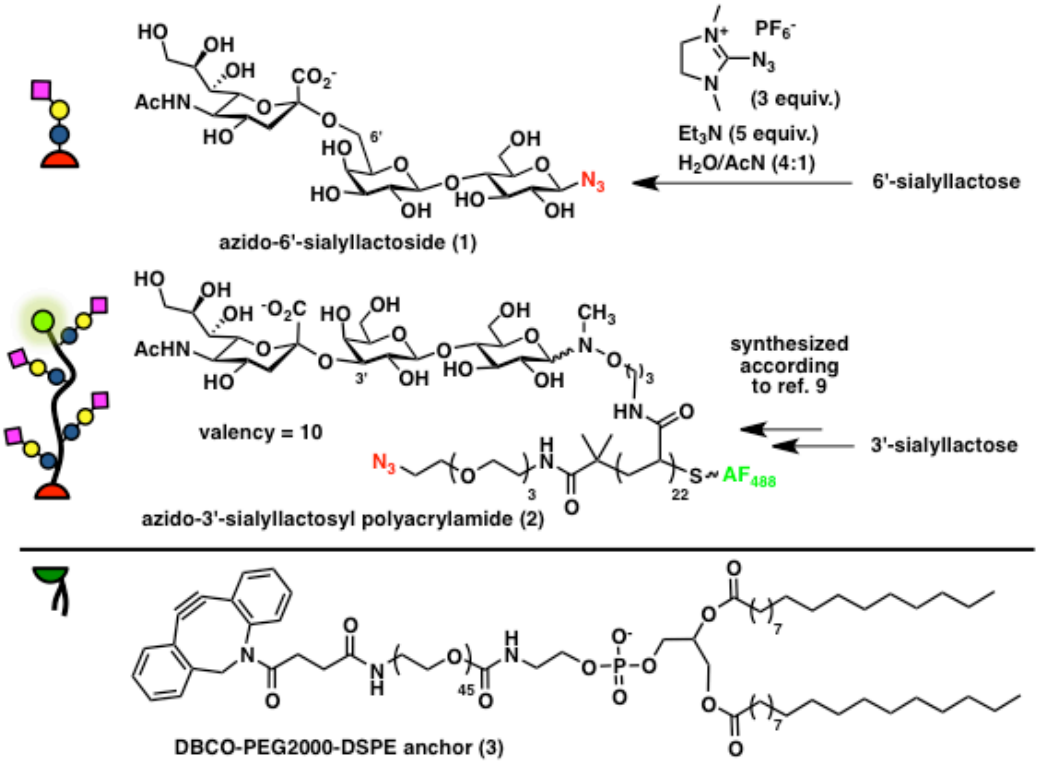

Figure 2.3 Glycocalyx building blocks. Monovalent glycolipid and multivalent glycopolymer precursors **1** and **2** were prepared as azide conjugates for the attachment of dibenzocyclooctyne-lipid **3** via the SPAAC (or "copper-free click") reaction.

With the desired lipidated monovalent (**4**) and polymeric (**5**) glycoconjugates in hand, we set to test their incorporation into the glycocalyx of living cells (Fig 2.4). For our model cell system, we chose the Chinese hamster ovary Lec 2 (CHO-Lec2) cells.[17] The CHO-Lec2 cells are mutants with defective transport of the activated nucleotide sugar precursor, CMP-sialic acid, into the Golgi apparatus. As a consequence, these cells show low levels of sialic acid modification on their glycoproteins and glycolipids.[17] (Fig. 2.S12) First, we evaluated cell membrane insertion of the monovalent 6'-sialyllactose glycolipid **4** (Fig 2.4A; Fig. 2.S13). The CHO-Lec2 cells were incubated in the basal MEM medium containing increasing

amounts of **4** for 1 hr at 37 °C. The sialoglycan introduced to the cell surface was detected by staining with Dylight649 conjugated *Sambucus nigra* agglutinin (SNA), which has known specificity for sialic acids with α2-6 linkages (Fig 2.4B).[18] Flow cytometry analysis revealed that cell surface saturation is reached at concentrations of glycolipid **4** above ~ 500 μM (Fig 2.4C). Next, we assessed the incorporation of the lipidated 3'-sialyllactose glycopolymer **5** by incubating the CHO-Lec2 cells with **5** at concentrations ranging between 2.5-100 μM (or 25 μM – 1 mM with respect to 3'-sialyllactose, Fig 2.4D). The presence of the AlexaFluor488 label in polymer **5** allowed for a direct observation of membrane remodeling. (Fig. 2.4E; Figs. 2.S14 and 2.S15) Interestingly, the amount of polymer delivered to the cell surface increased linearly with concentration of **5** in the incubation media without reaching a saturation point (Fig 2.4F). Staining of the remodeled cells with biotinylated *Maackia amurensis* lectin II (bMALII) with specificity for α2-3 sialosides[18] followed by visualization with Cy5-streptavidin, also showed a linear increase in lectin binding as a function of polymer concentration (Fig 2.4G). Both glycoconjugates can be used to tune the sialoglycan composition of the cellular glycocalyx, with monovalent glycolipid **4** reaching a saturation of lectin binding sites at lower concentrations compared to the multivalent glycopolymer **5**.

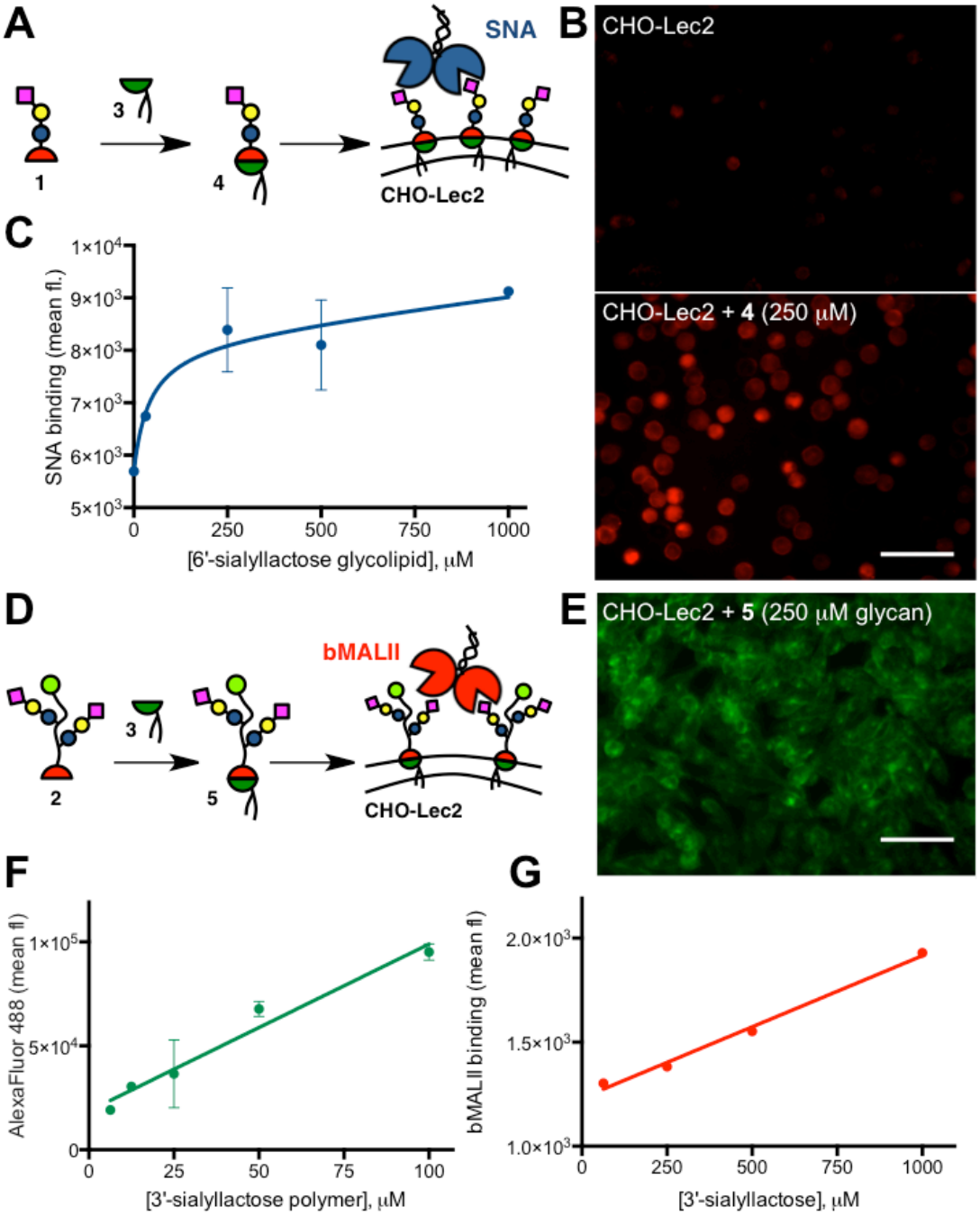

Figure 2.4 Glycocalyx remodeling with glycomimetics 4 and 5. A) Remodeling of CHO-Lec2 cells with glycolipid **4**. (B) Fluorescence micrograph of SNA-stained CHO-Lec2 cells before and after remodeling with **4**. (C) Levels of incorporation of **4** were determined by Dylight648-SNA staining and flow cytometry. (D) Remodeling of CHO-Lec2 cells with glycopolymer **5.** (C) Fluorescence micrograph of cells after introduction of AlexaFluor488-labeled **5**. Flow cytometry analysis of polymer incorporation based on polymer fluorescence (F) and biotin-MALII/Cy5-streptavidin staining (G).

In cells, different sialoglycan structures are targeted to distinct regions of the glycocalyx to perform specific biological functions. We set out to test whether our cell surface engineering approach can artificially recapitulate this behavior, by presenting sialic acid ligands for SNA and bMALII either directly on the plasma membrane via the α2-6 sialoglycolipid **4** or in the form of pre-organized multivalent ensembles on α2-3 sialoglycopolymer scaffolds **5** (Fig 2.5). To test this concept, CHO-Lec2 cells were incubated for 1 hr in media containing glycoconjugates **4** and **5** premixed at specific concentrations (**4**:**5** = 1000:0, 500:200, 250:250, and 0:1000 μM sialoglycan). The cells were stained with SNA and bMALII and analyzed by flow cytometry. We observed reduction in SNA staining commensurate with the decreasing fraction of **4** in the incubation media, and in agreement with lectin-binding activities previously observed for cells remodeled with the glycolipid only (Fig 2.4). The gradual decrease in SNA binding is mirrored by enhanced bMALII signal corresponding to the growing contributions from the sialoglycan polymers **5** introduced into the cellular glycocalyx (Fig. 2.S16).

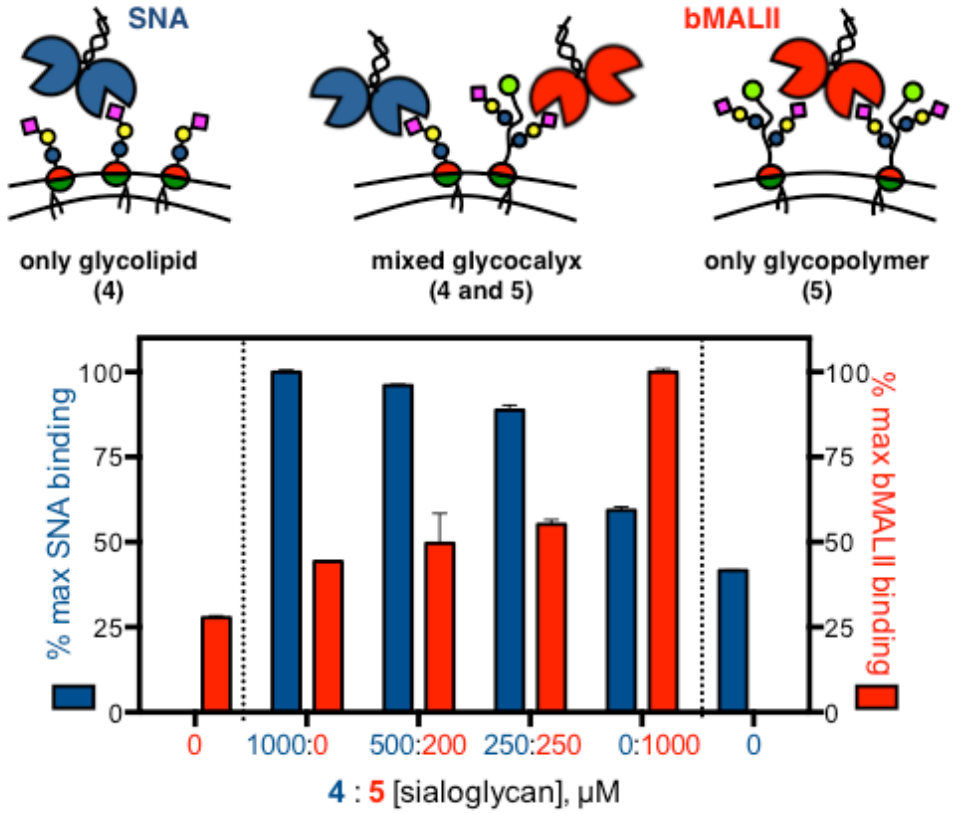

Figure 2.5 Glycocalyx scaffolding. The glycocalyx of CHO-Lec2 cells were remodeled with glycolipid **4** and glycopolymer **5** at varying ratios to modulate the levels of SNA and MALII binding. The nanoscale architecture of **4** and **5** confines the lectin-binding activity into the membrane proximal and distal regions of the glycocalyx, respectively.

2.3 Conclusions

Collectively, our data demonstrate that more than one glycoconjugate can be simultaneously introduced into the glycocalyx of live cells to modulate their responses toward lectins. At the same time, the nanoscale organization of the newly acquired biological activity can be defined through molecular design of the synthetic glycomaterial. Whereas our study validates the concept of hierarchical assembly of glycocalyx complexity using simple glycolipids and linear

glycopolymers, this method can be extended to any type of glycoconjugate, such as a glycocluster, glycodendrimer, branched glycopolymer and others, as long as they can be functionalized with a membrane-targeting lipid anchor. The ability to tailor complex glycan interactions at the cell-matrix interface with nanoscale precision is poised to provide new insights into the biological roles of glycans and open new opportunities for controlling cellular functions in artificial tissue scaffolds and cell-based therapeutics.

2.4 Acknowledgements

This work was supported by the NIH Director's New Innovator Award (1DP2HS087954-01) to K.G. and the Glycoscience Common Fund (1R21AI129894-01). M. L. H. was supported in part by the Program of Excellence in Glycosciences (PEG, NHLBI: 4P01HL107150-06). We thank Dr. Lisa Adamiak for assistance with the purification and analysis of **1**.

Chapter two, in full, is a reprint of the material as it appears: Huang, M.; Purcell, S.; Verespy, S.; Wang, Y.; Godula K. Glycocalyx Scaffolding with Synthetic Nanoscale Glycomaterials. *Biomater. Sci.* 2017, 5, 1537-1540. The dissertation author is a co-author of this work.

2.5 References

1. A. Varki and J. B. Lowe, in Essentials of Glycobiology, ed. A. Varki. Cold Spring Harbor Press, Cold Spring Harbor, NY, 2nd edition, 2009, Chapter 2.
2. A. Varki. Trends Mol. Med., 2008, 14, 351-360.
3. S. A. Springer and P. Gagneux. J. Biol. Chem., 2013, 288, 6904-6911.

4. B. E. Collins, O. Blixt, A. R. DeSieno, N. Bovin, J. D. Marth, J. C. Paulson. Proc. Natl. Acad. Sci., 2004, 101, 6104-6109.

5. A. Varki and P. Gagneux. Ann. N. Y. Acad. Sci., 2012, 1253, 16-36.

6. T. K. Dam, C. F. Brewer. Biochemistry, 2008, 47, 8470-8476.

7. M. Cohen and A. Varki. OMICS, 2010, 14, 455.

8. Y. Miura, Y. Hoshino and H. Seto. Chem. Rev., 2016, 116, 1673-1692.

9. M. L. Huang, M. Cohen, C. J. Fisher, R. T. Schooley, P. Gagneux and K. Godula. Chem. Commun., 2015, 31, 5326-5329.

10. M. Cohen, C. J. Fisher, M. L. Huang, L. L. Lindsay, M. Plancarte, W. M. Boyce, K. Godula and P. Gagneux. Virology, 2016, 493, 128-135.

11. D. Rabuka, M. B. Forstner, J. T. Groves and C. R. Bertozzi. J. Am. Chem. Soc., 2008, 130, 5947-5953.

12. M. L. Huang, R. A. A. Smith, G. W. Trieger and K. Godula. J. Am. Chem. Soc., 2014, 136, 10565-10568.

13. A. Pulsipher, M. E. Griffin, S. E. Stone and J. M. Brown. J. Am. Chem. Soc., 2014, 136, 6794-6797.

14. J. C. Jewett, E. M. Sletten and C. R. Bertozzi. J. Am. Chem. Soc., 2010, 132, 3688-3690.

15. D. Lim, M. A. Brimble, R. Kowalczyk, A. J. Watson and A. J. Fairbanks. Angew. Chem. Int. Ed. Engl., 2014, 53, 11907-11911.

16. T. Tanaka, H. Nagai, M. Noguchi, A. Kobayashi and S-I Shoda. Chem. Commun., 2009, 23, 3378-3379.

17. P. Stanley. Meth. Enzymol. 1983, 96, 157-184.

18. I. J. Goldstein and R. D. Poretz in The Lectins-Properties, Functions, and Applications in Biology and Medicine, ed. I. E. Liener, N. Sharon, I. J. Goldstein. Academic Press, Orlando, 1986, S. 33-243.

2.6 Supporting Information

2.6.1 Materials and instrumentation

6'-sialyllactose and 3'sialyllactose glycan were obtained from Carbosynth (San Diego, CA). Unless otherwise stated, all other chemicals were purchased from Sigma Aldrich. Purchased starting materials were used as received unless otherwise indicated. Size exclusion chromatography was performed on a Hitachi Chromaster system equipped with an RI detector and a 5 μm, mixed bed, 7.8 mm I.D. x 30 cm TSKgel column (Tosoh Bioscience). Polymers were analyzed using an isocratic method: 0.7 mL/min in DMF (0.2% w/v LiBr, 70 ^{o}C). AlexaFluor 488-C_5-maleimide was purchased from Molecular Probes (Cat # A10254). DSPE-PEG(2000)-DBCO was purchased from Avanti Lipids (Cat # 880229). PD-10 columns were purchased from GE Healthcare Life Sciences (Cat. # 17085101). Quick Spin Columns for radiolabeled DNA purification were purchased from Roche Diagnostics (Cat. # 11273913001).

2.6.2 Synthetic procedures and characterization

*2.6.2.1 Synthesis of 6'-sialyllactose-azide triethylammonium salt **1**.*

Installation of the reducing-end azide was achieved by using similar methods previously reported.[19,20] In 1 mL of 4:1 D_2O:CH_3CN, 6'-sialyllactose (28.4 mg, 0.0433 mmol) and triethylamine (30 µL, 0.2116 mmol) were mixed and stirred at 0 °C for 5 minutes. Freshly recrystallized ADMP (2-azido-1,3-dimethylimidazolinium hexafluorophosphate; 37 mg, 0.1300 mmol; previously synthesized as previously described[21]) was added to the stirred solution at 0 °C and allowed to react for 3h. NMR of the crude mixture after 3h showed loss of anomeric peaks from 6'-sialyllactose (65% conversion). The reaction mixture was then diluted with 4 mL of water containing 0.1% trifluoroacetic acid (TFA) and a 1.8 mL aliquot was purified by semipreparative HPLC (column, Jupiter Proteo C12, ϕ10 x 250 mm; eluent = 5:100:0.1 CH_3CN:H_2O:TFA; flowrate = 4 mL/min; column oven, 27 °C; detection, UV (214 nm). The collected fractions were pooled and lyophilized to yield clear colorless crystals (5.54 mg per aliquot).

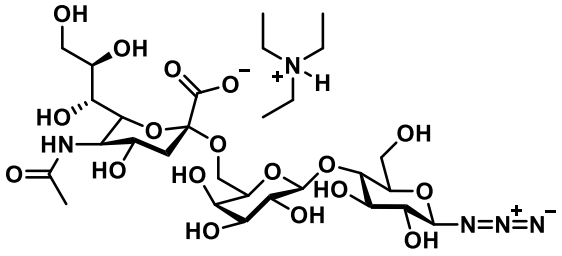

Figure 2.S1 Structure and characterization of 6'sialyllactose-azide triethylammonium salt. ^{1}H NMR (500 MHz, D_2O); δ (ppm) 5.34 (s, 1H) 4.67 (d, J = 7.88, 1H), 4.40 (d, J = 7.88 Hz, 1H), 4.04 (d, J = 7.88 Hz, 1H), 3.92 – 3.44 (m, 16H), 3.27 (t, J = 8.95 Hz, 1H), 3.13 (q, J = 7.30 Hz, 6H), 2.68 – 2.61 (m, 1H), 1.96 (s, 3H), 1.77 – 1.63 (m, 1H), 1.21 (t, J = 7.40 Hz, 9H). Mass Spectrometry (ESI-MS) calculated for $C_{29}H_{52}N_5O_{18}$ [M-Et_3N]$^{1-}$, m/z 657.21, found [M-Et_3N]$^{1-}$, m/z 658.31; [M+H-Et_3N-N_3]$^{1-}$, m/z 615.36.

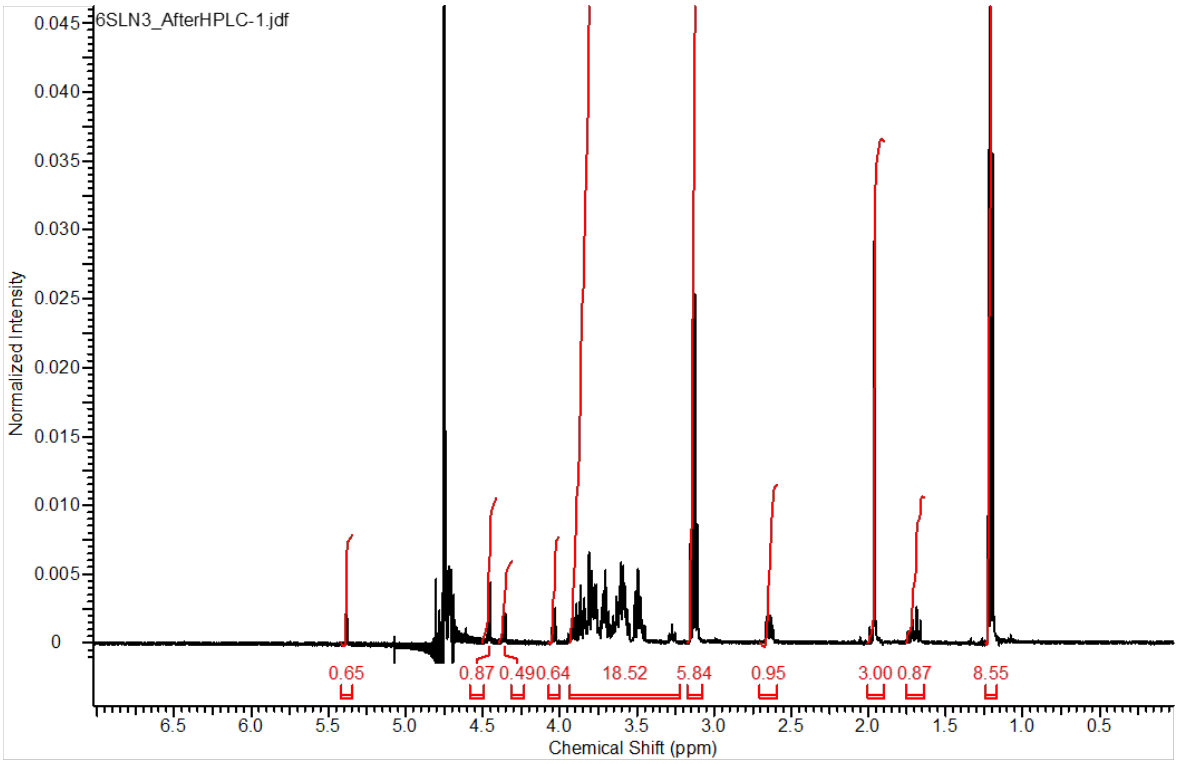

Figure 2.S2 ^{1}H NMR of 6'sialyllactose-azide **1**.

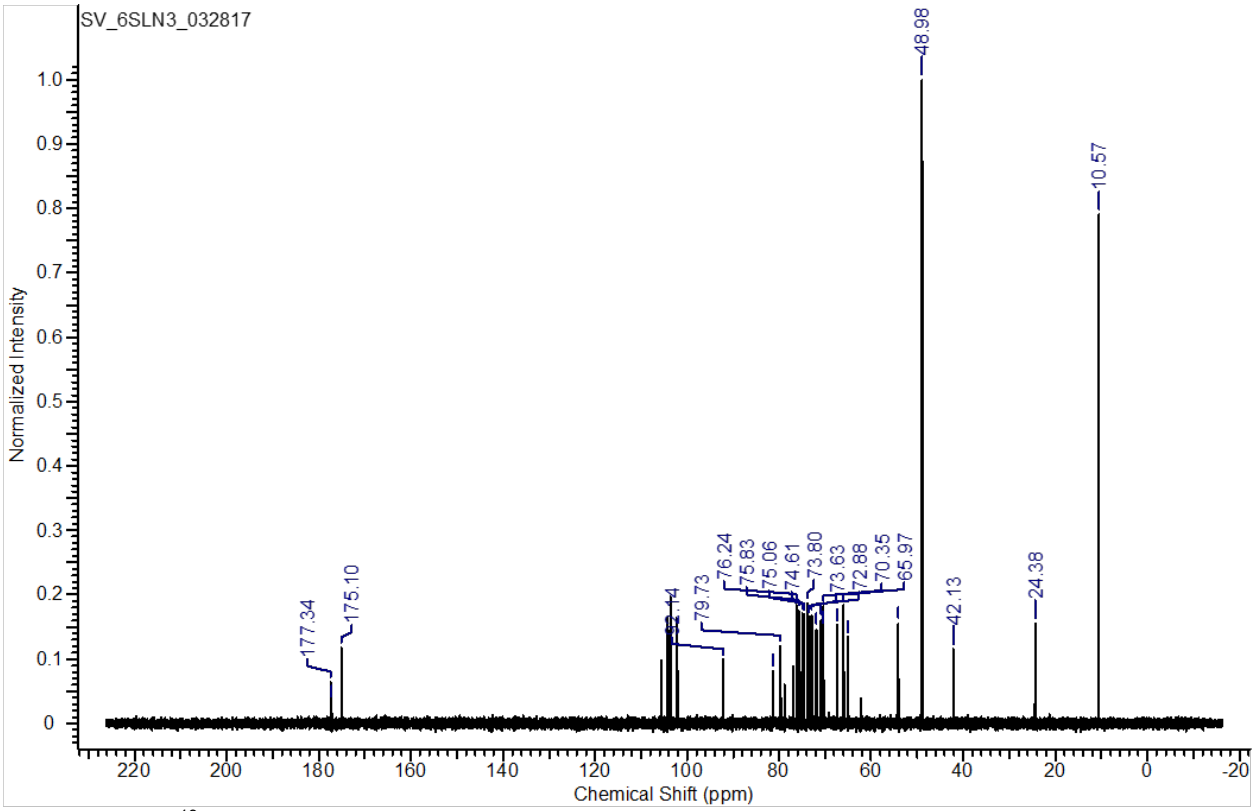

Figure 2.S3 ^{13}C NMR of 6'sialyllactose-azide **1**.

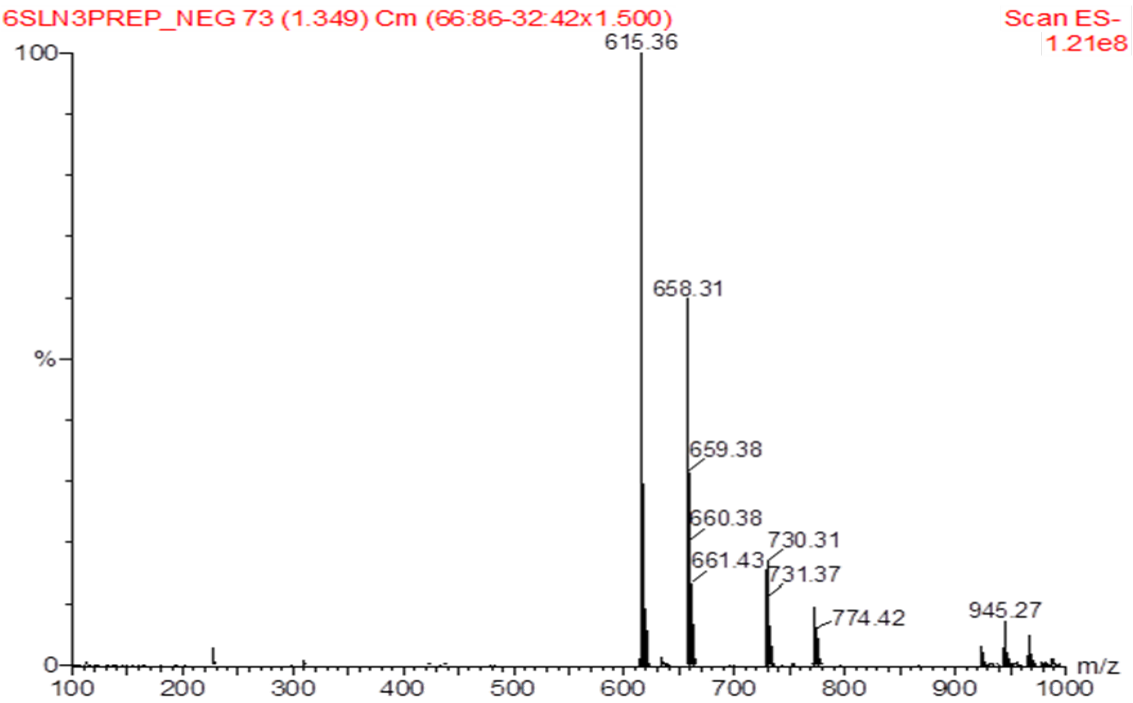

Figure 2.S4 ESI-MS of 6'-sialyllactose azide **1**.

2.6.2.2 Synthesis of 3'-sialyllactose glycopolymer 2 from monomer 2a.

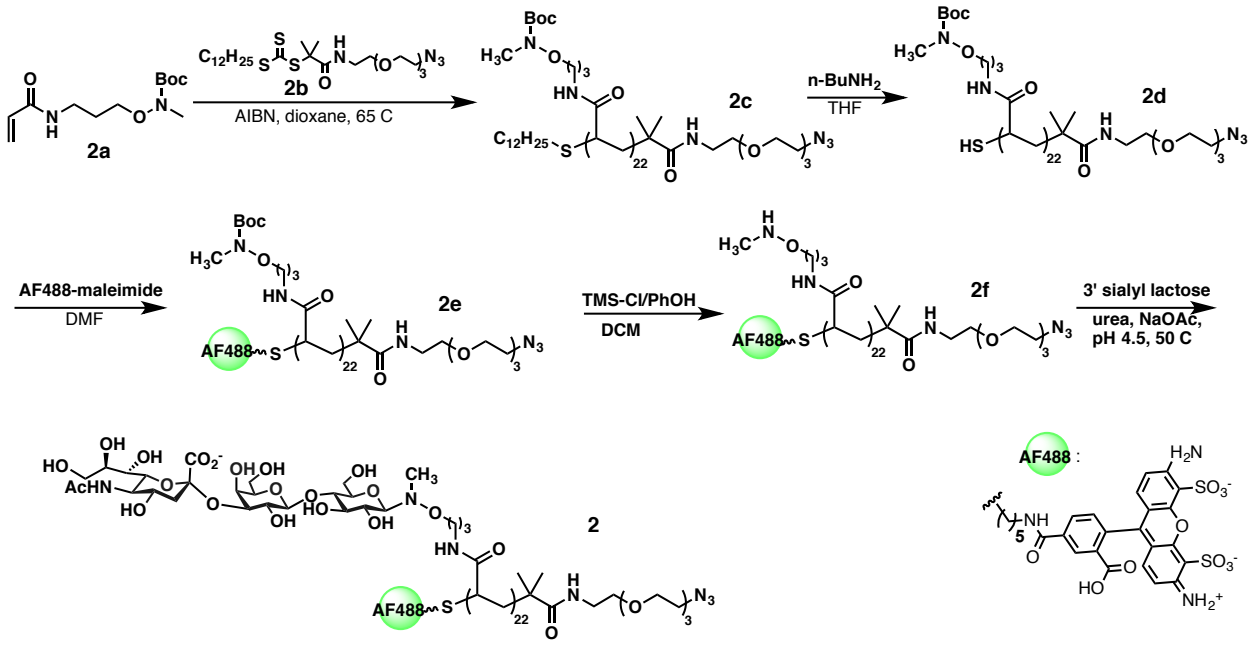

Scheme 2.S1 Overview of 3'sialyllactose glycopolymer (2) synthesis.

2.6.2.2.1 RAFT Polymerization of monomer 2a.

The RAFT polymerization of this Boc-protected N-methylaminooxy propylacrylamide (2a) monomer has previously been described.[22] A Schlenk flask equipped with a magnetic stir bar was charged with an azide-terminated chain transfer agent (2a, 38.58 mg, 80.9 umol, 0.07 mol% with respect to 2a), followed by the radical initiator AIBN (11.25 mg. 68.5 umol, 0.06 mol% with respect to 2a), and the tert-butyl (3-acrylamidopropoxy)methyl carbamate monomer (2a; 296 mg, 1.15 mmol, delivered as 420 uL of a 360 mM solution in anhydrous dioxane), and anhydrous dioxane (172 mg). After degassing with six free-pump-thaw cycles, the reaction was allowed to proceed at 65 °C for seven hours. The reaction was quenched by submerging the flask in a dry ice-acetone bath. The mixture was then diluted in ether, and precipitated three times in hexanes. The resulting residue was concentrated in $CHCl_3$ and dried under high-vacuum to yield polymer (2c; 184 mg, 62.2%). ^{1}H NMR ($CDCl_3$, 300 MHz): δ (ppm): 3.90-3.65 (bs, 2H), 3.35-2.80 (bm, 5H), 1.80-1.05 (bm, 16H). GPC (DMF, 0.2% LiBr): Mw = 6824, Mn = 6010, Đ = 1.136, DP (n) = 22.

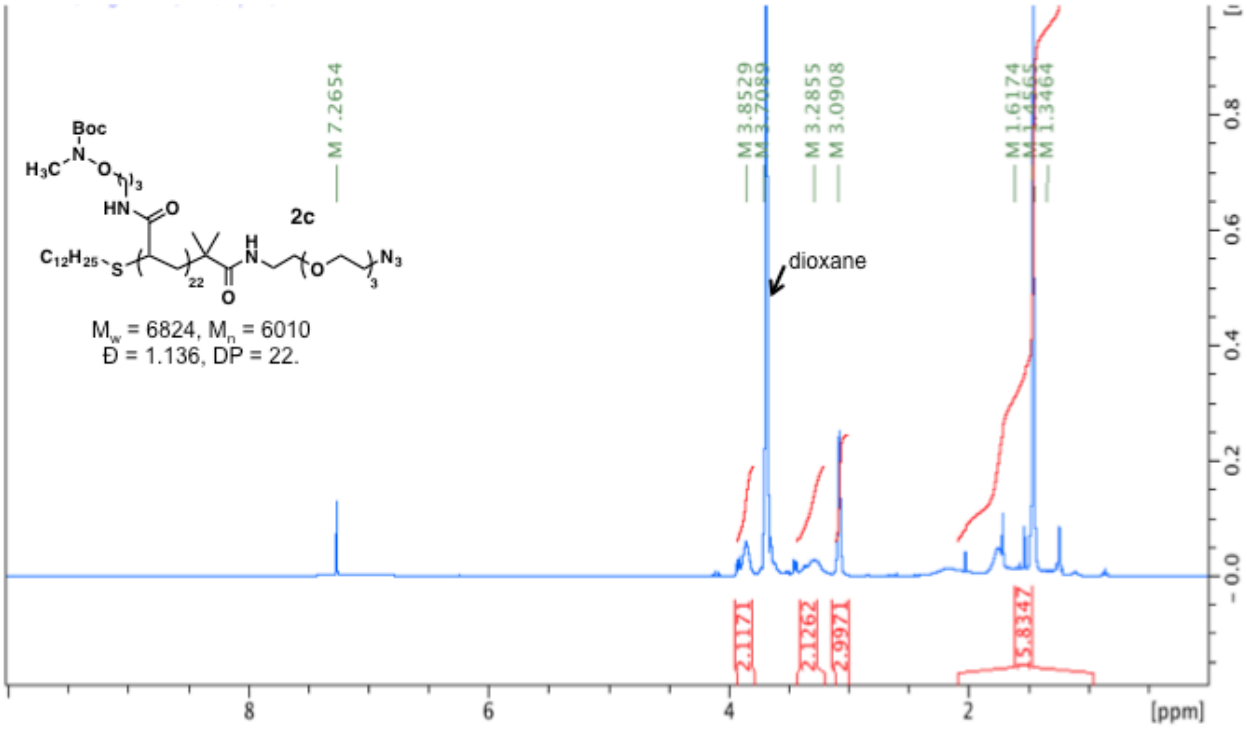

Figure 2.S5 ^{1}H NMR analysis of polymer backbone 2c.

2.6.2.2.2 End deprotection and fluorophore labeling.

Polymer 2c (9.38 mg) end-deprotection was achieved by reaction with n-butylamine in THF (20 mM, 0.5 mL) for 2 hours at 0 °C. Following dilution in ether and precipitation with excess hexanes (3x), the end-deprotected polymer (2d) was isolated as a white solid (7.99 mg, 81.3%). ^{1}H NMR ($CDCl_3$, 300mHz) δ (ppm): 3.90-3.65 (bs, 2H), 3.35-2.80 (bm, 5H), 1.80-1.05 (bm, 16H). GPC (DMF, 0.2% LiBr): Mw = 6826, Mn = 6030, Đ = 1.132, DP ≈ 22. UV–Vis 310 nm (CH_2Cl_2, 100 μM) = 0.075. The isolated material (7.99 mg) was then reacted with an AlexaFluor 488 C_5-maleimide/DMF solution (1.1 eq; 2 mM, 694 μL) overnight at room temperature. The resulting material was diluted in ether, precipitated in excess hexanes (3x), and dried under high-vacuum to yield the AlexaFluor488-labeled polymer (2e; 6.63 mg, 82.9%).

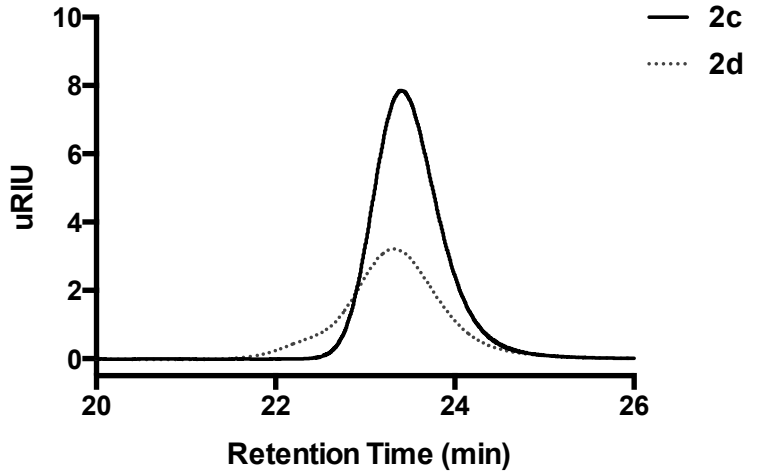

Figure 2.S6 GPC analysis of polymer backbone (2c; solid) and end-deprotected polymer (2d; dotted). A higher molecular weight species is observed in 2d (dotted) due to spontaneous oxidation of the free thiols of the polymer to form disulfide bridges.

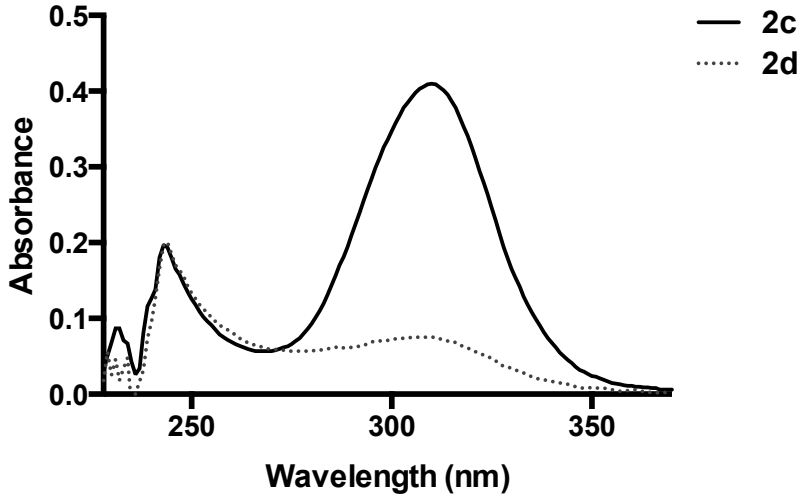

Figure 2.S7 UV-Vis analysis of polymer backbone (2c; solid) and end-deprotected polymer (2d; dotted). The loss of the peak at 310 nm for 2d indicates removal of the trithiocarbonate protecting group.

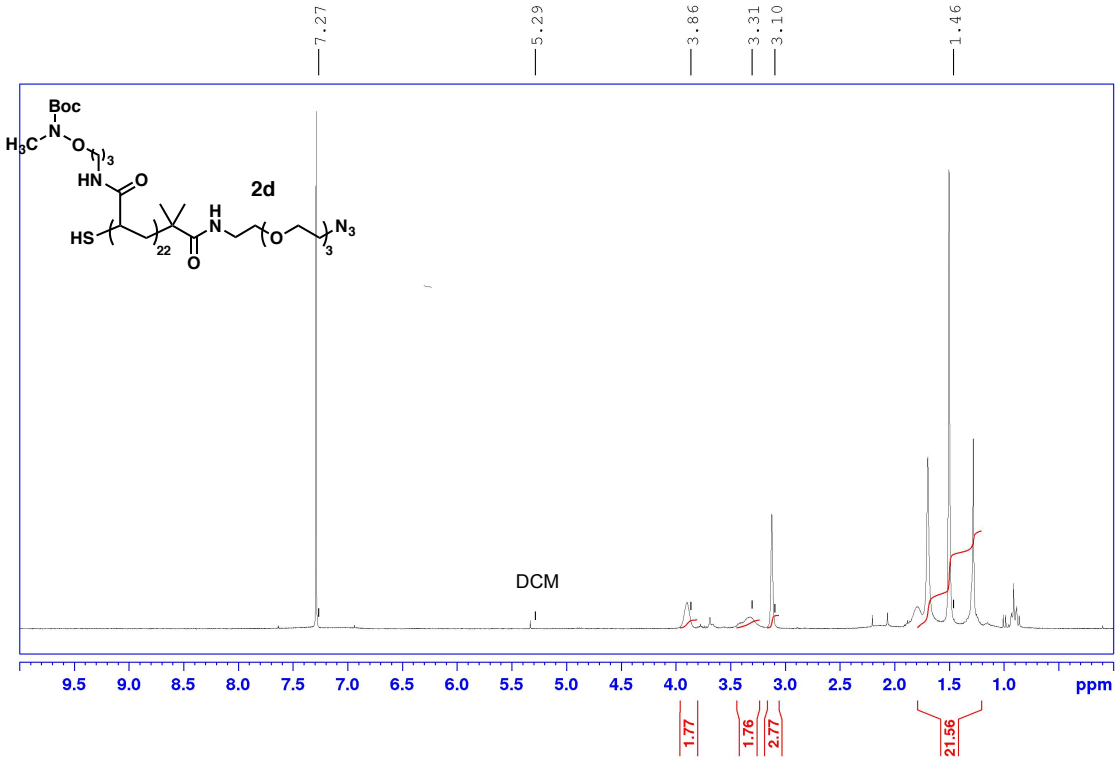

Figure 2.S8 ^{1}H NMR analysis of end-deprotected polymer backbone 2d.

2.6.2.2.3 Side chain Boc deprotection and glycan ligation

The AlexaFluor488-labeled polymer backbone 2e (6.63 mg) was reacted with a freshly prepared mixture of chlorotrimethylsilane (3 M) and phenol (1 M) in DCM (0.5 mL) for 2 hours, dark, at RT. The mixture was then precipitated in ether following dilution in methanol. After drying the precipitate under a nitrogen stream, the product was dissolved in water, isolated by a PD-10 column, frozen, and lyophilized to yield the Boc-deprotected polymer 2f (2.69 mg, 61%). ^{1}H NMR (D_2O, 300 MHz) δ (ppm): 3.90-3.65 (bs, 2H), 3.35-2.80 (bm, 5H), 1.80-1.05 (bm, 16H). UV–Vis spectrophotometry was used to determine AlexaFluor488 labeling efficiency of this water-soluble polymer: 2f, (AlexaFluor488, λ_{max}: 495 nm in H_2O) = 58%. The resulting polymer 2f (2.69 mg) was then dissolved in a sodium acetate buffer (1 M NaOAc, 1 M urea, pH 4.5) such that the solution contains 200 mM of

the polymer side chains. Then, a PCR tube (0.5 mL) containing 3'-sialyllactose (9.12 mg, 1.1 eq.) was charged with the solution of 2f (63.3 uL), and the viscous solution was heated to 50 °C in a thermocycler for 72 hours. The resulting glycopolymer was purified via QuickSpin DNA columns using deuterated phosphate buffer (150 mM NaCl, 100 mM phosphate, pD 7.4), to yield 2 (0.5 mL). The final concentration was determined by UV-Vis analysis and the AlexaFluor488 labeling efficiency ([pol] = 908 uM). ^{1}H NMR analysis was used to determine glycan ligation efficiencies (45%).

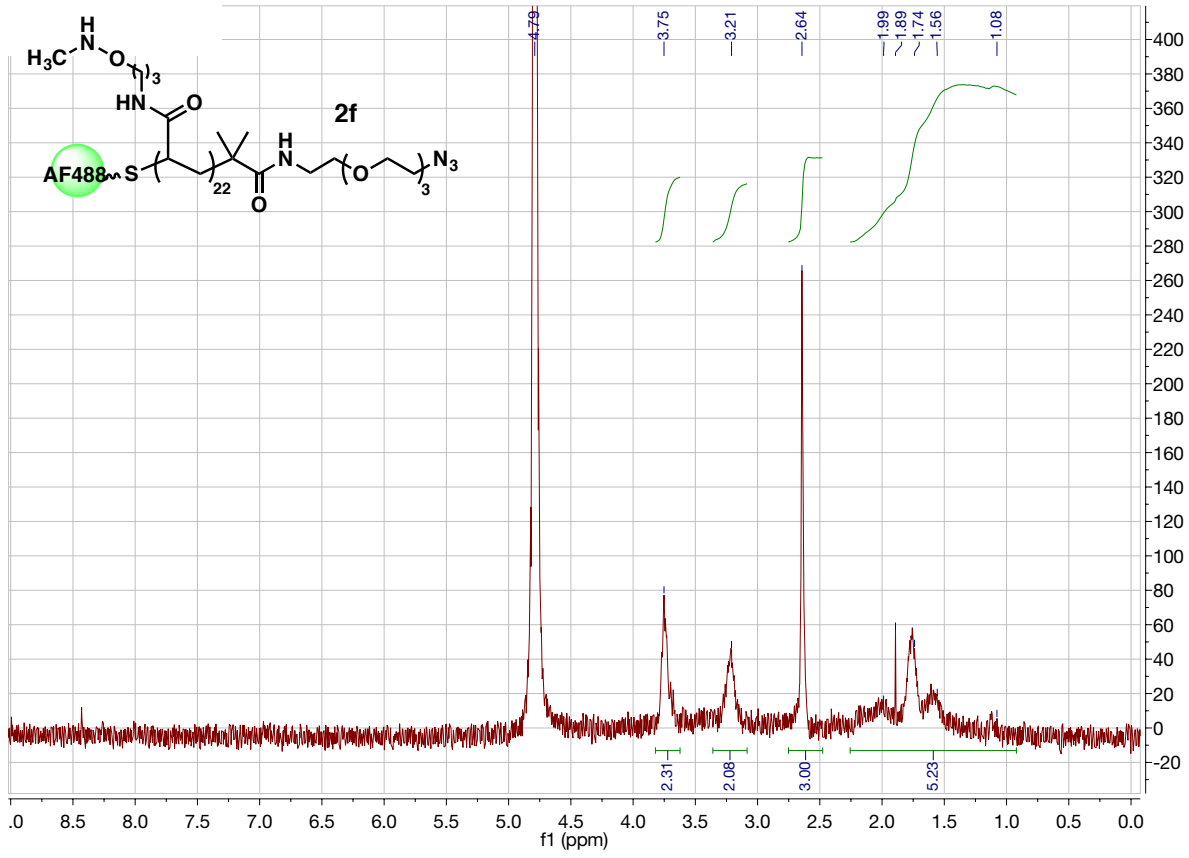

Figure 2.S9 ^{1}H NMR analysis of Boc-deprotected polymer (2f).

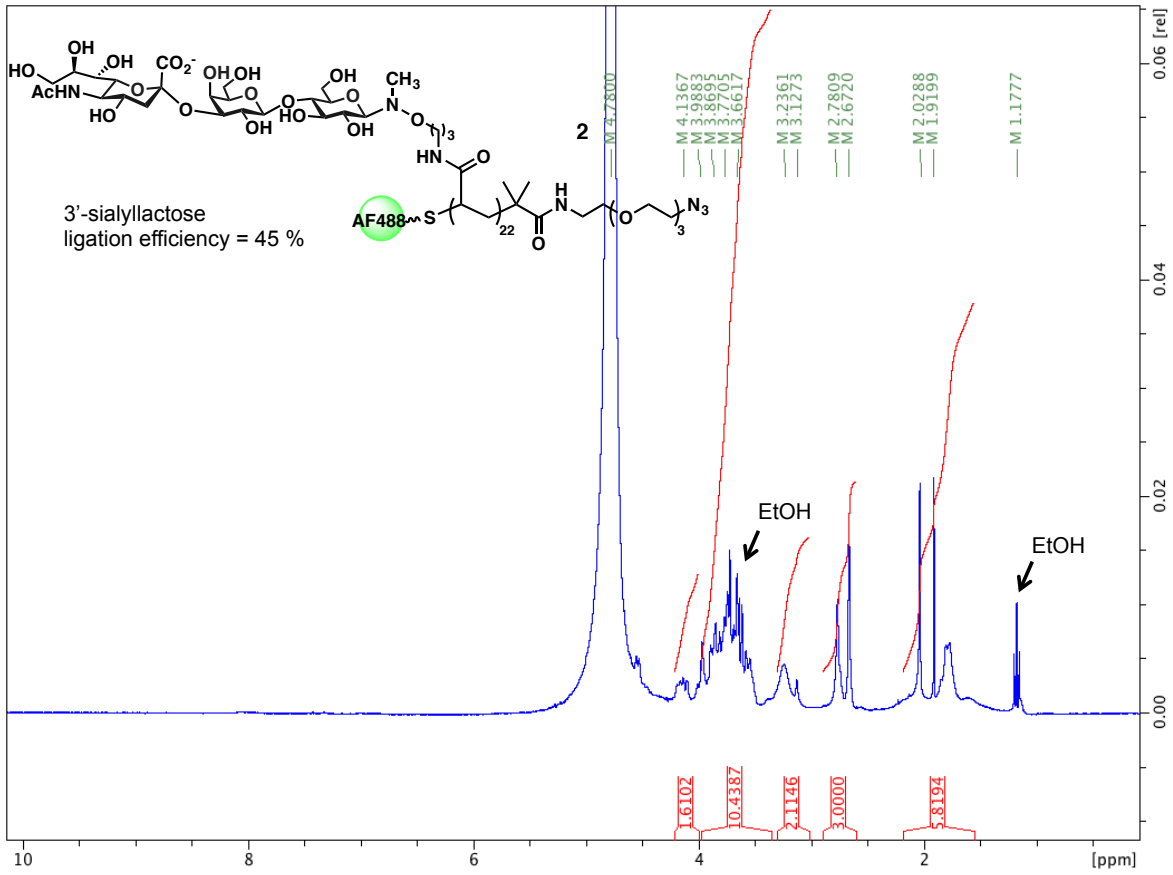

Figure 2.S10 ^{1}H NMR analysis of 3'-sialyllactose azide glycopolymer (2).

2.6.2.3 Synthesis and characterization of lipid conjugates.

6'-sialyllactose-azide (1) or 3'-sialyllactose glycopolymer-azide (2) were reacted with 1.1 eq. of DSPE-PEG(2000)-DBCO (3, 10 mM) in a 10% d6-DMSO/D_2O solution overnight at RT. The resulting crude mixture was used directly for experiments.

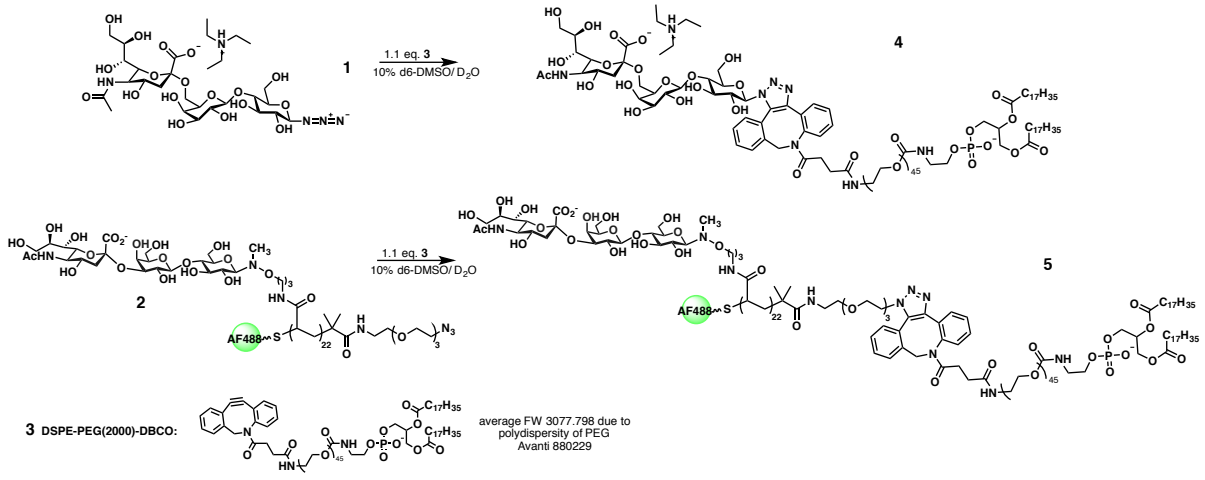

Scheme 2.S2 Synthesis of glycolipid and glycopolymer conjugates (4 and 5).

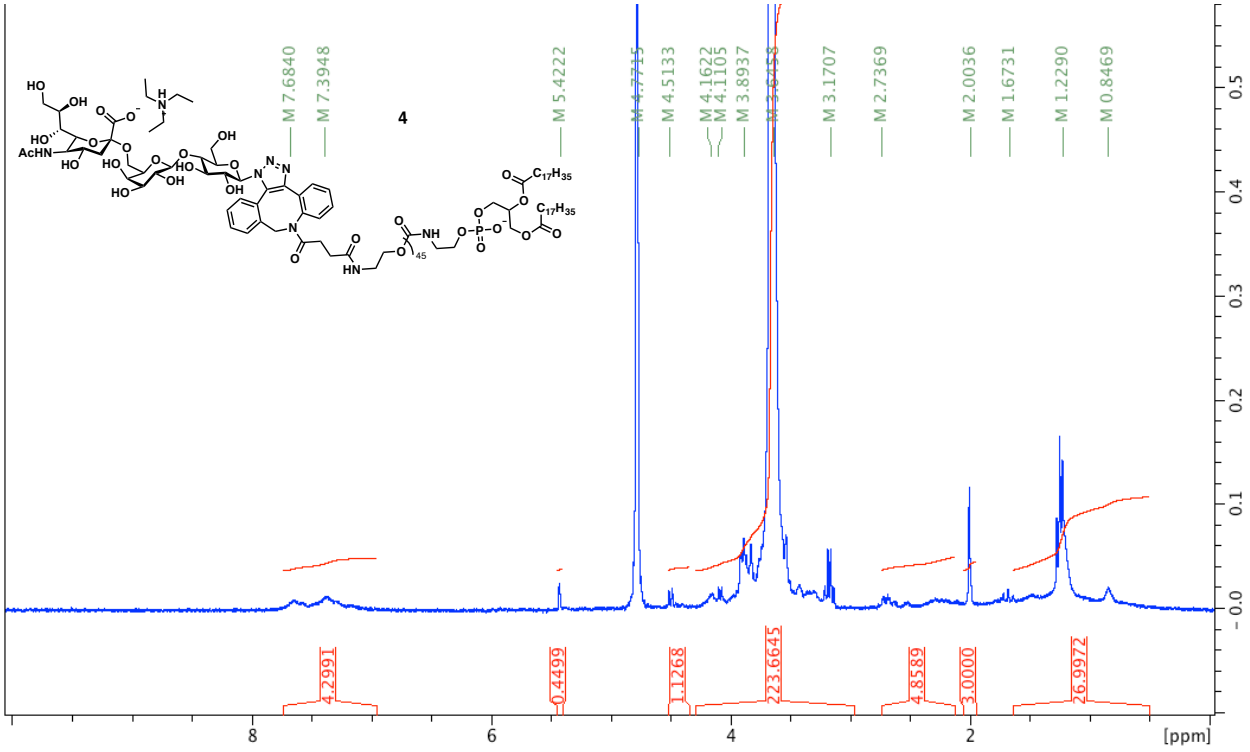

Figure 2.S11 ^{1}H NMR of 6'-sialyllactose glycolipid conjugate (4).

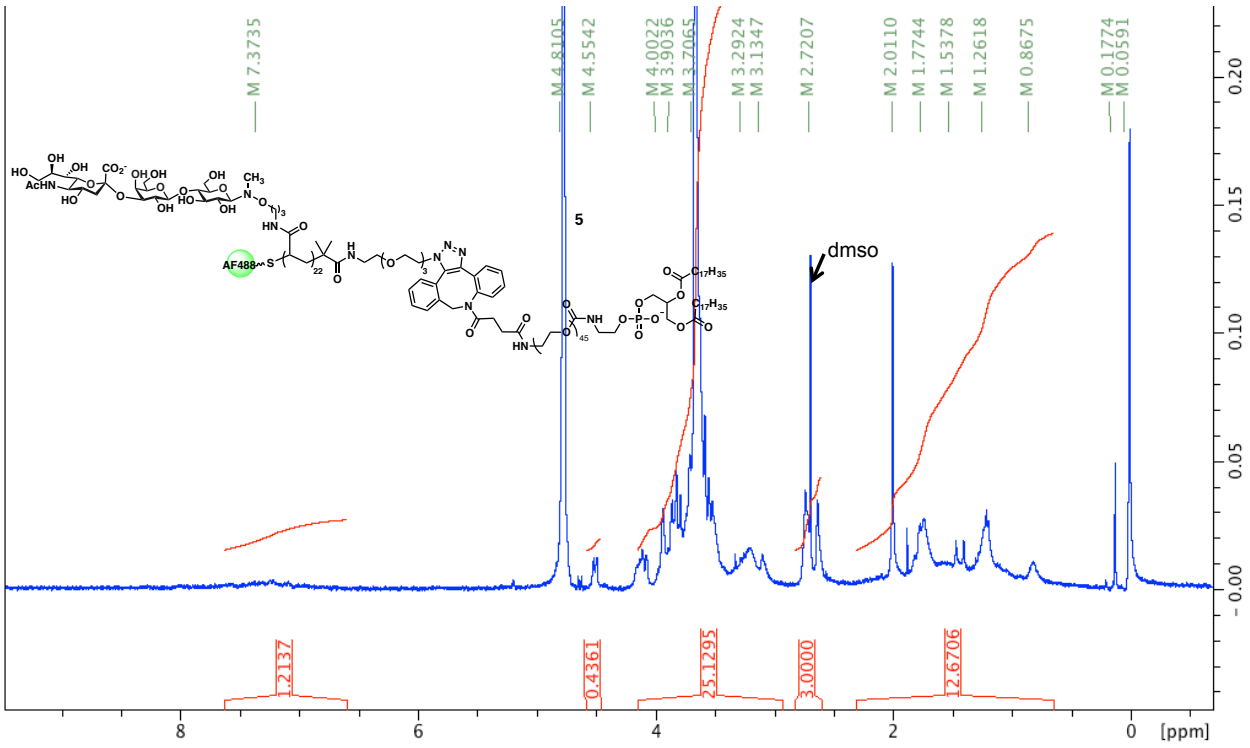

Figure 2.S12 ^{1}H NMR of glycopolymer lipid conjugate (5).

2.6.3 Biological materials

CHO-Lec2 cells (originally named Pro-5WgaRII6A) were obtained from ATCC (Cat # CRL-1736). CHO-Lec2s were cultured in MEMα (no nucleosides; Gibco Cat# 12561056) + 10% FBS (Origin: Australia; Life Technologies 1009133, lot 1647565). CHO-Lec2s were cultured as adherent cells on tissue-culture treated plastic dishes, and passaged every two days 1:10, by trypsinization with 0.05% Trypsin-EDTA (Gibco Cat # 25300120). The following conjugates were obtained commercially: biotinylated Maackia amurensis lectin II (bMALII, Cat # B-1265, 1 mg/mL) from Vector Labs (Burlingame, CA); Dylight649 conjugated Sambucus nigra lectin (Dy649-SNA, Cat # Dy649-6802-1) and biotinylated Sambucus nigra lectin (bSNA, Cat # B-1305, 1 mg/mL) were purchased from EY Labs (San Mateo, CA); Cy5 conjugated streptavidin (Cy5-Strep, Cat # SA1011) from Molecular Probes (Grand Island, NY).

2.6.4 Biological methods and supporting data

2.6.4.1 Cell surface remodeling with 6'-SL glycolipid or 3'-SL glycopolymer

CHO-Lec2 cells were seeded to confluency 24 hours prior to incubation on tissue-culture treated 24-well plates. Next day, cells were washed once with DPBS (-Ca, -Mg), and incubated with desired concentrations of the material in MEMα for 1 hour at 37 °C, 5% CO_2. Cells were visually checked for general health after incubation with the polymers by microscopy. No significant effects on cellular morphology were observed up to 1 mM final concentrations of either material. The cells were then washed twice with DPBS, trypsinized for 3-5 minutes to detach adherent cells, neutralized with an equal volume of

MEMα + 10%FBS, and harvested into 1.5 mL Eppendorf tubes. Cell suspensions were then pelleted (300 xg, 4 min, RT), washed once with DPBS, and fixed (1% PFAPBS) for 30-60 minutes at 4°C. After two sequential pelleting and washing steps, the cell suspensions were then stained for sialic acids with bMALII (1:100; 10 μg/mL) or Dy649 (1:100; 5 μg/mL) in 1% BSA/DPBS (+Ca, + Mg) overnight at 4°C, with gentle agitation. bMAL samples were washed and pelleted twice prior to labeling with Cy5-Streptavidin (1:500) in 1% BSA/DPBS (+Ca, + Mg) for an additional hour at 4 °C. Samples were further washed and pelleted twice prior to flow cytometry analysis. Graphs were generated using GraphPad Prism (v 6.0). Bar graphs and XY-graphs are depicted as means ± SD of duplicate wells.

2.6.4.2 Flow cytometry

CHO-Lec2 or CHO-K1 (WT) cells were dissociated as before and analyzed on a BD Accuri C6 flow cytometer. During collection, cells were gated using a FSC-H vs. SSC-H scatter plot, and 10, 000 cells in the relevant gate were collected per sample. FlowJo (v. 10) was then used to analyze the results.

2.6.4.3 Fluorescence microscopy

All imaging and processing was performed with a Zeiss AxioVert.A1 epifluorescence microscope and ZEN software, respectively. For visualizing polymer incorporation via the AlexaFluor488 fluorophore, cells in 24-well plates were fixed in 4% PFA/PBS for 10 mins at RT, washed twice with DPBS, and imaged directly in DPBS. To visualize SNA staining, cells were similarly fixed, and were then incubated with bSNA

(1:25; 40 μg/mL) in 1% BSA/DPBS (+Ca, +Mg) overnight at 4°C, with gentle agitation. After washing twice, cells were further incubated in Cy5-Streptavidin (1:400) in 1% BSA/DPBS (+Ca, + Mg) for an additional hour at RT. Cells were imaged directly in DPBS after two additional washes.

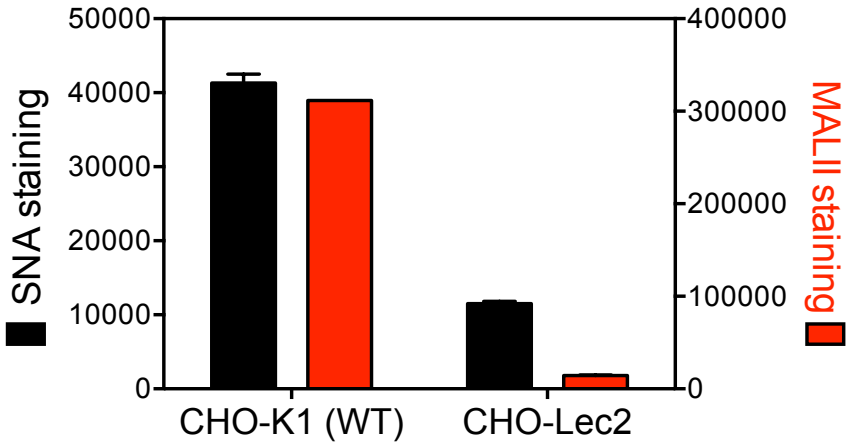

Figure 2.S13 Comparison of CHO-K1 (WT) and CHO-Lec2 sialic acid content. CHO-Lec2 mutants display significantly less α(2-6) and α(2-3) sialic acids, as indicated by reduced SNA and MALII lectin staining, respectively.

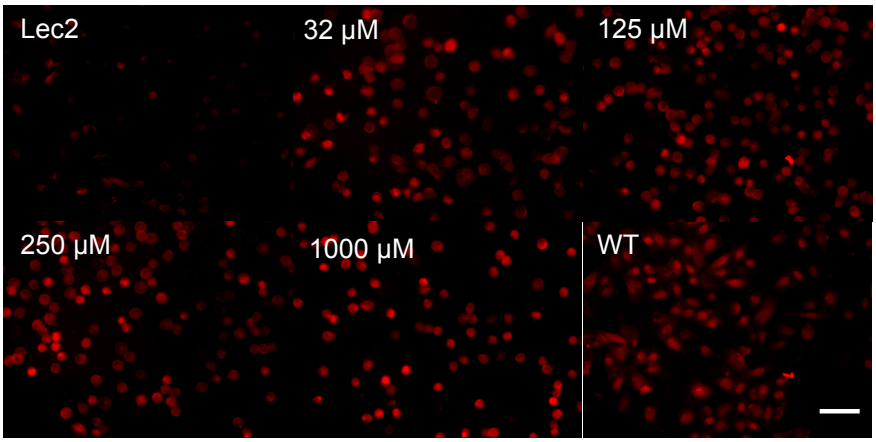

Figure 2.S14 SNA staining (red) of CHO-Lec2 cells remodeled with or without increasing concentrations of (4), compared to CHO-K1 (wild-type) cells. Scale bar: 50 μm.

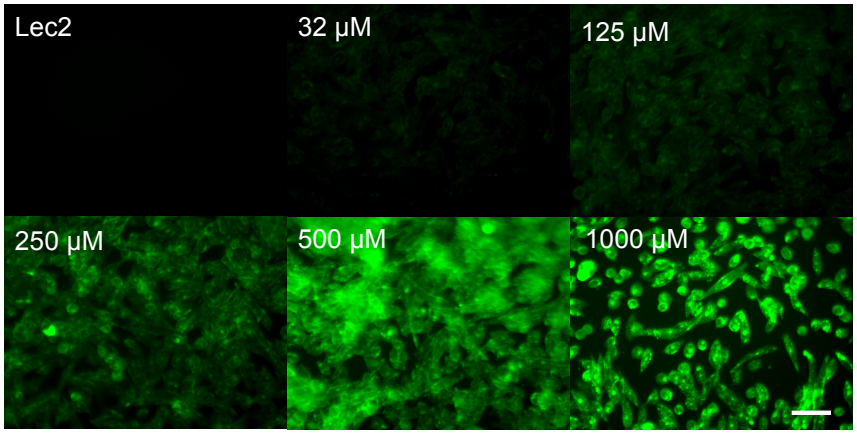

Figure 2.S15 AlexaFluor488 polymer fluorescence of CHO-Lec2 cells remodeled with increasing concentrations of (5). Scale bar: 50 μm.

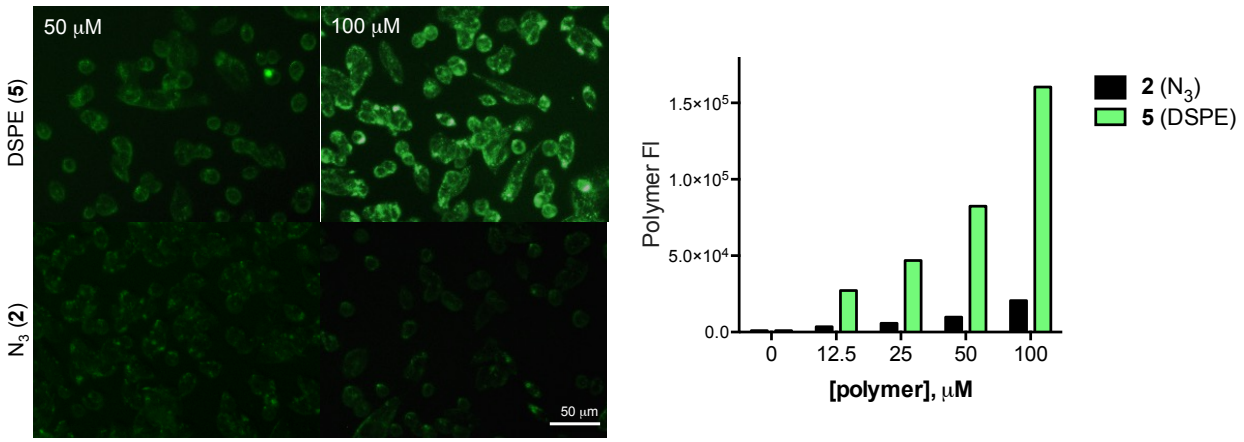

Figure 2.S16 AlexaFluor488 polymer fluorescence to evaluate nonspecific binding of azido-polymer 2 versus incorporation of DSPE-terminated polymer 5. Left: fluorescence microscopy, scale bar: 50 μm. Right: Flow cytometry analysis.

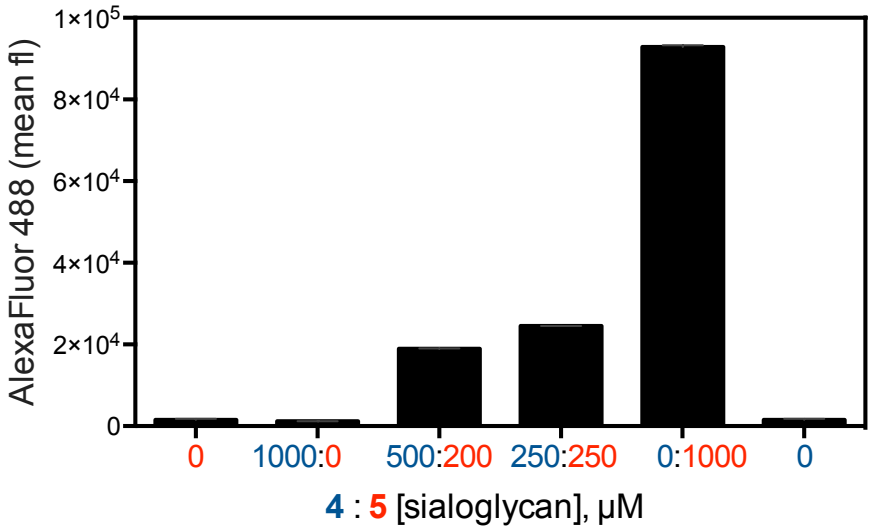

Figure 2.S17 AlexaFluor488 polymer fluorescence of CHO-Lec2 cells resulting from the incubation of AlexaFluor488-labeled 3'-sialyllactose polymer 5 mixed with 6'-sialyllactose glycolipid 4. Polymer fluorescence 5 still responds in a dose-dependent manner, even when mixed with 4.

2.6.5 References

1. T. Tanaka, H. Nagai, M. Noguchi, A. Kobayashi and S-I Shoda. Chem. Commun., 2009, 23, 3378-3379.

2. D. Lim, M. A. Brimble, R. Kowalczyk, A. J. Watson and A. J. Fairbanks. Angew. Chem. Int. Ed. Engl., 2014, 53, 11907-11911.

3. M. Kitamura and K. Murakami. Org. Synth., 2015, 92, 171-181.

4. M. L. Huang, R. A. A. Smith, G. W. Trieger and K. Godula. J. Am. Chem. Soc., 2014, 136,10565-10568.

3 Glycocalyx photoengineering enables modeling of cell surface mucin shedding dynamics

3.1 Abstract

The surfaces of mucosal epithelial cells are densely populated by large, extended glycoproteins, called mucins. Mucins deliver important protective functions against infection by creating a physical barrier at the cell surface and by capturing and clearing pathogens through shedding. Evaluating these mucin functions may provide better understanding of early stages of pathogenesis; however, the tools to tailor the composition and dynamics of the mucosal glycocalyx are currently limited. Here, we report a chemical cell surface engineering strategy to model the shedding behavior of mucins with spatial and temporal control. We generated synthetic mucin mimetic glycopolymers terminated with a photolabile membrane anchor, which could be introduced into the membranes of living cells and, subsequently, released upon exposure to UV light. Using glycan-specific interactions between lactose-bearing mucin mimetics and the *Ricinus communis* agglutinin (RCA), we showed that crosslinking lectins can stabilize the glycocalyx and limit shedding. Our findings indicate that endogenous and pathogen-associated lectins, which are known to interact with the host-cell glycocalyx, may alter mucin shedding dynamics and influence the protective properties of the mucosal barrier. More broadly, when combined with recent advances in mucin-mimetic synthesis, this glycocalyx engineering approach is poised to provide new mechanistic insights into the functional roles of mucins in cellular interactions.

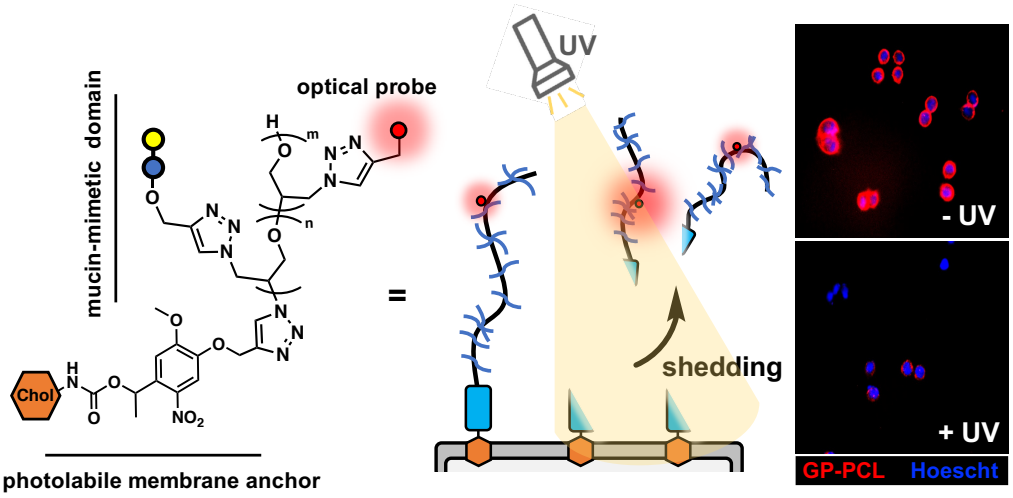

Figure 3.1 Glycocalyx photoengineering concept. Glycopolymers bearing a photolabile cholesterol membrane anchor incorporate into the cell membrane and are released in response to ultraviolet light.

3.2 Introduction

The epithelial glycocalyx, composed of membrane-associated glycoproteins and glycolipids, is an important functional component of the mucosal barrier that regulates interactions between the epithelium and various components of its external environment.[1] A class of extended, highly glycosylated proteins, known as mucins, which are expressed at high levels on mucosal cells and project away from the membrane, form a physical shield that protects cells from pathogenic challenge. Mucins do so by either limiting the access of pathogens to their cell-surface receptors[2] or by presenting decoy receptors to capture the pathogens and clear them from the cell surface via shedding.[3] In response, pathogens have evolved mechanisms to overcome the barrier functions of the glycocalyx, such as by expressing enzymes that can break down mucins and expose the cell surface.[4] Another possible mechanism through which pathogens may resist clearance

through shedding is by exploiting glycan-binding proteins (GBPs) to crosslink to multiple cell surface glycoconjugates.[5] Crosslinking of the glycocalyx by extracellular lectins, such as galectins, has been previously shown to contribute to its stabilization and to reduce endocytic turnover of native[6] and synthetic[7] glycoconjugates. However, the effects of glycocalyx crosslinking by oligomeric GBPs, including pathogen associated lectins, on mucin shedding are yet to be investigated; likely due to the lack of tools to induce mucin shedding from cells with spatial and temporal control.

Genetic tools to control mucin structure and expression to tailor the physical characteristics of the mucosal glycocalyx are rapidly emerging.[8] While the recent isolation and characterization of a suite of mucinase enzymes[9] enables selective removal of mucins from the glycocalyx, this leads to complete digestion of the mucin structure and does not fully recapitulate the process of shedding which leaves the glycosylated mucin ectodomains largely intact and capable of interacting with crosslinking lectins.

Synthetic glycopolymers, which approximate the structure of mucins and can be introduced into cell membranes, have provided a useful tool for the modeling the mucinous glycocalyx to study its biological functions.[10] Here we describe cell surface engineering with mucin mimetics bearing photocleavable membrane anchors to model mucosal glycocalyx shedding with spatial and temporal control using light. The synthetic mucin mimetics showed membrane-density dependent crosslinking by the oligomeric lectin, *Ricinus communis agglutinin*, which resulted in increased protection against shedding from the cell surface induced by light. This strategy is poised to enable future investigations into the regulation of mucin shedding by host- and pathogen-associated lectins and provide new insights into the protective functions of the mucosal barrier.

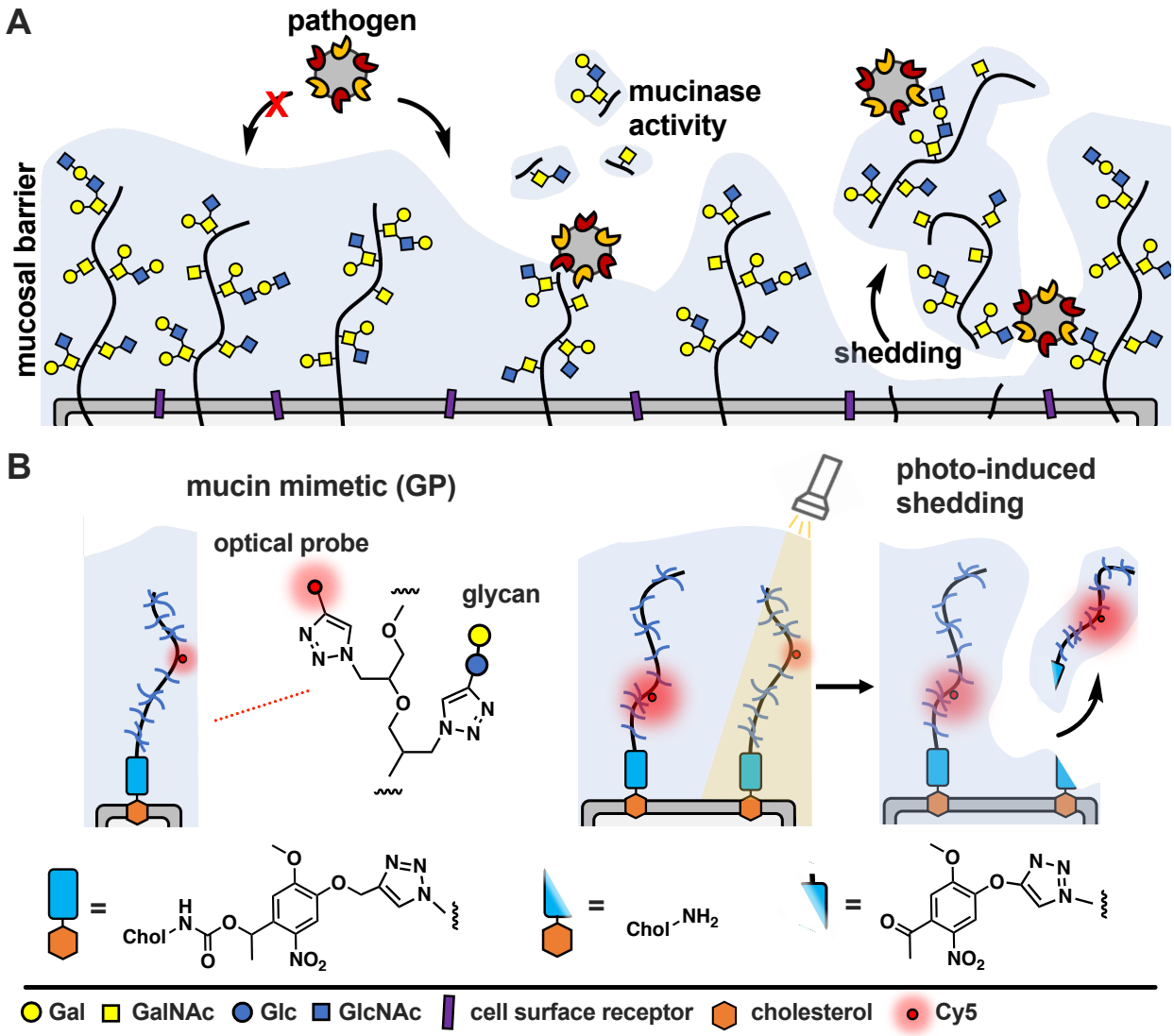

Figure 3.2 Shedding of the mucosal glycocalyx. A) Cell-surface mucins provide a protective physical barrier against infection. Pathogens disrupt this barrier by inducing proteolytic mucin glycocalyx degradation or shedding. B) Synthetic mucin mimetics with photocleavable membrane anchors enable modeling of mucin glycocalyx shedding behavior.

3.3 Results and Discussion

3.3.1 Generation of mucin mimetics with photo-cleavable membrane anchors

To model mucin glycoprotein shedding from cell surfaces, we designed mucin mimetic glycopolymers that can be presented on the plasma membrane of cells and

subsequently released upon application of an external stimulus, such as light (Fig 3.2B). The membrane targeting mucin-mimetic glycopolymers comprised a poly(ethylene oxide) (PEO) backbone glycosylated to produce the mucin-mimetic glycodomain and terminated with a hydrophobic anchor linked through a photocleavable nitrobenzyl group. Additionally, small percentage of the polymer sidechains (~ 1%) were functionalized with a fluorescent reporter (Cy5) for visualization.

The glycopolymer synthesis began by generating an azide-terminated poly(epichlorohydrin) scaffold **P1** primed for copper-catalyzed azide-alkyne cycloaddition (CuAAC) with cholesterol alkyne **1** containing a previously reported photocleavable (**PCL**) nitrobenzyl linker group[11] (Fig 3.3A). Monomer-activated anionic ring opening polymerization of **ECH**[10] in the presence of tetrabutylammonium azide (0.3 mol%) initiator and triisobutyl aluminum activator (0.7 mol%) furnished polymer precursor **P1** near the target molecular weight (Mw = 29 kDa, DP ~ 300) and narrow chain-length distribution (Đ = 1.23). Treatment of **P1** with **1** (10 equiv.) in the presence of a copper(I) iodide catalyst (1 equiv. per end group) and diisopropylethylamine, afforded a photocleavable cholesterol end group-modified **ECH** polymer intermediate **P2-PCL**. Introduction of the cholesterol end-group was difficult to observe directly by ^{1}H NMR spectroscopy; however, it could be confirmed by the disappearance of the IR characteristic, albeit weak, azide group absorption at ν = 2100 cm^{-1} (Fig 3.S9). Following chain end functionalization, the chloromethyl side chains were primed for glycosylation by reaction with sodium azide to generate azidomethyl side chain modified polymer **P3-PCL**. Quantitative side-chain conversion was confirmed by ^{1}H NMR and IR spectroscopy. The assembly of the desired mucin mimetic glycopolymer **GP-PCL** was accomplished through a sequential copper-

click reaction with sub-stoichiometric (1 mol%) alkynyl-Cy5 to introduce the fluorescent label followed by excess propargyl lactoside (1.5 eq.) as a model glycan. We assessed fluorescent labeling efficiency of **GPs** by UV-Vis spectroscopy to be ~ 2 – 3 fluorophores per **GP**, as expected for a polymer DP = 300. IR spectroscopy confirmed full consumption of the azide side chains following glycan attachment (Fig 3.S10).

We also generated two analogous mucin-mimetic glycopolymer controls (for details, see SI). The first was glycopolymer **GP-NPCL**, in which the cholesterol anchor was connected to the backbone through a non-photocleavable alkyl chain linker (introduced via 5-hexynoyl cholesteroamide **2**, Fig 3.3A) to serve as a mucin mimetic control resistant to cleavage by UV light. The second was glycopolymer **GP-Ø** lacking the cholesterol end group used to confirm hydrophobic anchor-dependent membrane incorporation of the mucin mimetics.

To characterize photocleavage of the Chol-PCL linker, the UV absorption spectrum was recorded following irradiation of **1** in chloroform (λ = 365 nm) at increasing time intervals (Fig 3.3B). The formation of a new peak at λ = 370 nm is indicative of photocleavage and this absorbance was used to determine the rate of photolysis (k = 6.4 ± 0.3 min^{-1}). Photocleavage of **1** neared completion within 0.75 min of UV exposure. We observed a similar photocleavage rate for the intermediate **P2-PCL** (k = 5.1 ± 2.3 min^{-1}, Fig 3.S12). These experiments confirmed the photolysis of the membrane anchor after UV irradiation and suggested that **GP-PCL**, in which the end group photolysis could not be detected directly in aqueous solution, should be suitable for cell-surface engineering.

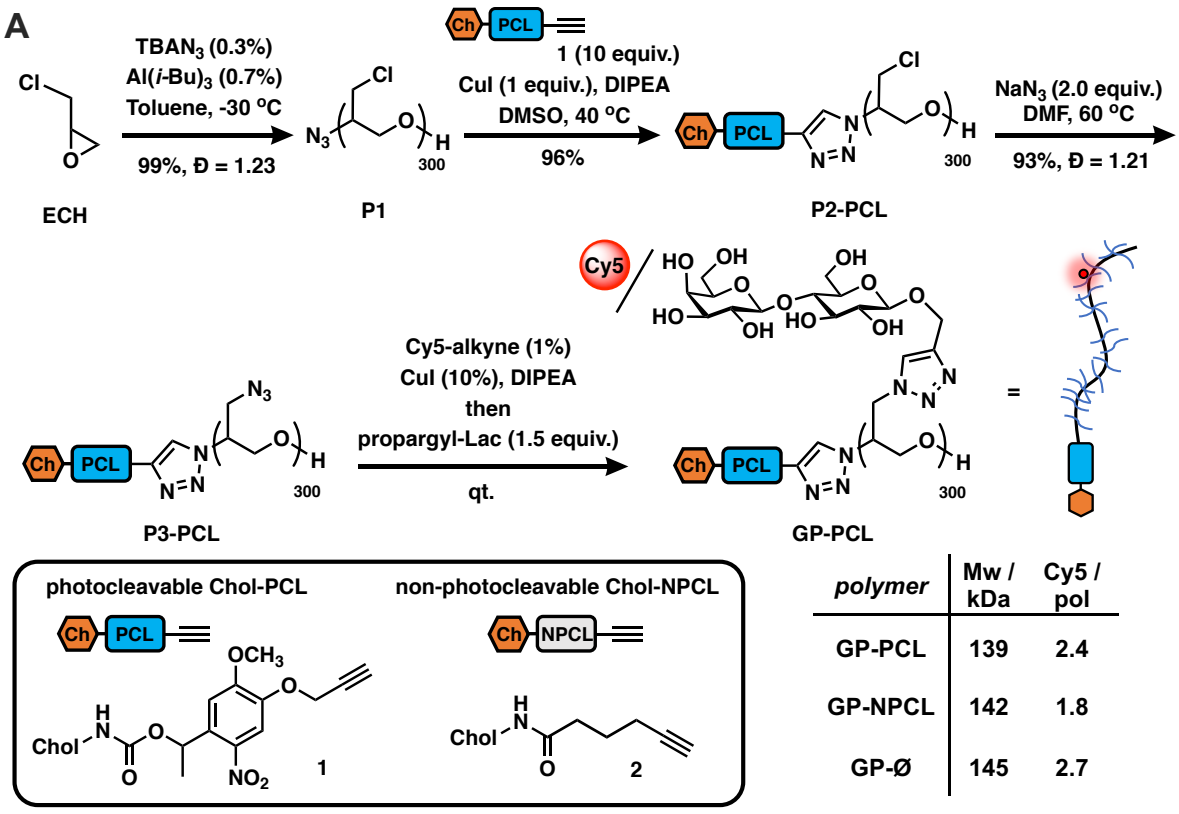

Figure 3.3 Synthesis and characterization of mucin mimetics with photocleavable membrane anchors. A) Mucin mimetic glycopolymers (**GPs**) terminated with photocleavable (PCL) and non-photo cleavable (NPCL) cholesterol anchors were elaborated from a common poly(epichlorohydrin) precursor (**P1**). A sequential end- and side-chain modification via the CuAAC reaction was used to introduce cholesterol anchors **1** and **2** and to construct a mucin mimetic domain comprised of lactosylated side chains and a fluorescent probe for visualization (Cy5, ~ 2-3 per **GP**). B) The photocleavage of cholesterol anchor Chol-PCL (**1**, 10 mg/mL in chloroform) with light at λ = 365 nm was analyzed by UV spectroscopy. The change in absorbance at λ = 370 nm over time was used to determine the rate of photocleavage (k = 6.4 ± 0.3 min^{-1}, n = 3).

3.3.2 ***Photoengineering of the mucin-mimetic glycocalyx***

For the construction of mucin glycocalyx models using our glycopolymer mimetics, we chose mutant Chinese hamster ovary cells, CHO *Lec8*, depleted in Golgi uridine diphosphate galactose (UDP-Gal) pools due to impaired transport of the nucleotide sugar from the cytosol.[12] As a result, these cells do not incorporate Gal into their cell surface glycans, thus providing a suitable cell system for membrane engineering with lactosylated mucin mimetics presenting b1,4-linked Gal residues. To establish optimal concentrations of the glycopolymers for cell-membrane remodeling, suspended CHO Lec8 cells were incubated with the Cy5-labeled **GP-PCL** and **GP-NPCL** at increasing polymer concentrations (0.63 – 20.00 mM, Fig 3.4A) at 4 °C. After one hour, the cells were washed to remove unincorporated polymers and analyzed by flow cytometry based on glycopolymer fluorescence. Both polymers inserted into the cell membrane with similar efficiency, nearing signal saturation at ~ 5 mM. The mucin mimetic **GP-Ø** lacking the cholesterol anchor exhibited no signal above untreated cell background, indicating the requirement for this group for membrane insertion and further confirming successful end-group functionalization of polymer precursors **P2-PCL** and **P2-NPCL**, which was difficult to detect using spectroscopic techniques (Fig 3.3A and Fig 3.S9-3.S10). We observed slightly greater total fluorescence intensity for cells remodeled with **GP-PCL** compared to **GP-NPCL**, consistent with the ~30% higher fluorophore labeling of the **GPs** (Fig 3.3A).

Cell surface remodeling was performed at 4 °C to limit endocytosis and polymer internalization. The low temperature can decrease membrane fluidity and limit polymer insertion. Therefore, we assessed the cell-surface incorporation of **GP-PCL** (~ 5 uM) in CHO Lec8 monolayers at 4, 21, and 37 °C. After a 1-hour incubation with the polymer,

the cells were washed and analyzed via fluorescence microscopy (Fig 3.S13). Remodeling at higher temperatures did not significantly improve membrane incorporation but facilitated polymer uptake by the cells, as evidenced by newly visible punctate cytosolic staining (see white arrows, Fig 3.S13b).

We next evaluated light-induced shedding of the mucin mimetics from the plasma membrane by exposing cells remodeled with both **GPs** to ultraviolet light (λ = 365 nm, Fig 3.4B). CHO Lec8 cells remodeled in suspension with **GP-PCL** and **GP-NPCL** (5 mM) on ice were exposed to UV light at increasing time intervals for up to 3 min and the loss of cell fluorescence was measured by flow cytometry (Fig 3.4B). We only observed a light- and time-dependent reduction in Cy5 intensity for **GP-PCL**, indicating clearance of the mucin mimetics from the cell surface via photo-induced cleavage of the nitrobenzyl cholesterol anchor **1**. The UV treatment of cells remodeled with the non-photocleavable polymer **GP-NPCL** resulted in no loss of Cy5 intensity, indicating resistance of the fluorophore to photobleaching under these conditions (Fig 3.4B). Within 2 minutes of UV exposure, mucin mimetic density at the cell surface was reduced by more than 70%, with minimal further photocleavage observed after additional exposure. The small fraction of UV-cleavage resistant mucin mimetics may result from polymer internalization by the cells or, possibly, through crosslinking of the excited state radical intermediate to other membrane components. The rate of **GP-PCL** photocleavage from the cell surface (k = 2.5 ± 0.6 min^{-1}) was similar to that measured for precursor **P2-PCL** in chloroform (k = 5.1 ± 2.3 min^{-1}). The UV light treatment in the presence or absence of the **GPs** resulted in little apparent cytotoxicity, as determined by a live-dead staining assay (> 93% cell viability, Fig 3.S17).

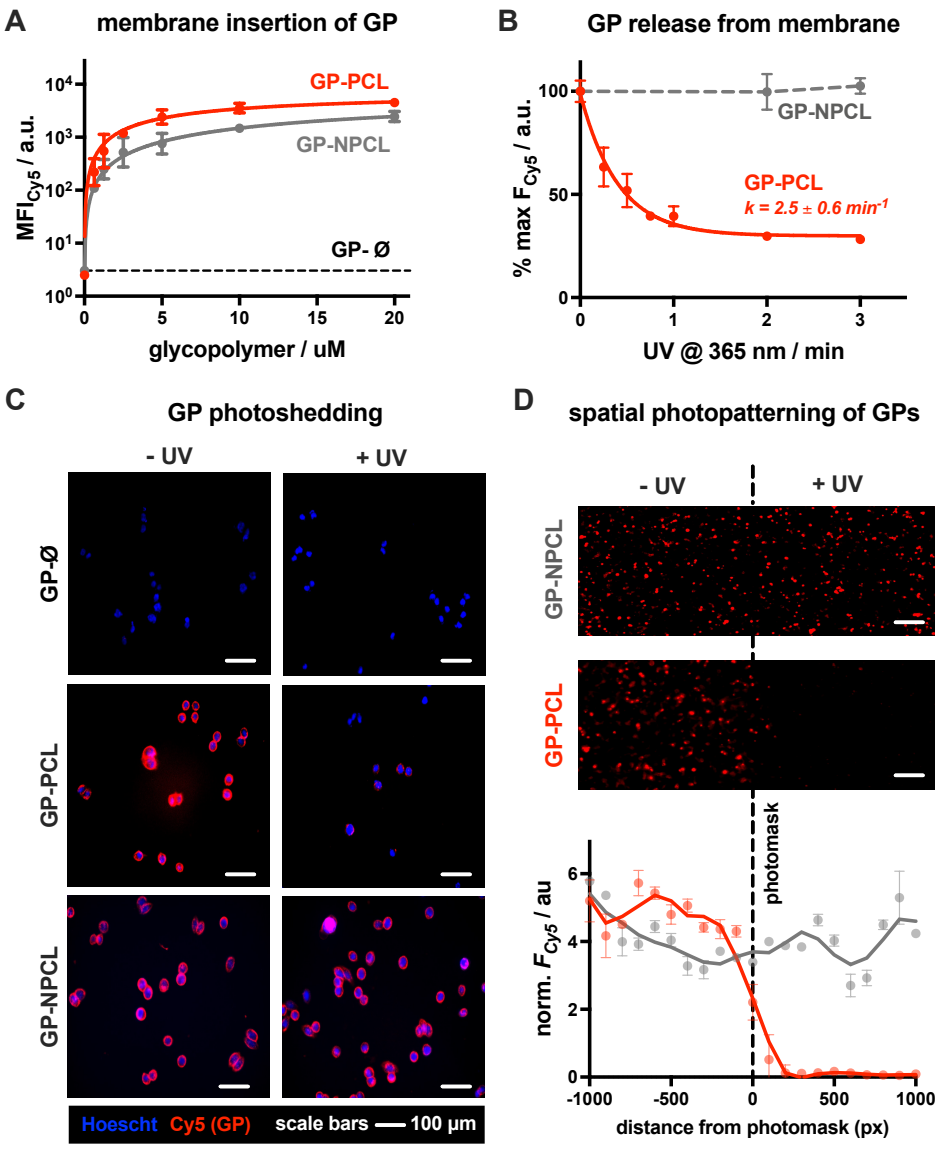

Figure 3.4 Photo-engineering of the mucin-mimetic glycocalyx in cells. A) Mucin mimetics containing photo-cleavable (**GP-PCL**) and non-photocleavable (**GP-NPCL**) cholesterol anchors incorporate into the plasma membranes of CHO Lec8 cells in a concentration dependent manner. Glycopolymers lacking the cholesterol anchor (**GP-Ø**) showed no association with the cells surface. B) Photo-shedding of the mucin mimetics upon irradiation with UV light (365 nm) was observed only for **GP-PCL** containing the photo-cleavable (PCL) anchor. Flow cytometry was used to determine the rate of photocleavage from the cell surface (k = 2.5 ± 0.6 min^{-1}) and the half-life for mucin mimetic shedding ($t_{1/2}$ = 0.28 ± 0.1 min, n = 3). Loss of fluorescence was not observed for the non-photocleavable mucin mimetic **GP-NPCL**. C) Fluorescence micrographs of CHO cells remodeled with Cy5-labeled **GP-PCL** and **GP-NPCL** (c_{GP} = 5 mM) before and after UV irradiation (I = 365 nm, 3 min). Cell nuclei were stained with Hoechst 33342 dye. (D) Spatial photopatterning of CHO Lec8 cells remodeled with mucin mimetics GP-PCL was accomplished through application of a mask during UV irradiation (I = 365 nm, 3 min). A plot of average fluorescence intensity per cell area with respect to the positioning of the photomask indicates mucin mimetic photo-shedding was specific to the subset of cells carrying the photocleavable **GP-PCL** and exposed to UV light (scale bars = 200 µm).

Next, we assessed the light-dependent mucin mimetic shedding from CHO *Lec8* cells in adherent culture via microscopy (Fig 3.4C). The cells were incubated with all three **GPs** at sub-saturation conditions (2 mM) at 4 °C for 1 hr. Unincorporated polymers were washed and a subset of the cells was exposed to UV light (λ = 365 nm), after which all cells were washed again and treated with a nuclear stain for imaging. Mucin mimetics **GP-PCL** and **GP-NPCL**, but not **GP-Ø**, showed robust cell surface labeling in the absence of UV light, confirming cholesterol-dependent membrane remodeling (Fig 3.4C). While cells treated with the non-photocleavable mucin mimetic, **GP-NPCL**, retained their fluorescence after UV exposure, most of the **GP-PCL** signal was lost. The cytosolic punctate staining that remained visible was consistent with polymer internalization and the flow cytometry analysis (Fig 3.4B).

The light responsiveness of the mucin mimetic **GP-PCL** enables patterning of the glycocalyx withing a subpopulation of cells. To demonstrate this concept, CHO Lec8 cell monolayers remodeled with either **GP-PCL** or **GP-NPCL** (2 mM) were exposed to UV light (λ = 365 nm) on ice for 3 min in the presence of a photomask. After illumination, the cells were washed, treated with a nuclear stain and imaged (Fig 3.4D). The fluorescence micrographs show a clear drop in Cy5 signal beyond the photomask for **GP-PCL**, which was quantified by plotting fluorescence intensity averaged over 100-pixel bins extending in both directions from the boundary. Cells remodeled with **GP-NPCL**, which is resistant to photocleavage, showed uniform fluorescence distributions. These experiments demonstrate the applicability of the light-responsive mucin mimetics for tailoring of the glycocalyx composition across a cell population with spatial resolution, which is difficult to achieve using existing glycan engineering techniques.

3.3.3 Effects of lectin interactions on mucin-mimetic glycocalyx shedding

The capture and shedding of pathogens by cell surface mucins are important defense mechanisms by which host cells can limit entry and infection.[13] Pathogens, which often exploit lectin interactions to bind to glycoconjugates on host cells[14], may counteract the shedding process by stabilizing the glycocalyx. Better understanding how lectin crosslinking affects mucin shedding from cells may reveal new insights into this important aspect of mucosal barrier function.

To evaluate whether lectin crosslinking can stabilize the mucinous glycocalyx and prevent its shedding, we investigated the interactions and photoshedding of cell-surface displays of GP-PCL in the presence or absence of *Ricinus communis* agglutinin (RCA). This lectin, with specificity for terminal b1,4-linked galactosides, is known for its ability to crosslink glycoconjugates and induce cell agglutination.[15] In the absence of endogenous Gal on the surfaces of the mutant CHO Lec8 cells, RCA binding after remodeling and photocleavage could be attributed solely to the presence of the lactose-bearing GP-PCL mucin mimetics (Fig3.S15 – 3.S16).

We first established an optimal concentration of RCA for use in binding assays (Fig 3.S14). Accordingly, a suspension of wild type CHO Pro5 cells was incubated with biotinylated RCA (0-20 mg/mL) on ice, stained with excess AlexaFluor488-streptavidin, and analyzed by flow cytometry. We observed concentration-dependent RCA staining with maximal signal intensity and no evidence of cell aggregation at lectin concentration of 5 mg/mL (Fig 3.S14a). CHO Pro5 cells in monolayer culture were then stained with RCA at this concentration and analyzed by fluorescence microscopy to confirm robust staining for imaging (Fig 3.S14b).

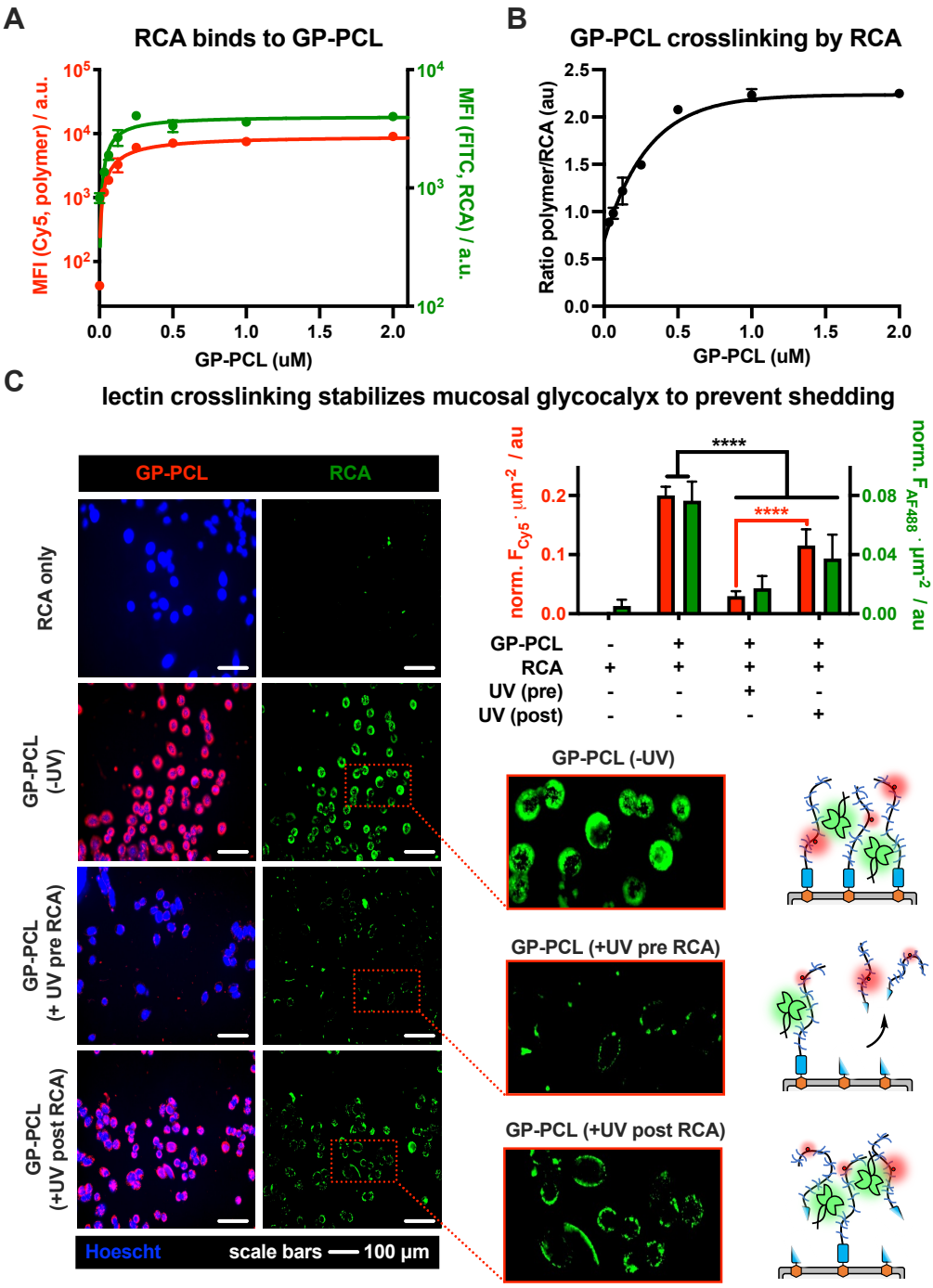

Figure 3.5 Lectin crosslinking limits photo-shedding of mucin mimetic glycocalyx. A) Remodeling of CHO Lec8 cells with mucin mimetic **GP-PCL** (red) introduces galactose binding sites for RCA (green) on the cells surface in a concentration-dependent manner. B) The plot of fluorescence intensity ratios for RCA and **GP-PCL** indicates enhanced lectin crosslinking with increasing polymer density in the membrane. C) Fluorescence micrographs and bar graph representations of CHO Lec8 cells remodeled with **GP-PCL** and irradiated either before (UV pre) or after (UV post) RCA crosslinking. Photo-shedding of the mucin mimetics prior to RCA incubation reduces the number of available binding sites for the lectin. RCA crosslinking of the mucin mimetic stabilizes the glycocalyx and limits photo-shedding of the polymer from the cell surface.

Using the optimized RCA staining conditions, we evaluated the binding of the lectin to CHO Lec8 cells remodeled with increasing concentrations of the photocleavable mucin mimetic ($c_{GP\text{-}PCL}$ = 0 – 2 mM). As expected, flow cytometry analysis revealed mucin mimetic concentration-dependent RCA binding (Fig 3.5A). Anticipating that RCA crosslinking may be affected by the membrane-density of the mucin mimetic, we plotted the ratio of GP-PCL and RCA fluorescence intensities as a function of polymer concentration (Fig 3.5B). We observed an increase in the polymer/RCA ratio, indicating more extensive crosslinking with increasing polymer density, until the saturation of glycan binding sites for the lectin.

Next, we evaluated the effects of RCA crosslinking on mucin-mimetic shedding. We induced cleavage of GP-PCL from the cell surface either before or after crosslinked by the lectin (Fig 3.5C). CHO Lec8 cells in monolayer were remodeled with GP-PCL at a concentration sufficient to induce maximal RCA crosslinking (2 mM), stained with RCA (5 mg/mL), and analyzed by fluorescence microscopy (Fig 3.5C, Fig3.S18). We observed robust labeling of the remodeled cells by RCA prior to exposure to UV light. Pearson's correlation analysis showed strong colocalization of the RCA and GP-PCL signals, confirming association of the lectin with the mucin mimetic in the glycocalyx. When RCA was added to the remodeled cells following UV treatment (3 min), minimal binding was observed in agreement with the decrease in availability of lectin binding sites after photo-induced shedding of the mucin mimetic. When RCA was added before illumination, a significant portion of GP-PCL remained on the cell surface (Fig 3.5C), which was quantified by measuring the mean Cy5 fluorescence intensity per cell area. This indicates that crosslinking by the lectin prior to shedding prevents clearance of the mucin mimetics

from the cell surface, presumably through tethering to remaining polymers or entanglement with native glycocalyx structures. In the native environment of the mucosal glycocalyx, oligomeric lectins can bridge mucins with other endogenous glycoconjugates present at the cell surface and further decrease the efficiency glycocalyx shedding.

3.4 Conclusions

In this study, we have developed light-responsive glycomimetic materials to model the shedding behavior of mucin glycoproteins in the mucosal barrier. The introduction of a photo-cleavable cholesterol anchor into the mucin mimetics enabled their installation into the plasma membranes to augment the glycocalyx of living cells and enable subsequent photo-release. We demonstrated the utility of these materials for the photo-patterning of cell surfaces and their interactions with lectins. We used RCA to model the effects of lectin binding on mucin shedding dynamics and observed that crosslinking can enhance their retention on the cell surface. This glycocalyx engineering strategy may provide new insights into the roles of mucins in regulating host-pathogen interactions and the contributions from endogenous and pathogen-associated lectins to the protective functions of the mucosal barrier.

3.5 Methods

3.5.1 General materials and methods

All chemicals, unless otherwise stated, were purchased from Sigma Aldrich and used as received. Cuprisorb resin was purchased from SeaChem Labs. Reaction progress was monitored by analytical thin-layer chromatography (TLC, Merck silica gel plates) with UV illumination or via CAM, ninhydrin, or $KmnO_4$ staining. Column

chromatography was performed on a Biotage Isolera One automated flash chromatography system. Nuclear magnetic resonance (^{1}H and ^{13}C NMR) spectra were recorded on Bruker 300 MHz and Jeol 500 MHz NMR spectrometers. Spectra were recorded in $CDCl_3$ or D_2O at 293K and are reported in parts per million (ppm) on the δ scale relative to residual solvent as an internal standard (for ^{1}H NMR: $CDCl_3$ = 7.26 ppm, D_2O = 4.79 ppm, for ^{13}C NMR: $CDCl_3$ = 77.0 ppm, CD_3OD = 49.0 ppm). HRMS (high-resolution mass spectrometry) analysis was performed on an Agilent 6230 ESI-TOFMS in positive ion mode. UV-Vis spectra were collected in a quartz cuvette using a Thermo Scientific Nanodrop2000c spectrophotometer. IR spectroscopy was performed on a Nicolet 6700 FT-IR spectrophotometer. Size exclusion chromatography (SEC) was performed on a Hitachi Chromaster system equipped with an RI detector and two 5 μm, mixed bed, 7.8 mm I.D. x 30 cm TSK gel columns in series (Tosoh Bioscience) using an isocratic method with a flow rate of 0.7 mL/min in DMF (0.2% LiBr, 70 °C).

3.5.2 Synthesis of azide-terminated poly(epichlorohydrin), P1

Epichlorohydrin was polymerized according to published procedures[16]. Briefly, to a 10 mL flame-dried Schlenk flask equipped with a magnetic stirrer was added tetrabutylammonium azide ($TBAN_3$, 30.0 mg, 60.0 mmol) under Ar atmosphere. Distilled epichlorohydrin (1.29 mL, 16.50 mmol) in anhydrous toluene (4.00 mL) and triisobutylaluminum in toluene (1.07 M, 0.10 μL, 0.11 mmol) were then added at −30 °C. The reaction was stirred for 4 hours before quenching with ethanol. The resulting polymer **P1** was precipitated into hexanes and dried under vacuum to yield a clear viscous oil

(1500 mg, 99%). The polymer was analyzed by SEC (0.2% LiBr in DMF): Mw = 29,000, Mn = 27,700, Đ = 1.23 and ^{1}H NMR ($CDCl_3$, 500 MHz, FigS5).

3.5.3 Synthesis of poly(epichlorohydrin) polymers, P2

To separate 1-dram vials with a magnetic stirrer were added p(ECH) polymer **P1** (7.50 mg, 0.25 µmol, 1 equiv) and anhydrous DMSO (500 µL). Photocleavable cholesterol anchor **1** (1.70 mg, 2.50 µmol, 10 equiv) or non-photocleavable cholesterol anchor **2** (1.20 mg, 2.50 µmol, 10 equiv) was added, followed by CuI (0.05 mg, 0.30 µmol, 1.0 equiv) and one drop diisopropylethyl amine (~ 5 µL). The reactions were stirred at 40 °C for 12 hours before quenching with DCM and mixing with Cuprisorb beads (18 hrs) to sequester copper. The polymers were filtered through celite, concentrated under vacuum, and triturated with chloroform in EtOH (30% v/v) to remove residual **1** or **2**. The resultant polymers **P2** were dried under vacuum to yield **P2-PCL** (7.2 mg, 96%) and **P2-NPCL** (6.7mg, 89%). **P2** were characterized by ^{1}H NMR ($CDCl_3$, 500 MHz, FigS6), IR spectroscopy (FigS9), and UV-Vis spectroscopy (FigS12).

3.5.4 Synthesis of cholesterol poly(glycidyl azide) polymers, P3

Three separate 1-dram vials were charged with cholesterol-terminated p(ECH) polymers **P2** (6.7 – 7.2 mg, 0.22 – 0.24 µmol, 1 equiv.) in anhydrous DMF (200 µL) and a magnetic stirrer. To the solutions was then added NaN_3 (2.0 mg, ~ 2.0 equiv.) and the reactions was stirred at 60 °C for 72h under Ar. The reaction solutions were filtered, dried, and concentrated from DCM to yield p(GA) polymers **P3-PCL** (7.0 mg, 93%), **P3-NPCL** (6.70 mg, 89%), and **P3-Ø** (7.18 mg, 88%). **P3** were characterized by ^{1}H NMR ($CDCl_3$,

500 MHz, FigS7), size exclusion chromatography (FigS11), and IR spectroscopy (FigS10).

3.5.5 Synthesis of glycopolymers, GP

To three separate 1-dram vials were added p(GA) polymers **P3** (7.50 mg, 0.075 mmol) dissolved in anhydrous DMSO (0.25 mL) and magnetic stirrers. Solutions of Cy5-alkyne (7.50 mg, 0.75 μmol) in DMSO (75 μL) were added, followed by CuI (1.67 mg, 7.50 μmol) and DIPEA (13.3 uL, 0.075 mmol). After 2 hours at 40 °C under Ar, propargyl lactose[16B] (50 μL, 0.113 mmol, 1.5 eq per azide side-chain) in anhydrous DMSO was added to the reactions and stirred at 40 °C overnight. The glycopolymers were diluted in water and treated with Cuprisorb beads for 18 hours to sequester copper before filtration over celite and lyophilization. Methanol was used to remove excess glycoside and **GPs** were again lyophilized to yield the Cy5-labeled glycopolymers as pale blue solids **GP-PCL** (7.50 mg, quant.), **GP-NPCL** (7.50 mg, quant.), and **P2-Ø** (7.50 mg, quant.). **GPs** were characterized by ^{1}H NMR (D_2O, 500 MHz, FigS8) and Cy5 labeling efficiency was quantified via UV-Vis spectroscopy (λ_{max} = 633 nm, ~ 2-3 fluorophores per polymer).

3.5.6 General cell culture

All biological reagents were purchased from Gibco (ThermoFisher) unless otherwise stated. CHO Lec8 and CHO Pro5 cells used were obtained from ATCC (CRL-1737 and CRL-1781, respectively). Biotin-labeled *Ricinus communis agglutinin I* was purchased from Vector Labs (B-1085-5). Cells were cultured at 37 °C and 5% CO_2 following standard tissue culture practices. CHO (Chinese Hamster Ovary cells, Pro5 and

Lec8) were cultured in MEMa medium supplemented with 10% FBS, 100 U/mL penicillin, and 100 U/mL streptomycin. Cells were suspended utilizing 0.25% trypsin-EDTA and passaged every 2-4 days to achieve desired confluency on tissue-culture treated lab plastics. Live cell flow cytometry analysis was performed using a FACSCalibur or FACSCanto II system (BD Biosciences). Microscopy was performed on either a Keyence BZX800 epifluorescent microscope or a ThermoScientific EVOS imaging system and images were analyzed using ImageJ.

3.5.7 GP membrane incorporation

Flow cytometry: CHO Lec8 cells were suspended, washed, and 10^6 cells were pelleted into Eppendorf tubes. GPs prepared in DPBS (0 – 20 mM, 100 mL) were added to the cell pellets, mixed, and incubated on ice for 1 hour. Following two washes with DPBS, cells were resuspended and analyzed by flow cytometry.

Microscopy: CHO Lec8 cells grown in 12-well plates were rinsed with DPBS and **GPs** (2 mM) were added. Plates were incubated on ice for 1 hour before three DPBS washes. Nuclei were stained using Hoescht 33342 (10 mg/mL, 10 min) followed by two additional DPBS washes. Fluorescent micrographs were captured on a Keyence epifluorescent microscope.

3.5.8 Photo-induced shedding of GPs from cell surface

Flow cytometry: Remodeled CHO Lec8 cells in clear plastic tubes were subjected to ultraviolet light (l = 365nm, 0 – 3 min) using a handheld 15W lamp. Following irradiation cells were washed twice with DPBS and resuspended for flow cytometry analysis.

Microscopy: Remodeled CHO Lec8 cells were irradiated in well plates using a handheld 15W lamp (l = 365nm, 3 min) directly below the plate. Cells were then washed three times with 1mL of DPBS and nuclei were stained using Hoescht 33342 (10 mg/mL, 10 min). Following two additional DPBS washes fluorescent micrographs were captured.

3.5.9 Photopatterning of GPs in cell membrane

CHO Lec8 cells were grown until confluent in 6-well plates. Standard **GP** membrane incorporation protocols were utilized and fluorescent micrographs were captured within a selected region suitable for stitching. A portion of the well was masked before irradiation using a handheld 15W lamp (l = 365nm, 0 – 3 min). Following mask removal, images were collected within the region, stitched using Keyence BZX Analyzer software, and quantified by ImageJ.

3.5.10 RCA binding to GP-PCL remodeled cells

CHO Lec8 cells were suspended (0.25% trypsin-EDTA), washed, and 10^6 cells were pelleted in Eppendorf tubes. **GP-PCL** prepared in DPBS (0-5uM, 100 mL) were added to the cell pellets and incubated on ice for 1hr. Following two DPBS washes cells were incubated in RCA-biotin (5 ug/mL, 300mL) for 40 min on ice. After two additional washes cells were incubated in excess AlexaFluor488 labeled streptavidin (300mL, 1:750) for 20 min, washed twice with DPBS, and resuspended for flow cytometry analysis.

3.5.11 Lectin crosslinking during GP shedding

CHO Lec8 cells grown in 12-well plates were remodeled with **GP-PCL** (2 mM) on ice for 1 hour. Cells were then washed three times with DPBS and incubated with RCA-biotin (5 mg/mL) either before (pre RCA) or after (post RCA) UV irradiation using a 15W lamp (l = 365nm, 3 min). After an additional three DPBS washes, cells were incubated on ice for 30 min with an excess of AlexaFluor488 labeled streptavidin (300uL, 1:750) and nuclei were stained with Hoescht 33342 (10 mg/mL, 10 min) for visualization. Following two additional DPBS washes fluorescent micrographs were captured on a Keyence epifluorescent microscope and ImageJ was used to analyze micrographs.

3.6 Acknowledgements

K.G. conceived of the research; S.C.P., M.H.Z., D.J.H. and K.G. designed the research; S.C.P., M.H.Z., H.J.C.N., D.J.H., and A.L.M. performed the research; S.C.P., M.H.Z., H.J.C.N, and K.G. analyzed data; S.C.P. and K.G. wrote the manuscript and supporting information; all authors approved the manuscript for publication. This work was supported in part by the NIH Director's New Innovator Award (NICHD: 1DP2HD087954-01). We thank the UCSD Microscopy Core Facility for assistance with fluorescence microscopy (via NINDS P30 Grant: P30NS047101) and the UCSD Glycobiology Research and Training Center for providing access to critical analytical instrumentation. KG was supported by the Alfred P. Sloan Foundation (FG-2017-9094) and the Research Corporation for Science Advancement via the Cottrell Scholar Award (grant #24119); S.C.P. was supported by a GAANN fellowship (U.S. Dept. of Education, P200A150251).

Chapter three, in full, is a reprint of the material as it appears in a manuscript submitted for publication: Purcell, S.; Zhang, M.Z.; Honigfort, D.J.; Ng, H.J.C.; Michalak, A.L.; Godula, K. Glycocalyx photoengineering enables modeling of cell-surface mucin shedding dynamics. The dissertation author is the primary co-author of this work.

3.7 References

1A. Varki A,; Gagneux P.;Biological Functions of Glycans. 2017. In: Varki A, Cummings RD, Esko JD, et al. Essentials of Glycobiology, 3rd edition. Cold Spring Harbor (NY): *Cold Spring Harbor Laboratory Press*; 2015-2017.

1B. Linden, S.K.; Sutton, P.; Karlsson, N.G.; Korolik, V.; McGuckin, M.A. Mucins in the mucosal barrier to infection. *Mucosal Immunol.* 2008, 1, 183–197. DOI: 10.1038/mi.2008.5

2A. Purcell, S.C.; Godula. K.; Synthetic glycoscapes: addressing the structural and functional complexity of the glycocalyx. *Interface Focus*. 2018, 9, 20180080. DOI: 10.1098/rsfs.2018.0080

2B. McGuckin, M.A.; Linden, S.K., Sutton, P.; Florin, T.H. Mucin dynamics and enteric pathogens. *Nat. Rev. Microbiol.* 2011, 9, 265–278. DOI:10.1038/nrmicro2538

3A. Honigfort, D.J.; Altman, M.O.; Gagneux, P.; Godula, K.; Glycocalyx crowding with mucin mimetics strengthens binding of soluble and virus-associated lectins to host cell glycan receptors. *Proc. Nat'l. Acad. Sci.* 2021, 118 (40). DOI:10.1073/pnas.2107896118

3B. Delaveris, S.C; Webster, R.E.; Banik, M. Stephen; Boxer, G.; Bertozzi, C.R.; *Proc. Nat'l. Acad. Sci*. 2020, 17 (23) 12643-12650. DOI: 10.1073/pnas.1921962117

4. Cohen, M.; Zhang, X.Q.; Senaati, H.P.; Chen, H.W.; Varki, N.M.; Schooley, R.T.; Gagneux, P. Influenza A penetrates host mucus by cleaving sialic acids with neuraminidase. *Virol. J*. 2013 10, 321. DOI: 10.1186/1743-422X-10-321

5. Van Breedam, W.; Pöhlmann, S.; Favoreel, H.W.; DeGroot, R.J.; Nauwynck, H.J. Bitter-sweet symphony: glycan-lectin interactions in virus biology. *FEMS Microbiol. Revs.* 2014, 38(4), 598-632. DOI: 10.1111/1574-6976.12052

6. Argueso, P.; Guzman-Aranguez, A.; Mantelli, F.; Cao, Z.; Ricciuto, J.; Panjwani, N. Association of the cell surface mucins with galectin-3 contributes to the ocular surface epithelial barrier. *J. Biol. Chem.* 2009, 284(34), 23037-23045. DOI: 10.1074/jbc.M109. 033332

7A. Belardi, B.; O'Donoghue, G.P.; Smith, A.W.; Groves, J.T.; Bertozzi, C.R. Investigating cell surface galectin-mediated cross-linking on glycoengineered cells. *J. Am. Chem. Soc.* 2012, 134, 23, 9549-9552. DOI: 10.1021/ja301694s

7B. Belardi, B.; Bertozzi, C.R. Chemical lectinology: tools for probing the ligands and dynamics of mammalian lectins in vivo. *J. ChemBiol*. 2015, 22(8), 983-993. DOI: 10.1016/j.chembiol.2015.07.009

8. Shurer, C. R., Colville, M. J., Gupta, V. K., Head, S. E., Kai, F., Lakins, J. N., & Paszek, M. J. Genetically encoded toolbox for glycocalyx engineering: tunable control of cell adhesion, survival, and cancer cell behaviors. *ACS Biomat. Sci. Eng*. 2018, 4(2), 388–399. DOI: 10.1021/acsbiomaterials.7b00037

9A. Shon, D. J., Malaker, S. A., Pedram, K., Yang, E., Krishnan, V., Dorigo, O., & Bertozzi, C. R. An enzymatic toolkit for selective proteolysis, detection, and visualization of mucin-domain glycoproteins. *Proc. Nat'l. Acad. Sci*. 2020, 117(35), 21299–21307. DOI: 10.1073/pnas.2012196117

9B. Malaker, S. A., Pedram, K., Ferracane, M. J., Bensing, B. A., Krishnan, V., Pett, C., Yu, J., Woods, E. C., Kramer, J. R., Westerlind, U., Dorigo, O., & Bertozzi, C. R. The mucin-selective protease StcE enables molecular and functional analysis of human cancer-associated mucins. *Proc. Nat'l. Acad. Sci*. 2019, 116(15), 7278–7287. DOI: 10.1073/pnas.1813020116

10A. Kramer, J.R.; Onoa, B.; Bustamante, C.; Bertozzi, C.R. Chemically tunable mucin chimeras assembled on living cells. Proceedings of the National Academy of Sciences, 112(41), 12574 – 12579. DOI: pnas.1516127112

10B. Pan, H.; Colville, M. J.; Supekar, N. T.; Azadi, P.; Paszek, M. J. Sequence-specific mucins for glycocalyx engineering. ACS synthetic biology, 8(10), 2315–2326. DOI: 10.1021/acssynbio.9b00127

11A. Gaur, P.; Kucherak, O.A.; Ermakova, Y.G.; Shvadchak, V.V.; Yushchenko, D.A. Nitrobenzyl-based fluorescent photocages for spatial and temporal control of signaling lipids in cells. *Chem Comm*. 2019, 55(82), 12288-12291. DOI :10.1039/c9cc05602e

11B. Kaneko, S.; Nakayama, H.; Yoshino, Y.; Fushimi, D.; Yamaguchi, K.; Horiike, Y.; Nakanishi, J. Photocontrol of cell adhesion on amino-bearing surfaces by reversible conjugation of poly(ethylene glycol) via a photocleavable linker. *Phys. Chem. Chem. Phys*. 2011, 13(9), 4051- 4059. DOI: 10.1039/c0cp02013c

12. Oelman, S.; Stanley, P.; Gerardy-Schahn, R. Point mutation identified in Lec8 chinese hamster ovary glycosylation mutants that inactivate both the UDP-galactose and cmp-sialic acid transporters. *J. Biol. Chem*. 2001, 276(28), 26291-26300. DOI: 10.1074/jbc. M011124200

13A. Dhar, P.; McAuley, J. The role of the cell surface mucin MUC1 as a barrier to infection and regulator of Inflammation. Frontiers Cell. And Infect. Microbiol. 2019, 9. DOI: 10.3389/fcimb.2019.

13B. McAuley, J.L, Corcilius, L., Tan, H.X. Payne, R.J, McGuckin, M.A, Brown, L.E. The cell surface mucin MUC1 limits the severity of influenza A virus infection. *Mucosal Immunol.* 2017, 10, 1581–1593. DOI: 10.1038/mi.2017.16

13C.Turner, J. Intestinal mucosal barrier function in health and disease. *Nat. Rev. Immunol.* 2009, 9, 799–809. DOI: 10.1038/nri2653

14A. Corfield, A.P. Mucins: a biologically relevant glycan barrier in mucosal protection. *Biochim. Biophys. Acta.* 2015, 1850(1), 236-52. DOI: 10.1016/j.bbagen.2014.05.

14B. Wagner, C.E.; Wheeler, K.M.; Ribbeck, K. Mucins and their role in shaping the functions of mucus barriers. Annu*. Rev. Cell Dev. Biol.* 2018, 6(34), 189-215. DOI: 10.1146/annurev-cellbio-100617-062818M

15A. Cummings R.D, Schnaar R.L. R-Type lectins. 2017. In: Varki A, Cummings R.D, Esko J.D, et al., editors. Essentials of Glycobiology [Internet]. 3rd edition. Cold Spring Harbor (NY): Cold Spring Harbor Laboratory Press; 2015-2017. Chapter 31. DOI : 10.1101/glycobiology.3e.031

15B. Gupta, D.; Kaltner, H.; Dong, X.; Gabius, H.J.; Brewer, C.F. Comparative cross-linking activities of lactose-specific plant and animal lectins and a natural lactose-binding immunoglobulin G fraction from human serum with asialofetuin. *Glycobiology*. 1996, 6(8), 843-849. DOI: 10.1093/glycob/6.8.843

16A. Gervais, M.; Labbé, A.; Carlotti, S.; Deffieux, A. Direct synthesis of α-azido,ω-hydroxypolyethers by monomer-activated anionic polymerization. *Macromolecules*, 2009, 42, 2395–2400. DOI: 10.1021/ma802063s

16B. Honigfort D.J.; Zhang, M.Z.; Verespy, S.; Godula, K. Engineering of spectator glycocalyx structures to evaluate molecular interactions at crowded cellular boundaries. Faraday Discussions. 2019, 219, 138-153. DOI: 10.1039/C9FD00024K

3.8 Supporting Information

3.8.1 Abbreviations

CAM: cerium ammonium molybdate stain

CHO cells: Chinese hamster ovary epithelial cells

Chol: cholesterol

CuAAC: copper(I)-catalyzed azide alkyne cycloaddition

DCM: dichloromethane

DIPEA: N,N-Diisopropylethylamine

DMF: dimethylformamide

DMSO: dimethylsulfoxide

DP: degree of polymerization

DPBS: Dulbecco's phosphate buffered saline

ECH: epichlorohydrin

FBS: fetal bovine serum

GP: glycopolymer

GPC: gel permeation chromatography

HRMS: high resolution mass spectroscopy

IR: infrared spectroscopy

M_n: number average molecular weight

M_w: weight average molecular weight

NHS: N-hydroxysuccinimide

NMR: nuclear magnetic resonance

NPCL: nonphotocleavable

PCC: Pearson's correlation coefficient

PCL: photocleavable

pECH: poly(epicholorhydrin)

PEG: polyethylene glycol

p(GA): poly(glycidyl azide)

RCA: *Ricinus communis agglutinin I*

$TBAN_3$: tetrabutylammonium nitride

THF: tetrahydrofuran

TLC: thin layer chromatography

wt: wild type

Ø: no cholesterol endgroup

Đ: polydispersity index

3.8.2 Materials

All chemicals, unless otherwise stated, were purchased from Sigma Aldrich and used as received. Cuprisorb resin was purchased from SeaChem Labs. Reaction progress was monitored by analytical thin-layer chromatography (TLC, Merck silica gel plates) with UV illumination or via staining with CAM, ninhydrin, or $KmNO_4$. CHO Lec8 and CHO Pro5 cells used were obtained from ATCC (CRL-1737 and CRL-1781, respectively). Biotin-labeled *Ricinus communis agglutinin I* was purchased from Vector Labs (B-1085-5) and streptavidin Alexafluor488 conjugate was purchased from ThermoFisher Scientific (S11223).

3.8.3 Instrumentation

Column chromatography was performed on a Biotage Isolera One automated flash chromatography system. Nuclear magnetic resonance (^{1}H and ^{13}C NMR) spectra were recorded on Bruker 300 MHz and Jeol 500 MHz NMR spectrometers. Spectra were recorded in $CDCl_3$ or D_2O at 293K and are reported in parts per million (ppm) on the δ scale relative to residual solvent as an internal standard (for ^{1}H NMR: $CDCl_3$ = 7.26 ppm, D_2O = 4.79 ppm, for ^{13}C NMR: $CDCl_3$ = 77.0 ppm, CD_3OD = 49.0 ppm). HRMS (high-resolution mass spectrometry) analysis was performed on an Agilent 6230 ESI-TOFMS in positive ion mode. UV-Vis spectra were collected in a quartz cuvette using a Thermo Scientific Nanodrop2000c spectrophotometer. IR spectroscopy was performed on a Nicolet 6700 FT-IR spectrophotometer (Thermo Scientific). Size exclusion chromatography (SEC) was performed on a Hitachi Chromaster system equipped with an RI detector and two 5 µm, mixed bed, 7.8 mm I.D. x 30 cm TSK gel columns in series (Tosoh Bioscience) using an isocratic method with a flow rate of 0.7 mL/min in DMF (0.2% LiBr, 70 °C). Live cell flow cytometry analysis was performed using a FACSCalibur or FACSCanto II system (BD Biosciences). Data were collected using FACS Diva software and analyzed in FlowJo. Microscopy was performed on either a Keyence BZX800 epifluorescent microscope or a ThermoScientific EVOS imaging system. Images were analyzed using ImageJ. UV treatment was administered with a handheld 15W lamp (l = 365nm) at < 2cm distance from the sample.

3.8.4 Chemistry

3.8.4.1 Scheme S1 Synthesis of Control GPs

Analogous synthetic schemes for non-photocleavable polymer control **GP-NPCL** (A) and for control polymer lacking a membrane anchor **GP-∅** (B). General **GP** elaboration[1] from **P1** (**ECH** polymerized as described by Gervais, et.al.[2]).

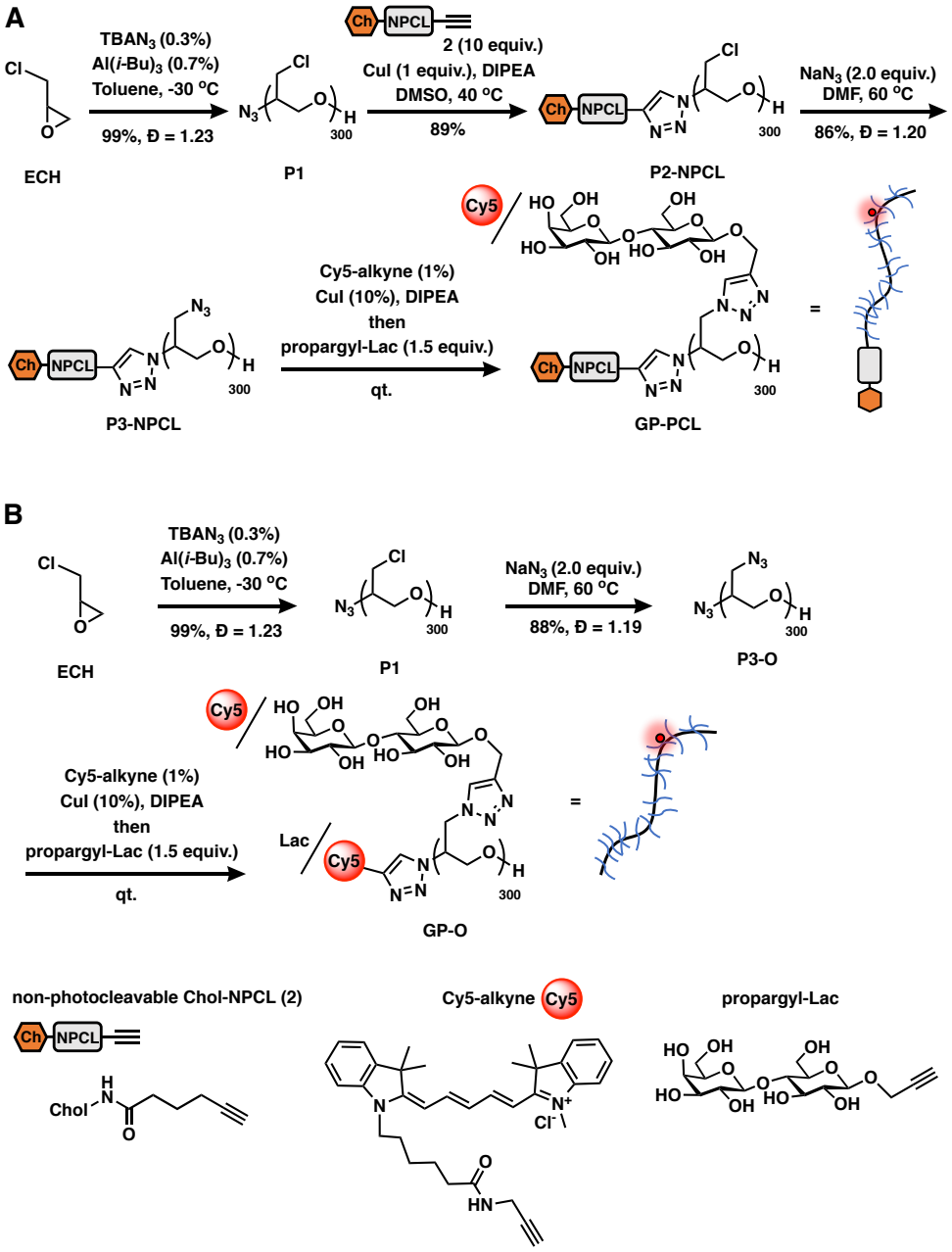

Scheme 3.S1 Synthesis of control GPs.

3.8.4.2 Synthesis of Chol-PCL (1)

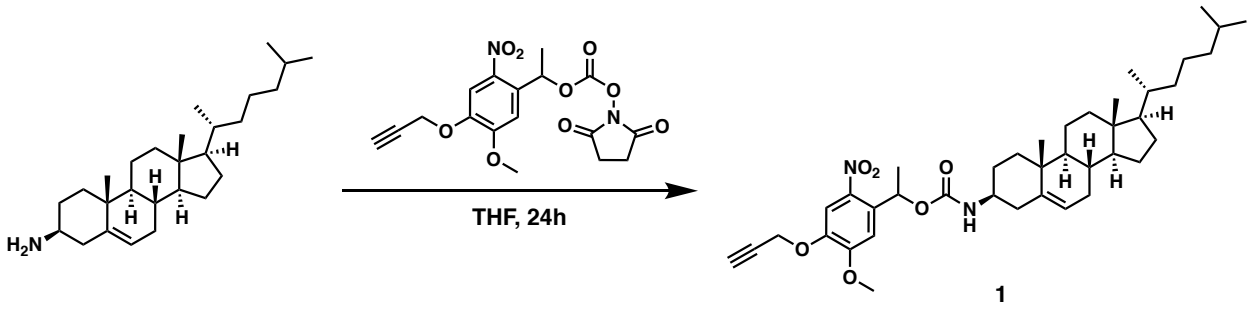

Scheme 3.S2 Synthesis of Chol-PCL (1).

Synthesis of Chol-PCL (1). To a vacuum dried 1-dram glass vial with a magnetic stirrer was added 1-(5-Methoxy-2-nitro-4-prop-2-ynyloxyphenyl)ethyl N-succinimidyl carbonate[3] (0.0357 g, 0.091 mmol, 1 equiv) and Chol-amine[4] (3β-cholest-5-en-3-amine, 0.0352 g, 0.091 mmol, 1 equiv). Anhydrous tetrahydrofuran (0.50 mL) was added, and the reaction proceeded at ambient temperature for 18hr, during which time progress was monitored by TLC. The mixture was evaporated under reduced pressure and purified by normal phase flash chromatography in EtOAc/Hexanes (1:4). The purified product was concentrated to yield Chol-PCL **1** (0.0603 g, 60%). ^{1}H NMR ($CDCl_3$, 500 MHz) δ (ppm): 7.86-7.69 (s, 1H), 7.08-6.97 (s, 1H), 6.47-6.28 (d, 1H), 5.41-5.25 (br, 1H), 4.87-4.77 (d, 2H), 4.71-4.61 (m, 1H), 4.04-3.92 (s, 3H), 3.47-3.29 (br, 1H), 2.61-2.54 (m, 1H), 2.40-1.72 (br, 8H), 1.66-0.77 (br, 48H), 0.72-0.57 (s, 3H). ^{13}C NMR (500 MHz, $CDCl_3$) δ (ppm): 154.33, 153.99, 153.78, 153.66, 153.61, 153.54, 153.47, 152.35, 145.30, 140.02, 139.36, 135.36, 122.12, 110.13, 108.10, 68.70, 56.89, 56.63, 56.41, 56.07, 51.32, 49.96, 39.68, 39.51, 36.16, 35.81, 31.81, 28.25, 28.04, 23.83, 22.86, 22.59, 19.35, 18.71, 11.87. Calculated $C_{40}H_{58}N_2O_6$, 662.43, $[M+Na]^+$:685.42. HRMS found: 685.47. UV–Vis absorbance at 370 nm of **1** (CH_2Cl_2, 10 μg/mL) = 0.145.

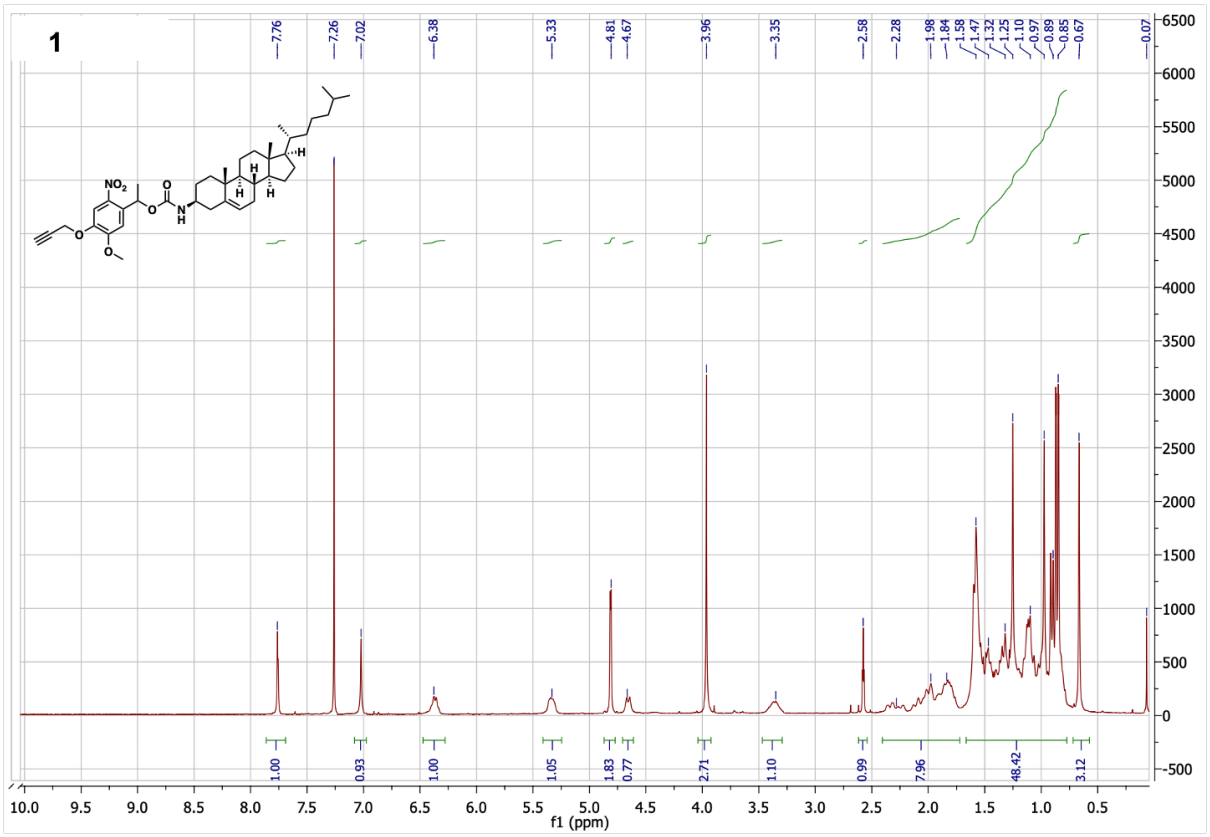

Figure 3.S1 ^{1}H NMR spectra (500mHz, $CDCl_3$) of **1**.

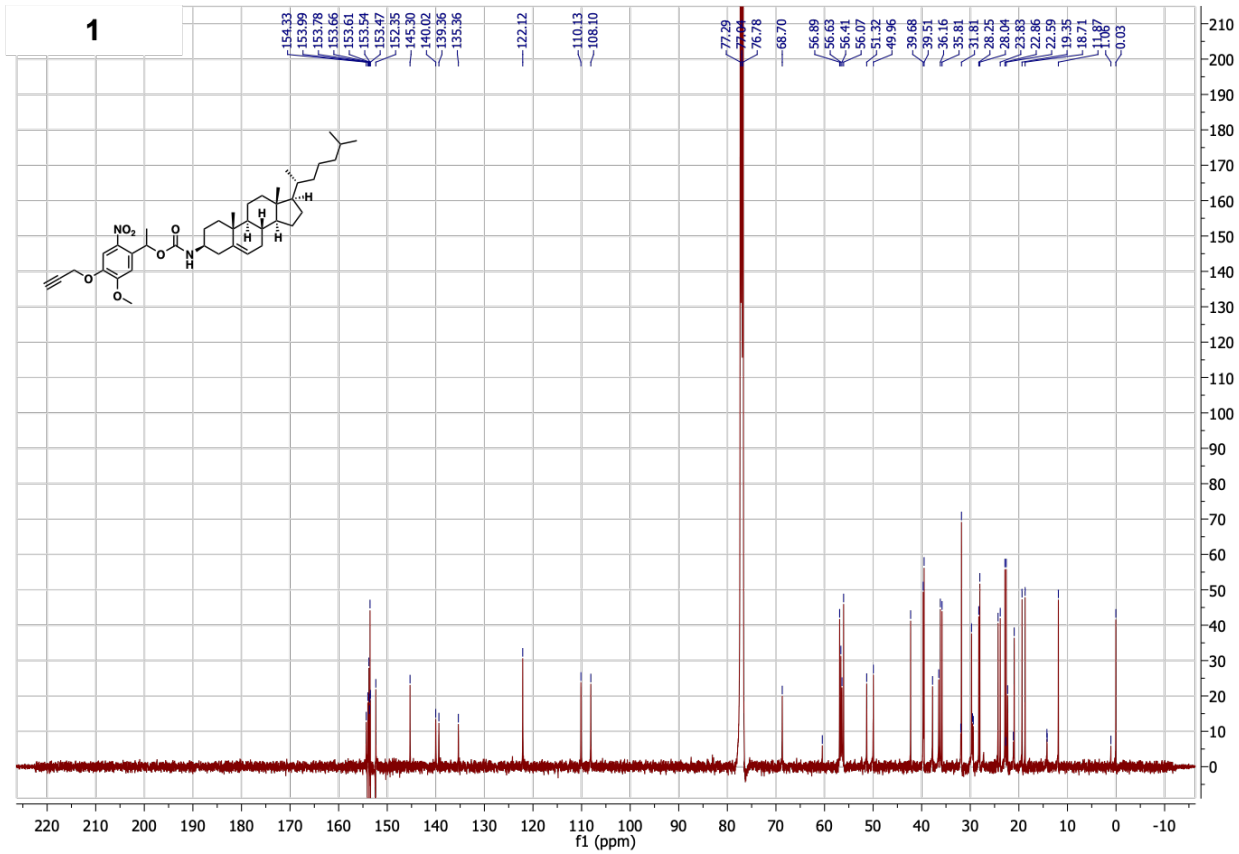

Figure 3.S2 ^{13}C NMR spectra (500mHz, $CDCl_3$) of **1**.

3.8.4.3 Synthesis of Chol-NPCL (2)

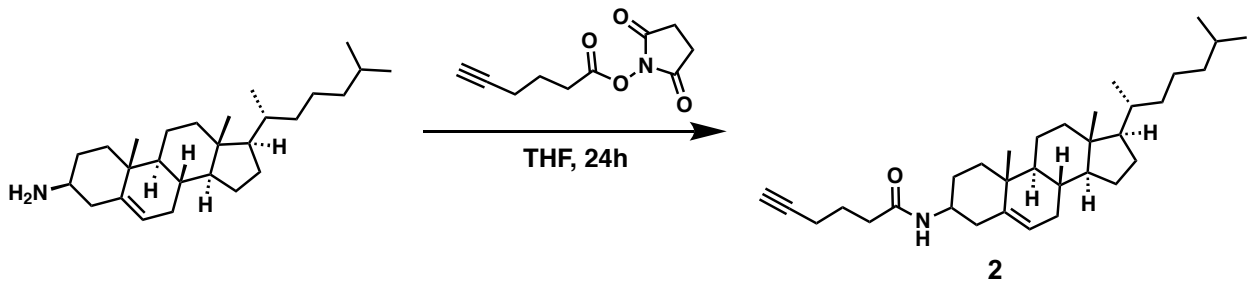

2

Scheme 3.S3 Synthesis of Chol-NPCL (2).

Synthesis of Chol-NPCL (2). A vacuum dried 1-dram glass vial with a magnetic stirrer was charged with hexynoic acid NHS-ester[5] (0.0263 g, 0.126 mmol, 1.00 equiv) and Chol-amine[4] (3β-cholest-5-en-3-amine, 0.0485 g, 0.126 mmol, 1.00 equiv). Anhydrous tetrahydrofuran (0.63 mL) was added and the reaction proceeded at ambient temperature for 18hr, during which time progress was monitored by TLC. The mixture was evaporated under reduced pressure and purified by normal phase flash chromatography in EtOAc/Hexanes (1:4). The purified product was concentrated to yield Chol-NPCL **2** (0.0449 g, 74%). ^{1}H NMR ($CDCl_3$, 500 MHz) δ (ppm): 5.49-5.19 (s, 1H), 3.87-3.45 (s, 1H), 2.94-2.64 (br, 4H), 2.49-2.16 (br, 4H), 2.05-1.77 (br, 6H), 1.63-1.41 (br, 4H), 1.39-0.61 (br, 34H). ^{13}C NMR (500 MHz, $CDCl_3$) δ (ppm): 11.87, 17.79, 18.72, 19.37, 22.59, 22.86, 24.19, 28.04, 31.83, 35.32, 37.81, 39.35, 39.51, 42.28, 49.61, 50.02, 56.07, 56.65, 69.18, 83.64, 122.04, 140.14, 153.61, 153.75, 153.77, 153.87, 154.06 171.29. Calculated $C_{33}H_{53}NO$, 479.41, $[M+H]^+$: 480.42. HRMS found: 480.5033.

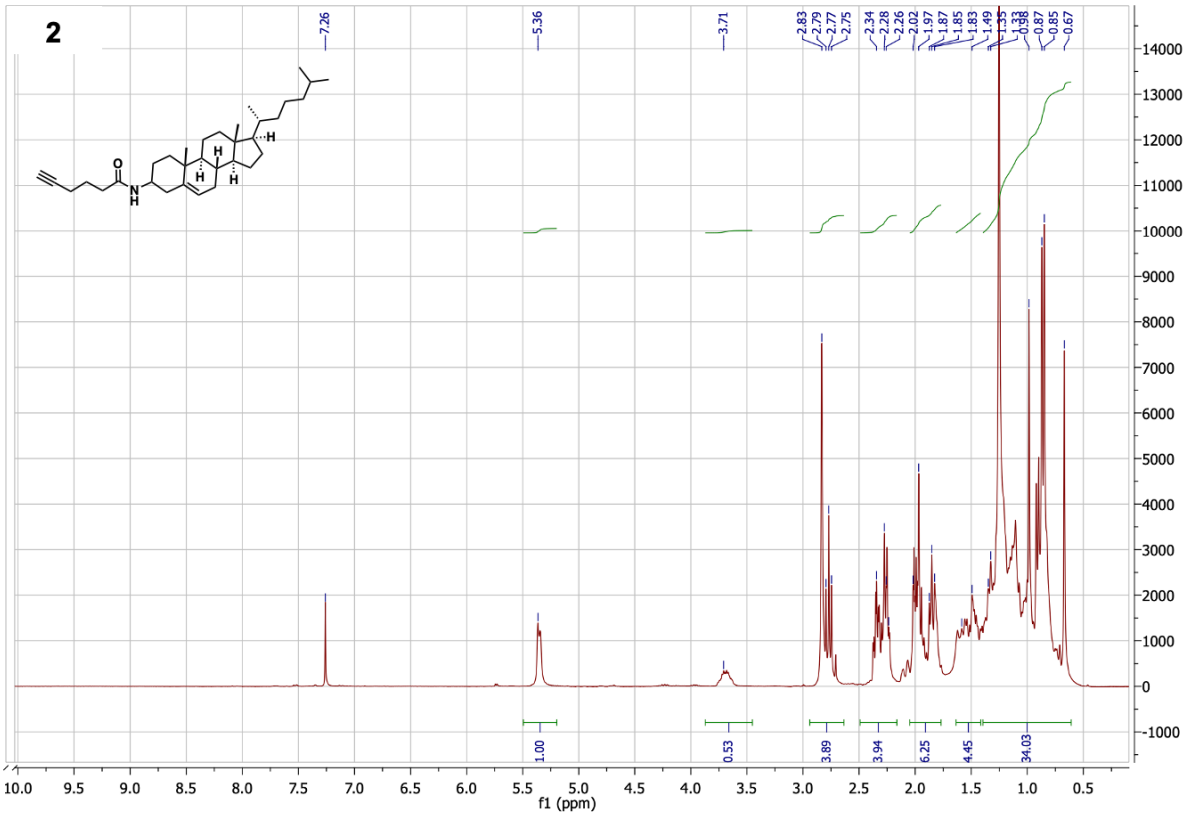

Figure 3.S3 ^{1}H NMR spectra (500mHz, $CDCl_3$) of **2**.

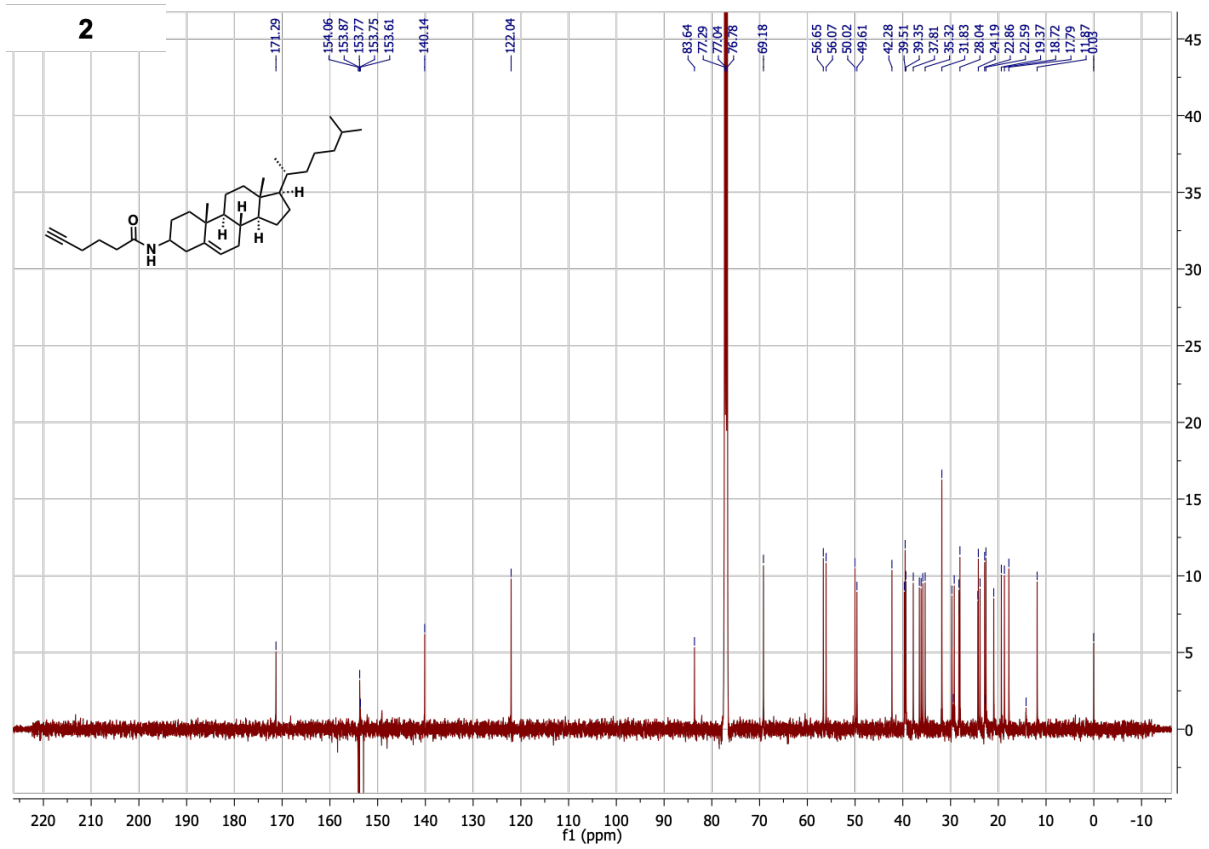

Figure 3.S4 ^{13}C NMR spectra (500mHz, $CDCl_3$) of **2**.

3.8.4.4 *Characterization of GPs and their synthetic intermediates P1, P2, and P3*

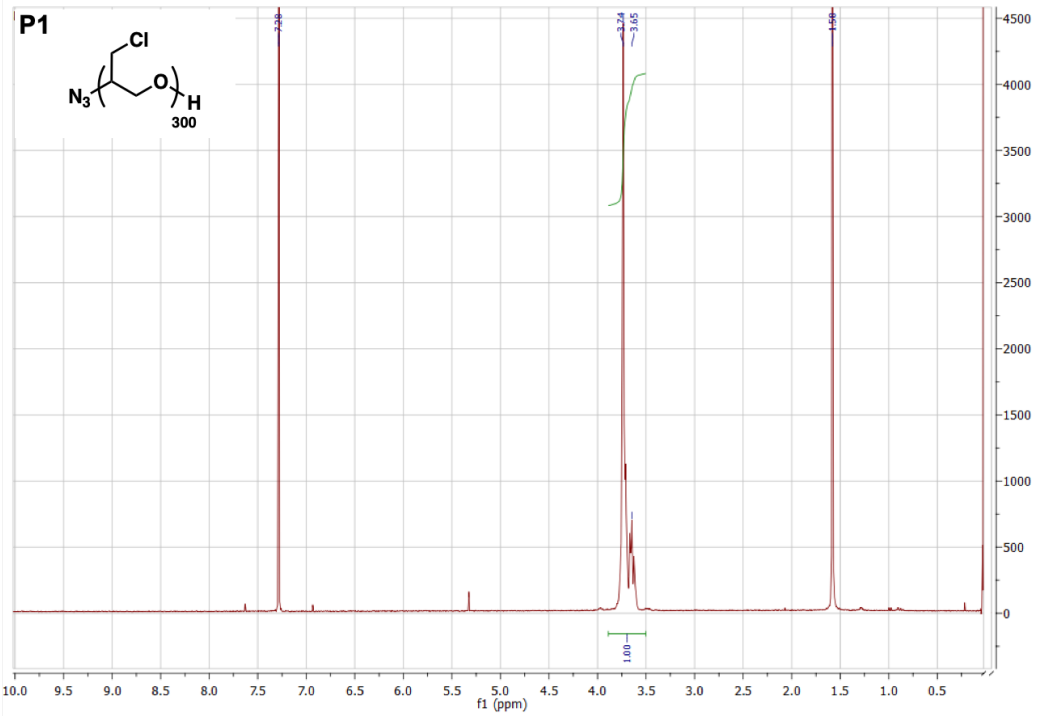

Figure 3.S5 ^{1}H NMR spectra (500mHz, $CDCl_3$) of p(ECH) backbone **P1**.

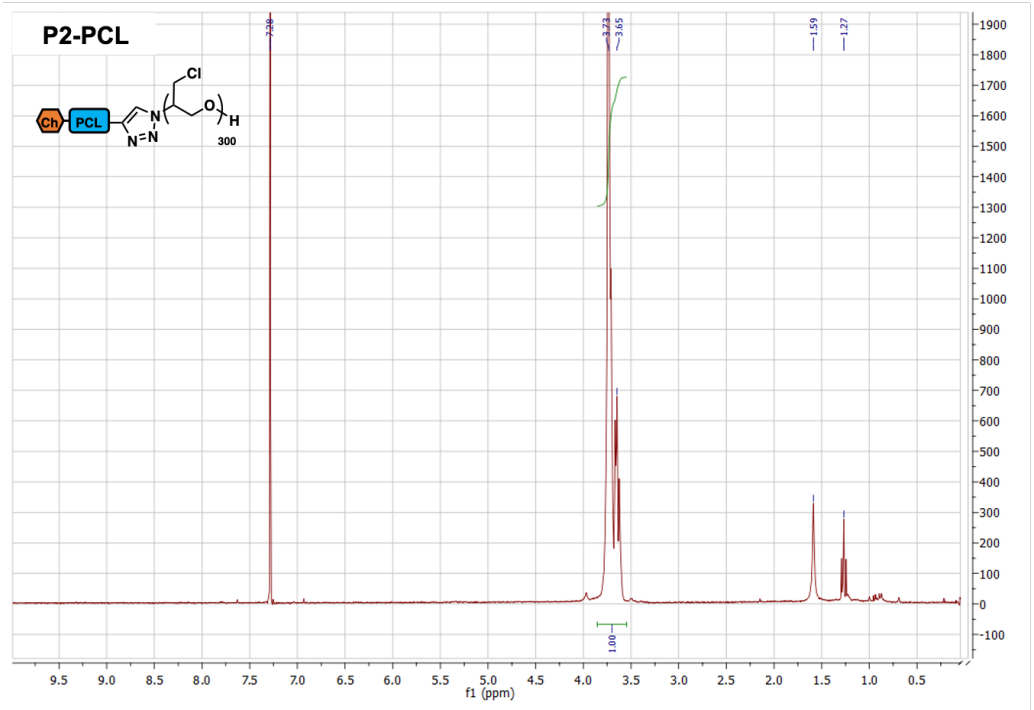

Figure 3.S6a ^{1}H NMR spectra (500mHz, $CDCl_3$) of **P2** polymer intermediates.

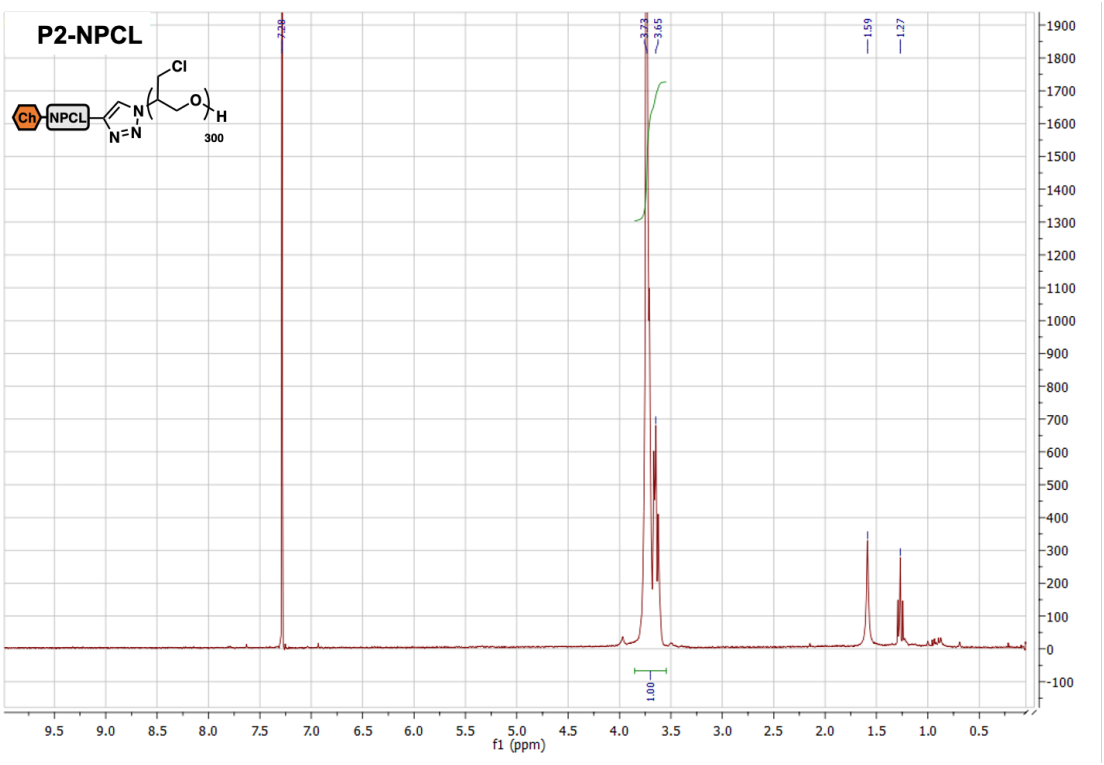

Figure 3.S6b ^{1}H NMR spectra (500mHz, $CDCl_3$) of **P2** polymer intermediates.

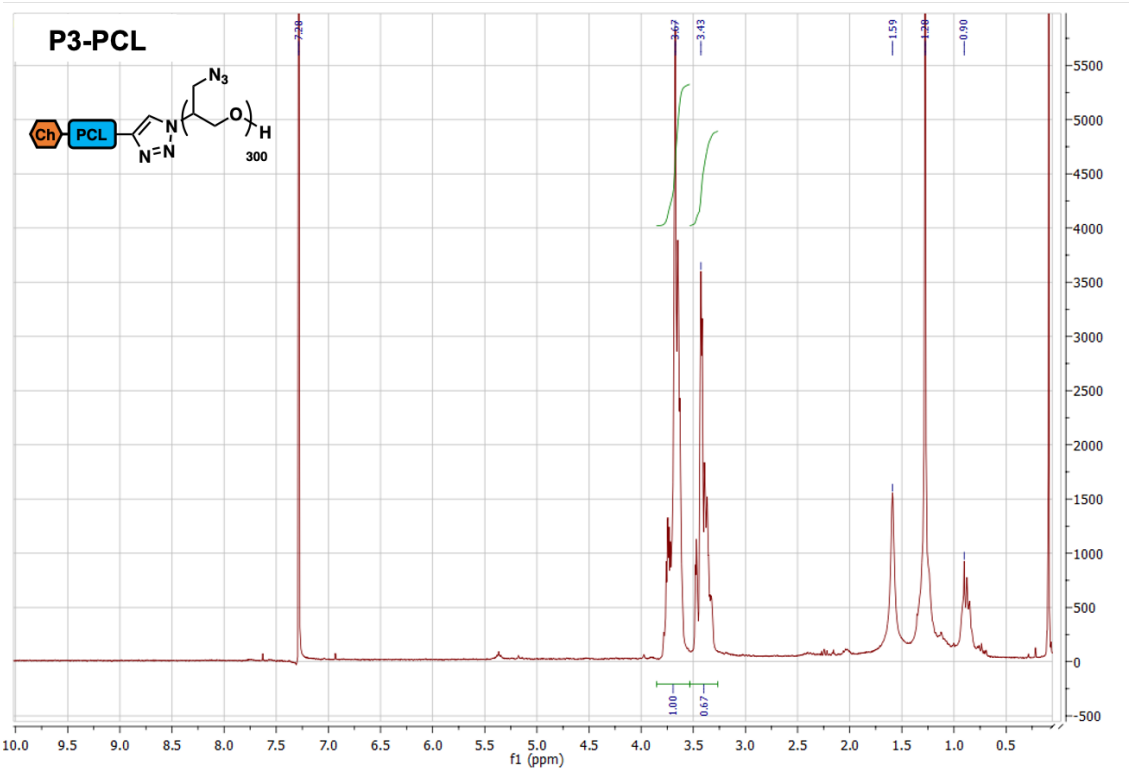

Figure 3.S7a ^{1}H NMR spectra (500mHz, $CDCl_3$) of **P3** polymer intermediates.

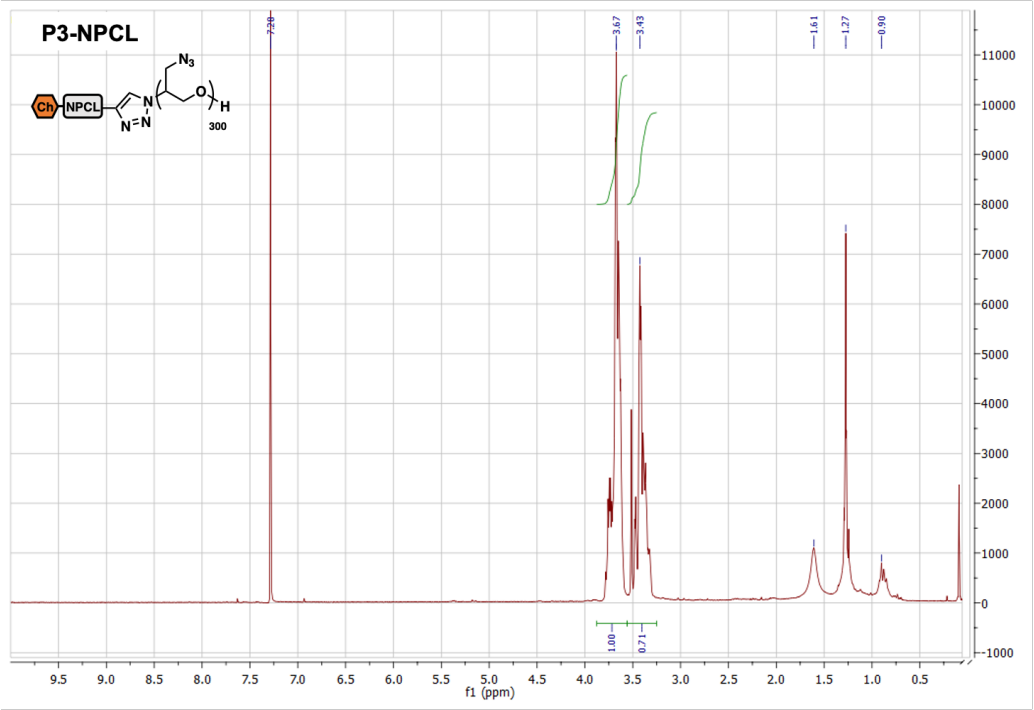

Figure 3.S7b ^{1}H NMR spectra (500mHz, $CDCl_3$) of **P3** polymer intermediates.

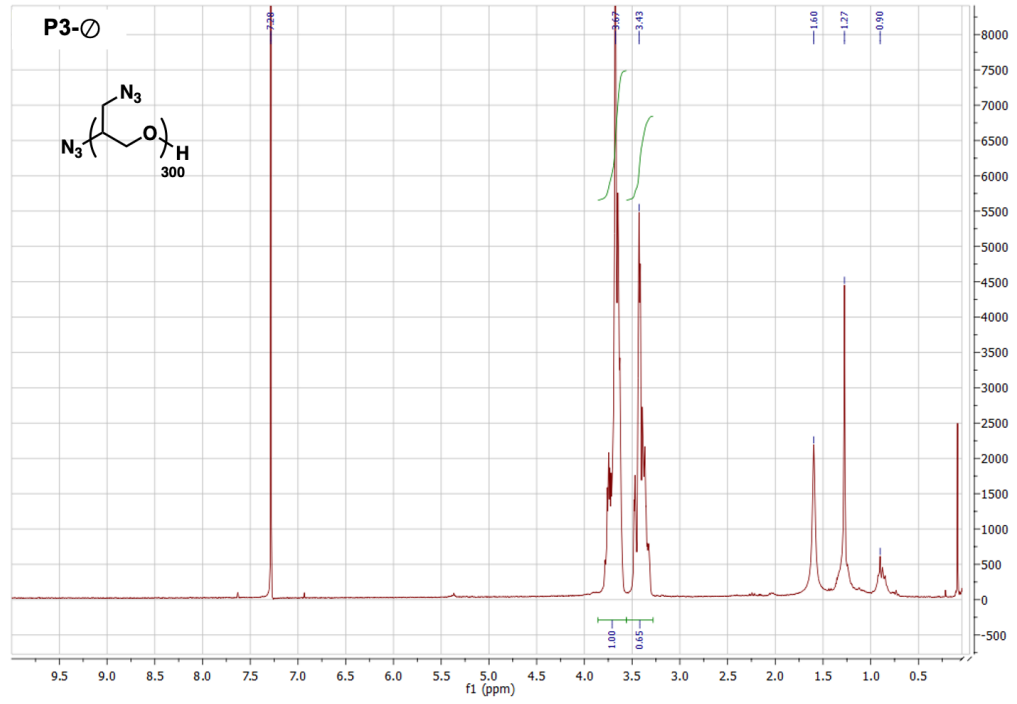

Figure 3.S7c ^{1}H NMR spectra (500mHz, $CDCl_3$) of **P3** polymer intermediates.

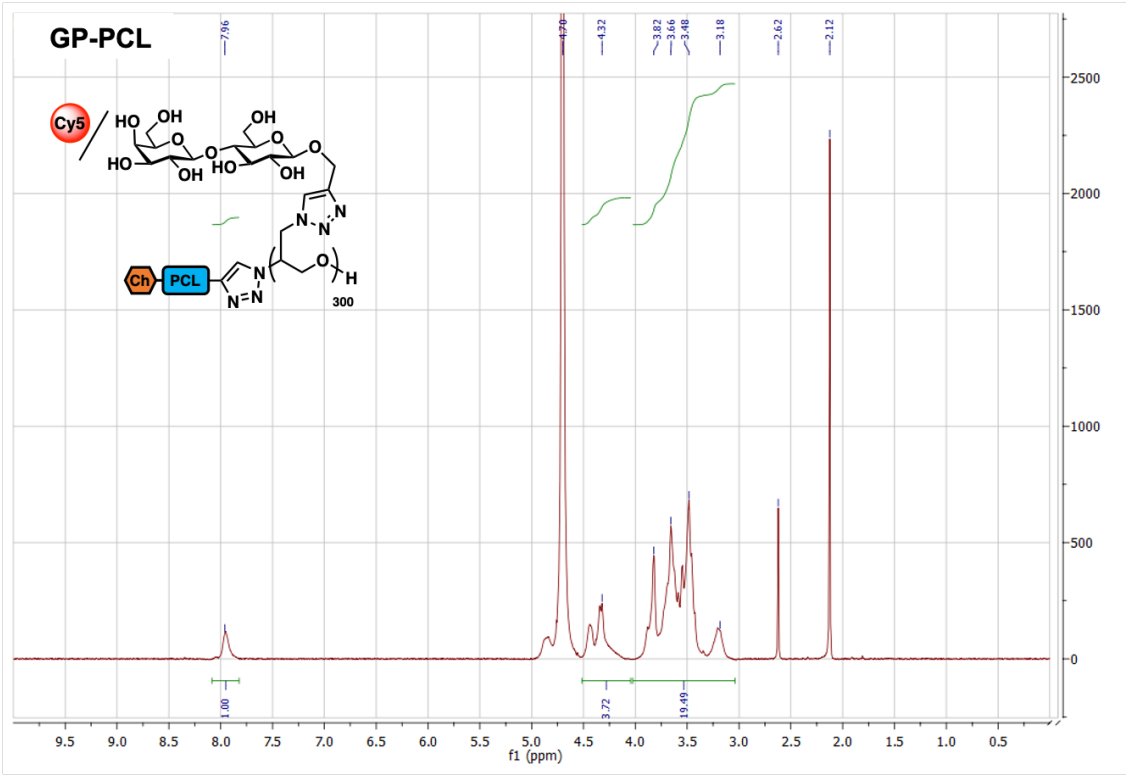

Figure 3.S8a ^{1}H NMR spectra (500mHz, D_2O) of **GPs**.

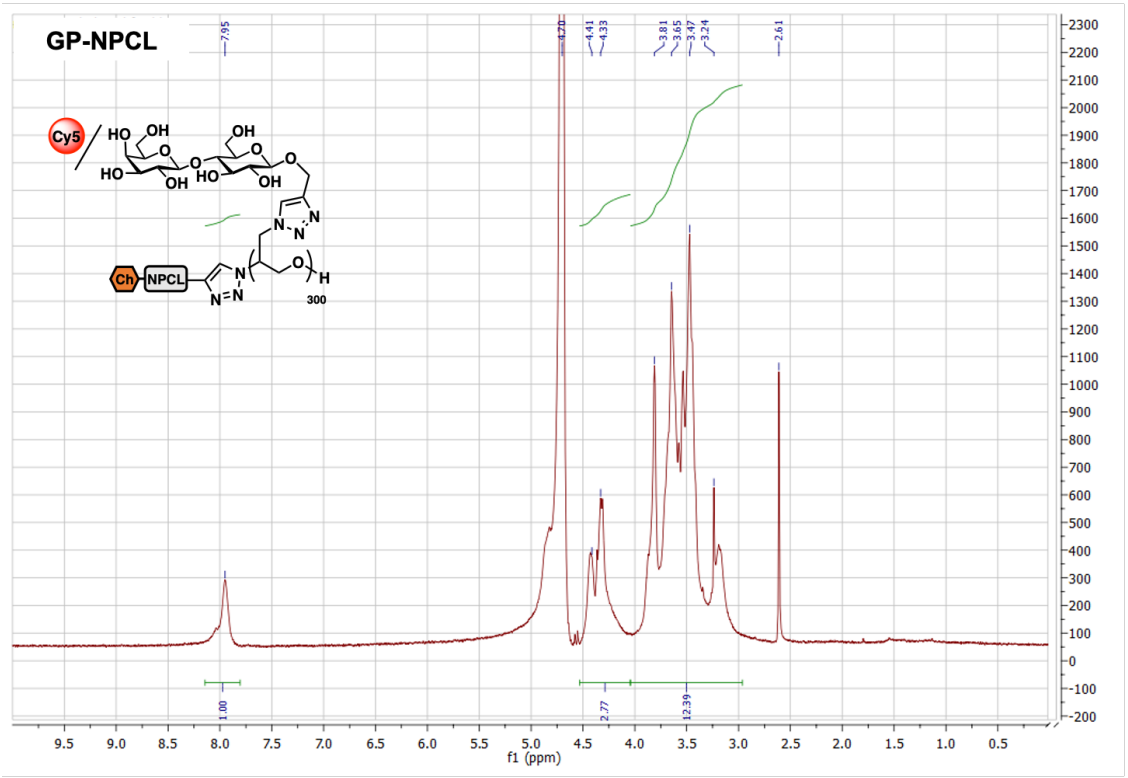

Figure 3.S8b ^{1}H NMR spectra (500mHz, D_2O) of **GPs**.

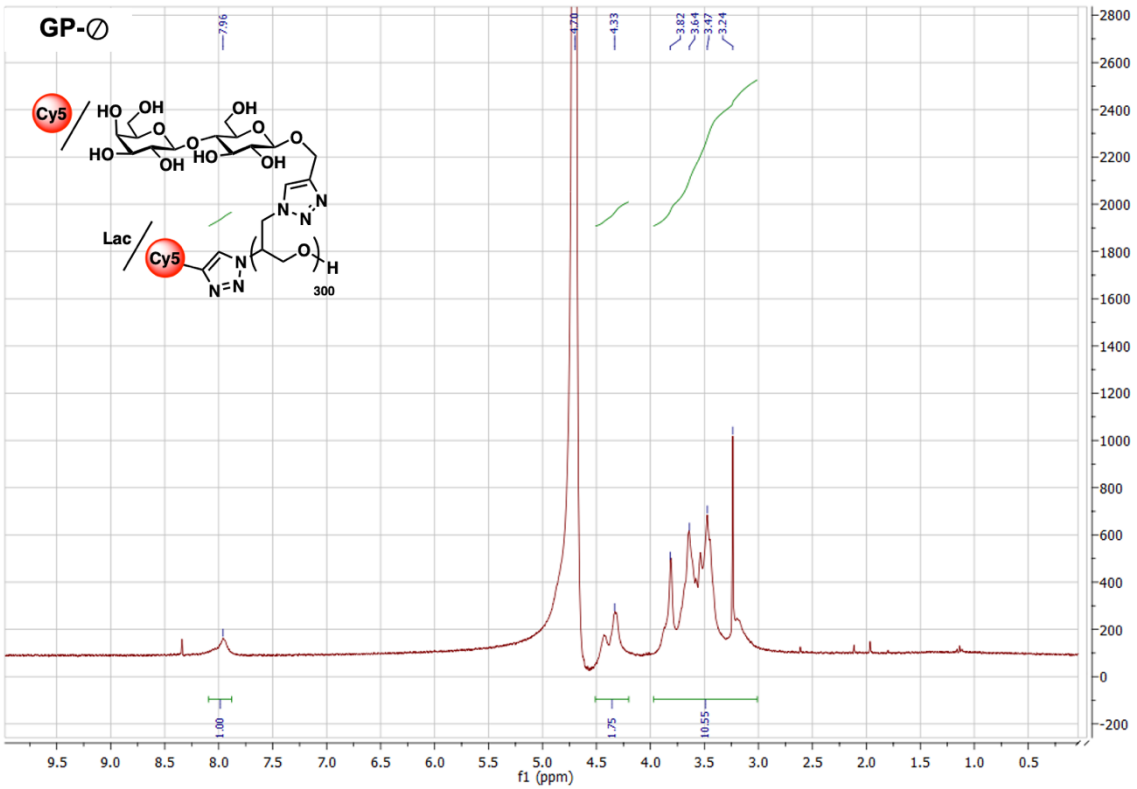

Figure 3.S8c ^{1}H NMR spectra (500mHz, D_2O) of **GPs**.

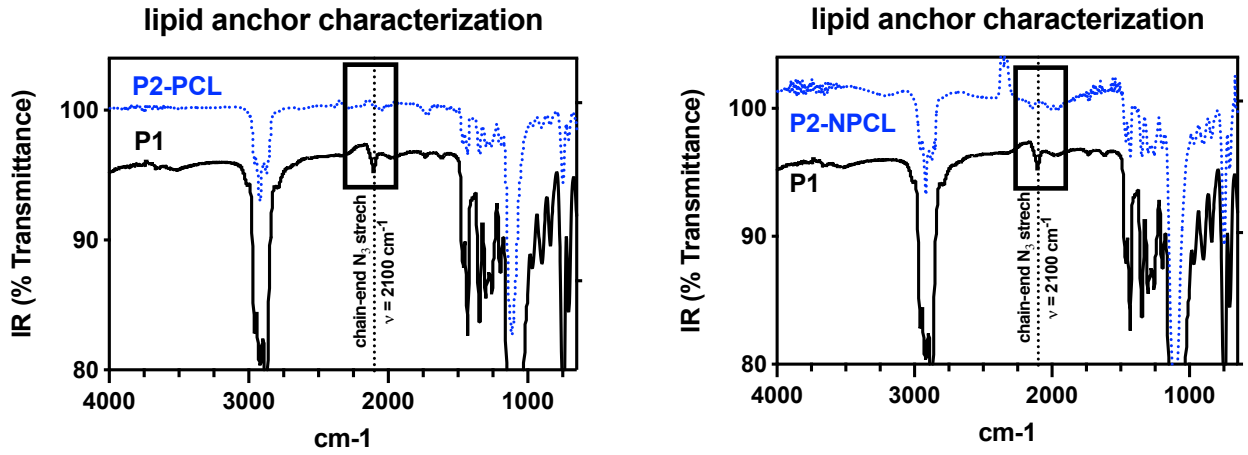

Figure 3.S9 IR spectra showing chain-end modification of polymer **P1**.

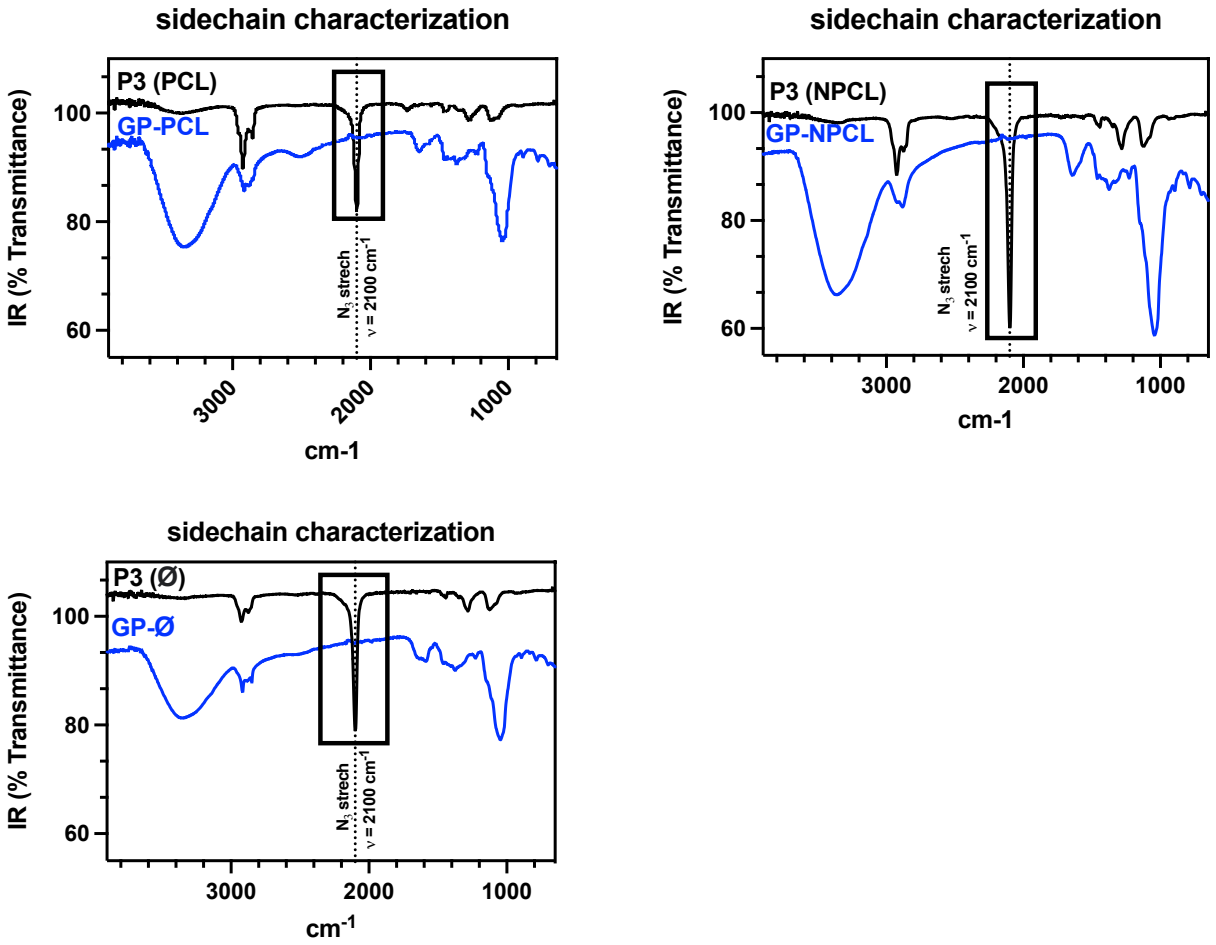

Figure 3.S10 IR spectra showing side chain modification of **P3** polymer intermediates.

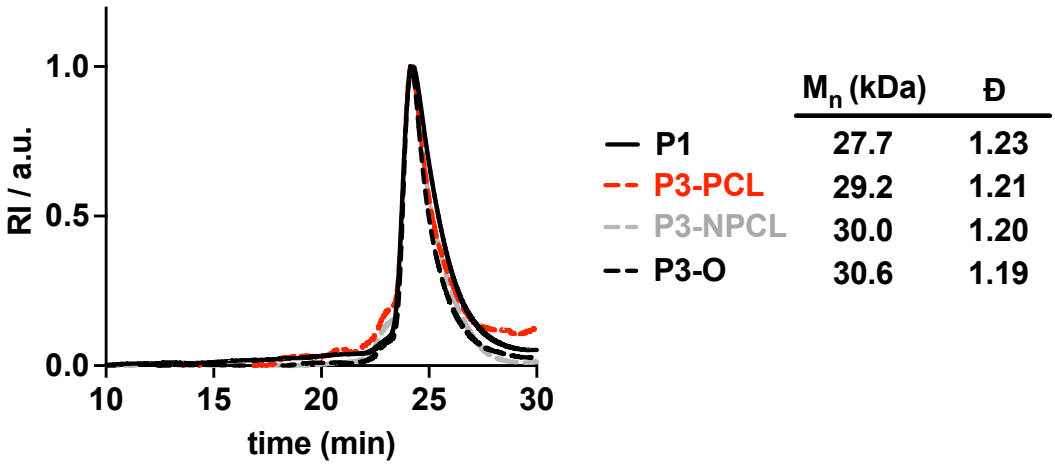

Figure 3.S11 GPC spectrum (DMF, 0.2% LiBr) of **P1** and **P3** polymer intermediates.

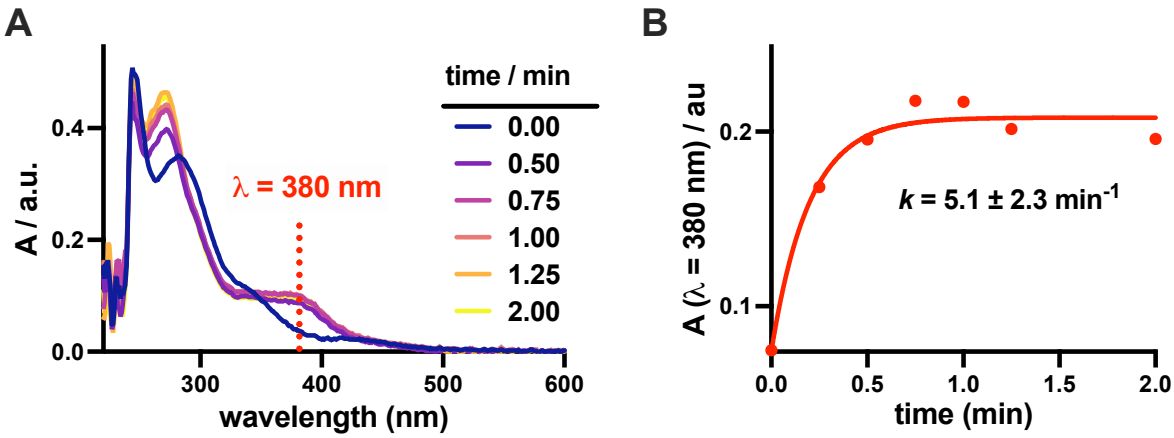

Figure 3.S12 P2-PCL photocleavage kinetic characterization. The photocleavage of the polymer intermediate **P2-PCL** (100 mg/mL) with light at λ = 365 nm was analyzed by UV spectroscopy (A). The change in absorbance at λ = 380 nm over time was used to determine the rate of photocleavage (B, k = 5.1 ± 2.3 min^{-1}).

3.8.5 Biology

3.8.5.1 General Methods

All biological reagents were purchased from Gibco (ThermoFisher) unless otherwise stated. Cells were cultured at 37 °C and 5% CO_2 following standard tissue culture practices. Chinese Hamster Ovary (CHO) cells (*wt* Pro5 and Lec8) were cultured in MEMa media supplemented with 10% FBS, 100 U/mL penicillin, and 100 U/mL streptomycin. Cells were passaged utilizing 0.25% trypsin-EDTA every 2-4 days to achieve desired confluency for or flow cytometry or microscopy on tissue-culture treated lab plastics.

Cells were washed with DPBS ($^{+}$Ca/$^{+}$Mg) and flow cytometry was performed on living cells with > 10,000 events per sample analyzed. All data were collected in biological triplicate. Live-dead cell analysis was performed using a commercial dead cell stain kit (Thermo-L34970) and a heat-treated control condition.

All microscopy experiments were performed in biological triplicate with 5 or more representative micrographs collected per replicate in all channels analyzed (BF, Hoescht, Cy5, and GFP). Photopatterned wells were masked using black electrical tape and ensuring that adhesive did not contact the imaging surface directly. ImageJ software was utilized to analyze all images. Cell nuclei were stained with Hoescht 33342. For photopatterning, the profile of Cy5 mean fluorescent intensity was recorded across the stitched images and bins were calculated at 100px width extending in both directions from the mask boundary. Prism software was utilized to fit a smoothed average across bins as a function of distance from the photomask. For lectin crosslinking experiments Cy5 and AF_{488} mean fluorescent intensity were quantified as a function of area and normalized to

cell count. Plotted values represent the normalized Cy5 mean fluorescent intensity / area averaged across 5 replicates. Scale bars are 100 mm except where otherwise noted.

3.8.5.2 Temperature dependence on GP incorporation

Glycopolymers bearing cholesterol membrane anchors can be inserted into the membranes of living cells. To determine the temperature dependence of **GP** incorporation into the membranes of CHO Lec8 cells, cells were grown in 12-well plates and treated with **GP-PCL** or **GP-Ø** (2 mM, 1 hr) at increasing temperature (4 °C – 37 °C). While incorporation was observed at all temperatures (A), some **GP** internalization was observed at 25 °C and 37 °C (B, examples of internalized **GP-PCL** shown with white arrows).

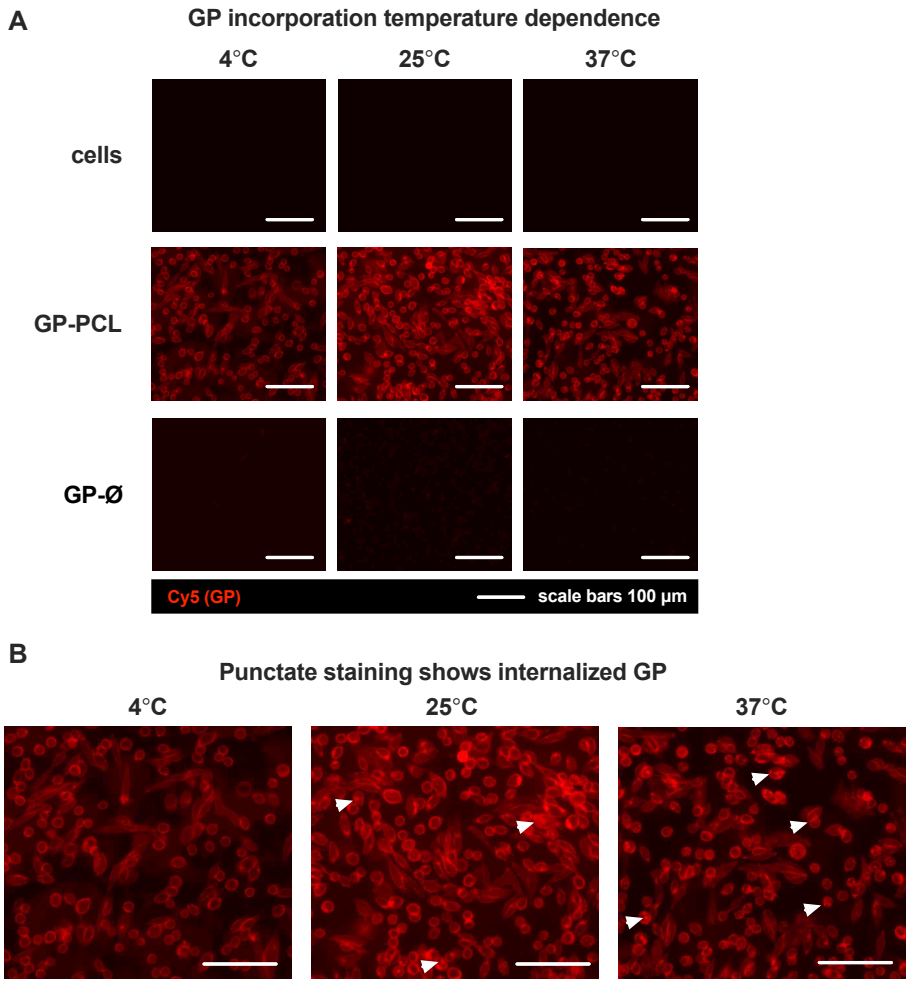

Figure 3.S13 Temperature dependence of GP membrane incorporation

3.8.5.3 RCA binding optimization

To determine the optimal binding concentrations for RCA and lactose bearing glycoconjugates, flow cytometry (A) and fluorescent microscopy (B) were performed on *wt* CHO cells (Pro5). Dose-dependent RCA binding was observed by flow cytometry with a maximum signal without evidence of cell agglutination at 5 mg/mL RCA. This concentration was also suitable for fluorescent microscopy, where concentrations ranging from 0 – 50 mg/mL where evaluated and binding was visualized at concentrations above 2.5 mg/mL.

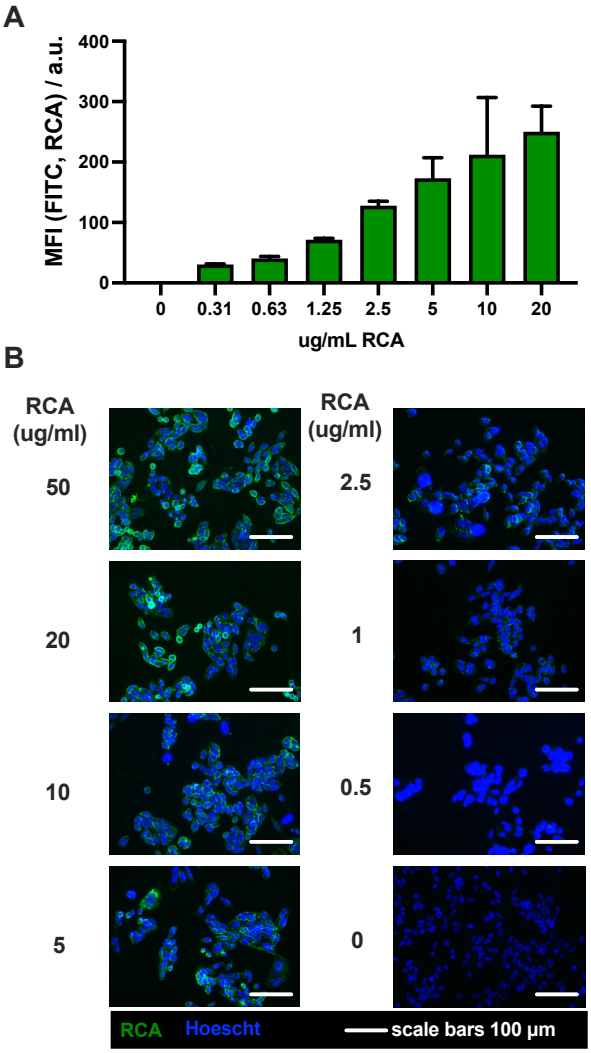

Figure 3.S14 RCA binding optimization.

3.8.5.4 RCA binding lactose competition assay

CHO cells (Pro5) were grown in 12-well plates. To demonstrate the binding specificity of RCA for lactose, cells were incubated with RCA (5 mg/mL, 0 °C, 40min) in the presence or absence of 200 mM soluble lactose. After three DPBS washes cells were and incubated with an excess of AlexaFluor488 labeled streptavidin (300mL, 1:750, 30 min) and then washed three additional times. Hoescht 33342 was used to visualize nuclei and the cells were imaged on a ThermoScientific EVOS imaging system. RCA binding was observed for Pro5 cells only in the absence of soluble lactose.

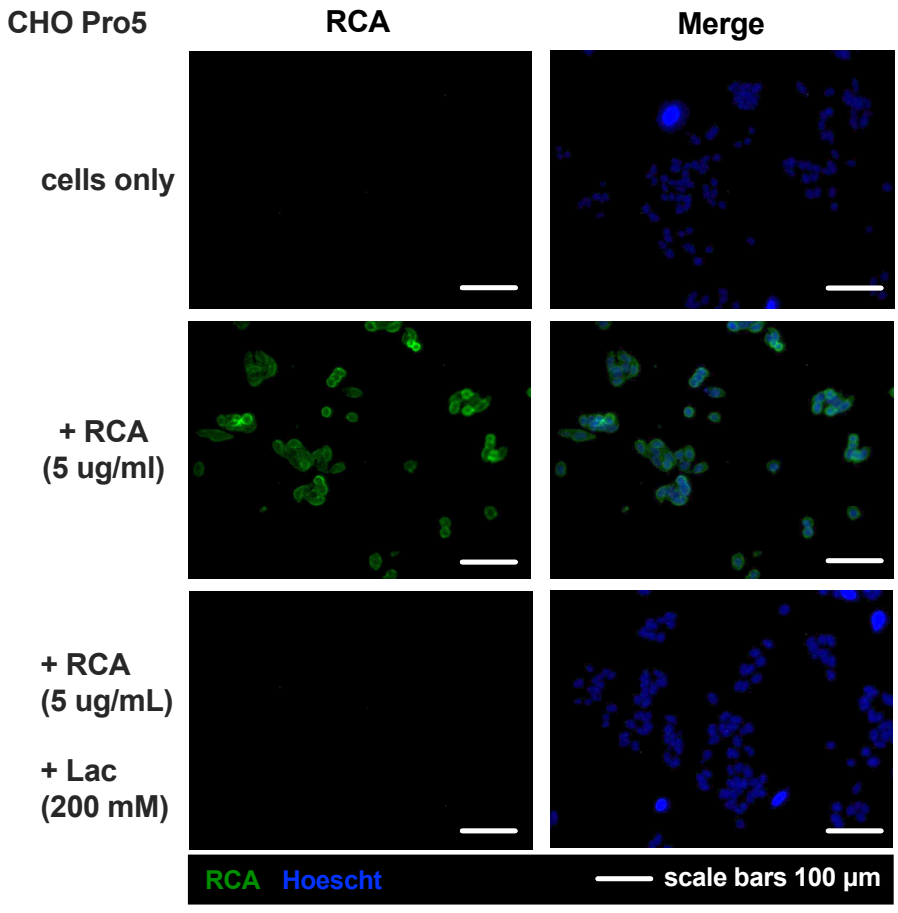

Figure 3.3S15. RCA binding lactose competition assay.

3.8.5.5 GP and RCA colocalize at the cell surface

To assess the colocalization of the lactosylated **GPs** with RCA at the cell surface, CHO Lec 8 cells in 12-well plates were remodeled with **GP-PCL** and **GP-NPCL** (2 mM, 0° C, 1 hr) and washed three times with DPBS. Cells were then incubated with RCA (5 mg/mL, 0° C, 40 min), washed three more times with DPBS, and incubated with an excess of AlexaFluor488 labeled streptavidin (300mL, 1:750, 30 min). The cells were washed, and fluorescent micrographs were captured using a ThermoScientific EVOS imaging system. Strong colocalization between **GPs** and lectin signal was determined by Pearson's Correlation Coefficient (PCC) analyzed in Image J.

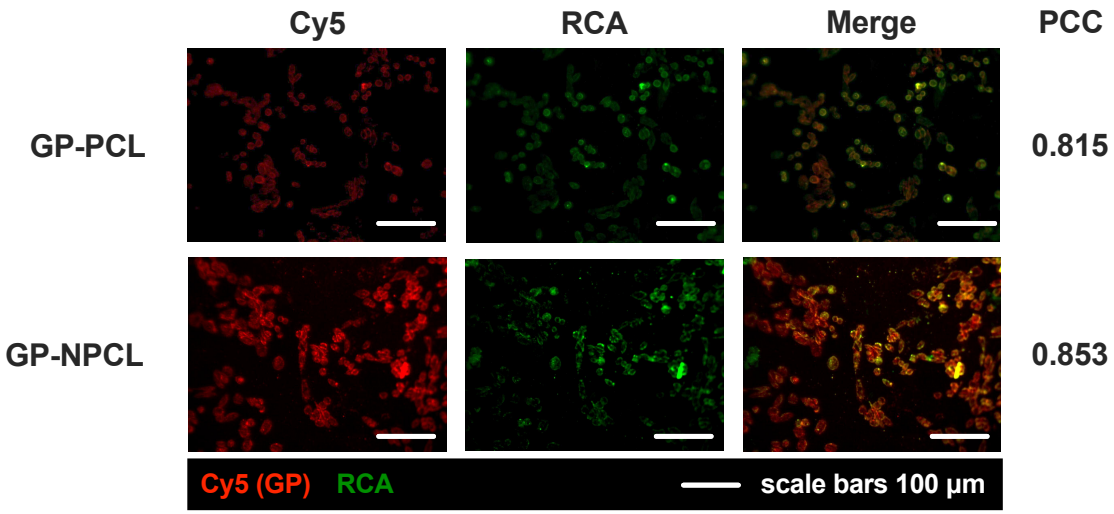

Figure 3.S16 GP and RCA colocalize at the cell surface.

3.8.5.6 Cell viability during GP remodeling and photoshedding

To assess cytotoxicity, a live-dead assay was performed using ThermoFisher Live/Dead fixable green dead cell stain kit (L34970). Briefly, 10^6 suspended CHO Lec8 cells were added to Eppendorf tubes. After remodeling cells using standard conditions described in this paper (2 mm, 0° C, 1 hr) with or without exposure to ultraviolet light (15W, l = 365nm, 3 min), cells were pelleted and washed. To each pellet was added 1.00 uL of the dissolved, amine-reactive, dye in 1.00 mL of DPBS and cells were incubated for 30 min. Cells were washed twice with DPBS and resuspended for flow cytometry. Dead cells show increased MFI_{AF488} owing to increased permeation of the dye across compromised cell membranes. The percentage of cells which remain viable (A) was identified following gating (B) of the cell population to remove debris and aggregates and then to identify dead cells. A control condition consisting of a 1:1 mixture of heat-treated cells (65° C, 2 min) and untreated cells was used to identify dead-cell population fluorescence levels. A sample histogram is shown overlayed with the $MFI(AF_{488})$ gate, showing a sample of untreated cells (red, viable) and a sample of heat-treated control cells (blue, dead).

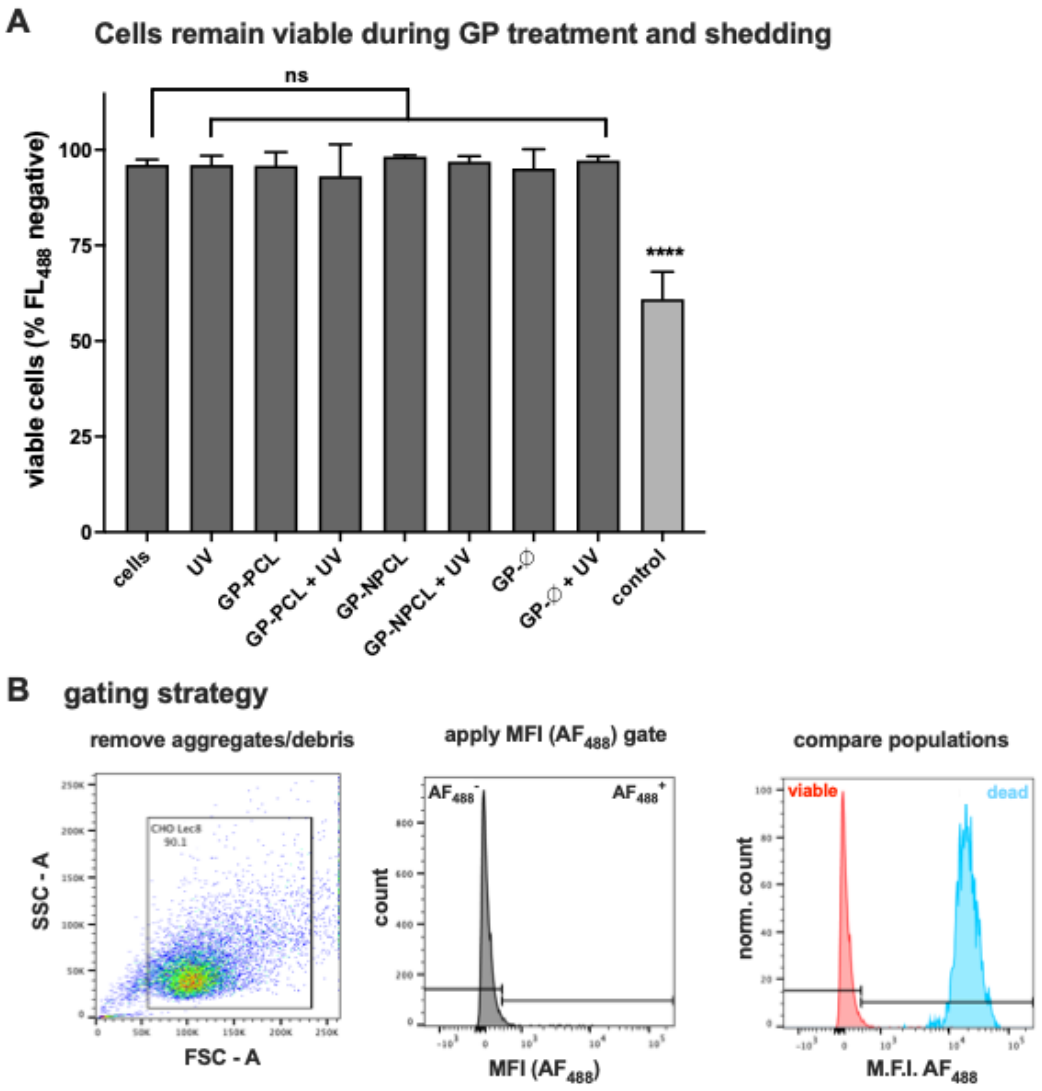

Figure 3.S17 Cell viability during GP remodeling and photoshedding.

3.8.5.7 Expanded lectin crosslinking imaging panel

Additional images (included in the Fig4C quantitative analysis of lectin crosslinking) show that RCA crosslinking of the mucin mimetic **GP-PCL** stabilizes the synthetic glycocalyx to photoinduced shedding. Remodeled cells which were illuminated by ultraviolet light *prior* to RCA binding (UV pre) show reduced signal attributed to photolysis and clearance of **GPs** from the cell surface. Remodeled cells which were illuminated by ultraviolet light *following* RCA binding and crosslinking (UV post) show a retention of polymer and RCA signal, relative to a control not treated by UV light (no UV).

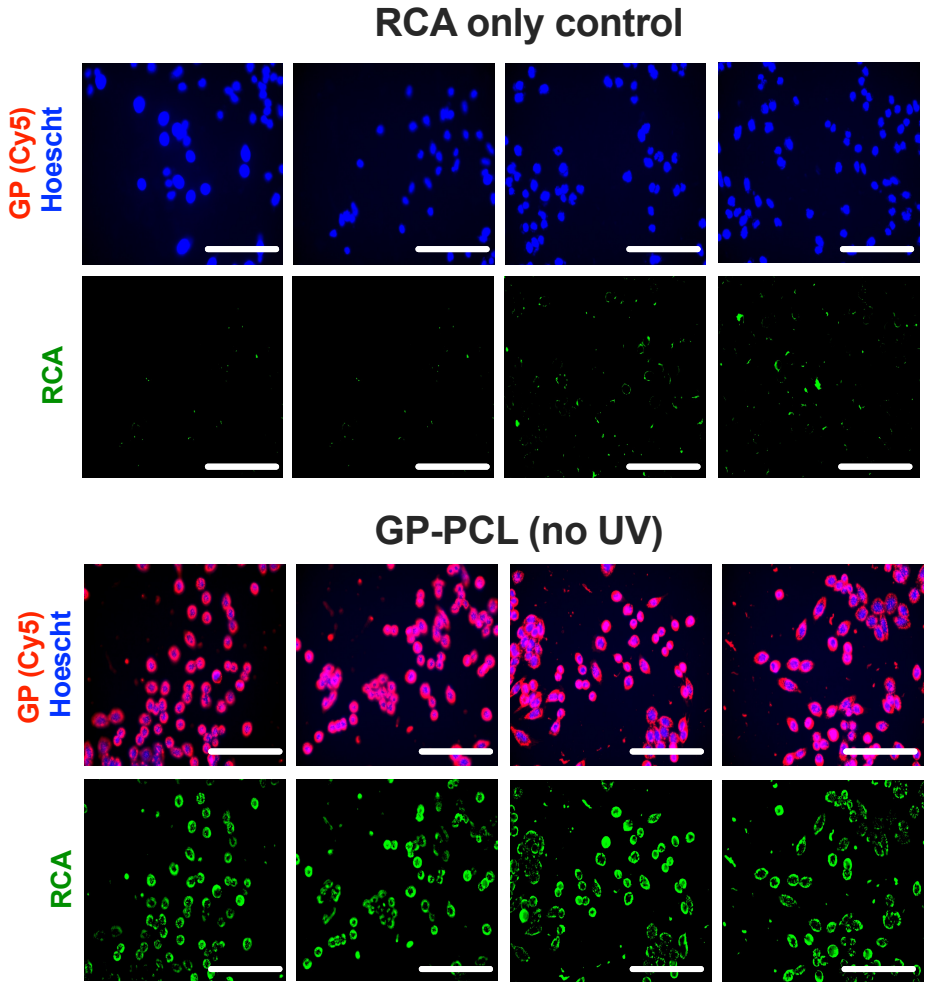

Figure 3.S18a Expanded lectin crosslinking imaging panel.

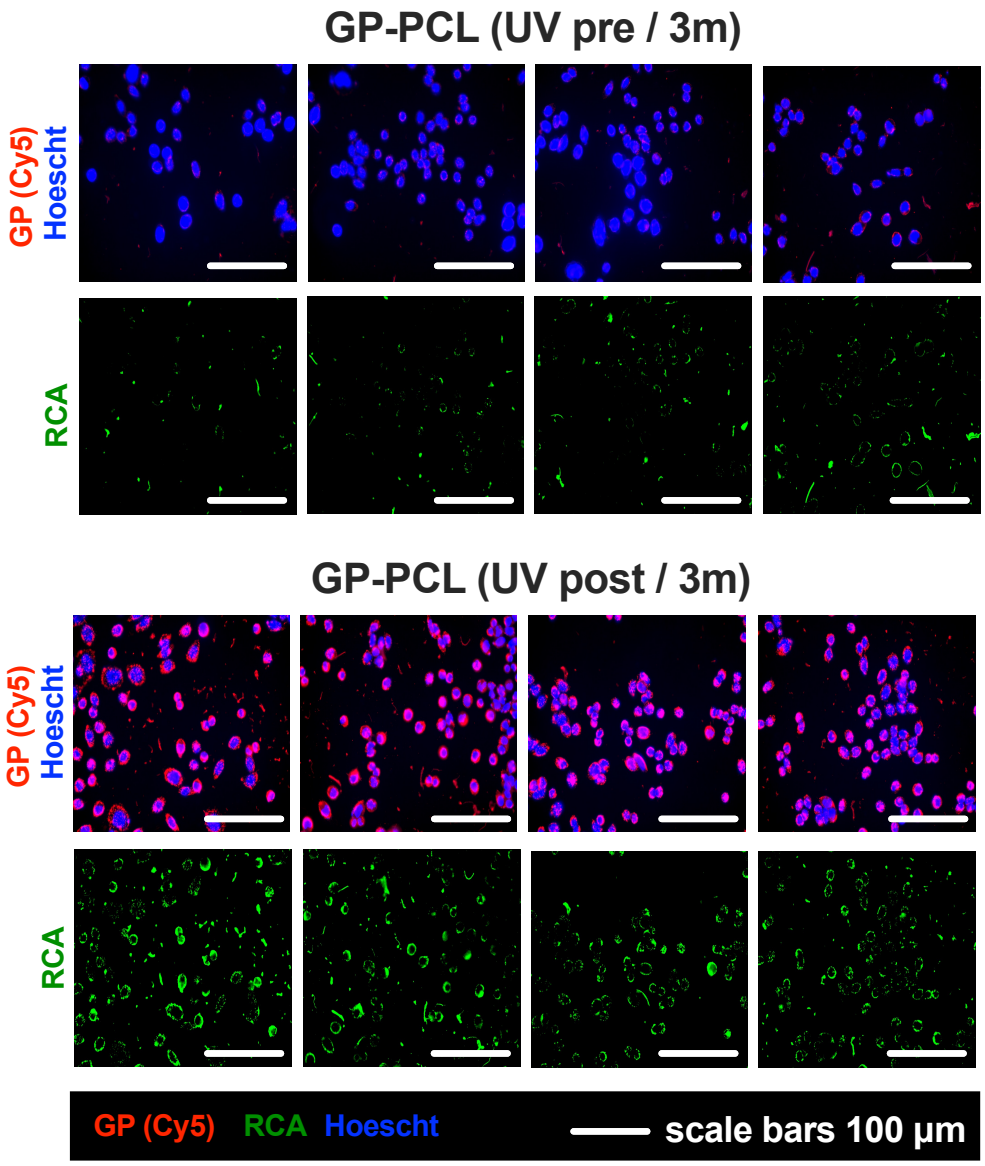

Figure 3.S18b Expanded lectin crosslinking imaging panel.

3.8.6 References

1. Honigfort, D.J.; Altman, M.O.; Gagneux, P.; Godula, K. Glycocalyx crowding with mucin mimetics strengthens binding of soluble and virus-associated lectins to host cell glycan receptors. *Proc. Nat'l. Acad. Sci.* 2021, 118 (40), e2107896118.

2. Gervais, M.; Labbé, A.; Carlotti, S.; Deffieux, A. Direct Synthesis of α-Azido,ω-hydroxypolyethers by Monomer-Activated Anionic Polymerization. *Macromolecules.* 2009, 42(7), 2395–2400.

3. Kaneko, S.; Nakayama, H.; Yoshino, Y.; Fushimi, D.; Yamaguchi, K.; Horiike, Y.; Nakanishi, J. Photocontrol of cell adhesion on amino-bearing surfaces by reversible conjugation of poly(ethylene glycol) via a photocleavable linker. *Phys Chem Chem Phys.* 2011,13(9), 4051- 4059.

4. Isabettini, S.; Liebi, M.; Kohlbrecher, J.; Ishikawa, T.; Fischer, P.; Windhab, E.J.; Walde, P.; Kuster, S. Mastering the magnetic susceptibility of magnetically responsive bicelles with 3β-amino- 5-cholestene and complexed lanthanide ions. *Phys Chem Chem Phys.* 2017, 19(17), 10820- 10824.

5. Eirich, J.; Orth, R.; Sieber, S.A. Unraveling the protein targets of Vacomycin in living S. aureus and E. faecalis cells. *J. Am. Chem. Soc.* 2011, 133(31), 12144-12153.

4 HS aptamer chimeras enable embryonic stage-specific glycocalyx engineering

4.1 Abstract

Many chemical approaches have been developed to incorporate synthetic glycomaterials into the glycocalyx – allowing for glycan display to be tailored to promote growth factor interactions and activate or suppress downstream signaling. While this has allowed for strides in controlling the display of glycans on the cell surface via material design, methods for cell-specific glycocalyx engineering are limited to cases suited for prior genetic manipulation of target cells. In order to be viable in a therapeutic context, there is a need for less-invasive methods to target synthetic glycomaterials with enhanced specificity amidst the biological milieu. Here we report a facile, modular synthetic strategy to generate HS aptamer chimeras that can be selectively targeted and noncovalently anchored to the surface of living embryonic cells expressing the pluripotency marker alkaline phosphatase (Alpl). Using this approach, we armed a fluorescently tagged streptavidin protein core with well-defined oligosaccharides of HS capable of activating FGF2/FGFR mediated MAPK signaling and a DNA aptamer to target the conjugates to the surface of ESCs. Utilizing these materials for embryonic stage-specific glycocalyx engineering, we demonstrate that we can selectively modify the glycocalyx to activate cell signaling in ESCs in the pluripotent state, priming those cells for neural specification. The simple biosynthetic route and glycocalyx engineering strategy described allows for this approach to be rapidly expanded to a wide array of cell surface targets and signaling pathways, for the incorporation of additional functionalities, or multiplexing. The ability to precisely modify the glycocalyx of pluripotent cells within complex systems containing

cells at different developmental stages holds great potential for regulating cell signaling and development in the context of cell-based therapies and regenerative medicine.

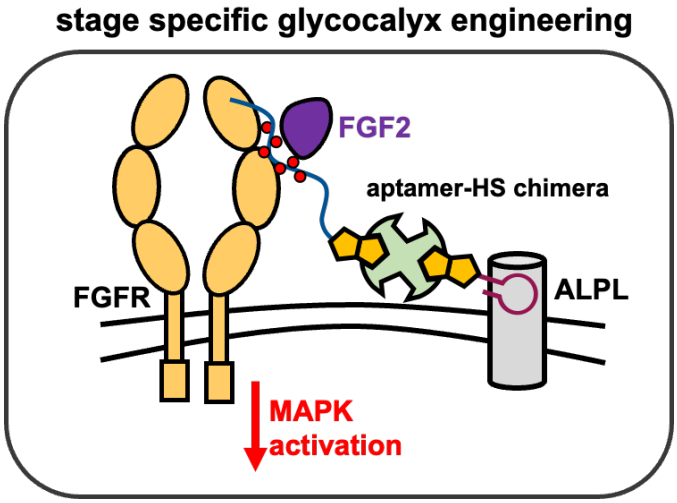

Figure 4.1 Embryonic stage specific glycocalyx engineering concept. Aptamer-HS chimera contains a bioactive HS glycodomain linked to an Alpl targeting aptamer via a protein core and is capable of activating MAPK activity by facilitating FGF2/FGFR interactions.

4.2 Introduction

The glycocalyx is an extensive network of glycosylated biomolecules populating the cellular boundary capable of regulating biological events including cellular communication and development.[1] Of particular interest are proteoglycans, biomolecules composed of a membrane bound protein core from which pendant glycosaminoglycan (GAG) chains are displayed and heavily modified by sulfation enzymes, amongst others. It is increasingly appreciated that GAGs serve as coreceptors for growth factors (GFs) and their cognate receptors, and that the sulfation motifs serve to regulate competing growth factor mediated signaling pathways. One such interaction, between fibroblast

growth factor 2 (FGF2) and its cell surface receptor (FGFR) facilitated by heparan sulfate proteoglycans (HSPGs) is known to promote the neural specification of stem cells through activation of the Erk1/2 protein-kinase signaling cascade.[2] Specifically, heparan sulfate (HS) by means of multivalent glycan display, provides a high affinity binding domain and promotes interactions between FGF2 and FGFR.

Because glycosylation is a post-translational modification, manipulating the functions of the glycocalyx requires new chemical tools and methods by which to modify the cell surface glycans. In order to better understand glycan mediated interactions at the cellular boundary, several chemical, chemoenzymatic, and biological strategies have been employed to control or edit the glycocalyx of living cells.[3] While powerful tools for controlling glycan composition, these top-down approaches fail to control the three-dimensional complexity of the glycocalyx. It is increasingly appreciated that the spatial distribution of glycans is as important as composition in controlling biological recognition.[3] Strategies which construct *de novo* a synthetic glycocalyx via insertion of synthetic nanoscale glycomaterials, including proteoglycan mimetics, into the outer leaflet of the cell membrane have emerged as a tool by which to better control both composition and spatial arrangement of cell surface glycans. Paired with the use of knockout cell lines deficient in GAG biosynthesis, this can be an effective approach for studying and influencing GAG mediated cell signaling and cell development.[4]

There are now many examples of glycocalyx engineering whereby GAGs or polymeric scaffolds with glycan components are immobilized on the cell surface via passive insertion of a lipid anchor into the cell membrane.[5] This strategy can even be

used to scaffold glycomaterials, generating a spatially complex 'glycoscape' at the cell surface.[6] By using GAGs with defined sulfation motif or short GAG oligosaccharides displayed on polymeric scaffolds with high affinity for GFs of interest, the glycomaterials can engage signaling processes once immobilized, influencing cell proliferation, differentiation, or interaction with other cells or viruses.[7] Of great interest to the community is the ability to impart selectivity into the design of glycomimetic materials such that biological processes can be manipulated with high levels of precision, progressing toward therapeutically relevant outcomes. This can be accomplished either by targeting glycomaterials to specific cells or cellular regions, or by utilizing materials which selectively engage a GF of interest after broad application across a cell system. The former is desirable as it both allows for minimal perturbation to the native system during the glycocalyx engineering process and can be applied to current-generation materials. Developments in array technologies and improved techniques for the isolation and synthesis of tissue-derived GAGs will likely enable the latter, but are still emerging.

Methods by which to anchor synthetic glycomaterials to the cell surface have expanded rapidly over the past decade, yet most rely on passive insertion of hydrophobic anchors into the cell membrane, offering no control over glycomaterial presentation or cell specificity. Amongst these passive insertion strategies, cell-surface retention often motivates the use of particular lipid tails or steroids over others.[5] Liposomal fusion with the cell membrane has also been utilized, but at present lacks the specificity required for glycomaterial delivery to cell selective incorporation.[8] Elegant examples of glycocalyx engineering from Hsieh-Wilson[9] and Bertozzi[10] demonstrate that GAGs or glycopolymers can be immobilized on the cell surface as chimeras after being covalently linked to

reactive handles engineered into cell surface proteins. While offering a more targeted approach, such strategies require prior genetic manipulation and their use in biomedical applications may consequently be limited. The challenge of targeted delivery has, however, been addressed by the broader research community with bioconjugates containing affinity-based targeting molecules including antibodies, peptides, and aptamers – but these strategies have not yet emerged for cell-surface glycan engineering.[11]

Aptamers are small nucleic acid structures that exhibit highly selective affinity for a target.[12] Their ability to target protein biomarkers makes them ideal for cell- or cell stage-specific delivery. Aptamers have gained momentum as delivery agents due to their small size and the favorable properties of oligonucleotides – yielding advantages over antibody-based delivery systems.[12] Utilizing whole-cell systematic evolution of ligands by exponential enrichment (cell-SELEX), researchers have identified several aptamers that selectively bind a cell surface pluripotency marker, alkaline phosphatase (Alpl), targeting pluripotent cells.[13] The aptamer 19S was shown to bind selectively to pluripotent stem cells expressing Alpl and was used as an enrichment tool in mixed cell populations.[13] While the utility of aptamer- bioconjugates has been explored in the targeted delivery of therapeutics and has even emerged in the clinic, to our knowledge no strategy for aptamer-mediated cell surface engineering currently exists. To address this challenge, we set out to generate HS-aptamer chimeras whereby a fluorescently labeled streptavidin core is non-covalently bound to an HS glycodomain and Alpl target DNA aptamer for cell stage specific binding activity.

4.3 Results and Discussion

4.3.1 HS-aptamer chimera design

To maximize the potential of our HS-aptamer chimeras to influence neuroectodermal differentiation we sought to identify a cell surface target which is expressed during pluripotency, but expression is quickly lost as the cell exits the pluripotent state. As such, we identified several mouse embryonic stem cell pluripotency markers including Oct4, SSEA-1, and Alpl. SSEA-1 and Alpl were further evaluated as these markers are expressed on the cell surface and ultimately Alpl was selected owing to both the relatively low background expression in other cell types and because a single-stranded DNA aptamer (aptamer 19S) had previously been identified to bind selectively to pluripotent stem cells in an elegant cell SELEX study by Thompson and colleagues[13] and Alpl was identified as the cell surface epitope. Thus, aptamer 19S was well suited for use in our HS-aptamer chimera glycoconjugates. Heparin was chosen as the bioactive component of the chimera as it could be obtained commercially and could demonstrate efficacy of the approach prior to the use of either tissue derived HS or selectively desulfated HS structures. Because direct bioconjugation of the aptamer and heparin glycodomain proved extremely challenging owing to the size and large negative charge of each component, we sought to link the chimera via a protein core. The display of HS from a protein core has been shown[14] to promote MAPK activity to a greater extent than soluble HS at the same concentration and this would physically separate the two negatively charged domains, aiding in their bioconjugation.

The strong binding constant of streptavidin-biotin interactions[15] presented an appealing alternative to covalent bioconjugation owing to the rapid, modular assembly of

non-covalent chimera structures. By modifying the aptamer and heparin with biotin, conjugates could be quickly generated with control over composition. Fluorescent labeling of the streptavidin protein core could also be used to introduce an optical probe for visualization of the materials on the cell surface. HS-chimeras assembled in 1:1:1 stoichiometric ratio would simultaneously anchor to the surface of pluripotent Alpl and Oct4 expressing cells (Figure 4.2A) Upon binding to the cell surface the materials would be primed to engage FGF2/FGFR complexes and promote MAPK activity, ultimately promoting neural differentiation of the cells toward the neural precursor state, which is assessed by expression of a neuroectodermal marker, Sox1.[16]

4.3.2 Evaluating markers for embryonic stage specification

To establish a model system utilizing mouse embryonic stem cells we first sought to determine the expression timeline for alkaline phosphatase. To benchmark expression against another pluripotency marker we used the nuclear marker Oct4. Sox1, an early nuclear marker of induction into the neuroectodermal cell lineage was also utilized.[16] Mouse embryonic stem cells lacking HS proteoglycans on their cell surface ($Ext1^{-/-}$) were differentiated following a well-established neural differentiation protocol (Figure 4.2B) over the course of six days. Cells were fixed in paraformaldehyde at each day of differentiation (Day 0 – Day 6) with Day 0 representing cells grown in standard culture media and not treated with N2B27 media. Because $Ext1^{-/-}$ mouse embryonic stem cells lack cell surface HS, exogenous heparin (5 ug/mL) must be supplied for differentiation to proceed. Cells were then stained for pluripotency markers Oct4 and Alpl as well as neuroectodermal marker Sox1 and fluorescent microscopy allowed for visualization of

protein expression level (Figure 4.2B). Corrected total cell fluorescence (CTCF) was determined and expression levels normalized to maximum signal, which occurred at Day 0 or Day 6. Over the course of differentiation, expression of embryonic markers Oct4 and Alpl quickly declined and were difficult to detect beyond Day 3. Sox1, conversely, began to express on Day 3 and robust expression was observed by Day 6 of differentiation. Similar expression patterns were observed in wild type E14TG2a mouse embryonic stem cells, which could be differentiated in the absence of exogenous heparin owing to the HS proteoglycans on their cell membranes (Figure 4.S14). Expression of Sox1 on Day 4 of differentiation appears well suited as a measure of the efficacy of HS-aptamer chimeras to promote neural differentiation as Sox1 is approaching maximum CTCF intensity.

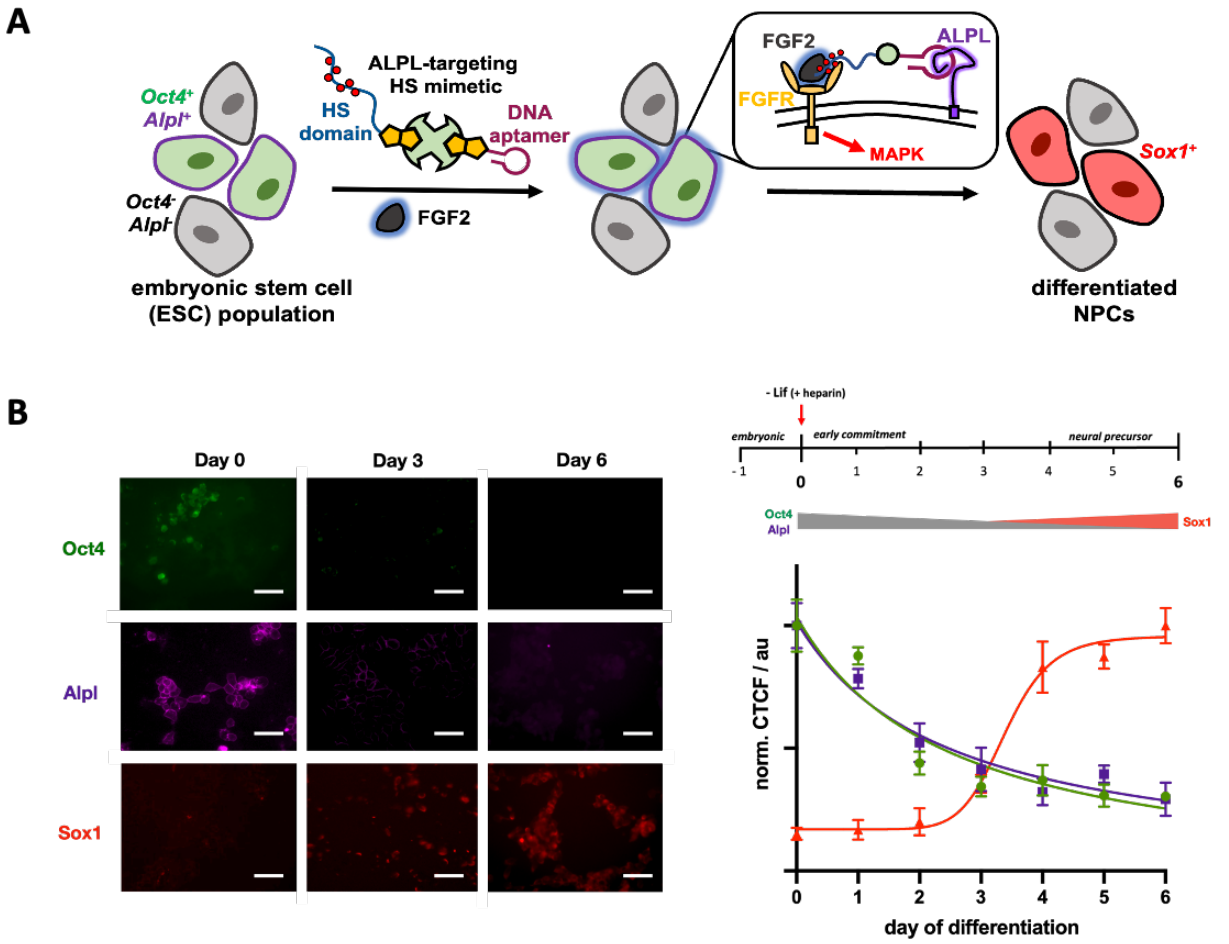

Figure 4.2 Embryonic stage specific glycocalyx engineering. (A) Cells expressing aptamer target and embryonic marker ALPL are remodeled by an ALPL-targeting HS mimetic containing a DNA aptamer targeting unit and a bioactive HS domain. After remodeling the cell surface the materials facilitate FGF2 binding to its cognate cell surface receptor FGFR. Activation of MAPK activity results in subsequent neural differentiation. (B) Ext1$^{-/-}$ mouse embryonic stem cells express embryonic markers Oct4 and Alpl early in neural differentiation and neural marker Sox1 is expressed later in differentiation, making Alpl a prime target for developmental stage specific glycocalyx engineering. Scale bars = 100 um.

4.3.3 Assembly of HS-aptamer chimeras

To generate the HS-aptamer chimeras we first sought to modify heparin exclusively at the reducing end. This could be accomplished using a propylamine linker bearing an N-methylaminooxy functional handle with reactivity toward the hemiacetal of reducing heparin under acidic conditions (Figure 4.3A). After installing an amine, n-

hydroxysuccinimide chemistry could be employed to biotinylate the heparin via a short tetraethylene glycol linker (Figures 4.S1 – 4.S3). The resulting heparin was characterized by carbazole[17] and 4-hydroxyazobenzen-2-carboxylic acid[18] (HABA) assays and determined to be approximately 20% end-functionalized (Figure 4.S4). The modest end-functionalization efficiency may be due to the method of heparin isolation, from which the extent of β-elimination is unknown. Because the Hep-SA intermediates will require purification, non-biotinylated heparin was removed from the Hep-aptamer chimeras via dialysis and molecular weight cut-off filtration. Aptamer 19S and a control sequence in which the aptamer binding domain is scrambled (Aptamer Scr) were obtained with 5' biotin modification from Integrated DNA Technologies and used as received. The sequences (Figure 4.3) contain identical wing sequences of approximately 10 bases and the high GC content of aptamer 19S affords a G-quadruplex binding motif with specificity for Alpl.[13]

To assemble the Hep-aptamer chimeras a two-step process was utilized (Figure 4.3) in which excess Streptavidin-AF_{488} (bearing approximately 5 fluorophores per streptavidin) was first mixed with biotinylated heparin and purified by a combination of dialysis and spin filtration to yield Hep-SA in a 1:1 stoichiometry, as determined by carbazole assay and UV-Vis spectroscopy (Figure 4.S5). The purified Hep-SA is then mixed with exactly 1 equivalent of biotinylated aptamer or scramble sequence to yield Hep-SA-19S or Hep-SA-Scr in 1:1:1 stoichiometry suitable for immediate use. We also explored chimera assembly as a one step process and in two steps with DNA aptamer addition first (Figure 4.S6). In the one-step process, multiple products were generated, and stoichiometry was difficult to control. In the case of DNA addition, we observed the

formation of 2:1 DNA-Streptavidin complexes by both size exclusion and native polyacrylamide gel electrophoresis, and complexes could not be separated efficiently by size exclusion chromatography. Unlike in the case of heparin in which greater than 10 equivalents of heparin were required to generate higher-order assemblies (Figure 4.S7) as indicated by greater mobility shift on agarose gel, multivalent DNA conjugates were generated in the presence of only 1 equivalent of DNA per streptavidin, and even in sub-stoichiometric quantities. This may be attributed to the repulsive forces between the large, extended heparin structures, potentially preventing access of additional heparin biotin to the remaining streptavidin binding sites.

To characterize the assembly of Hep-SA-Apt chimeras agarose gel electrophoresis was performed and samples were visualized via the AF488 optical probe. A mobility shift is observed upon addition of a heparin chain to the streptavidin protein core, pulling the assembly into the gel. A modest shift is observed upon the addition of aptamer, suggesting that electrophoretic mobility afforded by the increase in negative charge is, to some extent, counteracted by the decreasing ability of the material to move through the agarose gel. To corroborate these observations, agarose gels were also stained by SYBR Gold nucleic acid stain, enabling visualization of the DNA aptamer domain. Unsurprisingly, a mobility shift is observed between aptamer and Hep-SA-Apt bands, and colocalization of SA and Apt signal is observed. Addition of a single equivalent of DNA was optimal (Figure 4.S8) as complete consumption of the DNA band was observed, indicating that the material could be used directly in biological assays without further purification.

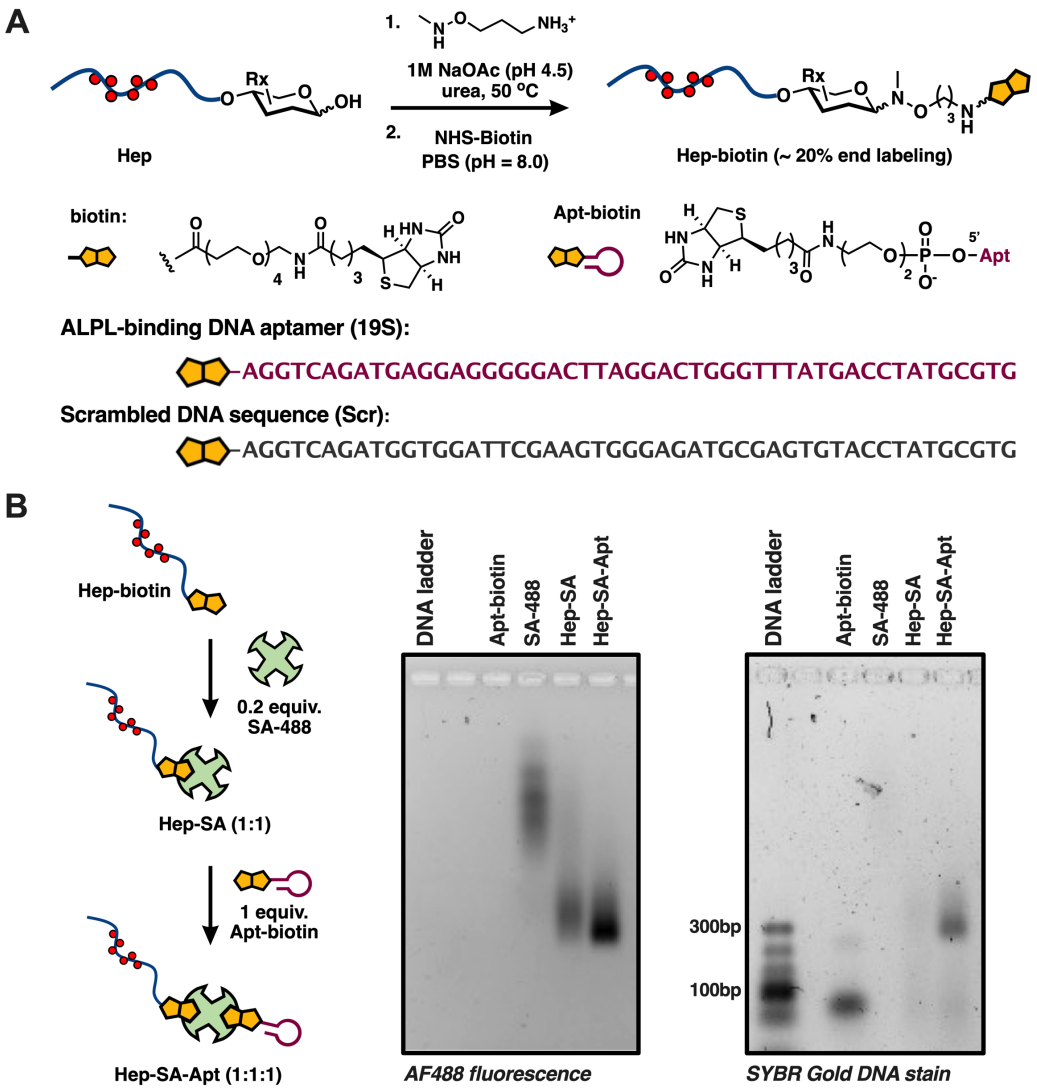

Figure 4.3 Preparation of aptamer glycoconjugates for targeted cell surface engineering. (A) Heparin is pre-functionalized at the reducing end with biotin over two steps to afford biotinylated heparin (approximately 20% functionalized. ALPL binding aptamer 19S or a scrambled control aptamer SCR is also biotinylated via a short PEG linker at the 5' terminus. (B) Assembly of Hep-SA-Apt conjugates in 1:1:1 stoichiometry is afforded by sequential addition of biotinylated heparin (5 equiv.) and biotinylated aptamer (1 equiv.). Purified materials are characterized by agarose gel (visualization via AF_{488} or SYBR Gold DNA stain).

4.3.4 Stage specific glycocalyx engineering with Hep-SA-Apt conjugates

To assess the ability of Hep-SA-Apt chimeras to remodel the surface of live cells expressing Alpl, we first evaluated the binding of aptamer biotin alone to the surface of mouse embryonic stem cells ($Ext1^{-/-}$) and differentiated mouse embryonic fibroblasts

which do not express Alpl (Figure 4.S9) and determined the EC_{50} of aptamer binding to be approximately 107 nM. Expecting that the addition of the Hep-SA domains would result in a similar binding coefficient, chimera binding to the $Ext1^{-/-}$ cell surface was measured at concentrations ranging from 0 – 200 nM. Hep-SA-19S bound to the cell surface, as determined by flow cytometry after 40 min incubation in suspension, with an observed EC_{50} of 70 nM while Hep-SA-Scr control and Hep-SA alone did not result in significant cell surface binding (Figure 4.4). Notably, the concentration ranges for cell surface remodeling afforded by the aptamer targeting strategy are significantly lower than traditional glycocalyx remodeling via passive insertion of glycomaterials bearing membrane anchors (typically used at concentrations of 0.5 – 10 uM *in vitro*).[2,5] Importantly, Hep-SA-19S showed binding specificity over the control chimeras at concentrations as low as 25 nM.

Next, to evaluate the embryonic stage-specificity of the glycocalyx engineering strategy mouse embryonic stem cells were subjected to neural differentiation protocols until Day 6 either in the presence (for $Ext1^{-/-}$) or absence (for E14) of soluble heparin at a concentration of 5 ug/mL.[19] Cells at D0 and D6 of neural differentiation were suspended, blocked, and mixed in suspension with conjugates for 40 minutes on ice. Following washes with DPBS the cells were analyzed by flow cytometry, with AF488 signal corresponding to immobilization of the material on the cell surface (Figure 4.4). In $Ext1^{-/-}$ cells, a significant decrease in Hep-SA-19S binding activity was observed following six days of differentiation. Hep-SA-Scr and Hep-SA controls did not result in significant binding before or after differentiation. Binding activity of Hep-SA-19S to Day 6 $Ext1^{-/-}$ cells which despite being reduced remains significantly greater than background may be

explained by the mixed population of embryonic (which still bind Hep-SA-19S) and differentiated cells (which do not bind Hep-SA-19S owing to a lack of Alpl). Similar trends were observed for wild type E14 cells. The reduced total immobilized conjugate on the surface of E14 cells relative to Ext1$^{-/-}$ cells may be due to the presence of native HS proteoglycans on the cell surface preventing access of Hep-SA-19S to Alpl or to lower observed levels of Alpl expression. Flow cytometry with Ext1$^{-/-}$ mouse embryonic stem cells and differentiated mouse embryonic fibroblasts (MEFs, which do not express high levels of Alpl) remodeled with conjugates at 25nM demonstrates cell-type specificity of this glycocalyx engineering strategy (Fig 4.S10).

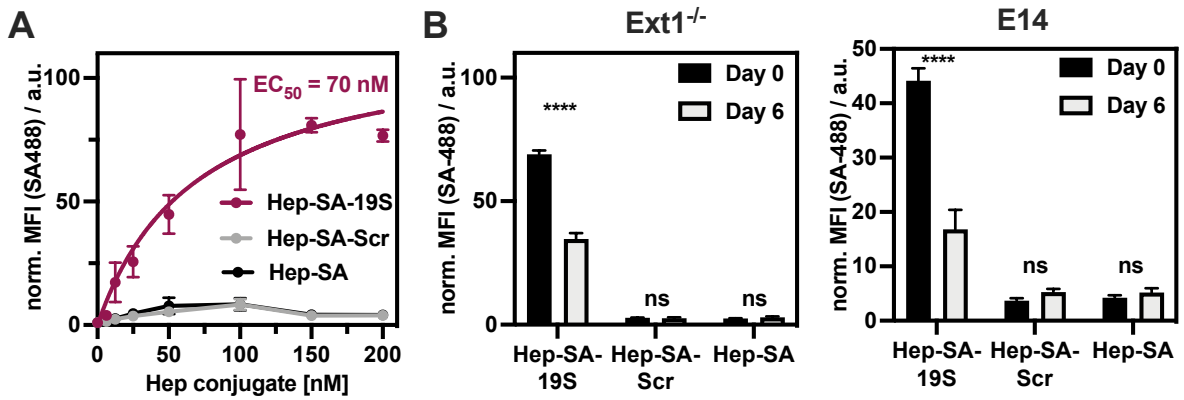

Figure 4.4 Cell surface engineering with stage specific aptamer-HS chimeras. (A) Ext1$^{-/-}$ mouse embryonic stem cells expressing Alpl are treated with conjugate at increasing concentration (0-200 uM) and analyzed by flow cytometry. Conjugates bearing the functional aptamer 19S result in a rapid increase in mean fluorescent intensity associated with strong binding (EC_{50} = 70 nM) which is significantly higher than conjugates bearing a control scrambled aptamer sequence (Hep-SA-Scr) or which lack an aptamer (Hep-SA). No binding was observed for control conjugates. (B) Glycocalyx engineering with aptamer-HS chimeras is embryonic stage specific. In both Ext1$^{-/-}$ and E14 (wt) mouse embryonic stem cells, Hep-SA-19S shows significant cell surface binding over control conjugates paired with a significant reduction ($p < 0.0001$) in binding to cells which have undergone six days of neural differentiation. Some binding is retained due to the mixed population of embryonic and differentiated cells following the differentiation protocol.

4.3.5 FGF2 Binding to cell surface bound Hep-SA-19S

Having established that Hep-SA-19S is capable of embryonic stage specific and cell-type specific glycocalyx engineering, we next sought to demonstrate the ability of surface immobilized chimeras to engage FGF2/FGFR complexes via the heparin glycodomain. Flow cytometry was utilized to assess the ability of remodeled cells to bind soluble FGF2 in a Hep- and 19S- dependent manner. First, we established an FGF2 binding protocol whereby Ext1$^{-/-}$ or E14 cells were incubated with increasing concentrations of soluble FGF2 (0 – 1000 nM) and subsequently detected by precomplexed anti-FGF2 and fluorescent AF647 labeled secondary antibodies (Figure 4.S11). FGF2 at 250nM concentration resulted in strong HS-dependent binding and was selected for use in two-color flow cytometry assays.

Suspended Ext1$^{-/-}$ cells (which do not bind FGF2 owing to a lack of cell surface HS) were first remodeled with Hep-SA-19S or Hep-SA-SCR at 100 nM to remodel the glycocalyx. The remodeled cells were then mixed with FGF2, washed, and fluorescent antibodies were used to detect cell-surface bound FGF2 by flow cytometry (Figure 4.5A). We observed an increase in AF488 fluorescence corresponding to immobilization of Hep-SA-19S on the cell surface relative to a control of cells only. In the presence of FGF2 we observe a corresponding dramatic increase in AF647 signal consistent with FGF2 binding to the remodeled cell surface (Figure 4.5B). Hep-SA-SCR, which resulted in background levels of cell surface remodeling also showed some FGF2 binding activity consistent with the strong interaction between heparin and FGF2. This highlights the importance of minimizing background remodeling of the cell surface by Hep-SA-Scr, as even low levels of cell surface binding may result in biological activity. Interestingly, Hep-SA showed

increased background binding and accordingly FGF2 binding activity relative to Hep-SA-Scr, suggesting that the presence of the Scr DNA sequence reduces non-specific interactions between heparin and the cell surface. This may provide an opportunity for the soluble glycomaterials to be present during differentiation (without washing after immobilization) if the increased affinity of Hep-SA-19S results in a shift in either FGF2 stimulation or Sox1 expression curves following differentiation. Importantly, the Hep- and 19S- specific FGF2 binding trends were observed to be dose-dependent at concentrations of glycoconjugate ranging from 0 – 100 nm (Fig 4.5C, additional scatterplots shown in Figure 4.S11).

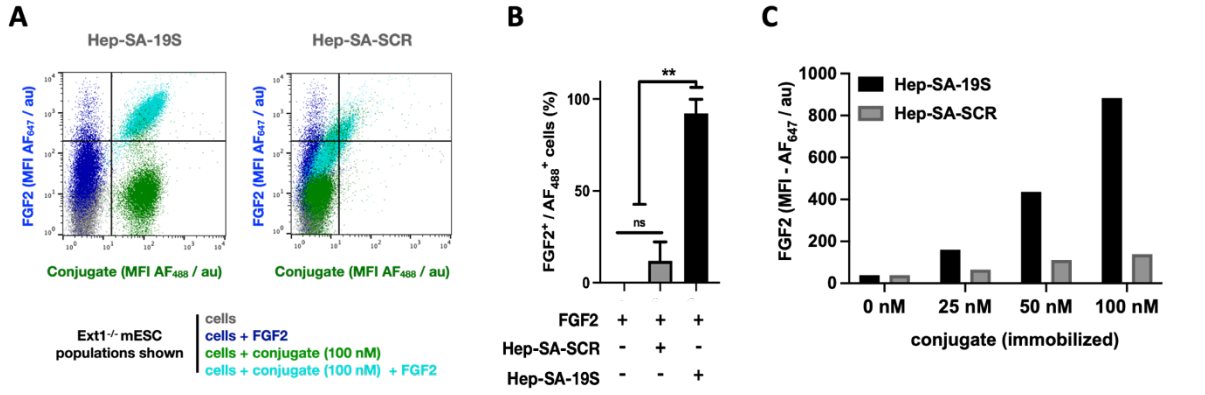

Figure 4.5 FGF2 binding activity of remodeled cells. Ext1$^{-/-}$ mouse embryonic stem cells lacking cell surface HS do not bind FGF2. Cells remodeled with Hep-SA-19S facilitate the binding of FGF2 to the cell surface, which is assessed by two-color flow cytometry. (A) Cell populations plotted by MFI (conjugate, AF_{488}) and MFI (FGF2, AF_{647}) show remodeling of the cell surface and conjugate dependent FGF2 binding after treatment with conjugates at 100 nM. A modest increase in FGF2 activity is observed in the absence of conjugate due to non-specific FGF2 antibody staining. Hep-SA-19S shows an increase in both AF_{488} and AF_{647} fluorescence over Hep-SA-Scr. (B) Quantification of percent cell population which is both $FGF2^+$ and AF_{488}^+ based on control gates shows significant aptamer dependent increase over multiple trials. (C) FGF2 binding activity increases as a function of cell-surface bound conjugate. The presence of the Scr aptamer sequence reducing non-specific binding of Hep-SA at all concentrations evaluated (0-100 nM) and a control lacking FGF2 shows minimal background signal.

4.3.6 MAPK Signaling Activity and Neural Differentiation

After confirming the ability of cell surface immobilized Hep-SA-19S to bind FGF2, we sought to determine if this binding activity could be used to rescue Erk1/2 phosphorylation in Ext1$^{-/-}$ cells, a crucial first step for neural specification. Ext1$^{-/-}$ cells were grown in well plates and serum starved to reduce signaling activity before being stimulated with soluble FGF2 (25 ng/mL) in the presence of Hep-SA, Hep-SA-19S, Hep-SA-Scr, soluble heparin, or controls (DNA aptamer or SA alone) at 100 nM (Figure 4.6A). We observed a dose dependent increase in Erk1/2 phosphorylation in heparin conditions as has been previously reported and saw increased phospho-Erk1/2 levels only in conjugate conditions containing Hep. Unfortunately, owing to the narrow concentration range and high sensitivity of the heparin stimulation assay (Figure 4.S12) we did not observe Hep-SA-19S specific stimulation when the glycoconjugate was present as a soluble factor during stimulation or immobilized and washed from the surface prior to FGF2 stimulation, due to background material binding. Nevertheless, because of the increased affinity of Hep-SA-19S for the cell surface and the potential to activate MAPK activity, differentiation in the presence of soluble glycoconjugates offered an attractive alternative.

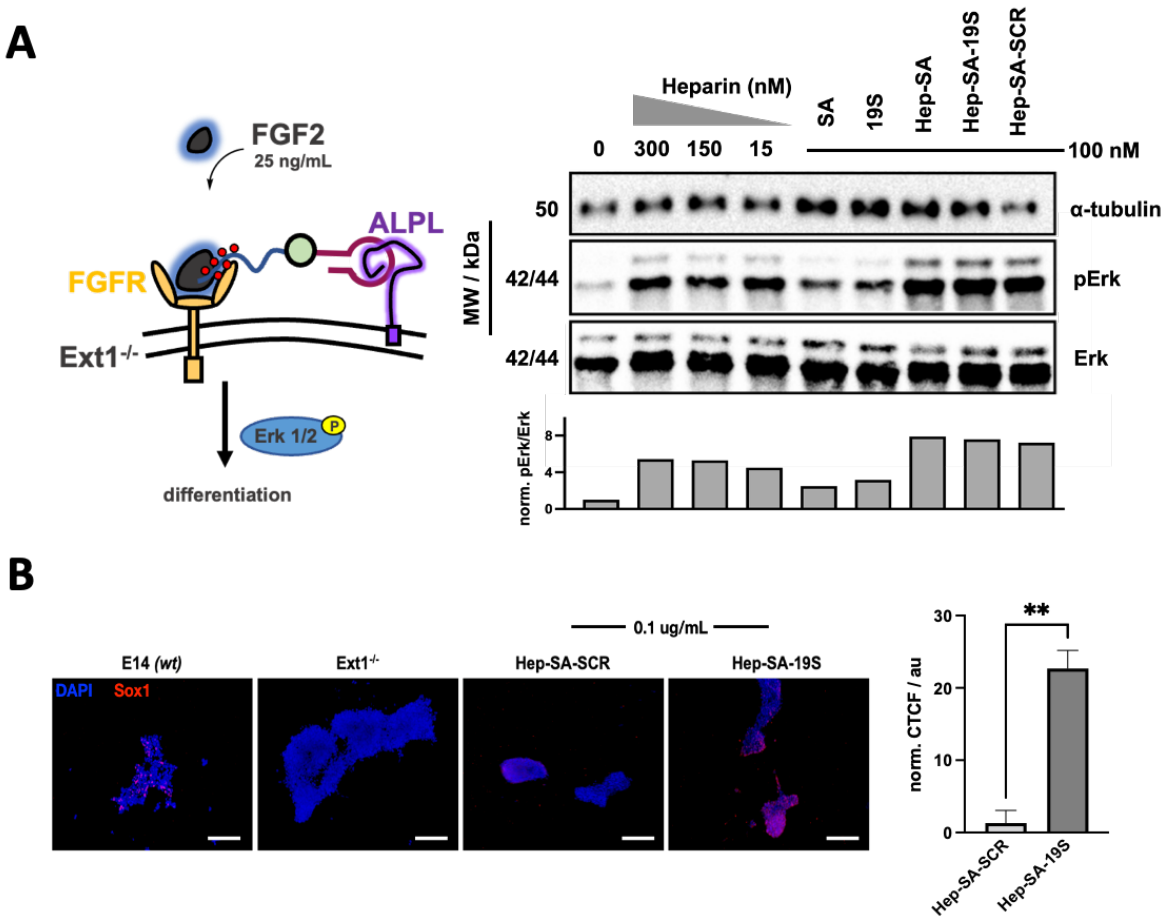

Figure 4.6 Aptamer-HS chimeras capable of activating MAPK signaling and promoting neuroectodermal differentiation. (A) Ext1$^{-/-}$ mouse embryonic stem cells stimulated with FGF2 in the presence or absence of aptamer conjugates which were used to remodel the cell surface at 100nM concentration. Increased phosphorylation of Erk1/2 is observed to be similar to that of heparin at concentrations ranging from 15-300 nM. This bioactivity is afforded by the HS domain. (B) Neuroectodermal differentiation in the presence of 0.1 ug/mL Hep-SA-19S resulted in a modest increase is Sox1 expression, suggesting that Hep-SA-19S promotes neural differentiation, relative to controls bearing a scrambled aptamer domain which express significantly less Sox1. Sox1 is expressed in Hep-SA-19S condition to a similar extent as that of E14 cells in the absence of heparin. Scale bars = 100 um.

Ext1$^{-/-}$ cells were subjected to differentiation conditions in the presence or absence of Hep-SA, Hep-SA-19S, Hep-SA-Scr, or Hep (0 ug/mL, 0.1 ug/mL, 0.25 ug/mL, 0.5 ug/mL). Soluble heparin resulted in the onset of Sox1 expression on Day 5 of differentiation as determined by immunohistochemical microscopy at concentrations above 0.25 ug/mL, corroborating FGF2 stimulation data (Figures 4.S12 – 4.S13). In the presence of soluble Hep-SA-19S Sox1 expression was observed at 0.1 ug/mL, below that

of soluble heparin and control materials, indicating that enhanced affinity for the cell surface resulted in a shifted dose-response of Sox1 expression to the conjugate (Figure 4.6B). Hep-SA-19S promoting neural differentiation dose-dependently at concentrations evaluated, as determined by Sox1 expression levels during immunostaining (Figure 4.7). Sox1 expression at 0.5 ug/mL Hep-SA-19S is similar to that observed for heparin at the same concentration, and in the presence of a potent FGFR inhibitor, PD173074 (1 uM), Sox1 expression is ablated suggesting that neuroectodermal specification proceeds in an FGF2/FGFR specific manner (Figure 4.S13).

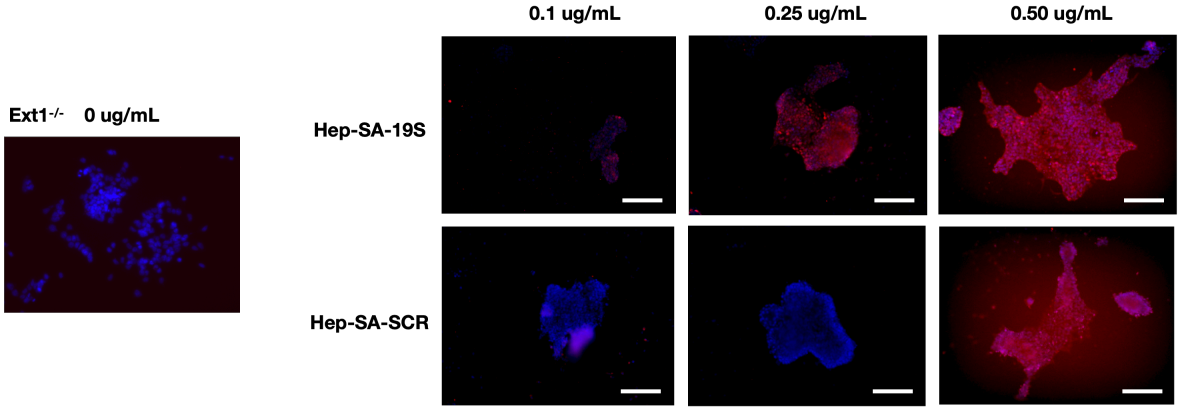

Figure 4.7 Dose dependent increase in Sox1 expression observed after treatment of $Ext1^{-/-}$ mouse embryonic stem cells with Hep-SA-19S. $Ext1^{-/-}$ cells lacking cell surface HS do not express Sox1 after 4 days of differentiation in neurobasal medium. Hep-SA-19S shows increased Sox1 expression with increasing concentration (0.1 ug/mL – 0.5 ug/mL) with expression at concentrations below which Hep-SA-Scr results in increased Sox1 expression (0.50ug/mL). Scale bars = 100 um.

4.4 Conclusions

The ability to engineer the glycocalyx of living cells selectively offers numerous opportunities to study the biological roles of the glycocalyx and is well suited for application in cell-based therapies. Until present, methods to cell- and stage- specifically remodel the glycocalyx have relied on genetic engineering strategies to incorporate reactive handles into cell surface proteins, limiting their application. Here, we present a

class of modular glycoconjugate chimeras composed of a DNA aptamer targeting domain, a fluorescent protein core, and a bioactive heparin domain. Using the Hep-SA-19S chimera we show cell-type and embryonic stage specific glycocalyx engineering can be achieved via non-covalent aptamer binding. Following cell surface remodeling, conjugates promote the neural specification of stem cells lacking native HS structures at concentrations below that of soluble heparin. This modular glycocalyx engineering platform can be applied to a wide array of cell surface targets and glycan based signaling pathways.

4.5 Methods

4.5.1 Materials and instrumentation

All chemicals, unless otherwise stated, were purchased from Sigma Aldrich and used as received. Heparin was purchased from Iduron (Hep-001). Streptavidin-AlexaFluor 488 conjugate was purchased from ThermoFisher scientific (S11223) as a lyophilized solid and reconstituted in ultrapure water. Reactions were monitored by thin layer chromatography using Silica gel plates and visualized by a combination of UV, iodine, and Ninhydrin staining. Bioconjugation was monitored by agarose gel electrophoresis as described. Mouse embryonic stem cells ($Ext1^{-/-}$ and E14Tg2a) were obtained as a gift from Dr. Cathy Merry, University of Nottingham, UK. Mouse embryonic fibroblasts were obtained as a gift from Dr. Philip Gordts, University of California San Diego.

Column chromatography was performed on a Biotage Isolera One automated flash chromatography system. Nuclear magnetic resonance (^{1}H and ^{13}C NMR) spectra were recorded on Bruker 300 MHz and Jeol 500 MHz NMR spectrometers. Spectra were recorded in $CDCl_3$ or D_2O at 293K and are reported in parts per million (ppm) on the δ scale relative to residual solvent as an internal standard (for ^{1}H NMR: $CDCl_3$ = 7.26 ppm, D_2O = 4.79 ppm, for ^{13}C NMR: $CDCl_3$ = 77.0 ppm, CD_3OD = 49.0 ppm). ESI-MS (electrospray ionization mass spectrometry) analysis was performed on an Agilent 6230 ESI-TOFMS in positive ion mode. UV-Vis spectra were collected using a Thermo Scientific Nanodrop2000c spectrophotometer. Live cell flow cytometry analysis was performed using a FACSCalibur or FACSCanto II system (BD Biosciences). Data were collected using FACS Diva software and analyzed in FlowJo. Microscopy was performed on either a Keyence BZX800 epifluorescent microscope or a ThermoScientific EVOS imaging system. Images were analyzed using ImageJ.

4.5.2 Synthesis and characterization of aminooxy linker for heparin functionalization

A 5 mL round bottom flask was charged with N-(3-aminopropoxy), N-methyl-carbamic acid, 1,1-dimethylester hydrochloride (30.32 mg, 125 umol, 1.0 eq) and a magnetic stirrer. A solution of trifluoroacetic acid (25% v/v in dicholoromethane, 0.5 mL) was then added. The reaction proceeded for 8 hours at ambient temperature after which time the reaction mixture was diluted with water and the aqueous layer was washed with dichloromethane. After the addition of an equal volume of toluene to the aqueous layer the mixture was concentrated under reduced pressure and the process was repeated to ensure removal of TFA. The product was then dissolved in methanol (3.0 mL),

concentrated under reduced pressure, dissolved in water and lyophilized to yield the purified linker as a viscous clear residue (12.42 mg, 82%). The material was characterized by ^{1}H NMR (300 MHz, D_2O) on δ ppm scale relative to residual solvent 4.69 ppm: 4.09 (t, 2H), 3.01 (t, 2H), 2.88 (s, 3H), 1.96 (m, 2H). Calculated $C_4H_{12}N_2O$, 104.15, $[M+H]^+$: 105.09, HRMS found: 105.10. The material was reconstituted in ultrapure water to a concentration of 1.125 mg/mL for use subsequent reactions.

4.5.3 Functionalization of Heparin

Functionalization of heparin with biotin at the reducing end proceeded over two steps. First, a PCR tube (0.5 mL) was charged with 11.10 mg of heparin sodium salt (Iduron Hep-001, 0.67 umol, 1.00 eq) and 0.19 mL of sodium acetate buffer (1 M NaOAc, 1M Urea, pH 4.5). After heating the solution to 50 C for approximately 5 minutes, a solution of 3-((methylamino)oxy)propan-1-aminium linker in water was added (0.01 mL, 11.25 umol, 16.7 eq). The reaction proceeded for an additional 72h at 50 C after which 300 uL of 2M Tris-HCl (pH 8.1) was added to quench the reaction. The reaction mixture was purified on a PD-10 column following manufacturer protocol (Cytiva), concentrated by spin filtration against water (3k MWCO, 4000x g, 25 m, 3 rounds) and lyophilized to afford the product as a white solid (11.16 mg, qt). Next, a clean PCR tube (0.5 mL) was charged with the isolated heparin amine (10.65 mg, 0.671 umol, 1 eq), 0.30 mL of sodium phosphate buffer (100 mM Na_3PO_4/NaCl, pH 8.0), and NHS-PEG4-biotin (18.3 mg, 20.2 umol, 30 eq). The reaction proceeded for 24h at ambient temperature before purification via PD-10 column following manufacturer protocol (Cytiva) and two rounds of spin filtration against water (3k MWCO, 4000x g, 25 m) followed by lyophilization to obtain the

product as a white solid 7.20 mg (67.61%). The resulting heparin-biotin was characterized by carbazole and HABA assays to determine approximately 20% end-biotinylation.

Carbazole assays were utilized to determine the concentration of heparin. Briefly, a standard 96-well plate was prepared by addition of heparin standards or heparin-biotin product at concentrations between 0 – 2.00 mg/mL (50 uL/well). A solution containing sodium tetraborate decahydrate (25 mM in 18M sulfuric acid) was then added to each well (200 uL) and the plate was heated to 100 C for a period of 10 minutes. After allowing the plate to cool to ambient temperature for 15 minutes, a solution of carbazole (1.25 mg/mL in absolute ethanol) was added to the wells (50 uL) and the plate was again heated to 100 C for 10 minutes during which time the colorimetric reaction proceeded. After cooling the plate for an additional 15 minutes to ambient temperature the absorbance at λ = 550 nm was determined using a SpectraMax plate reader. The concentration of Hep was determined by linear regression of heparin standards and corroborated the mass recorded for the desalted sample.

HABA assays were performed using a biotin quantitation kit (Pierce). Briefly, a solution of HABA-avidin premix was reconstituted in ultrapure water and the absorbance was recorded at λ = 500 nm. After the addition of Hep-biotin the absorbance was again recorded and the change in absorbance could be used to calculate the molar concentration of biotin in the sample. The ratio of the concentration of biotin/heparin was determined to be approximately 20%.

4.5.4 Hep-SA assembly and characterization

To a 0.65mL Eppendorf tube was added Streptavidin-AF_{488} conjugate (150 uL, 36 uM, Life technologies), ultrapure water (324 uL), and biotinylated heparin (5 equiv., 108 uL, 250 uM). The mixture was vortexed and placed on an orbital shaker protected from light for 24hours at ambient temperature. The crude mixture was analyzed by agarose gel electrophoresis as described below before being dialyzed against ultrapure water (Cole Parmer Spectra Pore – Snakeskin Dialysis tubing 50 kDa MWCO) for 24 hours. The dialyzed mixture was then concentrated and further purified by ten sequential rounds of spin filtration using 50 kDa MWCO filtration units (Millipore) supplemented with DPBS (10 min, > 8000 xg). The purified Hep-SA was then analyzed by gel electrophoresis.

For gel electrophoresis, agarose gels were cast at 1.5% (w/v) using low-EEO biology grade agarose (Millipore) dissolved in 1X Tris-borate EDTA (Life Technologies). Gels were cast in an EasyCast OWL electrophoresis chamber and run with ice cold 1X Tris-borate EDTA (Life Technologies) at 105 V for 75 minutes. Samples were loaded into wells in 1:2 glycerol in ultrapure water to obtain a final glycerol concentration of 10% (v/v). To visualize SA_{AF488}, a BioRad Gel Dock system was utilized, and ImageJ was used to further analyze collected images.

A ThermoFisher Scientific Nanodrop 2000c UV-Vis spectrophotometer was utilized to determine the concentration of protein (λ = 280, 495 nm) utilizing a standard curve consisting of SA at dilutions (0 – 36 uM in DPBS). Carbazole assays were utilized to determine the ratio of Hep:SA of the conjugates as previously described. Briefly, a standard 96-well plate was prepared by addition of heparin standards, SA, or Hep-SA materials at concentrations between 0 – 2.00 mg/mL (50 uL/well). A solution containing

sodium tetraborate decahydrate (25 mM in 18M sulfuric acid) was then added to each well (200 uL) and the plate was heated to 100 C for a period of 10 minutes. After allowing the plate to cool to ambient temperature for 15 minutes, a solution of carbazole (1.25 mg/mL in absolute ethanol) was added to the wells (50 uL) and the plate was again heated to 100 C for 10 minutes during which time the colorimetric reaction proceeded. After cooling the plate for an additional 15 minutes to ambient temperature the absorbance at λ = 550 nm was determined using a SpectraMax plate reader. The concentration of Hep in Hep-SA samples was determined by linear regression of heparin standards and was then used in conjunction with Nanodrop data to determine the assembly of approximately 1:1 Hep-SA complexes.

4.5.5 Hep-SA-Apt assembly and characterization

To a PCR-tube containing SA-Hep (10-50 uL, 10uM) was added HPLC purified 5'biotin modified DNA aptamer or 5'amine modified control (1 equiv., 100 uM, 1-5 uL) obtained from Integrated DNA Technologies (IDT) and resuspended in ultrapure water. The contents were mixed briefly and the reaction was allowed to proceed for 24 hours prior to use in biological assays. The 1:1:1 conjugate (Hep-SA-19S or Hep-SA-Scr) were used immediately as crude materials following confirmation by agarose gel electrophoresis that all DNA was consumed during the assembly process. To characterize the conjugates agarose gels were cast at 1.5% (w/v) using low-EEO biology grade agarose (Millipore) dissolved in 1X Tris-borate EDTA (Life Technologies). Gels were cast in an EasyCast OWL electrophoresis chamber and run with ice cold 1X Tris-borate EDTA (Life Technologies) at 105 V for 75 minutes. Samples were loaded into wells

in 1:2 glycerol in ultrapure water to obtain a final glycerol concentration of 10% (v/v). To visualize DNA, SYBR Gold nucleic acid stain was utilized at 1X concentration in TBE for 30 minutes before images were collected on a BioRad Gel Dock system and analyzed in ImageJ.

4.5.6 Cell culture

Cells were cultured following standard tissue culture practices using reagents which unless otherwise noted were purchased from Gibco/ThermoFisher Scientific. The mouse embryonic stem cell lines were obtained as a gift from Dr. Cathy Merry, University of Nottingham UK. Wild-type E14TG2a and $Ext1^{-/-}$ cells lacking cell surface heparan sulfate were cultured under identical conditions in 5% CO_2 at 37 C. Cells were cultured on standard tissue culture treated lab plastics after being coated with 0.1% porcine gelatin (Bloom 150) in DPBS for a minimum of 10 minutes. Cell culture growth medium consisted of Knockout DMEM (Dulbecco's modified eagle medium, #10829) which was supplemented with 10% (v/v) FBS (qualified serum, origin Australia), 1% (v/v) each of L-glutamine (from 200 mM stock) and Non-essential amino acids (NEAA, 100X stock), 0.1% (v/v) of mercaptoethanol, 100 U/mL penicillin, 100 U/mL streptomycin, and 1000 U/mL LIF (ESGRO Millipore). Cells were passaged every 3-5 days as required and diluted 1:10 in growth media before plating to yield robust colony formation.

4.5.7 Cell surface remodeling

In order to remodel the cell surface with aptamer-HS chimera conjugate materials, flow cytometry was utilized. Cells were cultured until confluent under desired conditions

(general pluripotent growth or neural differentiation) before being suspended using 0.05% Trypsin-EDTA and neutralizing with media. Suspended cells are counted and aliquoted into Eppendorf tubes, with a minimum of 10^6 cells per condition. Flow cytometry was performed on live cells and as such all steps were conducted on ice. Cells were then blocked in an aptamer buffer consisting of DPBS (+Mg/+Ca) supplemented with 5mM $MgCl_2$, 0.45% glucose, and 0.1% BSA) for 1 hour on ice. During that time aptamer glycoconjugates were diluted to the indicated concentration (0-1000 nM) in aptamer buffer and cooled on ice. Cells were pelleted and mixed with the aptamer glycoconjugates for 40 minutes on ice before washing with aptamer buffer an additional three times to remove any residual unbound conjugate. The cells were then transferred to tubes for flow cytometry and anlayzed on a BD FACS Calibur or BD FAC Cantos system. A minimum of 10,000 events were collected for each sample using FACS Diva software within the appropriate gates and data were analyzed using FlowJo.

4.5.8 FGF2 Binding

In order to assess FGF2 binding activity of conjugate materials immobilized on the cell surface flow cytometry was utilized. Cells were cultured until confluent under desired conditions (general pluripotent growth or neural differentiation) before being suspended using 0.05% Trypsin-EDTA and neutralizing with media. Suspended cells are counted and aliquoted into Eppendorf tubes, with a minimum of 10^6 cells per condition. Flow cytometry was performed on live cells and as such all steps were conducted on ice. The cells are washed with DPBS and pelleted before a 30-minute blocking step on ice in aptamer binding buffer. The aptamer binding buffer consists of DPBS ($+Ca^{2+}$/$+Mg^{2+}$)

supplemented with 5mM $MgCl_2$, 0.45% glucose, and 0.1% BSA. After blocking the cells are pelleted and conjugate materials (Hep-SA, Hep-SA-19S, Hep-SA-Scr, or controls) dissolved in aptamer binding buffer to the indicated concentrations (0-1000 nM) and mixed at 0 C for 40 minutes. Cells were then washed two times with cold DPBS and blocked in 2% BSA in DPBS for 30 minutes on ice. Following blocking FGF2 (Peprotech) at 250nM concentration in 2% BSA in DPBS was added and mixed with cells for an additional 40 minutes on ice. The cells were pelleted, supernatant removed, and washed two additional times with 2% BSA in DPBS to remove residual unbound FGF2. During this time Ms anti-FGF2 (R&D Biosystems, 1:100) and Gt anti-mouse AF647 secondary (Life Technologies, 1:300) were precomplexed on ice in 2% BSA in DPBS for 30 minutes. The precomplexed FGF2 antibodies were then added to the washed cell pellets and incubated for 30 minutes on ice. Following incubation the cells were washed with DPBS once, resuspended, and transferred in fresh DPBS to tubes for flow cytometry. Flow cytometry was performed on a BD FACS Caliubur or BD FACS Cantos system running FACS Diva software. A minimum of 10,000 events was collected for each sample within the relevant gate and events were analyzed using FlowJo software.

4.5.9 FGF2 Stimulations

Stimulation experiments were performed with E14 and Ext1-/- mouse embryonic stem cells as previously described. Briefly, stem cells were cultured in 6-well tissue culture treated lab plastics at a density of 10^5 cells per cm^2 after coating with 0.1% gelatin. After approximately 12hours of growth the cells were serum starved for approximately 18 hours in mESC growth media lacking FBS. Following serum starvation, cells were washed

with DPBS and treated with 25 ng/mL recombinant human basic FGF (Peprotech) in serum-free medium with conjugate materials or heparin (Hep-SA, Hep-SA-19S, Hep-SA-Scr) at indicated concentrations for a duration of 15 min at 37C, 5% CO2. The cells were then immediately cooled on ice and lysed using a 1X RIPA lysis buffer supplemented with PMSF (1 mM) and 1X protease/phosphatase inhibitor cocktail. Lysates were analyzed by BCA assay to determine total protein concentration and 10 ug of protein was separated on a 10% SDS-PAGE gel and transferred to a polyvinylidene fluoride (PVDF) membrane for blotting. The membrane was blocked with 5% BSA/TBST for a minimum of 1 hr at room temperature prior to staining (overnight, 4C) with anti-phospho Erk, anti-total Erk, or anti-alpha tubulin (1:750, 1:1000, 1:40000 respectively in 5% BSA). After multiple TBST washes the membrane was incubated with HRP conjugated secondary antibodies (1:2000 anti-rabbit HRP and 1:10000 anti-mouse HRP, respectively) for approximately 1.5 hours at room temperature. Following a series of TBST washes the blots were visualized using Luminata Forte HRP detection reagent and imaged on a gel scanner (BioRad GelDoc). For sequential staining blots were washed in TBST, stripped using Restore PLUS western blot stripping buffer, washed again in TBST and then blocked in 5% BSA for at least 1 hr at room temperature before further staining. Images were analyzed using FIJI, where either phospho-Erk1/2 or total-Erk1/2 was normalized to alpha tubulin, before phospho-Erk was normalized to total-Erk. The levels of relative Erk phosphorylation were determined by setting the phosphorylation of Erk in samples containg $Ext1^{-/-}$ mESCs without FGF2 or conjugates to baseline.

4.5.10 Differentiation

Cells were passaged following standard protocols and plated at a density of 5000 cells/cm^2 into gelatinized 24-well tissue culture treated plates (2.0 cm^2 per well) on Day -1 of culture. Cells were plated using standard embryonic stem cell maintenance media. The next day (after approximately 12 hours) the cells were washed with DPBS once and the media exchanged for neural differentiation media. Neural differentiation (N2B27) media is composed of 49% (v/v) Neurobasal media mixed with 49% (v/v) DMEM/F12 media and supplemented with 0.98% (v/v) B27, 0.49% (v/v) N2, 0.1% mercaptoethanol, 0.25% L-glutamine, and 50 ug/mL BSA fraction V. The media is supplemented with Hep-SA-Apt conjugates or the appropriate control and subsequently filtered through a 0.2 um filter. Once media is exchanged cells continue to grow under standard tissue-culture conditions (5% CO2, 37 C). Each day D0-D4 the cells are washed with PBS and the media is replaced with fresh media containing any conjugate materials at the indicated concentrations (Hep-SA, Hep-SA-19S, Hep-SA-Scr, or Hep). On D5, the cells are removed from the incubator, rinsed with PBS, and fixed using 2% PFA on ice for approximately 10 minutes. The cells are then washed twice with ice cold DPBS and permeabilized in 0.1% TritonX-100 in DPBS for 20 min before being washed with DPBS an additional two times. After blocking in 2% BSA in DPBS for two hours at 4 C, primary antibodies were added for an additional two hours at 4 C (Oct4 #sc-25401, Alpl #AF2910, Sox1 #MAB3369) at dilutions of 1:100 in 2% BSA/DPBS. Wells were washed following primary antibody incubation three times with cold DPBS before secondary antibodies were added for 2 hours (1:1000, Life Technologies AF_{488} or AF_{647} anti-goat and anti-rabbit secondaries). Following incubation, the cells were washed again three times with cold

DPBS and Prolong Gold antifade reagent containing DAPI was used to visualize nuclei and preserve the fixed, stained samples. Well plates were imaged on a ThermoFisher EVOS imaging system or Keyence BZX800 epifluorescence microscope. A minimum of five representative images were captured for each well and experimental conditions were run in biological triplicate. Images were processed and analyzed using ImageJ software. Scale bars, unless otherwise noted are 100 um.

4.6 Acknowledgements

S.C.P. and K.G. designed the research; S.C.P., M.R.N.; N.M.; and H.J.C.N. performed the research; S.C.P., M.R.N. and K.G. analyzed data; S.C.P. and K.G. wrote the manuscript and supporting information; all authors approved the manuscript for publication. This work was supported in part by the NIH Director's New Innovator Award (NICHD: 1DP2HD087954-01). We thank the UCSD Microscopy Core Facility for assistance with fluorescence microscopy (via NINDS P30 Grant: P30NS047101) and the UCSD Glycobiology Research and Training Center. KG was supported by the Alfred P. Sloan Foundation (FG-2017-9094) and the Research Corporation for Science Advancement via the Cottrell Scholar Award (grant #24119); S.C.P. and M.R.N. were supported by a GAANN fellowship (U.S. Dept. of Education, P200A150251).

Chapter four, in full, is work in preparation for publication: Purcell, S.; Naticchia, M.R.; Marroquin, N.; Ng, H.J.C.; Godula, K. Proteoglycan chimeras selectively potentiate neural differentiation in embryonic cells. The dissertation author is the primary co-author of this work.

4.7 References

1. Varki A, Gagneux P. 2017 Biological Functions of Glycans. In: Varki A, Cummings RD, Esko JD, et al., editors. Essentials of Glycobiology 3rd edition. Cold Spring Harbor (NY): Cold Spring Harbor Laboratory Press, 2015-2017. Chapter 7. DOI:10.1101/glycobiology.3e.007.

2. Huang ML, Smith RAA, Trieger GW, Godula K. 2014 Glycocalyx Remodeling with Proteoglycan Mimetics Promotes Neural Specification in Embryonic Stem Cells. J. Am. Chem. Soc. 136, 10565–10568. DOI: 10.1021/ja505012a.

3. Purcell, S.C.; Godula. K.; Synthetic glycoscapes: addressing the structural and functional complexity of the glycocalyx. *Interface Focus*. 2018, 9, 20180080. DOI: 10.1098/rsfs.2018.0080

4. Rawat, M.; Gama, C.I.; Matson, J.B.; Hsieh-Wilson, L.C. Neuroactive chondroitin sulfate glycomimetics. J. Am. Chem. Soc. 2008, 130, 10, 2959-2961. DOI: 10.1021/ja709993p.

5. Woods EC, Yee NA, Shen J, Bertozzi CR. 2015 Glycocalyx Engineering with a Recycling Glycopolymer that Increases Cell Survival In Vivo. Angew. Chem. Int. Ed. 54, 15782–15788. DOI: 10.1002/anie.201508783.

6. Huang ML, Purcell SC, Verespy S, Wang Y, Godula K. 2017 Glycocalyx scaffolding with synthetic nanoscale glycomaterials. Biomat. Sci. 5, 1537–1540. DOI: 10.1039/c7bm00289k.

7. Griffin ME, Hsieh-Wilson LC. 2016 Glycan engineering for cell and developmental biology. Cell Chem. Biol. 23, 108–121, (doi: 10.1016/j.chembiol.2015.12.007).

8. Pulsipher, A.; Griffin, M.E.; Stone, S.E.; Brown, M.E.; Hsieh-Wilson, L.C. Directing neuronal signaling through cell-surface glycan engineering. J. Am. Chem. Soc. 2014, 136, 19, 6794-6797. DOI: 10.1021/ja5005174.

9. Pulsipher, A.; Griffen, M.E.; Stone, S.E.; Hsieh-Wilson, L.C. Long lived engineering of glycans to direct stem cell fate. Angew. Chemie. Int. Ed. 2014, 54(5), 1466-1470. DOI: 10.1002/anie.201409258.

10. Kramer JR, Onoa B, Bustamante C, Bertozzi CR. 2015 Chemically tunable mucin chimeras assembled on living cells. Proc. Natl. Acad. U.S.A.112, 12574–12579. DOI: 10.1073/pnas.1516127112.

11. Srinivasarao, M.; Low, P.S. Ligand-targeted drug delivery. Chem. Rev. 2017, 117 (19), 12133-12164. DOI: 101.1021/acs.chemrev.7b00013.

12. Keefe, A.D.; Pai, S.; Ellington, A. Aptamers as therapeutics. Nat. Rev. Drug Discovery. 2010, 9, 537-550. DOI: 10.1038/nrd3141.

13. Hou, Z.; Meyer, S.; Propson, N.E.; Nie, J.; Jiang, P.; Stewart, R.; Thomson, J.A. Characterization and target identification of a DNA aptamer that labels pluripotent stem cells. Cell Res. 2015, 25(3), 390-393. DOI: 10.1038/cr.2015.7.

14. Porell R.; Follmar J.; Purcell, S.; Timm B.; Laubach, L.; Kozirovskiy, D.; Thacker, B.; Glass, C.; Gordts, P.L.S.M.; Godula, K. Development of biologically derived neoproteoglycans for protein binding and functional bioassays. BioRxiv. 2022.

15. Delgadillo, R.F.; Mueser, T.C.; Zaleta-Rivera, K.; Carnes, K.A.; Gonzalez-Valdez, J.; Parkhurst, L.J. Detailed characterization of the solution kinetics and thermodynamics of biotin, biocytin, and HABA binding to avidin and streptavidin. PloS ONE. 2019, 14(2), e0204194. DOI: 10.1371/journal.pone.0204194.

16. Pevny, L.H.; Sockanathan, S.; Placzek, M.; Lovell-Badge, R. A role for SOX1 in neural differentiation. Development. 1998, 125(10), 1967-1978. DOI: 10.1242/dev.125.10.1967.

17. Trieger, G.W.; Verespy, S.; Gordts, P.S.L.M.; Godula, K. Efficient synthesis of heparinoid bioconjugates for tailoring FGF2 activity at the stem cell-matrix interface. Bioconjugate Chem. 2019, 30(3), 833-840. DOI: 10.1021/acs.bioconjchem.8b00921.

18. Green, N.M. A spectrophotometric assay for avidin and biotin based on binding of dyes by avidin. Biochem J. 1965, 94, 23-24. DOI: 10.1042/bj0940023c.

19. Pickford, C.E.; Holley, R.J.; Rushton, G.; Stavridis, M.P.; Ward, C.M.; Merry, C.L.R. Specific glycosaminoglycans modulate neural specification of mouse embryonic stem cells. Stem Cells. 2011, 29(4), 629-640. DOI: 10.1002/stem.610.

4.8 Supporting Information

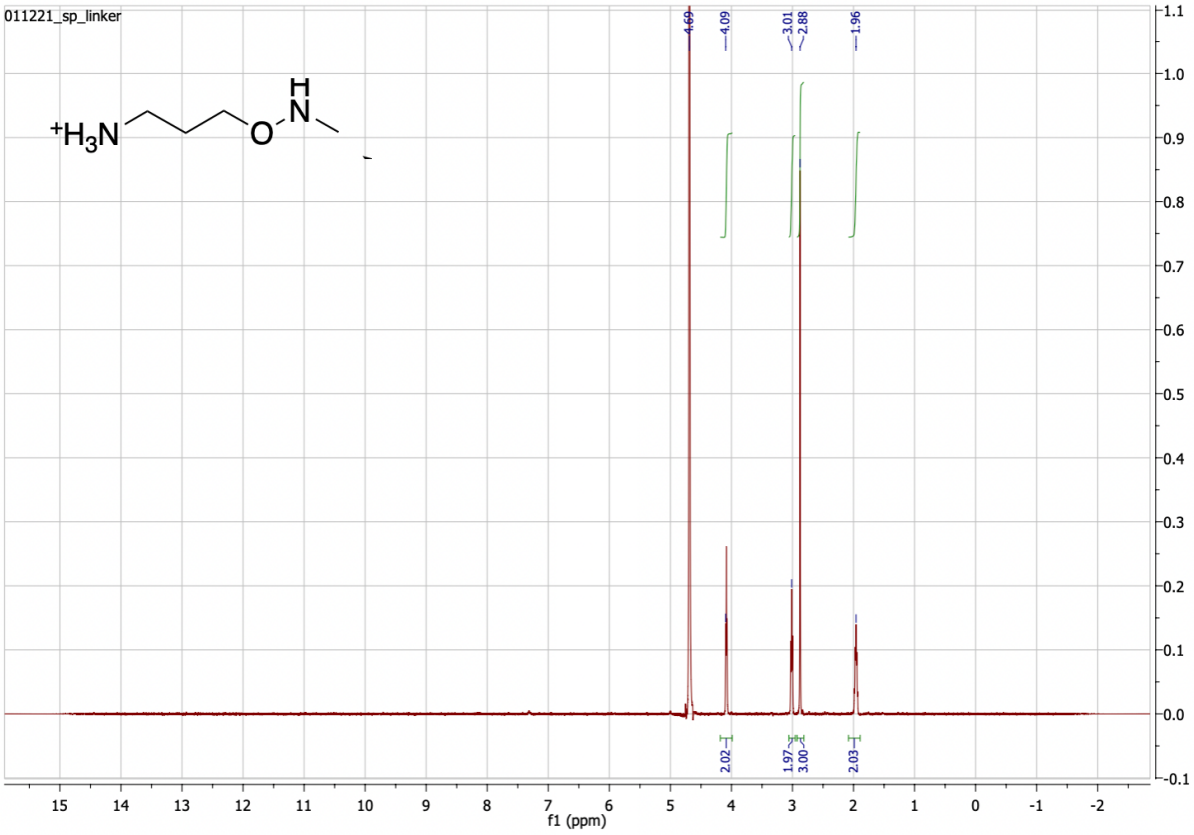

Figure 4.S1 ^{1}H NMR spectra of N-methylaminooxy linker for heparin prefunctionalization.

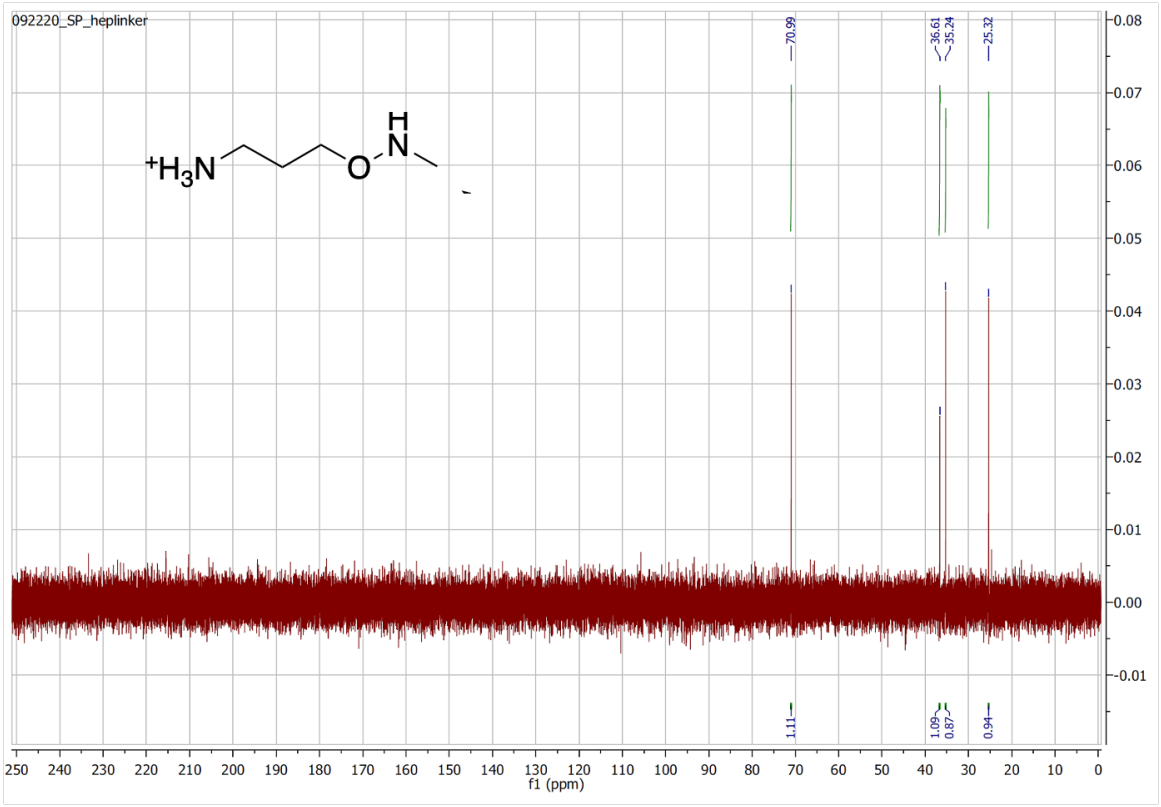

Figure 4.S2 ^{13}C NMR spectra of N-methylaminooxy linker for heparin prefunctionalization.

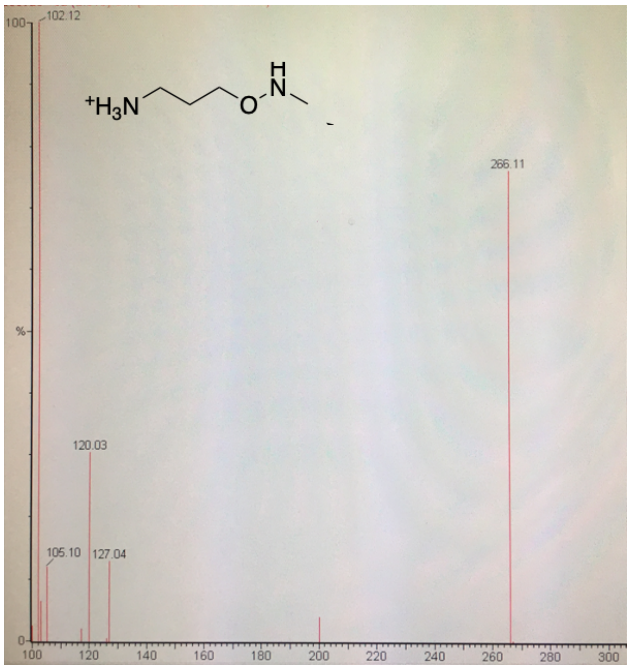

Figure 4.S3 ESI-MS spectrum of N-methylaminooxy linker for heparin prefunctionalization.

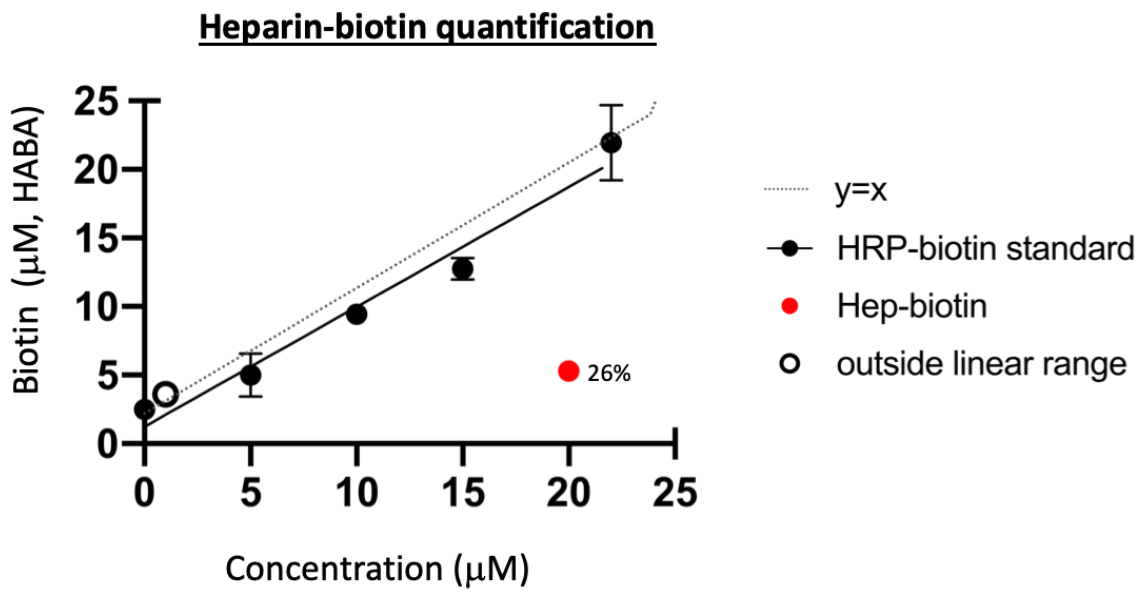

Figure 4.S4 HABA assay used to quantify degree of heparin biotinylation. Standard solutions of HRP-biotin were used as a reference at varying dilution (concentration of standard adjusted by degree of biotin labeling, 5 biotin/HRP per manufacturer). Quantitative biotinylation is shown as a dotted line of slope y = x, and the linear range for the assay was identified using the standard. Hep-biotin diluted to a known concetration (20 uM) was determined to be contain approximately 26% end-biotinylation (shown in red).

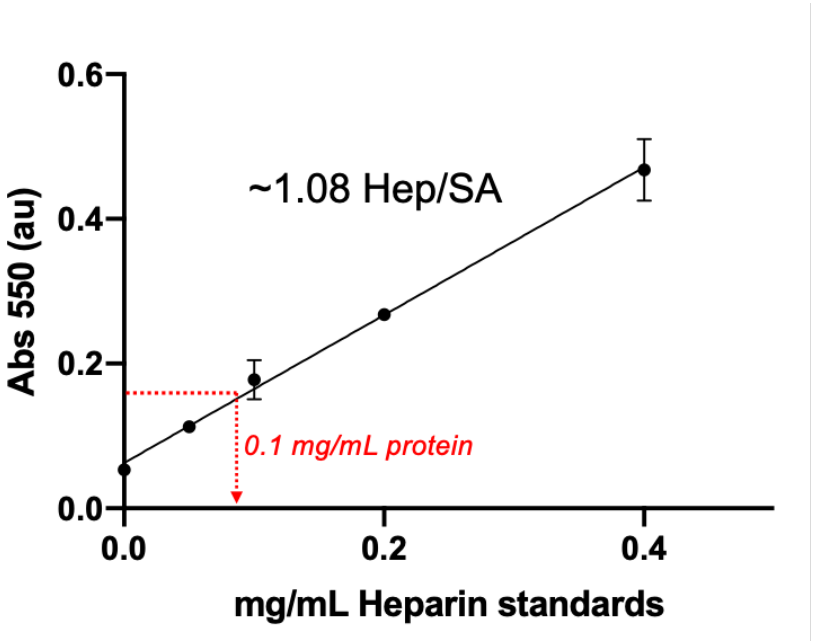

Figure 4.S5 Carbazole assay to determine extent of Hep-SA assembly. Standard solutions of heparin were prepared and absorbance at λ = 550 nm was monitored following carbazole reaction to quantify heparin content. Hep-SA prepared at known concentration (0.1 mg/mL) protein was also subjected to the carbazole reaction and the absorbance at λ = 550 nm was utilized to determine the degree of Hep-SA bioconjugation to be approximately 1.08 heparin per SA protein core.

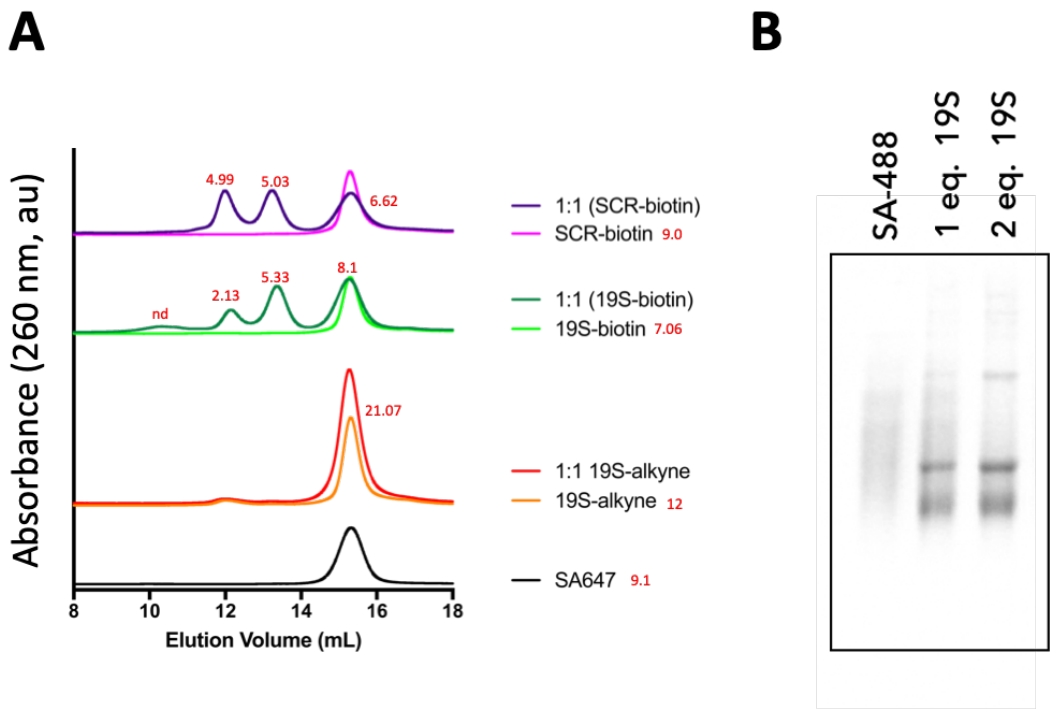

Figure 4.S6 Optimization of Hep-SA-Apt assembly. In order to determine the optimal strategy for assembling the aptamer-HS chimeras, biotin modified aptamers and biotinylated heparin were added either sequentially or simultaneously. To assess the order of sequential addition (A) fast protein liquid chromatography on a Superdex 200 Increase 300/10 column was utilized to determine if 1:1 SA-Apt conjugates could be assembled and isolated by isocratic elution with DPBS. SA_{647} could be detected during elution at λ = 260nm due to spectral overlap with the λ = 280 nm protein peak. A control Apt19S eluted as a single peak at approximately 15 mL and when mixed 1:1 with SA_{647} no conjugate formation was observed, demonstrating specificity for biotin modified DNA. Biotinylated aptamer 19S and control aptamer SCR were mixed 1:1 with SA_{647} and the formation of new conjugate peaks was observed. Integrations for all peaks are shown in red in arbitrary units and were used to determine the ratios of 1:1 and 2:1 conjugates in the crude mixtures. (B) Native PAGE was utilized to corroborate FPLC findings. A 10% native Tris-Gly gel was run for 45 min at 160V and visualized on a BioRad Gel Doc system. Lanes: SA_{488}, crude mixture of SA_{488} and Apt19S-biotin (1:1), crude mixture of SA_{488} and Apt19S-biotin (1:2). Multiple conjugate bands can be seen in the crude reaction mixture, indicating that DNA is complexed with SA at varying ratios.

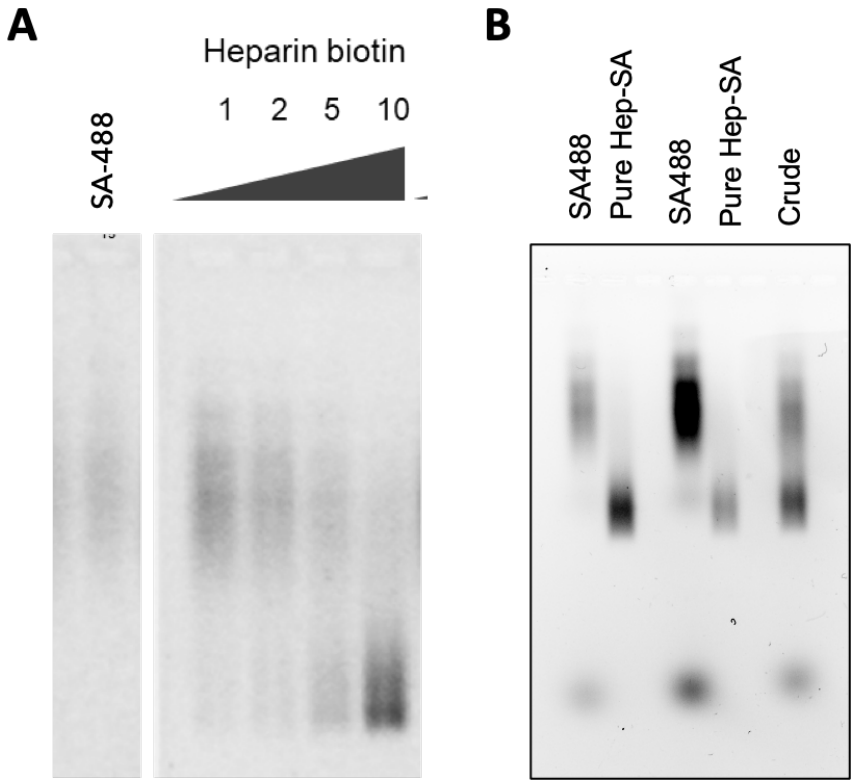

Figure 4.S7 Agarose gel electrophoresis of Hep-SA conjugates. Agarose gel electrophoresis (1.5% agarose w/v in 1x TBE, 105V, 75min) was utilized to determine the optimal conditions for generating 1:1 Hep-SA conjugates and to confirm purification of the Hep-SA material before addition of Apt-19S or Apt-Scr. Gels were imaged using a BioRad Gel Doc system set to detect the AF_{488} reporter on the conjugates. (1) SA_{488} was mixed with increasing number of equivalents of heparin biotin (~26% biotinylated) ranging from 1-10 equivalents. A mobility shift is observed for the SA_{488} beginning with 5 equivalents of heparin biotin. (B) Purified Hep-SA was analyzed by agarose gel. SA_{488} starting material shows a small band corresponding to free fluorophore which is purified away during dialysis. Excess SA488 present in the crude reaction is also purified away during this process.

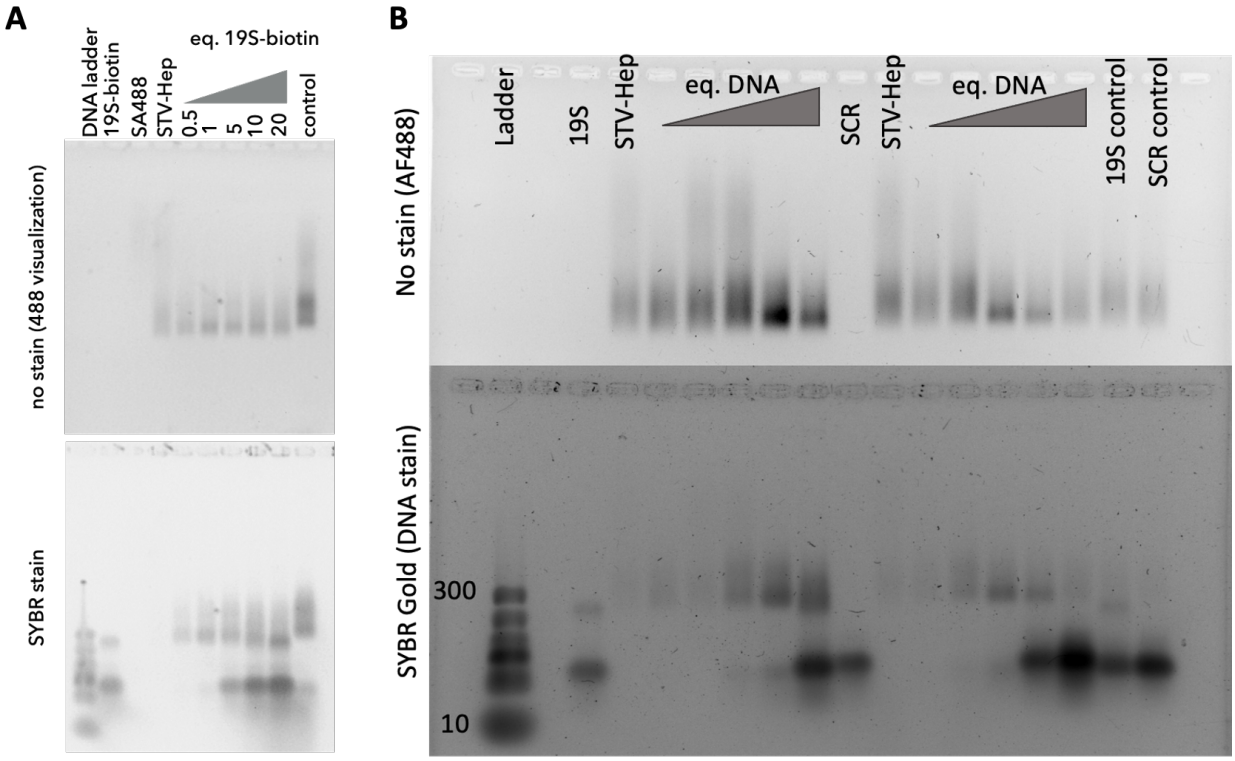

Figure 4.S8 Optimization of DNA aptamer coupling to Hep-SA. Agarose gel electrophoresis (1.5% agarose w/v in 1x TBE, 105V, 75min) was utilized to determine the optimal conditions for generating 1:1:1 Hep-SA-Apt conjugates. (A) Hep-SA (STV-Hep) was mixed with increasing equivalents of aptamer 19S-biotin, resulting in a modest mobility shift and consumption of the aptamer band. A control coupling in which aptamer lacked biotin modification did not result in the mobility shift or consumption of the DNA band. (B) An analogous agarose gel was run with both aptamer 19S and aptamer scramble SCR, where similar assembly efficacy was observed. Gels were visualized both without staining (to detect SA protein core) and after 30 min of staining with SYBR Gold nucleic acid stain to visualize the aptamer or scramble sequences.

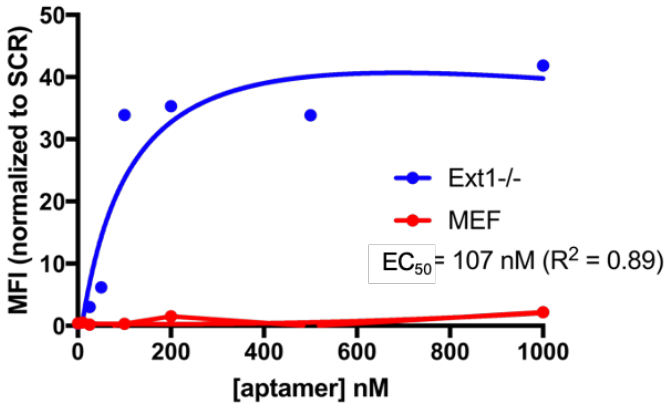

Figure 4.S9 Aptamer 19S binds mouse embryonic stem cells selectively at nanomolar concentrations. To validate the ability of Apt19S to bind selectively to pluripotent stem cells expressing alkaline phosphatase (Alpl), flow cytometry was performed. Ext1$^{-/-}$ mouse embryonic stem cells (expressing Alpl) or mouse embryonic fibroblasts (MEF, not expressing Alpl) were treated with biotinylated aptamer or scramble control for 40 minutes on ice. Streptavidin 488 conjugate was utilized to visualize cell surface bound aptamer and samples were analyzed on a BD FACS Calibur flow cytometer. Ext1$^{-/-}$ cells show robust aptamer binding relative to a scramble control sequence (EC_{50} = 107 nM, R^2 = 0.89) while MEFs do not show binding to the aptamer above scramble background.

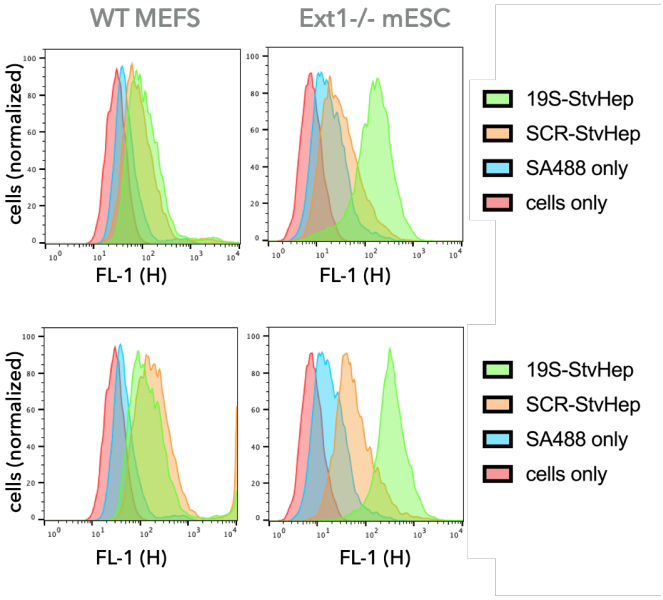

Figure 4.S10 Hep-SA-Apt conjugates capable of cell specific glycocalyx engineering. WT MEF cells (not expressing Alpl) or Ext1$^{-/-}$ mouse embryonic stem cells (expressing Alpl) were remodeled with Hep-SA-19S, Hep-SA-Scr, or SA alone at a concentration of 25 nM in suspension. Flow cytometry was utilized to determine the extent to which the cell surface was modified with the fluorescent conjugates. Histograms show that for MEF cells only a small shift is observed in fluorescence due to background binding of the materials whereas Ext1$^{-/-}$ cells remodeled with the Hep-SA-19S conjugate show a dramatic increase in fluorescence due to immobilization of the conjugate on the cell surface. Hep-SA-Scr also results in some background binding to the Ext1$^{-/-}$ cell surface, likely due to nonspecific interactions between Hep and cell surface proteins. Histograms are shown in biological duplicate, with each sample containing a minimum of 10,000 gated events.

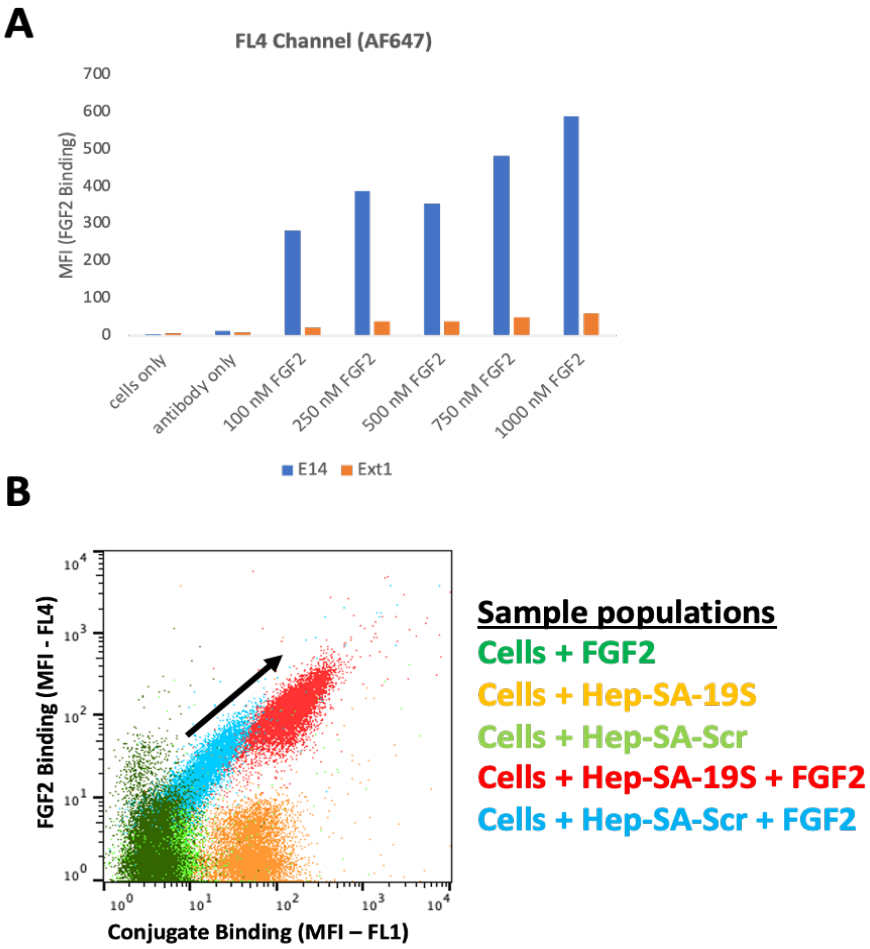

Figure 4.S11 Optimization of FGF2 binding to surface bound Hep-SA-19S. (A) To determine the optimal FGF2 concentration for cell surface binding E14 or Ext1$^{-/-}$ cells were incubated with FGF2 at increasing concentrations (0 – 1000 nM) prior to detection with a fluorescently labeled antibody precomplex by flow cytometry. Robust binding of FGF2 to HS on the cell surface was observed for E14 cells at all concentrations evaluated with minimal background binding to Ext1$^{-/-}$ cells lacking cell surface HS. 250 nM FGF2 was selected for subsequent studies in order to ensure adequate binding for detection by flow cytometry while minimizing reagent use. (B) Additional biological replicate data showing Hep-SA-19S dependent FGF2 activity at 50 nM by two color flow cytometry (FL1 = AF488, FL4 = AF647). Conjugate binding is shown as a measure of AF488 fluoresence on the x-axis while FGF2 binding is shown as a measure of AF647 fluorescence on the y-axis. Ext1-/- cells treated with FGF2 show little AF488 or AF647 signal. Addition of Hep-SA-19S but no FGF2 results in an increase in AF488 but not AF647 fluorescence while Hep-SA-Scr results in no change. Addition of Hep-SA-19S and FGF2 results in an increase in both AF488 and AF647 signal, associated with binding of FGF2 to surface bound conjugate. Hep-SA-Scr shows some non-specific FGF2 binding, likely due to the high affinity of FGF2 for HS and the presence of some non-specific surface bound conjugate.

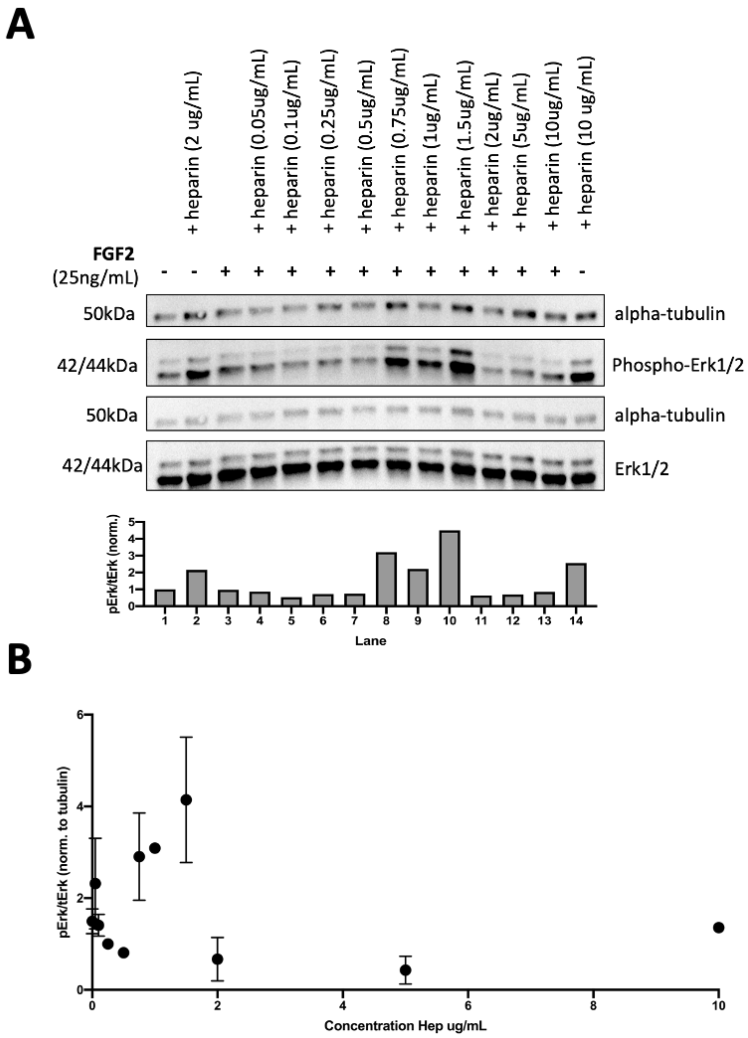

Figure 4.S12 FGF2 Stimulation of Ext1$^{-/-}$ cells in the presence of soluble heparin to identify effective concentration range for stimulation with Hep-SA-Apt conjugates. (A) Western blot analysis following FGF2 stimulation shows soluble heparin increase Erk1/2 phosphorylation in a narrow window between 0.5 – 1.5 ug/mL. Erk phosphorylation was quantified by densitometry and is shown as the ratio of pErk1/2 over Erk1/2 normalized to an alpha-tubulin loading control. (B) Aggregated densitometry analysis from three western blot experiments to demonstrate that this range occurs between 0.5 and 1.5 ug/mL under the experimental conditions evaluated and is not an artifact of the western blot. Note that despite the variability in densitometry this trend was consistent and suggests that Hep-SA-Apt which has enhanced affinity for the embryonic cell surface may be suitable for stimulation at concentrations at or below that of soluble heparin.

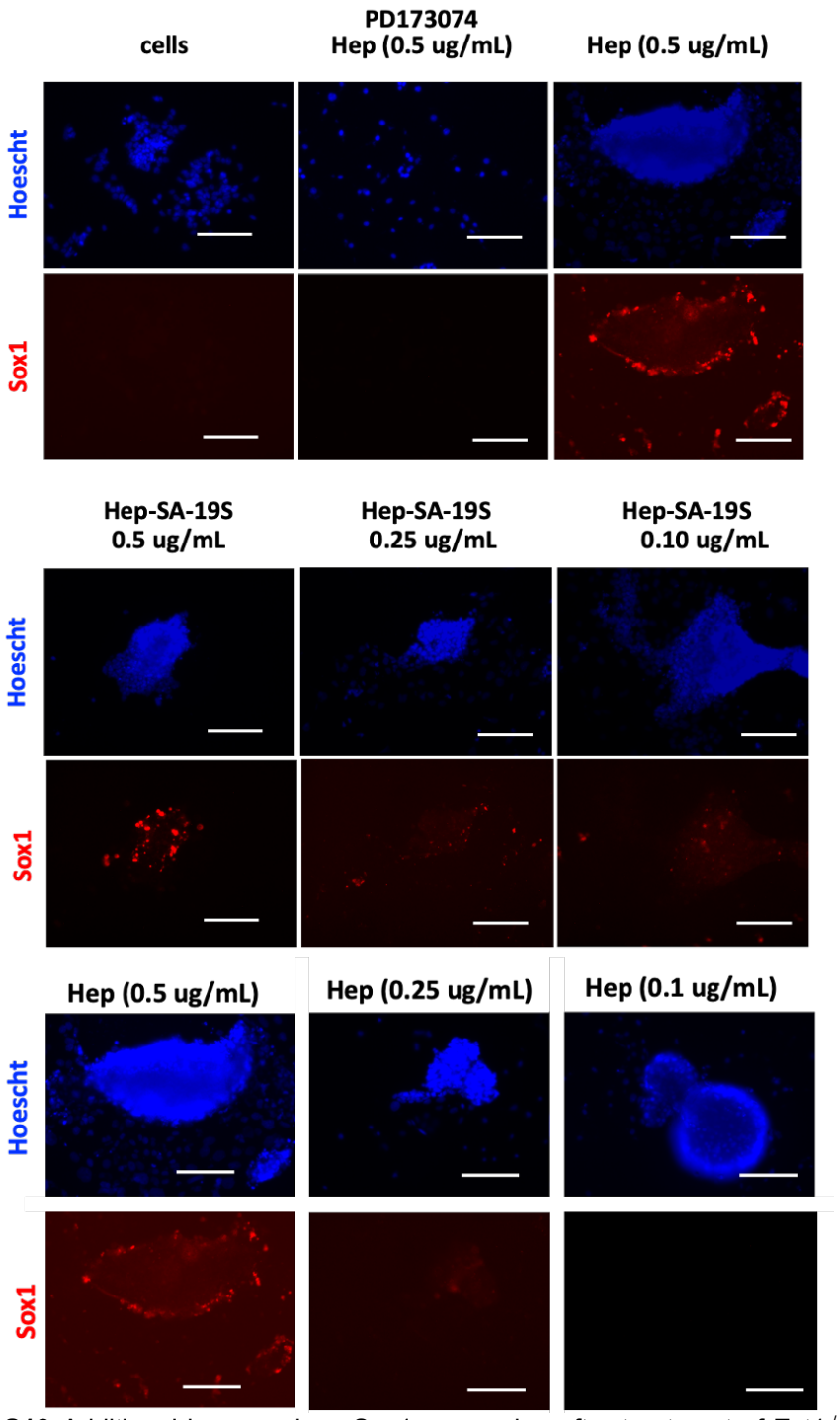

Figure 4.S13 Additional images show Sox1 expression after treatment of Ext1$^{-/-}$ mouse embryonic stem cells with soluble heparin. Ext1$^{-/-}$ cells lacking cell surface HS do not express Sox1 after 5 days of differentiation in neurobasal medium. Addition of 0.5 ug/mL soluble heparin results in neuroectodermal differentiation, as shown by the onset of Sox1 expression. Addition of soluble heparin in the presence of small-molecule inhibitor PD173074 does not result in onset of Sox1 expression. Minimal Sox1 expression is observed in a the 0.25 ug/mL heparin condition and no expression is observed at 0.1 ug/mL, unlike that of Hep-SA-19S, which showed modest Sox1 expression at 0.1 ug/mL. Scale bars = 100 um.

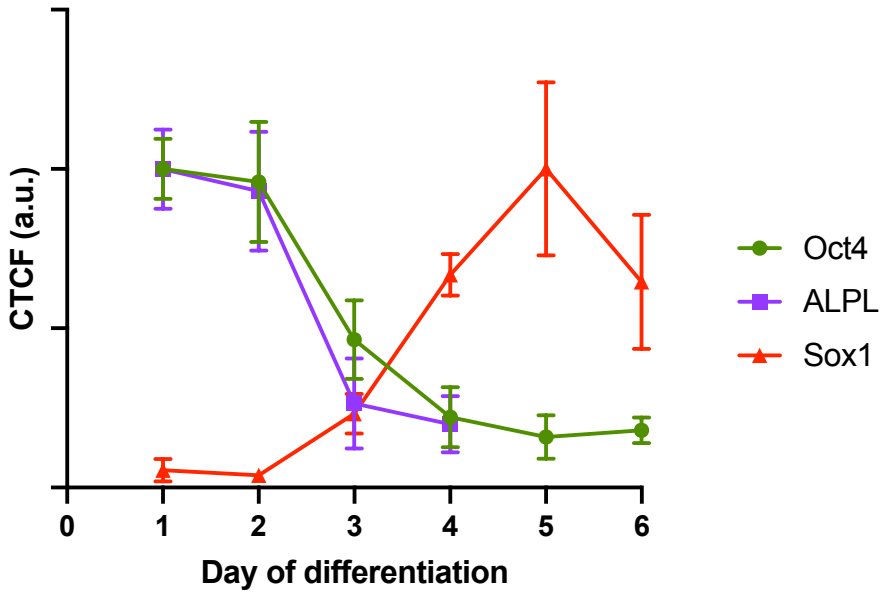

Figure 4.S14 E14TG2a (E14) wild type mouse embryonic stem cells express embryonic markers Oct4 and Alpl early in neural differentiation and neural marker Sox1 is expressed later in differentiation, similarly to that of Ext1$^{-/-}$ cells

5 Complementary glycocalyx engineering approaches and conclusions

Collectively, I present in Chapters 2-4 methods for glycocalyx engineering which expand the existing toolset to enable spatial programming of multiple glycoconjugates within a synthetic glycoscape, photopatterning and dynamic glycocalyx engineering with light-responsive mucin mimetics, and aptamer guided HS chimeras to remodel the glycocalyx with cell-type and embryonic-stage specificity. In this chapter, I highlight complementary efforts to generate covalent glycoconjugates for cell surface engineering and early efforts to assess the viability of using synthetic glycopolymers bearing membrane anchors *in vivo*.

5.1 General approaches to glycocalyx engineering

Strategies for glycocalyx engineering can be generally categorized as chemical and chemoenzymatic, genetic, and materials-based (Figure 5.1). Recent innovations in chemoenzymatic glycocalyx engineering have enabled the selective degradation of native glycocalyx structures, including for example, mucin protease StcE which recognizes and cleaves specific peptide and glycan motifs.[1] While these approaches result in a glycocalyx composed largely of native biological structures (as opposed to synthetic mimetics) that are modified by exogenous enzymes it is difficult to control precisely the composition and spatial distribution of glycans. Genetic engineering of target cells, including glycosylation enzyme knockout, improve upon these methods by imparting control over cell type modified but are primarily used to remove structures from the glycocalyx. The combination of genetic approaches with materials-based approaches

in which well-defined synthetic materials are introduced in combination with knockout models[2] or knock-in of protein anchors[3] is a particularly powerful combination. The assembly of chimeric glycoconjugates in which engineered membrane anchors are expressed under a cell or stage-specific promoter may enable greater specificity than currently possible. Materials based approaches in which synthetic or semi-synthetic glycomaterials are introduced *de novo* into the cellular glycocalyx allow for enhanced control over glycan composition and distribution, but glycomaterials with some exceptions[4] only approximate the structures of native glycoconjugates. Even so, this glycocalyx engineering approach enables temporal control over glycocalyx composition and materials can be designed to incorporate responsive functionalities or targeting elements.

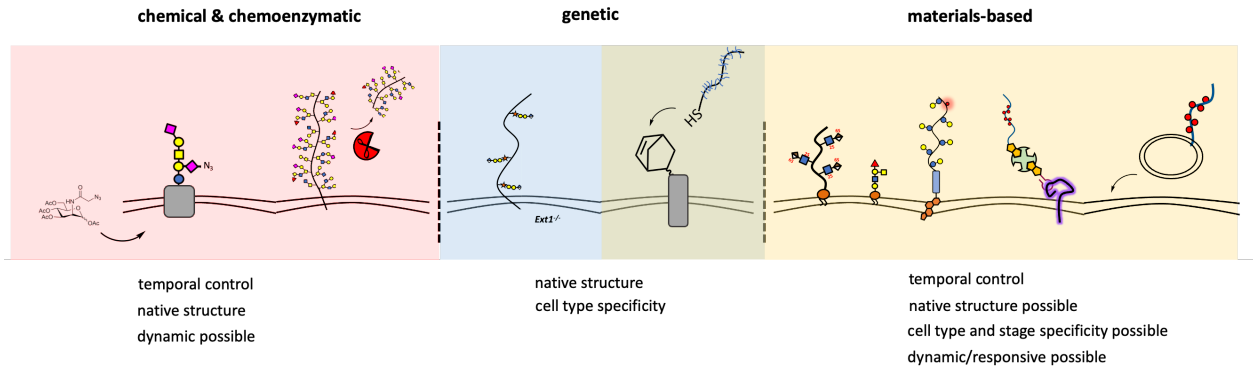

Figure 5.1 Innovations in glycocalyx engineering. Several approaches have emerged for glycocalyx engineering on living cells each with unique advantages including chemical and chemoenzymatic, genetic, and materials based. Chemical and chemoenzymatic approaches including incorporation of unnatural sugars into the native glycocalyx bearing functional handles and the use of enzymes to selectively remove glycocalyx structures offer the ability to rapidly modify the glycocalyx with temporal control and result in native glycocalyx structures being minimally modified. Genetic approaches allow for complete or partial knockout of glycocalyx structures with enhanced specificity but require significant manipulation of cells, potentially limiting some applications. Materials based approaches offer the ability to tailor the glycocalyx de novo with native-like structures. Methods to generate responsive and selective glycoconjugates are described here and offer more precise control over the glycocalyx and associated bioactivity. The combination of genetic and materials- based approaches is particularly useful as it allows for both the selective removal and addition of glycocalyx structure simultaneously and can be used to enhance glycomaterial selectivity.

5.2 Covalent glycopolymer conjugates for targeted glycocalyx engineering

An alternative strategy for aptamer targeted glycocalyx engineering was explored whereby synthetic azidoglycocpolymers modified with either HepIA disaccharides or a control 6O-sulfated GlcNac were covalently linked to DBCO modified aptamers via SPAAC (Figure 5.2). The synthesis of short azidoglycopolymers by RAFT polymerization was achieved as previously reported.[5] To link the glycopolymers to DNA aptamers, 5'-amine modified aptamers were purchased from Integrated DNA Technologies and DBCO functionalized via a sulfo-NHS DBCO linker (Figure 5.2). The DBCO-aptamers were purified on Nap columns (GE Healthcare) and the extent of DBCO modification was confirmed by UV-Vis spectroscopy before the click reaction was performed at elevated temperature for 48 hours.

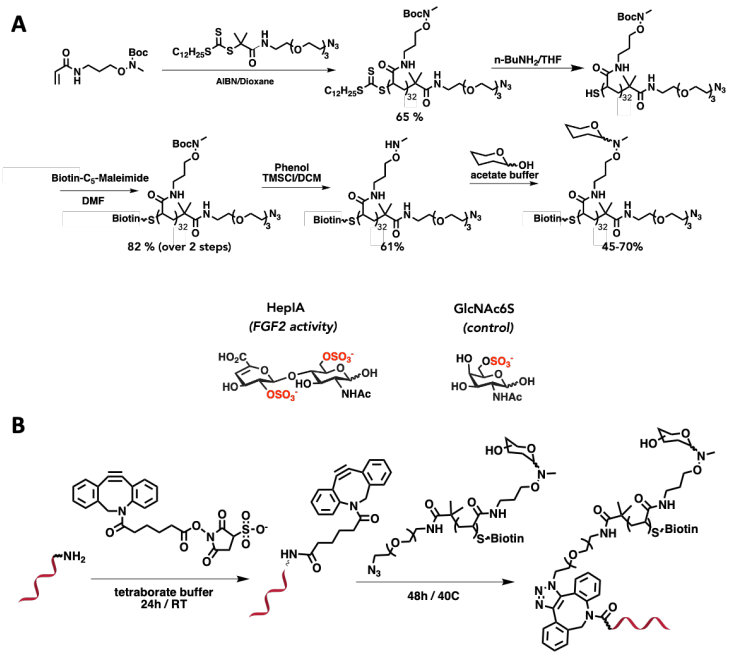

Figure 5.2 Covalent DNA-glycopolymer hybrids. (A) General synthesis of heparan-sulfate proteoglycan mimetics bearing either bioactive HepIA disaccharide side chains or control 6-O-sulfated GlcNAc side chains. Glycopolymers are labeled with biotin to be used as a reporter in subsequent assays. (B) Amine-modified DNA oligonucleotide are prepared for SPAAC reaction with azide bearing glycopolymers by modification with a strained cyclooctyne.

To assess the efficacy of the reaction agarose gels (3% w/v, in 1X Tris acetate EDTA) were used to resolve the reaction mixture and DNA was visualized by ethidium bromide staining. Indeed, the reaction resulted in the formation of a new band with less mobility in the gel and some consumption of the DBCO-modified aptamer band, indicative of a larger conjugate assembly being formed (Figure 5.3). To assess whether copper-catalyzed click chemistry could be used to generate aptamer glycopolymer conjugates in greater yield, 5'-hexynyl aptamer sequences were obtained from Integrated DNA Technologies and the click reaction was performed in the presence of $CuSO_4$, TBTA, and sodium acsorbate. The CuAAC conjugation also proceeded to generate a new band, however significantly less consumption of the DNA band and formation of a new conjugate band was observed, and as such SPAAC was used to generate the glycoconjugates.

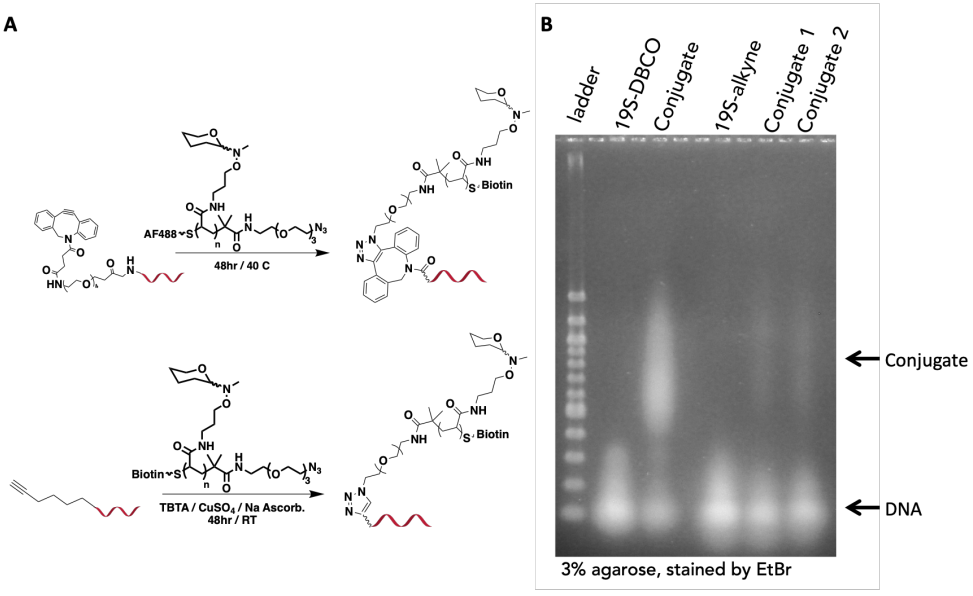

Figure 5.3 Click reaction of DNA aptamer with glycopolymers. (A) Aptamers functionalized at their 5' end with either a DBCO or alkyne functional group can be clicked to azidoglycopolymers to generate aptamer glycoconjugates. (B) Agarose gel used to characterize click reaction products. Lanes: DNA Ladder (Ultra-Low MW 50bp), 19S-DBCO, crude SPAAC conjugate, 19S-alkyne, crude CuAAC conjugate (lane run in duplicate). Ethidium bromide was used to visualize DNA, and a mobility shift is observed in conjugate lanes. Notably, the SPAAC reaction resulted in a greater conversion of DNA to conjugate than the CuAAC reaction.

Because the conjugation reaction did not proceed to completion under the conditions evaluated, it was necessary to isolate the aptamer-glycopolymer conjugate from excess unmodified aptamer, which would likely out-compete the conjugates in cell surface binding experiments. Having established differential mobility of the two materials in agarose gel and owing to the large difference in molecular weight (>15 kDa) of the aptamer glycopolymer conjugate, size exclusion chromatography (SEC) showed promise as a purification strategy. SEC was performed on a Superdex200 Increase Sepharose column, resulting in the observation of a new conjugate peak in crude reaction samples (Figure 5.4A, fraction B) that when run on agarose gel alongside the crude mixture corresponded to the broad conjugate band. By collecting small fractions and pooling sequential runs, purified conjugates could be isolated (Figure 5.4B, left), though this process was very low yielding (< 10% for HepIA glycopolymer conjugates). The formation of aptamer glycopolymer conjugates by SPAAC could also be assessed by change in polymer mobility on agarose gel (3% w/v prepared in 1% Tris-acetate EDTA) using streptavidin-488 to visualized the polymer (Fig 5.4B, right). In the case of glycopolymer conjugates prepared using GlcNAc glycopolymers, a large increase in mobility is observed upon ligation of the negatively charged DNA to the glycopolymer. Negatively charge GlcNAc-6S glycopolymers which already exhibit strong mobility in the gel show a slight increase upon addition of the negatively charged DNA. Importantly control reactions in which each polymer was mixed with amine modified DNA (no DBCO present) result in no change in mobility, indicating that the conjugates were not being formed via non-covalent interactions between the DNA aptamer and glycopolymer.

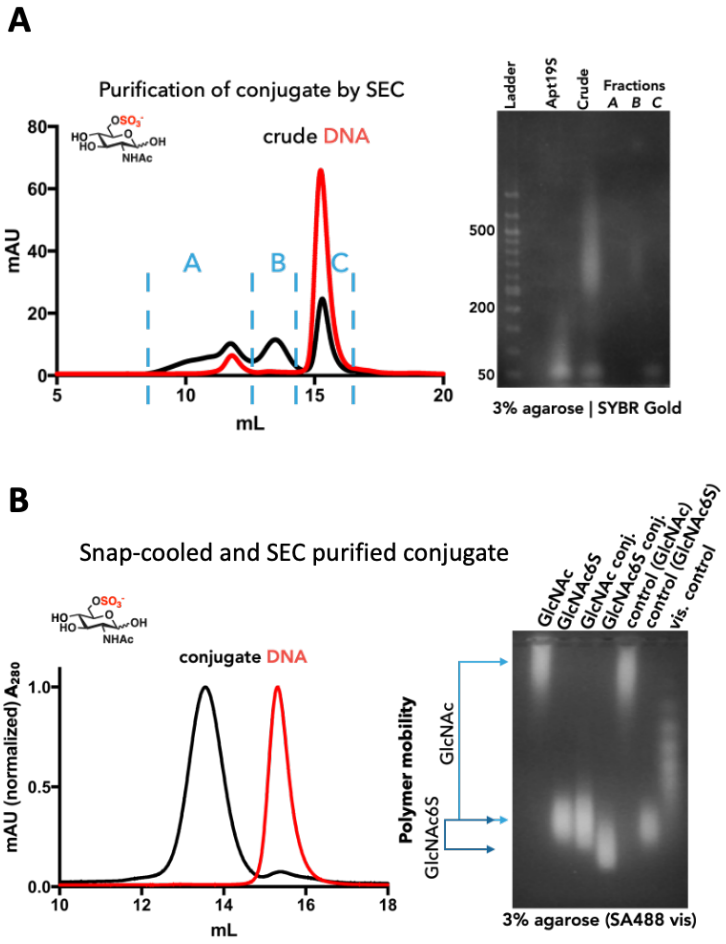

Figure 5.4 Purification of aptamer glycoconjugates. (A) Size exclusion chromatography was utilized to purify crude aptamer glycoconjugates afforded by SPAAC reaction of a GlcNAc6S azidoglycopolymer and Apt19S, resulting in the generation of a new peak in fraction B. Agarose gel analysis of isolated fractions and staining with ssDNA dye SYBR Gold confirms that fraction B contains the high-MW aptamer glycopolymer conjugate. (B) Snap-cooling of the aptamer sequence results in a single aptamer peak and pooled conjugate from fraction B shows a clear mobility shift during SEC corresponding to an increase in molecular weight following conjugation. Visualization of the polymer on agarose gel by streptavidin-AF_{488} staining shows changes in glycopolymer mobility associated with the increased negative charge following conjugation to DNA aptamers. Control reactions with aptamers lacking the DBCO handle do not result in shifted mobility.

Having isolated pure aptamer-glycopolymer conjugates by size exclusion chromatography, albeit in low yield, we next sought to assess their ability to bind to the surface of cells expressing their target, Alpl (Figure 5.5). To do so, a model system consisting of both $Ext1^{-/-}$ mouse embryonic stem cells (which express pluripotency marker Alpl) and differentiated mouse embryonic fibroblasts (which do not express pluripotency

marker Alpl in high levels) were suspended and treated with the glycopolymer conjugates. Both functional aptamer-19S glycopolymer conjugates and a control conjugates containing the scrambled sequence were evaluated in both cell types with both GlcNac-6S and Hep-IA glycopolymer conjugates. Guided by previously observed binding data for the aptamer 19S[6], 200 nM was selected as the concentration at which cells would be remodeled. After a 40-minute incubation, cells were washed with DPBS and streptavidin-488 (2') was utilized to detect the surface-bound glycopolymer conjugates via their biotin end-labels. First, in the case of GlcNAc-6S conjugates we observed strong immobilization of the GlcNAc6S-19S conjugate on the cell surface with approximately 10-fold greater signal than the scramble control, though some background binding was observed. No apparent change in cell fluorescence was observed for the MEF cells indicating a lack of immobilized glycoconjugate. Hep-IA glycopolymer conjugates similarly exhibited a nearly four-fold increase in cell fluorescence over the scramble control and significantly less background binding of the HepIA-SCR conjugate was observed than in the case of GlcNAc-6S- SCR. Again, no apparent change in MEF cell fluorescence indicates a lack of immobilized glycopolymer conjugates on the cell surface. These data suggest the suitability of the glycopolymer aptamer conjugate system for cell-type specific glycocalyx engineering.

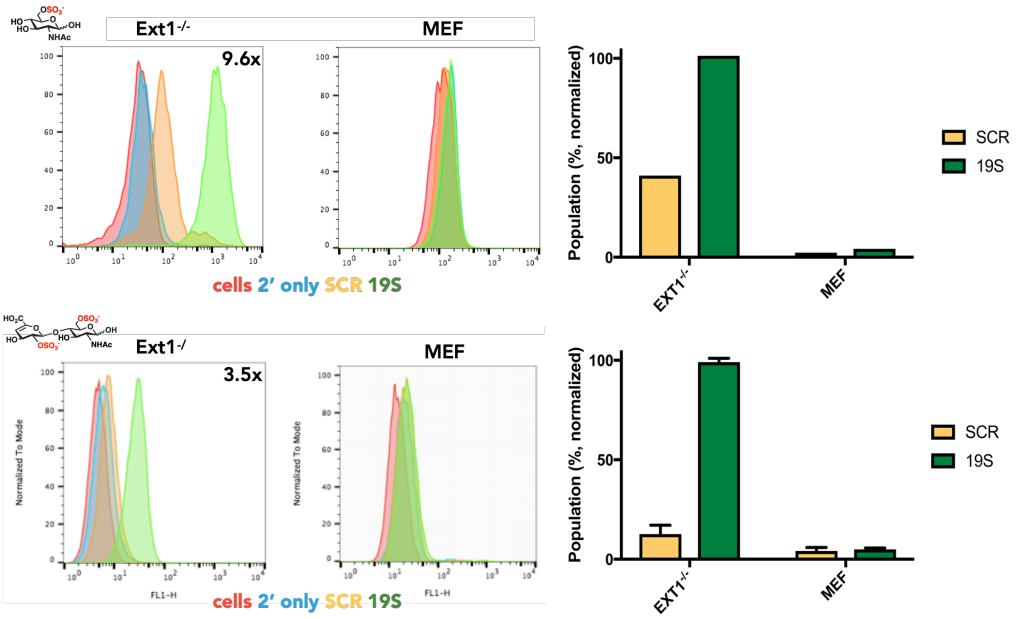

Figure 5.5 Cell-type specific glycocalyx engineering with aptamer glycoconjugates assessed by flow cytometry. Histograms show populations of *Ext1*$^{-/-}$ mESCs and MEF cells (red), treated with streptavidin-488 (2', blue) for visualization, and either SCR-glycopolymer (yellow) or 19S-glycopolymer (green) conjugates at 200 nM. An approximately 10-fold increase in fluorescence is observed for stem cells remodeled with aptamer-19S GlcNac6S conjugates over a scramble control, while no increase is observed in mouse embryonic fibroblasts lacking the aptamer target. The same glycocalyx engineering strategy utilizing HepIA bearing glycopolymers resulted in a 3.5-fold increase in fluorescence of aptamer-19S conjugate over the scramble control, while no increase was observed in mouse embryonic fibroblasts lacking the aptamer target.

Next, we sought to demonstrate the bioactivity of the glycopolymers toward FGF2 by ELISA assay (Figure 5.6) as previously reported.[7] FGF2 was immobilized in well plates and increasing concentrations of GlcNAc-6S or HepIA glycopolymers with biotin end-labels were bound to the immobilized FGF2. Following several washes, streptavidin-HRP was used to detect polymer bound to the immobilized FGF2 in combination with TMB substrate. We observed robust binding of the HepIA to FGF2 (EC_{50} = 1.4 nM) and benchmarked the assay to a biotinylated heparin control (EC_{50} = 7.6 nM). Importantly the GlcNAc-6S control polymer did not bind to FGF2.

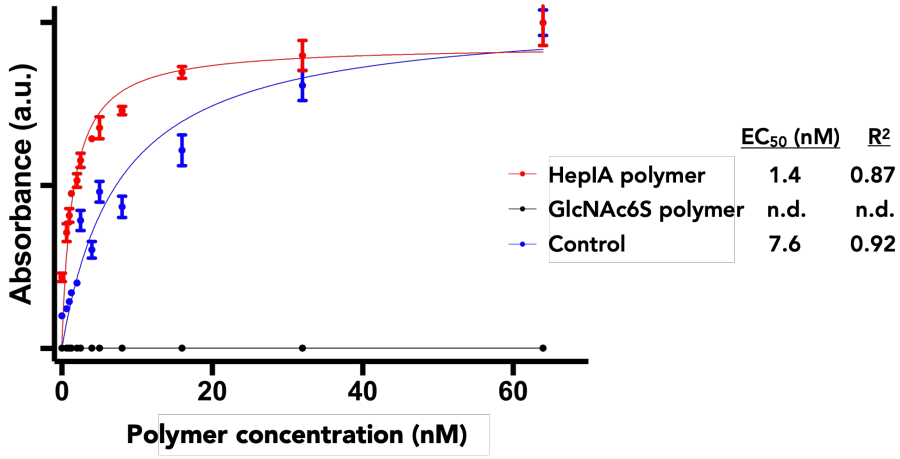

Figure 5.6 FGF2 binding activity of glycopolymers. HepIA glycopolymers show strong binding affinity for FGF2 (EC_{50} = 1.4 nM) while GlcNAc6S glycopolymers do not bind to FGF2, as determined by ELISA. A control with known FGF2 binding activity consisting of biotinylated heparin was used to benchmark the assay (EC_{50} = 7.6 nM).

While this approach shows promise as a method for cell-type specific glycocalyx engineering, it was ultimately limited by the poor conjugation efficiency the aptamer and glycopolymer. Linking a large, highly negatively charged glycopolymer (such as the HepIA bearing RAFT polymer) to a large, highly negatively charged biomacromolecule (DNA aptamer) presented numerous challenges in both conjugation and purification which together limit the applicability of this approach. Unsurprisingly, we observed decreasing conjugation efficiency with increasing negative charge of the glycopolymer component. Efforts to screen the negatively charged molecules with high salt (3M NaCl) did not improve efficiency. The feasibility of covalent aptamer-glycopolymer hybrids for cell-specific glycocalyx engineering will depend on improved methods for the bioconjugation of the aptamer and glycopolymer domains.

5.3 Covalent heparin conjugates for glycocalyx engineering

Another approach for the covalent assembly of DNA-glycoconjugates for targeted glycocalyx engineering involves the use of a protein core from which biologically derived or well defined glycans are displayed and to which a targeting element can be covalently appended. Heparinoid bioconjugates have previously been shown to tailor FGF2 activity at the cell surface, and as such BSA-heparin conjugates are well suited to this aim.[8] The recent development in our lab of an efficient method for the conjugation of a wide array of GAG structures to a BSA protein scaffold which can be readily quantified by a fluorogenic azidocoumarin sulfonylfluoride linker (ACSF) provided a useful platform for the assembly of neoproteoglycans capable of promoting FGF2/FGFR interactions and which could potentially overcome challenges in the covalent assembly of aptamer-GAG conjugates. Briefly, heparin modified at the reducing terminus by ACSF, or 5'-ACSF modified DNA aptamer is conjugated to BSA bearing cyclooctyne functional handles via SPAAC (Figure 5.7). After purification by spin filtration the Hep-BSA, Hep-Apt, or Hep-BSA-Apt conjugates are characterized by UV-Vis spectroscopy and can be utilized in biological assays. Importantly, the fluorogenic readout enables quantification of the composition of the neoproteoglycans during the assembly process as the ratio of fluorescence at $\lambda = 393$ nm and 477 nm.

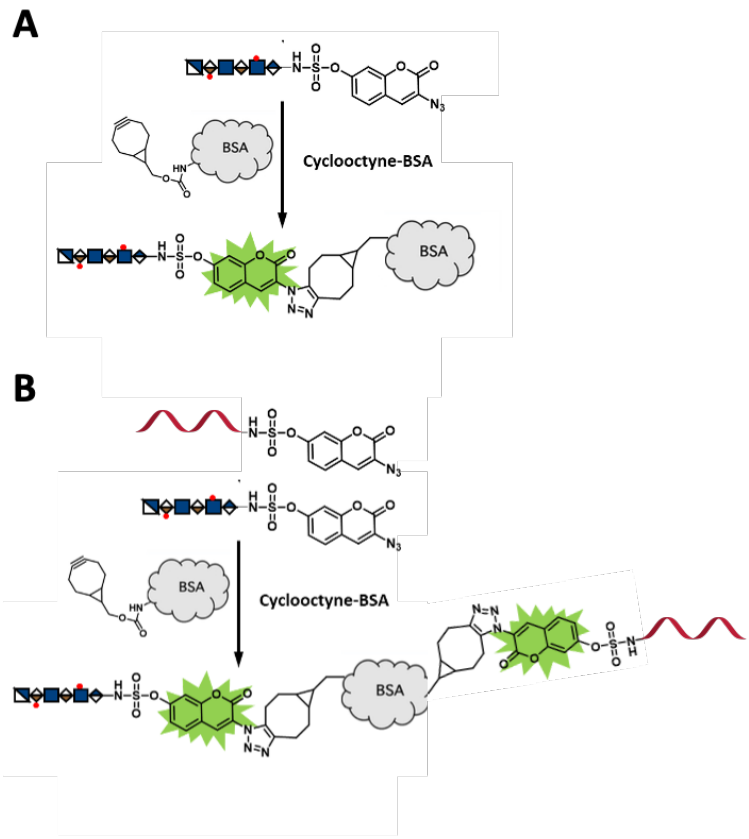

Figure 5.7 Approached for generating (A) Hep-BSA conjugates or (B) Hep-BSA-Apt conjugates via fluorogenic ACSF click reactions.

We evaluated the activity of the Hep-BSA conjugates prepared (Figure 5.8A) in FGF2 stimulation assays to measure their effect on downstream signalling, namely the phosphorylation of Erk1/2. Display of heparin from the BSA protein scaffold resulted in enhanced FGF2 signaling assay over a comparable quantity of soluble heparin at the suggesting that multivalent presentation of the heparin motif better engages growth factors at the cell surface and results in growth factor receptor complex formation to promote cell signaling. Soluble Hep-BSA promotes formation of FGF2/FGFR ternary complex and subsequent Erk1/2 phosphorylation (Fig 5.8A). Ext1$^{-/-}$ cells were serum starved before stimulation with exogenous FGF2 (25 ng/mL) in the presence of BSA, heparin, or Hep-BSA conjugates at increasing concentrations (Fig5.8B). While BSA alone

does not result in increased Erk1/2 phosphorylation a dose-dependent increase in phosphorylation is observed for both soluble heparin and Hep-BSA conjugates bearing seven heparin chains per BSA scaffold. Note that Erk1/2 phosphorylation for Hep-BSA conjugates is consistently higher than that of soluble heparin at the equivalent concentration by GAG. We also evaluated the signaling activity of Hep-BSA conjugates bearing an increased number of heparin chains normalized to Hep concentration (Fig 5.8C) and observed increased Erk1/2 phosphorylation with increasing valency, suggesting that the multivalent display allows the neoproteoglycan to better engage FGF2/FGFR at the cell surface. Together, these data indicate that the multivalent presentation of heparin from a protein scaffold improves bioactivity relative to soluble heparin.

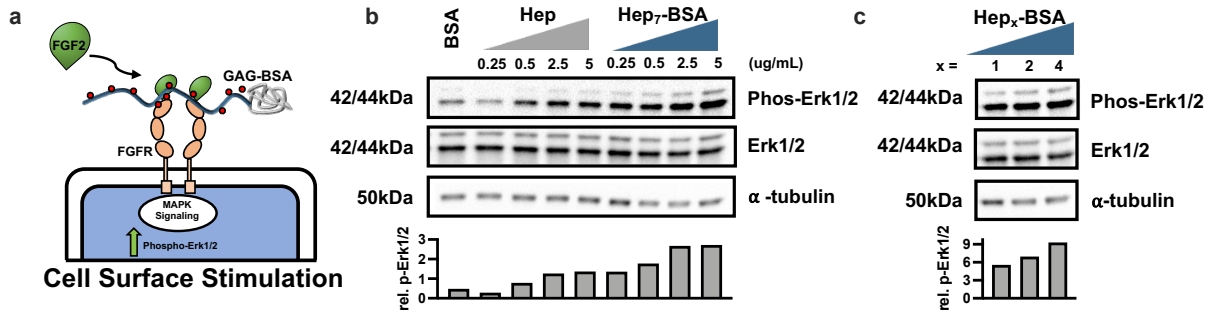

Figure 5.8 GAG-BSA conjugates can be used to stimulate MAPK activity. (A) Representation of GAG-BSA facilitated FGF2/FGFR interaction, resulting in higher levels of Erk1/2 phosphorylation. (B) GAG-BSA conjugates bearing approximately 7 heparin chains per BSA show a dose-dependent increase in Erk1/2 phosphorylation greater than that of soluble heparin at equivalent concentrations. (C) A dose-dependent increase in Erk1/2 phosphorylation is observed with increasing number of heparin chains per BSA conjugate.

This method may also be amenable to the installation of targeting elements including DNA aptamers capable of immobilizing the neoproteoglycan at the cell surface.

To evaluate the feasibility of this approach, 5'-amine modified DNA aptamers were functionalized with the fluorogenic ACSF linker and purified using a Nap5 column (GE Healthcare). BSA-cyclooctyne bearing 17 cyclooctyne groups per BSA was mixed with the ACSF-DNA and fluorogenic readout was monitored (Fig 5.9A). An increase in FL393/477 indicated covalent ligation of the BSA and DNA Apt at a stoichiometric ratio of ~1.5 DNA/BSA, indicating a mixture of BSA bearing 1 or 2 aptamers. BSA alone showed no increase in fluorescence, while free ACSF showed saturation of BSA cyclooctyne sites. A DNA control lacking ACSF showed minimal (background) fluorescent turn-on and a mixture of Hep-ACSF and BSA-cyclooctyne was used to benchmark the assay to previous results.

We also assessed the simultaneous addition of Hep-ACSF and DNA-ACSF to BSA cyclooctyne and observed an increase in FL 393/477 greater than that of heparin alone (Figure 5.9B, DNA-BSA condition). While it is likely that both DNA and Hep were conjugated to the BSA protein scaffold, the simultaneous addition of heparin and DNA complicated the characterization of the neoproteoglycans afforded. A two-step approach would obviate this challenge, and as such we sought to further modify the DNA-BSA prepared (Figure 5.9A) with Hep-ACSF (Fig 5.9C) and observed the formation of DNA-BSA-Hep conjugates, indicated by the further increase in FL 393/477 signal. Again, soluble ACSF quickly saturated BSA-cyclooctyne sites while BSA and DNA controls showed minimal background fluorescence. This approach may enable the rapid, quantitative assembly of more diverse glycomaterials suited for glycocalyx engineering.

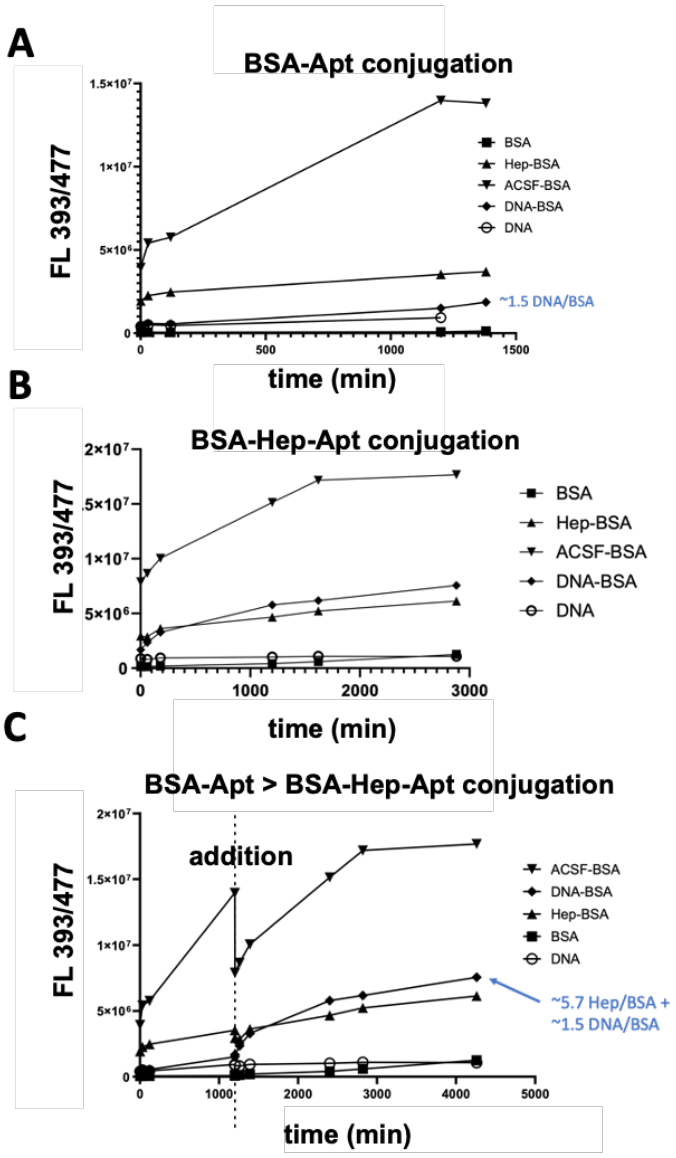

Figure 5.9 Conjugation kinetics of fluorogenic intensity versus time for conjugate assembly. (A) BSA-Apt conjugation results in ~1.5 aptamer per BSA over 21 hours. (B) Simultaneous Hep and Apt conjugation may be possible, but ratio of DNA:Hep:BSA cannot be readily determined. (C) Subsequent conjugation of Hep to BSA-Apt conjugates results in the preparation of glycomaterials bearing approximately 1-2 Apt and 5-6 Hep each as determined by increase in fluorescence upon click reaction.

5.4 Toward *in vivo* glycocalyx engineering

Despite advances[9] in materials-based glycocalyx engineering methods, *de novo* display of synthetic glycomaterials *in vivo* remains a considerable challenge. With an eye toward the application of our HS-glycomimetics to *in vivo* models, we sought to identify niches within the developing embryo suited for glycocalyx engineering and to evaluate the biodistribution of our synthetic materials. Having established several methods for targeting glycomaterials to Alpl$^+$ cells utilizing DNA aptamer 19S, we first looked at the expression of Alpl in whole embryos isolated from wild type mice at 9.5 dpc (Figure 5.10A). We performed immunohistochemistry and light sheet microscopy on intact embryos, staining for Alpl and the cell surface pluripotency marker SSEA-1 and observed robust binding. Alpl was widely expressed in these early stage embryos, and may provide a target for synthetic glycoconjugates.

We next evaluated the effects of HS mimetic RAFT glycopolymers bearing GlcNAc-6S and HepIA side chains on blood agglutination via activated partial thromboplastin time (aPTT) in human plasma (Figure 5.10B). We benchmarked the assay to soluble heparin, and observed minimal anticoagulant activity of the HepIA glycopolymers at 25-fold higher concentrations than soluble heparin to achieve the same effect. GlcNAc-6S glycopolymers exhibited even less anticoagulant activity.

Finally we sought to evaluate the toxicity and biodistibution of our synthetic HS-mimetic glycopolymers *in vivo* (Figure 5.10C). We injected wild type female mice at seven weeks with increasing concentrations of a near-IR labeled GlcNAc6S bearing glycopolymer mimetic and tracked their distribution via live dorsal imaging and subsequent organ analysis. We observed no toxicity or behavioral abnormalities up to the highest tested concentration evaluated (2 mg/kg). Live imaging revealed material

localized to the kidney and spleen. Bioavailability peaked approximately 30 minutes after retro-orbital injection and robust signal was observed as long as 120 min after injection. Subsequent organ analysis also revealed localization to the vasculature of the lungs. Together, these early experiments establish viability of a potential route toward the evaluation of our synthetic HS mimetic glycomaterials *in vivo*.

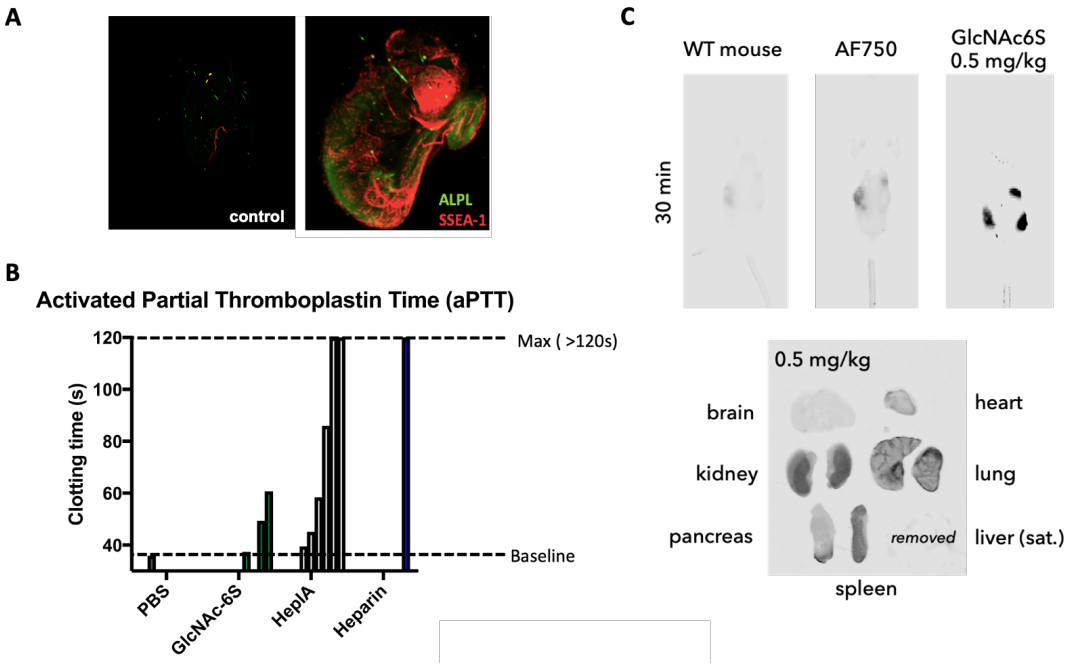

Figure 5.10 Early efforts toward *in vivo* glycocalyx engineering. (A) Whole mouse embryos were isolated and stained for embryonic markers SSEA-1 and ALPL to evaluate suitability of system for aptamer targeted glycocalyx engineering, as visualized by light-sheet microscopy. (B) The effect of GAG-mimetic glycopolymers on blood coagulation was determined to be minimal via activated partial thromboplastin time (aPTT) in human plasma, shown with increasing concentrations of material (0.05 - 5.00 μM). HepIA glycopolymers showed some anticoagulant activity at 25-fold higher concentrations than a heparin control to achieve the same effect. (C) WT mice were injected retro-orbitally with near-IR labeled GlcNAc6S glycopolymers to assess the toxicity and biodistribution of the material. The materials resulted in no toxicity up to the greatest concentration tested (2.0 mg/kg). Live dorsal imaging and organ imaging analysis revealed localization of the glycopolymer to the spleen and kidney, as well as the vasculature of the lung. Signal from the liver saturated the detector and was removed to facilitate imaging of the other organs. Robust signal was observed until 120 min after injection with bioavailability peaking at the 30min timepoint measured post injection. Soluble near-IR dye AF_{750} was injected as a control.

5.5 Remaining challenges and outlook

The glycan engineering space has emerged as a diverse and rapidly expanding research area which can provide critical insights into the functional roles of glycans at the cellular boundary. As techniques to interrogate the glycocalyx interactome continue to emerge, methods to control the composition and spatial distribution of glycocalyx structures will become increasingly important to elucidate the mechanisms by which glycans regulate biological processes and potentially inform therapeutic interventions. To that end, this work presents several methods which aim to enhance the specificity of synthetic materials for precision *de novo* glycan display. Identifying glycans with more specific binding profiles toward individual growth factor receptor pairs and developing strategies for their incorporation into synthetic materials primed for cell surface engineering will be crucial to implementing glycocalyx engineering in more complex and therapeutically relevant systems. Additionally, innovations in material design allowing for the incorporation of native or native-like structures will be needed to develop a more representative synthetic glycocalyx.

5.6 Methods

5.6.1 Aptamer – glycopolymer click reactions

SPAAC: DBCO modified DNA (100 μM) was mixed with 1.0 equivalent of azido-glycopolymer (0.1-0.8 mM) and allowed to mix for 48 hours at 40 ºC. CuAAC: Alkyne modified DNA (100 μM) was mixed with 1.0 equivalent of azido-glycopolymer (0.1-0.8

mM) in the presence of a precomplexed Copper(II)-TBTA mixture (10mM in 55% DMSO in water) and excess freshly prepared sodium ascorbate (40 equiv., 200mM in water) for 48 hours at room temperature.

5.6.2 SEC purification of aptamer glycoconjugates

Size exclusion chromatrography was utilized to purify crude aptamer glyocopolymer conjugation reactions (CuAAC and SPAAC) on Cytiva Akta fast protein liquid chromatography system equipped with a GE Superdex 200 Increase 10/300 GL column equilibrated in PBS. An isocratic method with PBS at 0.5 mL/min at 4C was utilized and samples were loaded onto a 100 uL sample loop following filtration through a 0.2um filter. Material was eluted into 0.50 mL fractions and UV monitoring at 254nm, 260nm, and 280nm was utilized to detect conjugates.

5.6.3 Agarose gel analysis and staining

Agarose was mixed in 1x TBE buffer (3% m/v) and boiled before being cast in a Thermo OWL Cast system. Samples were loaded in a 2:1 mixture of glycerol in water into the cooled gel, and ice cold TBE buffer was used to fill the gel tank. Gels were run at 105 V for 75 minutes, and aluminum foil was used to prevent photobleaching. To analyze gels, a BioRad GelDoc imaging system was utilized. Glycopolymer conjugates could be visualized either by polymer fluorescence (AF_{488}) with or without addition of Streptavidin-AF_{488} (1:1 equiv.) for biotinylated glycopolymers. To visualize by DNA, agarose gels were stained in 1X SYBR-Gold nucleic acid stain in TBE buffer for 30 min. Images were analyzed in ImageJ.

5.6.4 FGF2 ELISA assay

Antibodies against FGF2 were immobilized directly on the tissue-culture treated surface of standard 96-well plates (10 ug/mL in 1% BSA) for 24 hours at 4 ºC. Plates were washed with DPBS three times and 10nM FGF2 in 1% BSA was added for 4 hours at 23 ºC. After washing with a solution of 0.05% Tween-20 in DPBS the plates were blocked with 1%BSA (1 hr, 23 ºC) and biotinylated glycomaterials or biotin-heparin control were added (0-100 nM in 1% BSA) for 1 hour at 23 ºC. The wells were again washed three times and a 1:1000 dilution of streptavidin-HRP in 1% BSA was added for 30 min at 23 ºC. After washing three times, 100 uL of 1X TMB substrate was added and after approximately 2 min at 23 ºC sulfuric acid was added to quench the reaction (100 uL). The colorimetric assay was monitored by absorbance at 450 nm. All data were analyzed and fitted in Prism and points were collected in triplicate.

5.6.5 Cell surface remodeling with aptamer glycoconjugates

In order to remodel the surface of $Ext1^{-/-}$ mESCs and MEFs with aptamer glycoconjugates, cells were suspended with 0.05% Trypsin-EDTA and 10^6 cells were aliquoted into Eppendorf tubes. Cells were then blocked in an aptamer buffer consisting of DPBS (+Mg/+Ca) supplemented with 5mM $MgCl_2$, 0.45% glucose, and 0.1% BSA) for 1 hour on ice. During that time aptamer glycoconjugates were diluted to 200 nM in aptamer buffer and cooled on ice. Cells were pelleted and mixed with the aptamer glycoconjugates for 1 hour before washing with aptamer buffer an additional two times. Streptavidin-AF_{488} was then added (1:1000 in DPBS, 30 min) and cells were incubated

on ice before a final two DPBS washes. The cells were then anlayzed on a BD FACS Calibur system and data were analyzed in FlowJo. A minimum of 10,000 events were collected for each sample.

5.6.6 BSA-Hep conjugation reactions

DNA aptamer 19S with 5' amine modification (25 uL, 1mM in water) was mixed with >10 equivalents of ACSF (8.1 uL, 71.3 ug in DMSO) in the presence of 100 mM phosphate (5 uL, pH 8.0) and an additional 12 uL DMSO to a final volume of 50 uL. The mixture reacted at ambient temperature overnight. DNA was purified on a G-50 Sephadex column according to manufacturer protocol (Roche) and analyzed by nanodrop (800 pmoles per 100 uL). Reactions were prepared in PBS with 25uL of BSA-BCN (16-17 BCN/BSA) at a concentration of 1.0 mg/mL and either DNA-ACSF (75 uL) DNA-ACSF (20 uL) followed by Hep-ACSF (50 uL, 10 equiv.), or DNA-ACSF(25 uL) and Hep-ACSF (50 uL, 10 equiv.). Wells were monitored by fluorescence at (393 nm and 473 nm) and after 48hours were subjected to 50kDa MWCO spin filtration.

5.6.7 Cell stimulations with BSA-Hep conjugates

FGF2 Stimulation and Western Blotting was performed as previously reported. Briefly, mouse embryonic stem cells ($Ext1^{-/-}$) were cultured in 6-well plates treated with 0.1% gelatin before being serum starved for 20 h in mESC growth media lacking FBS. Cells were then treated with 25 ng/mL recombinant human basic FGF (Peprotech) in serum-free medium with heparin, BSA, or Heparin-BSA conjugates (5 ug/mL) for a duration of 15 min at 37C, 5% CO2. The cells were then immediately chilled and lysed

using a 1X RIPA lysis buffer supplemented with PMSF (1 mM) and 1X protease/phosphatase inhibitor cocktail. Cell lysates were analyzed by BCA assay to determine total protein concentration. 10 ug total protein from each sample was resolved on a 10% SDS-PAGE gel and transferred to a PVDF membrane for blotting. The membrane was blocked with 5% BSA/TBST for a minimum of 1 hr at room temperature prior to staining (overnight, 4C) with anti-phospho Erk, anti-total Erk, or anti-alpha tubulin (1:750, 1:1000, 1:40000 respectively in 5% BSA). After multiple TBST washes the membrane was incubated with HRP conjugated secondary antibodies (1:2000 anti-rabbit HRP and 1:10000 anti-mouse HRP, respectively) for approximately 1.5 hours at room temperature. Following a series of TBST washes the blots were visualized using Luminata Forte HRP detection reagent and imaged on a gel scanner (BioRad GelDoc). For sequential staining blots were washed in TBST, stripped using Restore PLUS western blot stripping buffer, washed again in TBST and then blocked in 5% BSA for at least 1 hr at room temperature before further staining. Images were analyzed using FIJI, where either phospho-Erk1/2 or total-Erk1/2 was normalized to alpha tubulin, before phospho-Erk was normalized to total-Erk. The levels of relative Erk phosphorylation were determined by setting the phosphorylation of Erk in samples containg Ext1-/- mESCs without FGF2 or material to equal 1.

5.6.8 Whole embryo staining and light sheet microscopy

Wild-type mice (C57BL/6) were utilized in accordance with UC San Diego animal care and use guidelines and all experiments were approved by UC San Diego. Embryos were isolated by dissection at 9.5 dpc and subsequently washed in PBS, transferred to

well plates, and fixed in 4% paraformaldehyde for 1.5 hours at 4 ºC. After six washes with PBS (5 min each) embryos were permeabilized in 0.1% Triton-X100 in PBS (PBT) for 1 hour at room temperature. Following an hour of blocking at room temperature in 10% FBS in 0.1% Triton-X100 in PBS primary antibody was added (1:200 dilution of either R&D Biosystems mALPL polyclonal Goat IgG or Santa Cruz Biotechnologies SSEA-1(480)-AF647) in 1% FBS/PBT overnight at 4 ºC. Following five additional washes in PBT (30 min each) secondary antibody was utilized (1:200 Molecular Probes Alexafluor488 Chicken anti-Goat IgG) in 1% FBS/PBT overnight at 4 ºC. An additional five washes (30 min, PBT) were used prior to mounting for light sheet microscopy. Briefly, CUBIC-R1 clearing reagent was used for approximately 2 minutes before embryos were mounted in agarose (approx. 1% in CUBIC) and the mounted embryos were soaked in CUBIC-R1 for an additional 48 hours. The mounted embryos were then imaged on a Zeiss Z.1 lightsheet microscope and images were processed utilizing Zeiss and Arivis software.

5.6.9 Biodistribution and toxicity assays

Wild-type mice (C57BL/6) were utilized in accordance with UC San Diego animal care and use guidelines and all experiments were approved by UC San Diego. Procedures were performed under anesthesia (isoflurane 1-2% with 1L/min O_2). Purified glycomaterials were filtered through 0.2 um filters and introduced by retroorbital injection at concentrations between 0.0-2.0 mg/kg in sterile DPBS. Near-IR optical probes on the materials allowed for live dorsal visualization on a Licor Odyssey system immediately following the injections at increasing time intervals. Following imaging at increasing timepoints (0 - 120 min) the mice were sacrificed in accordance with UC San Diego animal

care and use guidelines and major organs were harvested for additional scanning on the Licor system. Images were processed and analyzed in ImageJ.

5.7 Acknowledgements

Section 5.3 contains, in part, unpublished material coauthored by Ryan Porell, Julianna Follmar, and Kamil Godula. The dissertation author was the primary researcher for the data shown. The work described in Section 5.4 was conducted at the UCSD Glycobiology Research and Training Facility and Comparative Phenotyping Core Facility. I thank Qiongyu Chen of the UCSD murine hematology core for assistance with APTT assays. Mouse experiments were conducted with the assistance of Dr. Daniel Sandoval and Gregory Golden (Esko laboratory). I thank Dr. Chelsea Painter for murine husbandry, embryo isolation, and assistance with staining and light sheet microscopy. Light sheet microscopy was made possible by the UCSD Microscopy Core Facility (via NINDS P30 Grant: P30NS047101) and with assistance from Dr. Marcy Derb.

5.8 References

1. Malaker, S. A., Pedram, K., Ferracane, M. J., Bensing, B. A., Krishnan, V., Pett, C., Yu, J., Woods, E. C., Kramer, J. R., Westerlind, U., Dorigo, O., & Bertozzi, C. R. The mucin-selective protease StcE enables molecular and functional analysis of human cancer-associated mucins. *Proc. Nat'l. Acad. Sci*. 2019, 116(15), 7278–7287. DOI: 10.1073/pnas.1813020116.

2. Kraushaar, D.C.; Yamaguchi, Y.; Wang, L. Heparan sulfate is required for embryonic stem cells to exit from self-renewal. J. Biol. Chem. 2010, 285(8), 5907-5916. DOI: 10.1074/jbc.M109.066837.

3. Pulsipher, A.; Griffen, M.E.; Stone, S.E.; Hsieh-Wilson, L.C. Long lived engineering of glycans to direct stem cell fate. Angew. Chemie. Int. Ed. 2014, 54(5), 1466-1470. DOI: 10.1002/anie.201409258.

4. Kramer, J.R.; Onoa, B.; Bustamante, C.; Bertozzi, C.R. Chemically tunable mucin chimeras assembled on living cells. Proceedings of the National Academy of Sciences, 112(41), 12574 – 12579. DOI: 10.1073/pnas.1516127112.

5. Huang ML, Smith RAA, Trieger GW, Godula K. 2014 Glycocalyx Remodeling with Proteoglycan Mimetics Promotes Neural Specification in Embryonic Stem Cells. J. Am. Chem. Soc. 136, 10565–10568. DOI: 10.1021/ja505012a.

6. Hou, Z.; Meyer, S.; Propson, N.E.; Nie, J.; Jiang, P.; Stewart, R.; Thomson, J.A. Characterization and target identification of a DNA aptamer that labels pluripotent stem cells. Cell Res. 2015, 25(3), 390-393. DOI: 10.1038/cr.2015.7.

7. Naticchia MR, Laubach LK, Tota EM, Lucas TM, Huang ML, Godula K. 2018 Embryonic Stem Cell Engineering with a Glycomimetic FGF2/BMP4 Co-Receptor Drives Mesodermal Differentiation in a Three-Dimensional Culture. ACS Chem. Biol. 13, 2880–2887. DOI: 10.1021/acschembio.8b00436

8. Trieger, G.W.; Verespy, S.; Gordts, P.S.L.M.; Godula, K. Efficient synthesis of heparinoid bioconjugates for tailoring FGF2 activity at the stem cell-matrix interface. Bioconjugate Chem. 2019, 30(3), 833-840. DOI: 10.1021/acs.bioconjchem.8b00921.

9. Woods EC, Yee NA, Shen J, Bertozzi CR. 2015 Glycocalyx Engineering with a Recycling Glycopolymer that Increases Cell Survival In Vivo. Angew. Chem. Int. Ed. 54, 15782–15788, (doi: 10.1002/anie.201508783).